# **Journal Name**

# **ARTICLE TYPE**

#### Cite this: DOI: 00.0000/xxxxxxxxxx

# Dye-Sensitized Solar Cells Strike Back

Ana Belén Muñoz-García, a lacopo Benesperi, b Gerrit Boschloo, a Javier J. Concepcion, d Jared H. Delcamp, e Elizabeth A. Gibson, b Gerald J. Meyer, f Michele Pavone, Henrik Pettersson, h Anders Hagfeldt $^{*c,i}$  and Marina Freitag $^{*b}$ 

Received Date Accepted Date

DOI: 00.0000/xxxxxxxxxx

Dye-sensitized solar cells (DSCs) are celebrating their 30<sup>th</sup> birthday and they are attracting a wealth of research efforts aimed at unleashing their full potential. In recent years DSCs and dye-sensitized photoelectrochemical cells (DSPECs) have experienced a renaissance as the best technology for several niche applications that take advantage of DSCs' unique combination of properties: low cost, non toxic, colorful, transparent, and very efficient in low light conditions. This review summarizes the advancements in the field over the last decade, encompassing all aspects of the DSC technology: theoretical studies, characterization techniques, materials, applications as solar cells and as drivers for the synthesis of solar fuels, and commercialization efforts from various companies.

# 1 Introduction

Unprecedented changes in the world's energy production are required to meet with the urgent need to replace fossil fuels to mitigate their effects on climate change, and to keep pace with the ever-increasing global demand for energy. This calls for a rapid shift towards large scale implementation of renewable energy sources, of which sunlight has by far the largest potential. The challenge for scientists is to explore new materials for the creation of devices that can be mass-produced and efficiently convert light energy into electricity or solar fuels at a lower cost with sustainability in mind. Since renewable energy sources currently account for only about 10% of the total energy supply 1 (29% of the total electricity supply), 2 there is room for a large increase in energy production from solar cells in the near future.

The Sun is the largest source of energy when taking into account both sustainable and non-renewable sources, as it supplies

Exactly 30 years ago, in 1991, Michael Grätzel and his research group realized a new kind of solar cell: the dye-sensitized solar cell, DSC, or Grätzel cell. <sup>6</sup> This is a very promising alternative to classical inorganic p-n junction solar cells as it combines molecular systems and nanoparticles to create a device that mim-

the world with 173 000 TW of energy each year. 3 In other words, more energy from the Sun reaches the Earth in one hour than the human population consumes in a year. Photovoltaic electricity generation has grown at an average rate of more than 34% each year over the last 10 years, making it the world's fastest developing energy technology. 4 However, photovoltaic cells contribute only 1% of the global energy production. The International Energy Agency (IEA) predicts a 50% increase in renewable electricity production from 2019 to 2025. 5 Particularly, the rapid increase in the ability of consumers to generate their own electricity presents new opportunities and challenges for electricity providers and policymakers worldwide. As a result, distributed solar PV systems in homes, commercial buildings, and industries are predicted to gain a solid market position and their capacity is expected to increase up to 320 GW by 2025, <sup>5</sup> nearly doubling the current installation capacity and providing plenty of space for the enhancement of existing technologies and the production of new devices. There are currently no photovoltaic technologies that are as matured in production as the dominant Si-based solar technology. Rival inorganic technologies typically have achieved similar efficiencies to Si (e.g. GaAs or CIGS) for single cell systems; however, these systems all remain very costly either due to production processes or raw material costs. Cost concerns among these photovoltaic technologies has led researchers into a third generation of devices: hybrid solar cells, which are built on affordable and abundant raw materials with the potential for very high efficiencies.

<sup>&</sup>lt;sup>a</sup> Department of Physics "Ettore Pancini", University of Naples Federico II, 80126 Naples. Italy.

<sup>&</sup>lt;sup>b</sup> School of Natural and Environmental Science, Newcastle University, Bedson Building, NE1 7RU Newcastle upon Tyne, UK. E-mail: marina.freitag@newcastle.ac.uk

<sup>&</sup>lt;sup>c</sup> Department of Chemistry, Ångström Laboratory, Uppsala University, P.O. Box 523, 751 20 Uppsala, Sweden.

<sup>&</sup>lt;sup>d</sup> Chemistry Division, Brookhaven National Laboratory, Upton, New York 11973, USA.

Department of Chemistry and Biochemistry, University of Mississippi, University, MS 38677. USA.

f Department of Chemistry, University of North Carolina at Chapel Hill, Chapel Hill, North Carolina 27599, USA.

<sup>§</sup> Department of Chemical Sciences, University of Naples Federico II, 80126 Naples, Italy.

<sup>&</sup>lt;sup>h</sup> Dyenamo AB, Teknikringen 38A, 114 28 Stockholm, Sweden.

<sup>&</sup>lt;sup>1</sup> University Management and Management Council, Vice Chancellor, Uppsala University, Segerstedthuset, 752 37 Uppsala, Sweden. E-mail: anders.hagfeldt@uu.se

<sup>\*</sup> Corresponding author.

ics photosynthesis, with the objective of turning sunlight into a renewable, reliable, and low-cost source of energy closer to existence. The first demonstration of dye injection into a single crystal semiconductor was provided by Gerischer in 1966, 7,8 but it was Grätzel's introduction of a mesoporous semiconductor layer that let to the breakthrough in DSC technology. In DSCs, dyes are responsible for light absorption and charge separation and, therefore, for the conversion of photons to electrons. Dyes are bound to mesoporous semiconductors, which are only used to collect the resulting free electrons and transport them to the electrode as current. <sup>9</sup> Electrons flow back into the system through a charge transport material, which regenerates the dye molecules, thus closing the circuit. 10-12 DSC devices exhibit impressive energy efficiencies of over 13% under full sun illumination. 13 Further, they are based on inexpensive starting materials and simple production techniques. 14,15 Some concern has been raised about the sealing of liquid junction solar cells. <sup>16–19</sup> Therefore, improvements to seal approaches or the replacement of the liquid electrolyte with a solid charge transport material resulting in so-called solid-state dye-sensitized solar cells (ssDSCs) could have significant impact on industrialization. 20-24

With no clear third generation solar cell technology being dominant for mass production given significant concerns across all technologies, it is expected that DSCs will have years of thriving development ahead of them toward high efficiency outdoor applications. Additionally, DSCs are exceptional among third generation technologies with regard to specific applications. DSCs can be designed with a high degree of flexibility concerning shape, color, and size, as well as providing unique deployment scenarios. DSCs remain a competitive third generation alternative photovoltaic technology for several reasons including: (i) simple preparation methods, which will help to convert solar energy in a sustainable way, (ii) fabrication without the use of toxic materials, (iii) design flexibility, which allows DSCs to be implemented in many different environments, from transparent smart windows to consumer electronics to indoor applications which enables the powering of the next digital revolution of widely distributed sensors forming the Internet of Things (IoT).

The research progress during the past ten years in the field of DSCs is marked by important breakthroughs towards their use for a sustainable future. Relentless endeavours made it possible to achieve high efficiencies with DSCs in outdoor and indoor environments. These considerable advances were made by developing new panchromatic rigid structure dye systems, new redox shuttles and hole transport materials, and by gaining new knowledge about dye and redox shuttle fundamental behavior. Under full sun illumination (standard AM1.5G), power conversion efficiencies have reached 13% (certified value) 13 and 14% (non certified) with co-sensitized organic dyes. 25 The new redox couples and electrolytes based on cobalt and copper coordination complexes are able to regenerate the dye with less than 0.2 V driving force, which allows for the fabrication of lower thermal waste systems. Current research and developments are the perquisite to improve efficiencies beyond 20%. Here, this review offers an updated overview of advanced characterization methods and current research trends of this transitioning technology, from the perspectives of device and molecular modelling to state-of-art techniques and novel device structures. Every device component is acknowledged, from metal oxides and new dyes to novel hole transporters, dopants, and counter-electrodes. Additional applications and constructs are discussed including p-type DSCs, tandem DSCs, and dye-sensitized solar fuel production. Past and current commercialization efforts are also showcased.

#### 1.1 Light and energy

All photovoltaic devices, such as solar cells, convert solar radiation into electricity on the basis of the photovoltaic effect, discovered by the French physicist Alexandre Edmond Becquerel. <sup>26</sup> The photovoltaic effect is linked to the photoelectric one, a phenomenon in which electrons are expelled when light shines on a conducting material. For the explanation of this phenomenon, Albert Einstein received the 1921 Nobel Prize in physics, introducing new quantum principles. <sup>27</sup> It is described as the appearance of an electric voltage between two electrodes attached to a solid or liquid system when light shines onto it.

In space, the solar spectrum resembles that of a black body at a temperature of 5760 K and includes a wide range of wavelengths, from X-rays to radio waves, with the main peak in the visible range (see Fig. 1). While travelling through Earth's atmosphere, parts of the spectrum are filtered out (e.g. X-rays) and the solar spectrum reaching the planet surface is different compared to space. The light path through the atmosphere is defined as air mass (AM). <sup>28</sup> As the solar spectrum distribution varies during the day and at different locations, a standard reference spectrum was established in order to compare the performance of photovoltaic devices from various manufacturers and research labs. The AM1.5 Global (AM1.5G) spectrum has a combined power intensity of 1000 W  $\ensuremath{\text{m}}^{-2}$  (100 mW  $\ensuremath{\text{cm}}^{-2}$  ) and is used as standard for the efficiency measurement of solar cells. <sup>29,30</sup> The irradiance of sunlight, whose curve is shown in Fig. 1, is defined as the amount of energy of a certain light wavelength shone on a unit area per unit of time,  $J s^{-1} m^{-2} nm^{-1}$  (W m<sup>-2</sup> nm<sup>-1</sup>). This spectral irradiance can be integrated over all wavelengths to obtain the overall irradiance in W  $m^{-2}$ .

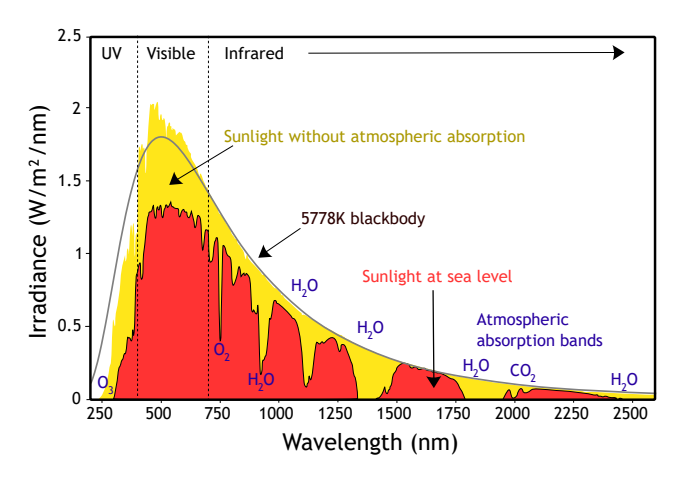
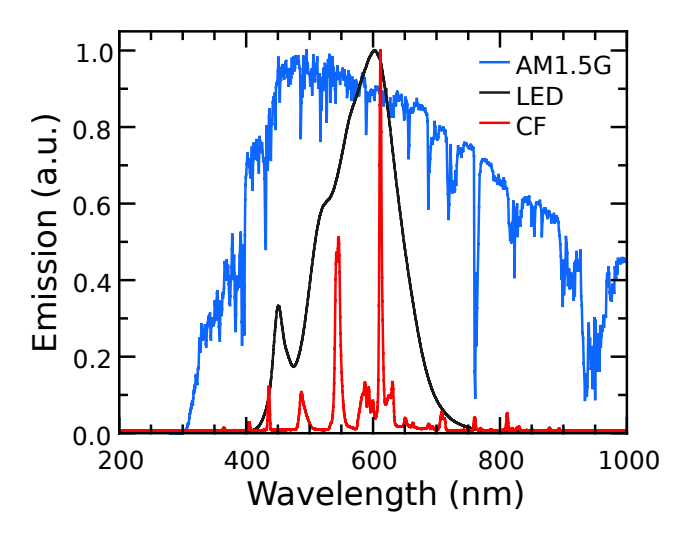


Fig. 1 Solar irradiance spectrum. Artwork created by Nick84 and released under Creative Commons BY-SA 3.0 license, ref. 31.

While DSCs perform well under sunlight, since dye light absorption profiles are commonly limited to the visible part of the solar spectrum, they perform even better when illuminated by artificial light sources, whose emission spectrum is similar to the visible range of that of the Sun (Fig. 2). 32-37 Since indoor light intensity is orders of magnitude smaller than sunlight and the spectra of the different light sources vary considerably between them, from an experimental point of view indoor lighting conditions are quite different from the solar irradiance outdoors. The intensity of typical indoor lighting has illuminance values ranging from 200 to 1000 lx (lux, which corresponds to lumen per unit area,  $lm m^{-2}$ ). For comparison, AM1.5G light has an illuminance value of about 100 000 lx. Illuminance is similar to irradiance (measured in W  $m^{-2}$ ), but it defines light intensity in terms of human eye perception rather than energy. Illuminance cannot be converted to irradiance via a simple mathematical operation and while the latter can be used to quantify solar cell performance directly, the former cannot. At the same illuminance, in fact, different light spectra will produce different irradiance. For example, a light bulb emitting blue light with 1000 lx illuminance will produce more irradiance than a bulb emitting red light with the same illuminance. Only after the lamp spectrum has been determined can the illuminance be obtained from irradiance using Eq. 1:

$$\mathit{IL}[lx] = \frac{683.002}{A} \left[ \frac{lm}{W \cdot m^2} \right] \int I(\lambda) \cdot E(\lambda) \left[ \frac{J}{s \cdot nm} \right] \cdot \bar{y}(\lambda) \cdot d\lambda \quad (1)$$

Where IL is the illuminance,  $I \cdot E$  is the irradiance (considering the area A outside of the integral), given by the product of the light intensity I and the photon energy E, and  $\bar{y}$  is the dimensionless photopic luminosity function of the human eye centered about 555 nm.



**Fig. 2** Normalized emission spectra of warm white fluorescent and LED bulbs, and of the AM1.5G standard. Reproduced from ref. 38 with permission from The Royal Society of Chemistry.

In the case of sunlight measurements there are several guidelines that describe standard experimental conditions, as well as how to test the solar cell, see e.g. ASTM standard E948.<sup>39</sup> For indoor measurements, however, no standard has been defined yet.

#### 1.2 Operation principles and structure

The basic components of a dye-sensitized solar cell are the dyesensitized semiconductor electrode (the working electrode or photoanode), the redox electrolyte and the counter electrode. A monolayer of dye molecules adsorbed on the semiconductor surface is responsible for light absorption in the device. In conventional DSCs, the semiconductor has an n-type character: electrons in the conduction band are responsible for electrical conductivity of the material. Furthermore, the semiconductor has a wide bandgap and does not significantly contribute to solar light absorption. By far the most applied semiconductor in DSCs is TiO<sub>2</sub> with the anatase crystal structure, which has a bandgap of  $\sim$ 3.2 eV and absorbs only UV light. TiO<sub>2</sub> will be assumed as the semiconductor for the remainder of this part, noting here that a large number of semiconductors can actually be used in the DSC. A flat and dense TiO<sub>2</sub> electrode with an adsorbed dye monolayer does not absorb enough light to give practically relevant solar-toelectric conversion efficiencies. In order to harvest a large part of the solar spectrum, TiO2 electrodes possessing high-surface areas are used, such as the mesoporous TiO2 electrode. This electrode consists of numerous interconnected nanoparticles that are typically about 20-30 nm in size. The porosity of the electrode is about 50% and its surface area can be several hundred times larger than the projected area. As such, the amount of dye adsorbed is also several hundred times larger than for a flat surface. Dye molecules that are chemically bound to the TiO2 have the best performances in the DSC. These molecules are also in contact with the redox electrolyte that fills the pores of the mesoporous electrode. The redox mediator transports positive charges to the counter electrode, which is typically located in parallel close to the working electrode.

Photoinduced electron transfer from a dye molecule to the conduction band of  $TiO_2$  is the first step in the working mechanism of a dye-sensitized solar cell, see Fig. 3. When light is absorbed by the dye (D), an electron is excited to a higher energy level. The excited dye (D\*) can subsequently inject an electron into the conduction band of  $TiO_2$ , which provides a variety of acceptor levels (reaction 1 in Fig. 3). This electron transfer process occurs on the femto- to picosecond time scale.

Electrons in the mesoporous semiconductor are charge compensated by ions in the surrounding electrolyte, and their transport is driven by diffusion. Electrons are collected at the back contact on a millisecond time scale under full sunlight illumination. The slow and light-dependent electron transport is generally explained using a multiple trapping model with an exponential trap distribution below the conduction band, <sup>40</sup> however the nature of the traps is still debated. In recent work, it was found that upon electron accumulation into mesoporous TiO<sub>2</sub>, cations adsorb onto the semiconductor surface. <sup>41</sup> This could lead to electrostatic traps for the electrons in mesoporous TiO<sub>2</sub> and account for the observation of similar trap distributions for different types of metal oxides.

The sensitized  $TiO_2$  is in contact with an electrolyte containing a redox mediator ( $R^+/R$ ) that regenerates the dye (i.e. reduction of the oxidized dye  $D^+$ , reaction 2 in Fig. 3), and also transfers

positive charges from the working to the counter electrode, by means of diffusion of  $R^+$ . At the counter electrode  $R^+$  is reduced to R (reaction 3). The dye regeneration process is typically on the microsecond time scale and must be fast enough to prevent recombination of electrons from the semiconductor to the oxidized dye (reaction 4). Electrons can also recombine with the oxidized form of the redox mediator (reaction 5).

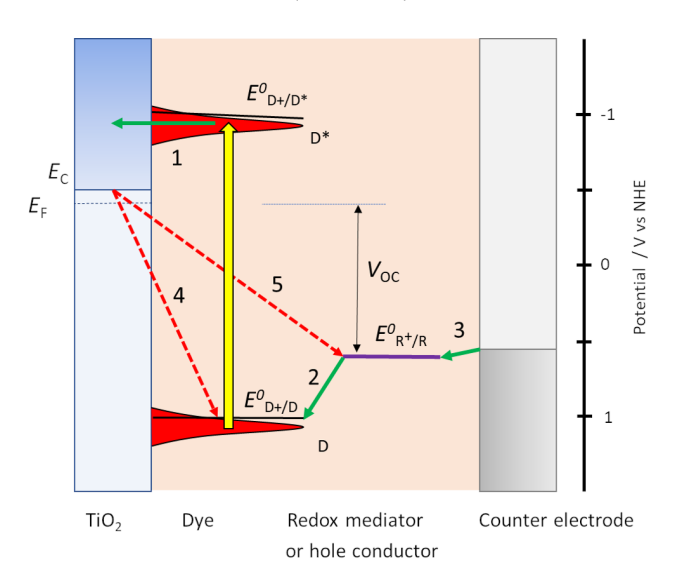


Fig. 3 Basic diagram of the dye-sensitized solar cell, displaying working mechanism and energy levels.

Fig. 3 also provides the basic energy level diagram of the DSC. The ground-state energy level of the dye is located just below  $E^0(\mathrm{D}^+/\mathrm{D})$ , the standard reduction potential of the dye, and is often referred to as the HOMO (highest occupied molecular orbital) level. The energy level of the excited dye  $\mathrm{D}^*$  is obtained by adding the absorbed photon energy. The lowest-lying excited state level is obtained by adding  $E_{0-0}$  (the zero-zero transition energy), which is generally obtained experimentally from the intercept of normalized absorption and fluorescence spectra. This level is often referred to as the LUMO (lowest unoccupied molecular orbital) level.

 $D^*$  levels should be higher than the conduction band edge  $E_{\rm C}$  of the semiconductor, so that there will be overlap with the conduction band levels, which leads to efficient photoinduced electron injection. Fluorescence of the dye and non-radiative decay processes are competing with the injection reaction. For optimum DSC performance,  $D^*$  and  $E_{\rm C}$  should be well matched, so that a high quantum yield of injection is obtained, while at the same time  $E_{\rm C}$  should be as high as possible to obtain a good output voltage in the DSC.

There should also be good matching between the energy levels of dye and redox mediator: sufficient driving force for reduction of the oxidized dye is needed to drive this reaction fast enough to prevent losses through electron/dye recombination. On the other hand, the driving force should not be excessive, as it lowers the voltage output of the DSC.

The voltage output of the DSC is the potential difference between working electrode and counter electrode, see Fig. 3. The potential of the counter electrode is close to that of the redox potential of the electrolyte, and equal to it when no current is flowing, under open-circuit conditions. The potential of the working electrode is equal to the Fermi level of the semiconductor at the back contact. The Fermi level  $E_{\rm F}$  is given by:

$$E_{\rm F} = E_{\rm C} - \frac{k_{\rm B}T}{e} \ln \frac{n_{\rm c}}{N_{\rm c}} \tag{2}$$

where  $k_{\rm B}$  is the Boltzmann constant, T the absolute temperature, e the elementary charge ( $k_{\rm B}T/e$  is 0.0257 V at room temperature),  $n_{\rm C}$  is the density of conduction band electrons, and  $N_{\rm C}$  is the effective density of electronic states at the bottom of the conduction band.  $N_{\rm C}$  is about  $10^{20}$  cm<sup>-3</sup> for TiO<sub>2</sub> anatase. Under solar cell operation,  $n_{\rm C}$  should as be high as possible to obtain a Fermi level close to the conduction band and a high output voltage. This requires relatively slow electron recombination kinetics.

#### 1.3 Device structures

The standard device structure for the DSC is the sandwich cell, in which both working and counter electrodes are based on conducting glass substrates that are placed face-to-face, with a thin layer of the redox electrolyte in between (Fig. 4a). The distance between the electrodes is usually determined by a thermoplastic frame that also acts as the sealing, and it is typically about 25  $\mu$ m. An even narrower spacing is favorable, as this decreases the resistance due to redox mediator transport in the electrolyte. 42 Fluorine-doped tin oxide (FTO)-coated glass is most frequently used as conducting glass in DSCs. FTO glass provides a good compromise between high chemical and thermal stability, low sheet resistance and high solar light transmittance. The photoelectrode consists of FTO glass with the dyed mesoporous TiO2 film sintered on top. An optional thin and dense TiO2 layer (the so-called blocking layer), whose function is to decrease electron recombination from the FTO to the redox electrolyte, can be located between the FTO and the mesoporous TiO<sub>2</sub>. A light-scattering TiO<sub>2</sub> layer can be added on top of the mesoporous layer to improve light capture in the device. The counter electrode is FTO glass with a catalyst, such as Pt nanoparticles, carbon, or a conducting polymer deposited on top of it. The sandwich structure allows for (semi-)transparent solar cell devices and the possibility for illumination from either side, provided that the counter electrode is transparent.

Monolithic DSC structures have advantages over the sandwich structure from a fabrication and cost point of view. Only one FTO glass substrate is used, onto which the different layers are screen-printed: first the mesoporous TiO<sub>2</sub>, then a porous insulating layer and finally a porous carbon layer that acts as counter electrode and electrical conductor (Fig. 4b). The redox electrolyte is infiltrated in all three layers, and a back sealing covers the whole device. This device structure is well suited for scaling up to modules with series or parallel interconnections. The highest reported efficiency for a monolithic DSC with a carbon counter electrode is 7.6%. <sup>43</sup> The carbon electrode in the monolithic DSC can be replaced by other conductors. For instance, highly-doped PEDOT films have been used in combination with a porous polyethylene separator film, reaching an efficiency of 7.7%, and also allowing

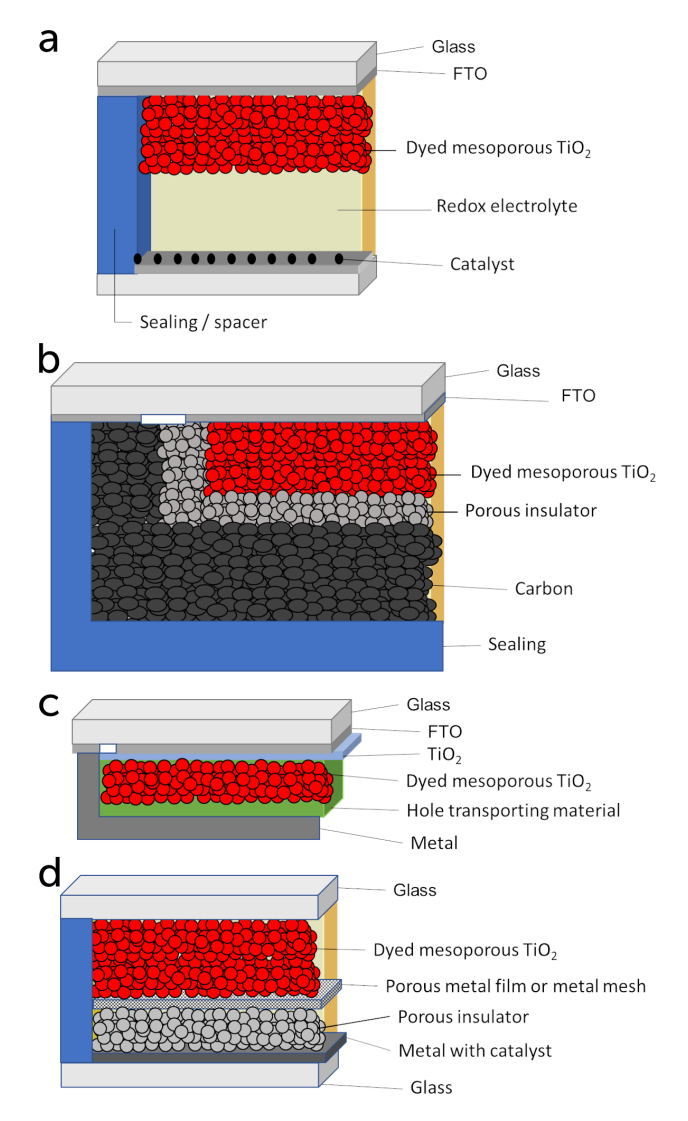


**Fig. 4** Device structures for dye-sensitized solar cells: (a) sandwich cell, (b) monolithic cell with carbon counter electrode, (c) solid-state DSC (monolithic), and (d) conducting glass-free DSC design.

for flexible devices.  $^{44}$  Recently, a Ni metal foil with Cr coating and Pt catalyst was implemented instead of the carbon electrode, and an efficiency of 8.0% was achieved.  $^{45}$ 

In the solid-state DSC the liquid redox electrolyte is replaced with a solid hole transporting material (HTM). It is also a monolithic structure, see Fig. 4c.  $^{46}$  A critical step in the fabrication is the infiltration of the hole conductor into the mesoporous  $\rm TiO_2$  layer. Solution-based methods do not result in complete pore filling.  $^{23}$  Furthermore, a thin capping HTM layer is needed, onto which the metal contact is evaporated.

It is possible to avoid FTO-coated glass altogether in DSC structures. Several types of back-contact DSC devices have been developed, where the mesoporous TiO<sub>2</sub> film is contacted at the back with a porous metal film <sup>47</sup> or a metal mesh. <sup>48</sup> A suitable metal is titanium, which forms a passivating oxide layer. Alternatively, a stainless steel mesh can be used if it is coated with a thin passivating layer. The counter electrode can also be Ti metal, but it should then be provided with a suitable catalyst. A possible lay-

out of a DSC avoiding conducting glass is shown in Fig. 4d. The advantages of such a DSC are a higher solar light transmittance of the top glass, and a very low sheet resistance of the working and counter electrodes, allowing for much larger area solar cells.

#### 2 Characterization

## 2.1 Power conversion efficiency and J-V characteristics

The efficiency of a solar cell is its most important performance parameter. We will refer to it as the power conversion efficiency (PCE), in order to clearly distinguish it from quantum efficiencies. The PCE is usually obtained from the current density (current per unit area, J) vs. potential (V) characteristics of the solar cell, recorded under illumination by a solar simulator. The standard measurement condition is illumination with 100 mW cm $^{-2}$  light with AM1.5G spectral distribution, while the cell is kept at 25 °C.  $^{39}$ 

J-V curves are recorded using a source meter or a potentiostat that can apply a controlled potential to the device and measure the current. Typically, *J-V* curves are recorded using voltage steps of 5 or 10 mV. After each voltage step some delay time should be applied (more than 100 ms) before the current measurement is done, in order to allow for the current to reach a stable value. <sup>49</sup> If the chosen delay time is too short, J-V curves recorded in the forward and reverse direction are not identical: hysteresis is observed. While hysteresis in J-V curves has been widely discussed in the field of perovskite solar cells, it has not attracted much attention in the DSC field. The origin of hysteresis in DSC is attributed to: (i) capacitive currents, caused by (dis)charging of the mesoporous electrode after the potential step, <sup>50</sup> and (ii) mass transport in the electrolyte and resulting concentration gradients in the redox couple concentrations. 51 Hysteresis becomes very apparent in DSCs with practical electrolytes that are more viscous than the volatile acetonitrile-based electrolytes that are used for record devices.

From the J-V curve several parameters can be determined:  $J_{SC}$ , the current density at zero applied potential; and  $V_{OC}$ , the opencircuit potential, which is the potential found at zero current. At the maximum power point (MPP) the power output of the device (which is the product of J and V) reaches a maximum,  $P_{MPP}$ , see Fig. 5. The fill factor (FF) is the ratio between  $P_{MPP}$  and the product of  $V_{OC}$  and  $J_{SC}$ . A high value of the FF (closer to 1) gives a more square-looking curve and indicates the ability of the solar cell to deliver current and potential at the same time. The PCE is given by Eq. 3, where  $P_{\text{light}}$  is the power density of the incoming light.

$$PCE = \frac{P_{\text{MPP}}}{P_{\text{light}}} \times 100\% = \frac{V_{\text{OC}}J_{\text{SC}}FF}{P_{\text{light}}} \times 100\%$$
 (3)

In order to correctly calculate the PCE, the active area of the solar cell device needs to be determined accurately. The most reliable method used in the DSC field is to place a black metal mask with an aperture – the area of which is used for the PCE calculation – directly on top of the solar cell. Also, any light entering from the sides should be blocked. This ensures that no light from outside the aperture area is channeled into the solar cell. The aperture area should be either similar to, or smaller than the DSC

working electrode. <sup>52</sup> If a small aperture is used, part of the DSC is not illuminated. This, however, does not affect the measured PCE much since the non-illuminated areas of the DSC do not contribute much to recombination current in most cases. It is useful to record the *J-V* curve in the dark as well for further analysis of the solar cell, which should not use the aperture area, but instead the measured working electrode area for correct analysis.

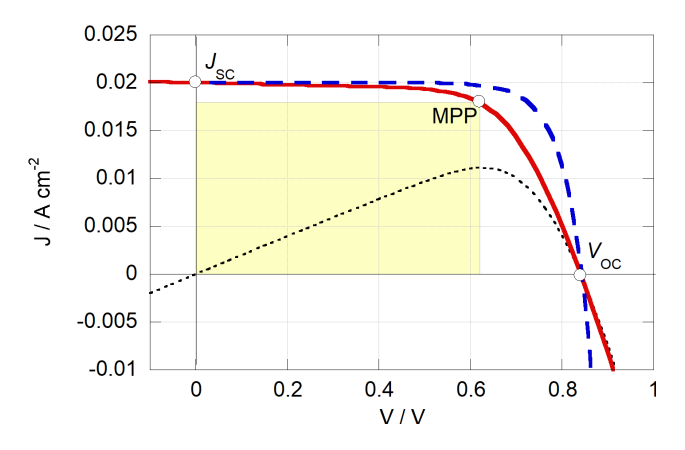


**Fig. 5** Simulated *J-V* curves of a solar cell using the Shockley diode model with (red line) and without (blue stripes) series and parallel resistance losses.  $R_{\rm s}$  and  $R_{\rm p}$  are 5 and 1000  $\Omega$  cm<sup>2</sup>, respectively;  $J_{\rm s}=1.5$  nA cm<sup>-2</sup>; n = 2. The resistance losses reduce the PCE from 13.1% to 11.2%, due of the reduced fill factor (from 78% to 66%). The black dotted line the is the device's power output with resistance losses. The yellow square represents the device's power output.

The general shape of the *J-V* curve of a DSC is well-described by the Shockley diode equation with additional resistive losses, see Eq. 4,

$$V = \frac{nk_{\rm B}T}{e} \ln \left( \frac{J_{\rm ph} - J}{J_{\rm S}} - \frac{V - JR_{\rm S}}{J_{\rm S}R_{\rm p}} + 1 \right) - JR_{\rm S}$$
 (4)

where n is the diode quality factor,  $k_{\rm B}$  the Boltzmann constant, T the absolute temperature,  $J_{\rm ph}$  the generated photocurrent density,  $J_{\rm S}$  the reverse bias saturation current density, and  $R_{\rm S}$  and  $R_{\rm p}$  the series and parallel (or shunt) resistances (units:  $\Omega$  cm²), respectively, see circuit in Fig. 6 and Eq 4. The series resistance originates from the resistance of the conducting glass, the charge transfer resistance at the counter electrode and the resistance due to diffusion of the redox mediator in the electrolyte. The parallel resistance can originate from physical contact between the working and counter electrodes, but it can also describe part of the electron recombination, which is not described by the diode.

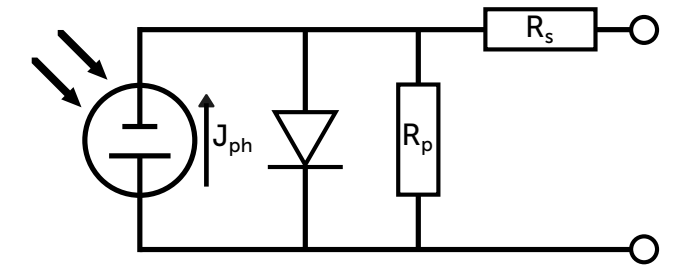


Fig. 6 Representation of a solar cell as a schematic circuit.

MPP tracking is an alternative method to obtain the PCE of a solar cell. The perturb-and-observe method is frequently applied where a step-wise change in potential is made and it is checked whether the product of J and V increases or decreases; then, depending on the outcome, the next step is made in either the positive of negative potential direction. MPP tracking is a useful method to prove that the DSC is a stable and regenerative system. For example, Boschloo and co-workers added a triphenylamine-based electron donor to a cobalt-based electrolyte and found a significantly improved performance. <sup>53</sup> In principle, a sacrificial donor in the DSC electrolyte could give very high apparent PCE from J-V analysis. However, MPP tracking during 250 h under 1 sun illumination demonstrated that every donor molecule had been cycled 3  $\times$  10<sup>5</sup> times without any apparent degradation. <sup>53</sup>

#### 2.2 J-V characterization in ambient light conditions

Although the practicalities of solar cell measurement in ambient light (indoor) conditions are the same as those described above for sunlight simulation, the interpretation of the results is more complex. A brief overview of the challenges and best practices for reporting ambient light *J-V* measurements is provided here, while a more detailed discussion can be found elsewhere. <sup>38</sup>

As detailed in Eq. 3, PCE is a function of the power provided by the light source,  $P_{\text{light}}$ . In the case of sunlight there is a unique source of light, with well-known characteristics and a constant, standardized value of  $P_{light}$ . Indoor, on the other hand, there is a great variety of different light sources. This leads to the conclusion that, while in simulated sunlight measurements the reported PCE value of a solar cell can always be translated to the device's absolute power output via a simple mathematical operation, the same does not apply to ambient light measurements. In the latter case, in fact,  $P_{\text{light}}$  is unknown, and it is the experimentalist's responsibility to measure it accurately for the light source in use. Therefore, when performing and reporting about indoor J-V measurements: (i) extra care should be taken in the determination of  $P_{light}$  for the correct computation of the PCE value, (ii) the make and model of the light source should always be specified, together with its emission spectrum, and (iii) the P<sub>MPP</sub> value should always be reported alongside the PCE value. This last point is particularly important to facilitate the comparison of results from different laboratories, because a given solar cell configuration may have a very similar P<sub>MPP</sub> output when illuminated by different light sources, but very different PCE values depending on the overlap between the device absorption and the light source emission spectra.

During practical experiments, in the case of sunlight the adjustment of the light intensity to the desired value is easily achieved through the use of a reference cell calibrated by a certification authority. However, there cannot be a calibrated reference cell in the case of indoor measurements, unless every laboratory in the world agrees to use the same light bulb. Light intensity determination in ambient light experiments is usually carried out with the use of a lux meter, which provides a value of the illuminance at the measuring spot. However, lux meters are generally bulky tools, and their correct placement inside the testing equipment

could be cumbersome. This difficulty arises from one more hurdle that ambient light measurements must overcome compared to simulated sunlight experiments. In the latter case, in fact, the intensity of the light source is about two orders of magnitude higher than that present in a common laboratory room. As such, the testing equipment can be easily placed on an open laboratory bench and the eventual contribution to the device photocurrent of the light present in the room will be negligible. In the former case, however, the intensity of the light source is of the same order of magnitude of that present in the laboratory room. Therefore, the testing equipment must be properly encased, so that it is completely isolated from the laboratory environment.

### 2.3 Incident photon-to-current conversion efficiency (IPCE)

In an IPCE measurement monochromatic light – typically generated by passing white light through a monochromator – falls onto the solar cell and the short-circuit photocurrent is recorded as a function of the light's wavelength. The IPCE is calculated using Eq. 5 and is normally plotted as function of wavelength, yielding a spectrum that is sometimes referred to as the photocurrent action spectrum.

IPCE[%] = 
$$\frac{1240}{\lambda [\text{nm}]} \times \frac{J_{\text{SC}}[\text{A cm}^{-2}]}{P_{\text{light}}[\text{W cm}^{-2}]} \times 100\%$$
 (5)

In the equation,  $\lambda$  and  $P_{\text{light}}$  are the wavelength and the power density of incident light, respectively. IPCE can be measured using DC or AC methods. In the DC method, only monochromatic light is used, while in the AC method chopped monochromatic light is applied, and a constant white light can be added. The AC photocurrent response is measured using a lock-in amplifier. The two methods should yield the same result, provided that the photocurrent scales linearly with light intensity and that the chopping frequency in the AC mode is sufficiently low.

Integration of the IPCE spectrum with respect to the AM1.5G irradiance ( $\phi_{AM1.5G}$ ) gives a calculated value of the  $J_{SC,IPCE}$  (Eq. 6):

$$J_{\rm SC,IPCE} = \int {\rm IPCE}(\lambda) \cdot e \cdot \phi_{\rm AM1.5G} \, d(\lambda) \tag{6}$$

A good match between  $J_{\rm SC,IPCE}$  and  $J_{\rm SC}$  measured using a solar simulator gives added confidence in the validity of IPCE and  $J_{\rm SC}$  measurements. Significant differences can point to calibration errors of the systems.

# 2.4 Impedance spectroscopy

Small-modulation techniques are particularly useful to study complex systems like the DSC. We can distinguish between electrical modulation techniques, such as electrochemical impedance spectroscopy, and optical modulation techniques, such as transient photovoltage (TPV), discussed below.

Electrochemical impedance spectroscopy (EIS) is a widely used general technique in science and technology. A small sinusoidal potential modulation with an amplitude of about 10 mV is superimposed onto a base potential, and the amplitude and phase-shifts of resulting sinusoidal current changes are measured. This

is repeated for a large series of frequencies, for DSC typically in the  $10^5-10^{-1}$  Hz range, to obtain a complete EIS spectrum. The impedance is given by  $z=\mathrm{d}V/\mathrm{d}I$  and is often represented as a complex number: z=z'+jz'', where j is  $\sqrt{-1}$ , z' is the real part of the impedance, and z'' the imaginary part, which is phase-shifted by  $90^\circ$ . The real part of the impedance reflects resistance, while the imaginary part originates from capacitance and inductance. For a resistor the impedance is independent of frequency, z=R, while for a capacitor  $z=-(j\omega C)^{-1}$ , where C is the capacitance and  $\omega$  the angular frequency. An equivalent circuit, consisting of electrical elements R, C, L (inductance), CPE (constant phase element, a non-ideal capacitor), and  $Z_{\rm d}$  (diffusion impedance or Warburg element) is used to fit the experimental EIS spectrum.

A convenient EIS analysis of DSC is done under illumination at open-circuit conditions. An example is shown in Fig. 7,54 where 3 semicircles can be found, corresponding to 3 processes in the DSC with significantly differing time constants. The lefthand semicircle, at higher frequencies, is due to the charge transfer resistance at the counter electrode ( $R_{\rm CE}$ ) and to the double layer capacitance at the counter electrode/electrolyte interface ( $C_{\rm CE}$ ), giving a time constant  $au_{\rm CE} = R_{\rm CE} \cdot C_{\rm TiO_2}$ . At intermediate frequencies, the recombination resistance at the mesoporous  $TiO_2$ /electrolyte interface,  $R_{rec}$ , and the capacitance of the mesoporous  $TiO_2$ ,  $C_{TiO_2}$ , form the second semicircle. The electron lifetime in  $TiO_2$ ,  $\tau_e$ , is given by  $\tau_e = R_{rec} \cdot C_{TiO_2}$ . At the lowest frequencies, the impedance due to diffusion of the redox mediator in the electrolyte,  $Z_d$ , forms the third semicircle.  $Z_d$  is given by  $Z_{\rm d}=R_{\rm d}\tanh(j\omega/\omega_{\rm d})\cdot(j\omega/\omega_{\rm d})^{-1}$ , where  $R_{\rm d}$  is the diffusion resistance and  $\omega_d$  is  $D/L^2$ , with D the diffusion coefficient and L the effective electrolyte layer thickness. 55 The high frequency intercept at the Z' axis is the series resistance caused by the conducting glass  $R_{TCO}$ .

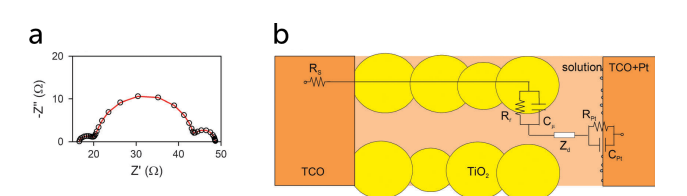


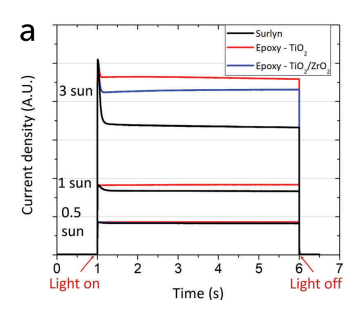
**Fig. 7** (a) Impedance spectrum (Nyquist plot) of a dye-sensitized solar cell under illumination, recorded at  $V_{\rm OC}$ . (b) Schematic model to fit the EIS under these conditions. Adapted from ref. 54 with permission from the PCCP Owner Societies.

An EIS measurement in the dark at the same applied potential would yield slightly different results: there is for instance no electron recombination to oxidized dye molecules. Furthermore, there could be a rather large current flow in the device, which leads to potential drops and a less well-defined Fermi level in the mesoporous TiO<sub>2</sub>. The local concentrations of the redox mediator in the device will also be different. However, the advantage of a dark EIS measurement is that it allows for the direct probing the sensitizer influence on recombination resistance from electrons in TiO<sub>2</sub> transferring to the redox shuttle in the absence of increased electrode heat and without competing processes such as recombi-

#### 2.5 Opto-electrical transient techniques

Opto-electrical transient measurements and charge extraction methods provide a very useful tool for understanding processes occurring in dye-sensitized solar cells. Detailed description and analysis of such techniques can be found elsewhere. <sup>57,58</sup> Opto-electrical transient techniques include photocurrent/voltage transients, that can be performed either as small or large modulation techniques.

Light off/light on modulation is easy to perform experimentally and can give useful information. Short-circuit photocurrent transients can provide evidence for accumulation or depletion of the redox mediator in different parts of the DSC. For instance, if the concentration of oxidized redox mediator is too low at the counter electrode, a high value of  $J_{\rm SC}$  cannot be maintained and electrons in TiO<sub>2</sub> will have to recombine with the oxidized dye or redox mediator. Such a situation can occur in viscous electrolytes when the oxidized form of the mediator is present in too low concentration, see Fig. 8. <sup>59</sup>



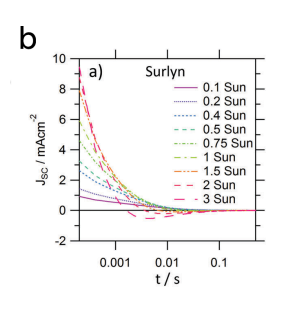


**Fig. 8** Photocurrent transients of a DSC with a Cu complex-based electrolyte. (a) Under high light intensities and with a relatively thick electrolyte layer (Surlyn:  $30~\mu m$ ) a clear spike is found in the photocurrent onset transient. (b) In the photocurrent decay transient a reversal of current can be found, due to accumulation of oxidized redox species in the mesoporous electrode, which are reduced by electrons in the  $TiO_2$ . Adapted from ref. 59 with permission from the PCCP Owner Societies.

Charge extraction methods provide information of the accumulated electrons in the mesoporous  ${\rm TiO_2}$  electrode as a function of potential and/or light intensity. During the extraction, part of the accumulated electrons may recombine before being collected. The extracted charge should therefore be considered as a lower limit of the actual accumulated charge. Integration of the photocurrent decay transient over time gives a good measure of the accumulated charge in mesoporous  ${\rm TiO_2}$  electrodes under short-circuit illumination conditions. To obtain the charge under opencircuit illumination conditions, a double switch is needed: light is switched off and simultaneously the cell is switched from opencircuit to short-circuit conditions. Plotting the extracted charge as a function of the  $V_{\rm OC}$  gives a useful trend that can be used to assess band-edge changes, for instance as a function of the sensitizer or of additives to the electrolyte.

Small optical modulation techniques, namely transient photocurrent (TPC) and photovoltage (TPV), provide information on electron transport in the mesoporous  $TiO_2$  and electron recom-

bination, respectively. The modulation can be in the form of a sine wave: the technique is then called IMPS or IMVS (intensitymodulated photocurrent or voltage spectroscopy, respectively), and multiple frequencies are analyzed. Alternatively, the modulation is in the form of a small pulse or of a step, and the response is recorded in the time domain. Similar information can be obtained from EIS measurements, but TPC and TPV in the time domain have the advantage of being a rapid measurement that can be analyzed quickly, since the photocurrent or photovoltage response to a small light modulation has a simple exponential form, where the time constant is the electron transport time (provided that no significant recombination takes place) for photocurrent transients, or the electron lifetime  $\tau_e$  for photovoltage transients. Fig. 9 gives an example of charge extraction and photovoltage transient results for different dyes used in co-sensitized DSC devices. 60

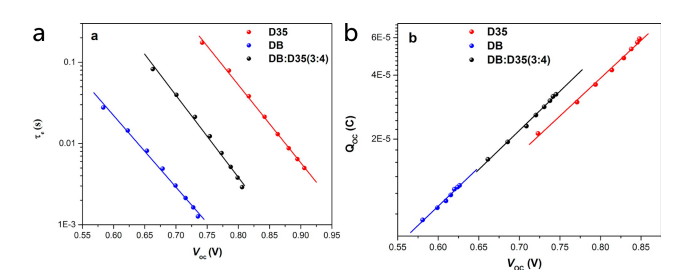


**Fig. 9** (a) Electron lifetime and (b) accumulated charge as a function of  $V_{\rm OC}$  for DSCs with a cobalt-based electrolyte, sensitized with D35, Dyenamo blue (DB), or both. Band-edge shifts of the different dyes are small, however a large difference in electron lifetime is found. Adapted with permission from ref. 60. Copyright 2016 American Chemical Society.

#### 2.6 Spectroscopy

An important attribute of the mesoporous anatase thin films introduced by Grätzel and O'Regan is that they are amenable to spectroscopic characterization from the visible to the terahertz region (400 nm – 3 mm) in transmission mode with high signal-to-noise ratios. 6 Spectroscopic studies have provided keen insights into the fundamental electron transfer reactions responsible for electrical power generation and recombination reactions that lower efficiency. Such spectroscopic data has also been used to test existing theories of interfacial electron transfer. <sup>61</sup> Steady-state spectroelectrochemical measurements provide thermodynamic information on the dye-sensitized interface, while pulsed or modulated light excitation provides access to kinetics. In this section, insights gained over the last ten years from spectroscopic studies of dye-sensitized interfaces are presented. Unless otherwise stated, sensitized anatase TiO2 thin films immersed in organic electrolytes at room temperature can be assumed.

Emphasis is placed on the kinetics and mechanisms for photoinduced interfacial charge separation, sensitizer regeneration, and charge recombination. The sensitizer ground and excited state reduction potentials are often taken from measurements in fluid solution and are assumed to remain unchanged upon surface anchoring. However, there is now growing evidence that the physical location of sensitizers within the electric double layer results in behavior very different from that in a fluid solution, a point that is elaborated upon here.  $^{62}$  An interesting observation is that the sensitizer redox chemistry rarely obeys the Nernst equation when anchored to TiO<sub>2</sub>. Recall that a 59 mV change in the applied potential should result in a factor of ten change in concentration at room temperature, but for sensitizers anchored to TiO<sub>2</sub> it typically requires an  $\sim$ 100 mV potential step. This behavior is typically quantified by the introduction of a "non-ideality" factor ( $\alpha$ ) in the modified Nernst equation (Eq. 7).

$$E = E^{\circ} + \frac{\alpha \times 59 \text{ mV}}{n} \log \frac{[Ox]}{[Red]}$$
 (7)

Insights into the origin(s) of this non-ideal equilibrium redox chemistry came from metalloporphyrin sensitizers that had two adjacent quantifiable redox couples when surface anchored, Co(III/II) and Co(II/I).  $^{63}$  The Co(III/II) reduction was nearly ideal yet the Co(II/I) process had a large non-ideality factor of  $1.6 \leq \alpha \leq 2.5$ . Such behavior was not easily rationalized with a "Frumkin" model wherein intermolecular interactions influence the redox equilibria. Instead, the data were most consistent with a model wherein a fraction of the electric field was present across the inner Helmholtz plane of the electric double layer. The results indicated that non-ideality was most significant when the TiO $_2$ (e $^-$ ) concentration was high with a percentage potential drop of only  $\sim \! 15\%$  for the Co(III/II) couple and 45% for Co(II/I).  $^{63}$ 

Further insights into non-Nernstian redox chemistry were gained from sensitizers where a redox active center closest to the oxide surface showed a higher non-ideality factor  $\alpha=1.4\pm0.2$  than a more remote center with  $\alpha=1.1\pm0.1$ . <sup>64</sup> This suggested that proximity to the oxide surface and location within the electric double layer contribute to non-Nernstian behavior. The impact of the electric field on the spectroscopic and the non-exponential kinetics described below remains unknown. More fundamental research is needed to fully elucidate the origin(s) of this intriguing interfacial redox chemistry.

# 2.6.1 Photoinduced, interfacial charge separation.

Light-initiated transfer of an electron from a sensitizer to a semiconductor provides a molecular means to convert light into potential energy in the form of an interfacial charge separated state comprised of an oxidized sensitizer and an injected electron. The charge separation mechanism that has received the most attention from a practical and fundamental point of view involves light absorption to form a sensitizer excited state followed by electron transfer to the semiconductor, a process that is often called electron injection. 65 This is the focus here. In addition to the aforementioned one, two alternative mechanisms have been identified to create an interfacial charge separated state with light. In a photogalvanic-type mechanism, the sensitizer excited state is first reduced by an electron donor followed by electron transfer from the reduced sensitizer to the semiconductor. In some cases, it has proven difficult to distinguish this mechanism from the case where the excited state is the donor. 66 The second involves specific classes of dyes that form strong adducts that give rise to a new absorption band(s) due to direct charge transfer to the semiconductor. <sup>67</sup> While these latter two mechanisms are well documented in the dye-sensitization literature, they have received less mechanistic and practical attention over the last ten years.

**2.6.1.1** Excited-state electron injection. It has been known for some time that electron transfer from a photoexcited sensitizer to  ${\rm TiO_2}$  can occur on ultrafast femtosecond time scales. <sup>65</sup> If such excited-state electron injection was quantitative and general, a wide variety of sensitizers and light absorbing materials could be widely employed. Unfortunately, this is not the case. Below, excited-state injection is discussed for inorganic charge transfer excited states and organic sensitizers.

#### Inorganic charge transfer excited states

A recent advance in excited-state injection was garnered from a kinetic study of  $[Ru^{II}(4,4'-(PO_3H_2)_2-2,2'-bipyridine)(LL)_2]^{2+}$ sensitizers, where (LL) is an ancillary 2,2'-bipyridine ligand that tuned the excited-state potentials from -0.69 to -1.03 V vs. NHE. 68 Excited-state injection showed biphasic kinetics occurring mainly at the 3-30 ps and 30-500 ps range in acidic aqueous solution. The slower process was assigned to injection from the thermally-equilibrated excited state with rate constants that were directly correlated to the excited-state potential E° (RuIII/II\*). Strong photoreductants transferred electrons to TiO2 more quickly than did weaker excited state reductants. Electrochemical measurements were used to estimate the TiO2 acceptor state distribution and the overlap with  $E^{\circ}(Ru^{III/II^*})$  was correlated with the injection rate constant. Such behavior is expected based on Gerischer's model for interfacial electron transfer. The faster injection components were not analyzed in detail and were assigned to injection from higher energy unequilibrated excited states. The data indicate that the commonly reported non-exponential kinetics for electron injection can be rationalized by a continuous decrease in the injection rate constants that accompany excited-state relaxation from the initially formed Franck-Condon state to the thermally-equilibrated photoluminescent state (Fig. 10). 68

Historically, Fe(II) diimine complexes have resulted in very low excited-state injection yields and there is now a detailed theoretical 69,70 and experimental 71,72 understanding of this. In brief, the charge transfer excited states are rapidly deactivated through low-lying metal-centered states. The exciting discovery of luminescent N-heterocyclic Fe(II) carbene complexes with long-lived excited states has dramatically changed this landscape. 73-77 A comprehensive study with electron paramagnetic resonance spectroscopy, transient absorption and terahertz spectroscopies, and quantum chemical calculations revealed an injection yield of 0.92 from the MLCT excited state. 74 Such injection yields were unprecedented for charge transfer excited states based on iron sensitizers. The key to success was the realization of a 18  $\pm$  1 ps charge transfer excited state whose lifetime exceeds that of iron polypyridyl complexes by about a thousand-fold. The nearly quantitative injection yield has motivated many to explore related Fe(II) carbene complexes with ground state Fe(III/II) potentials favorable for regeneration with donors like iodide. 75-77 First row transition metal sensitizers based on Cu(I) and Co(I) have also

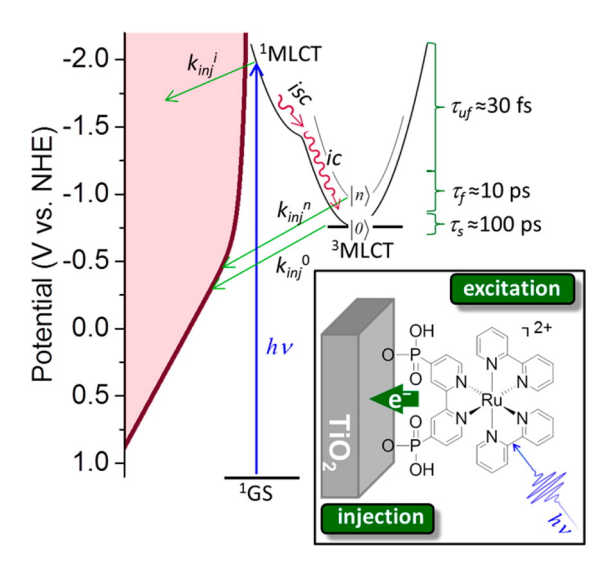


Fig. 10 The energetic overlap of the initially-formed Frack-Condon state ( $^1 \text{MLCT}$ ) and the photoluminescence  $^3 \text{MLCT}$  with the acceptor states in anatase TiO $_2$  at pH 1. Intersystem crossing (isc) and internal conversion (ic) compete kinetically with excited-state injection. Inset shows the sructure of a Ru(II) sensitizer undergoing excited-state injection. Adapted with permission from ref. 68. Copyright 2016 American Chemical Society.

been found to inject electrons efficiently into TiO<sub>2</sub>. <sup>78–80</sup>

## Organic excited states

The late Charles Schmuttenmaer reported novel terahertz injection studies of porphyrins and metalloporphyrins anchored to TiO<sub>2</sub> and SnO<sub>2</sub>. <sup>79–82</sup> The long-term goal of these studies was dyesensitized water oxidation, and high potential porphyrins that were weak excited state reductants was the predominant focus. The injection yields were often less than unity on to TiO2 surfaces and were enhanced on  $SnO_2$  by virtue of a  ${\sim}0.5$  eV more positive conduction band edge. On both substrates and similar to the ultrafast injection studies with Ru(II) sensitizers, more rapid injection was observed with porphyrins that were stronger photoreductants in the fluorescent singlet excited state. The THz measurements were made in the absence of an electrolyte. An interesting aspect of the porphyrin sensitizers is the presence of low-lying triplet states whose population was shown to impact the injection yield. The orientation of the porphyrin with respect to the oxide surface was also controlled by functional groups for surface binding on the aromatic porphyrin ring or through axial ligation in metalloporphyrins. It is interesting to note that injection from porphyrins with hydroxamate binding groups was as good as that measured with the more commonly used carboxylate groups. <sup>79</sup>

Ultrafast excited-state injection studies of porphyrins anchored to  ${\rm TiO_2}$  through well-defined rigid linkers have been reported. <sup>83</sup> Application of a time domain vibrational spectroscopy pump degenerate four-wave mixing technique enabled identification of the Raman-active modes triggered by light absorption. The spectral data were assigned to modes based on the linker group and that localized on the porphyrin ring. The data suggested that this four-wave mixing technique can distinguish between vibra-

tional modes generated by light absorption from those generated by excited-state injection. <sup>83</sup>

In a related study, excited-state injection by (perylene-9-yl)carboxylate into TiO<sub>2</sub> was shown to be complete within 12 fs. <sup>84</sup> The ultrafast transient absorption data mapped the decay of the singlet excited state and the appearance of the oxidized perylene. Nonadiabatic quantum dynamic simulations indicated that injection was complete within 20 fs, in close agreement with the experimental value. The reorganization energy for electron transfer was estimated to be 220 meV. Non-equilibrium modes in the 1000-1800 cm<sup>-1</sup> region were assigned to in-plane asymmetric vibrations of the perylene sensitizers. The agreement between theory and experiment in these experiments indicates that these are powerful tools for quantifying vibronic effects at dyesensitized interfaces. <sup>84</sup>

# 2.6.2 Sensitizer regeneration.

Upon excited-state injection the oxidized sensitizer is reduced by an electron donor present in the electrolyte in a process known as sensitizer regeneration. It is not sufficient for the oxidized sensitizer to be thermodynamically competent of donor oxidation, the reaction must occur more rapidly than the competitive recombination, i.e. the electron transfer from the semiconductor to the oxidized sensitizer, with rate constant  $k_{\rm cr}$ . The most common and successful donor by far is iodide, with Co(II) diimine complexes also having a long history. Emergent new mediators based on Fe(III/II) and Cu(II/I) transition metal complexes have been characterized by transient spectroscopic techniques.

The classical iodide/triiodide redox mediators have been the subject of several prior reviews and are only summarized here. 85-87 Iodide oxidation yields a metastable species di-iodide,  $I_2^{-\cdot}$ , either through the iodine atom intermediate  $I^{\cdot} + I^{-} \rightarrow I_2^{-\cdot}$ or (possibly) through a concerted pathway. Di-iodide is unstable with respect to disproportionation:  $2I_2^{-} \rightarrow I_3^- + I^-$ . In acetonitrile solutions, the 1-electron reduction of I<sub>3</sub><sup>-</sup> by TiO<sub>2</sub>(e<sup>-</sup>) is thermodynamically uphill and the equilibrium concentration of I<sub>2</sub> is small. These factors allow for efficient transport of the injected electrons with minimal recombination. For champion sensitizers, iodide oxidation occurs on a hundreds of nanosecond time scale. Quantitative incident photon-to-current efficiencies (IPCE) at the short-circuit condition led many to conclude that regeneration by iodide was fully optimized. However, at the open-circuit or power point conditions, where the number of electrons in each nanocrystallite is large, there is now clear evidence that regeneration is non-quantitative.  $^{88,89}$  The regeneration quantum yield,  $\Phi_{reg}$ , has been determined spectroscopically by Eq. 8, where  $k_{reg}$  is the pseudo-first-order regeneration rate constant at molar donor concentration [D].

$$\Phi_{\text{reg}} = \frac{k_{\text{reg}}[D]}{k_{\text{cr}} + k_{\text{reg}}[D]}$$
(8)

Nanosecond transient absorption kinetic measurements were made with D- $\pi$ -A sensitizers as a function of the applied potential to simulate conditions along the current-voltage curve. It was found that  $\Phi_{reg}$  decreased from unity to 0.83 at the open-circuit condition with 0.5 M I<sup>-</sup>. For 0.3 M [Co(bpy)<sub>3</sub>]<sup>2+</sup>, the quan-

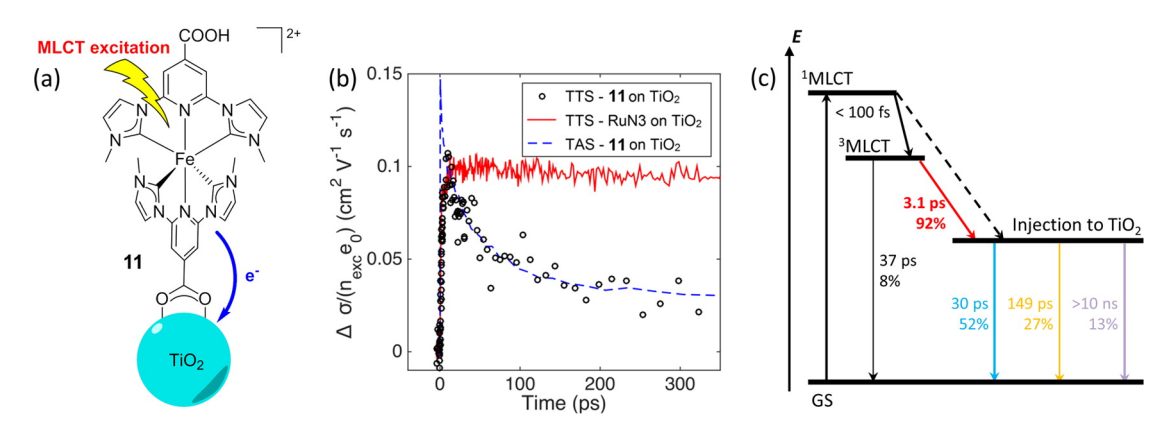


Fig. 11 (a) Chemical structure of the N-heterocyclic Fe(II) carbene complex anchored to TiO<sub>2</sub>. (b) Transient absorption and terahertz kinetic data for the iron carbene complex and for N3. (c) A Jablonski-type diagram. Reprinted with permission from ref. 75. Copyright 2016 American Chemical Society.

tum yield decreased to 0.60. <sup>88</sup> Irradiance-dependent photoelectrochemical measurements with the classical N3 sensitizer provided the same conclusion: regeneration is quantitative at short-circuit and non-quantitative at the open-circuit and power point conditions. <sup>89</sup> For alternative oxides, such as SnO<sub>2</sub>, regeneration has also been shown to be non-optimal due to the more rapid recombination. <sup>90</sup> Realization that regeneration can be better optimized to enhance fill factors and open-circuit photovoltages continues to inspire researchers to design interfaces capable of more rapid regeneration without a significant loss of free energy.

Regeneration kinetics have been enhanced with sensitizers competent of halogen and chalcogen bonding.  $^{91-93}$  Kinetic regeneration studies of organic D- $\pi$ -A sensitizers where the triphenyl amine donor was substituted with halogen atoms were conducted, Fig. 12. In their oxidized form the presence of a  $\sigma$ -hole for halogen bonding was apparent in the sensitizers with Br and I. Transient spectroscopic studies revealed a correlation between the sensitizer halogen bonding ability and the second-order regeneration rate constant by iodide, yet no trend was observed with [Co(bpy) $_3$ ] $^2+$ , which is incapable of halogen bonding. While the power conversion efficiency enhancements were small, these studies provided compelling evidence that halogen bonding can be utilized to enhance regeneration kinetics and yields at dyesensitized/TiO $_2$  interfaces.

A notably rapid regeneration process was reported for highly cationic Ru(II) sensitizers, [Ru(tmam)<sub>2</sub>(dcb)]<sup>6+</sup>, where tmam is the quaternary ammonium derivative, i.e. 4,4′-bis-(trimethylaminomethyl)-2,2′-bipyridine. <sup>94</sup> When anchored to TiO<sub>2</sub>, these sensitizers showed clear evidence for ion-pairing with iodide and anionic cobalt redox mediator ( $K_{\rm eq} > 10^4 \ {\rm M}^{-1}$ ) in acetonitrile. With the Co mediators, excited-state injection and regeneration occurred on time scales less than 10 ns. Ion-pairing removed the diffusional limitations associated with sensitizer regeneration and almost doubled the IPCE. <sup>94</sup>

An interesting aspect of Cu(II/I) bipyridyl mediators is that the two redox states often have very different coordination environments.  $^{95-102}$  The Cu(I) redox state is typically four-coordinate with a pseudo-tetrahedral geometry, while Cu(II) is subject to a Jahn-Teller distortion that is often manifest in five-coordinate

complexes with the fifth ligand derived from solvent or counterion. In a comprehensive study with three different D- $\pi$ -A sensitizers, regeneration by the four Cu(I) diimine mediators shown was investigated, Fig. 13.  $^{95}$ 

These mediators possess methyl groups in the 6,6' positions of bipyridine and the 4,7-positions of 1,10-phenathroline that prevent planarization of the two ligands in the Cu(II) state, resulting in a significant positive shift in  $E^{\circ}(Cu^{II/I})$ . For two of the three sensitizers, the regeneration rates increased with thermodynamic driving force and  $\Phi_{reg}\sim 1$  in all cases. Regeneration by [Cu(eto)<sub>2</sub>]<sup>+</sup> was so rapid that in some cases it was unclear experimentally whether injection occurred first or whether a photogalvanic mechanism was operative. Prior work revealed that these Cu diimine complexes were able to quench the sensitizer excited states. 96 Density functional theory calculations were used to estimate the reorganization energy,  $\lambda$ , for regeneration in the presence and absence of Lewis basic 4-tert-butylpyridine (tBP). Interestingly, this analysis indicated that tBP binding to Cu(II) had a dramatic  $\sim$ 1 eV increase in  $\lambda$ that was predicted to result in charge recombination in the normal region, with Marcus inverted recombination in the absence. The ability to tune redox reactivity with external Lewis bases is a novel aspect of these mediators that may be further optimized for dye-sensitized solar cell applications. 95–102

A significant advance in regeneration at dye-sensitized p-type NiO was realized with tris(acetylacetonato)iron mediators, abbreviated [Fe<sup>III/II</sup>(acac)<sub>3</sub>]<sup>0/-</sup>. <sup>103</sup> The second-order regeneration rate-constant measured spectroscopically was large,  $k'_{\rm reg}=1.7\times10^8~{\rm M}^{-1}~{\rm s}^{-1}$ . At the mediator concentrations employed, this rate constant indicated a regeneration yield  $\Phi_{\rm reg}=0.99$ . This is a particularly notable advance as these iron mediators significantly enhanced the efficiency of dye-sensitized p-type materials. <sup>103</sup>

# 2.6.3 Charge recombination.

Recombination of an injected electron with an oxidized sensitizer yields ground-state products and typically wastes >1 eV of free energy. It has been known for decades that recombination occurs on a micro- to millisecond time scale with non-exponential

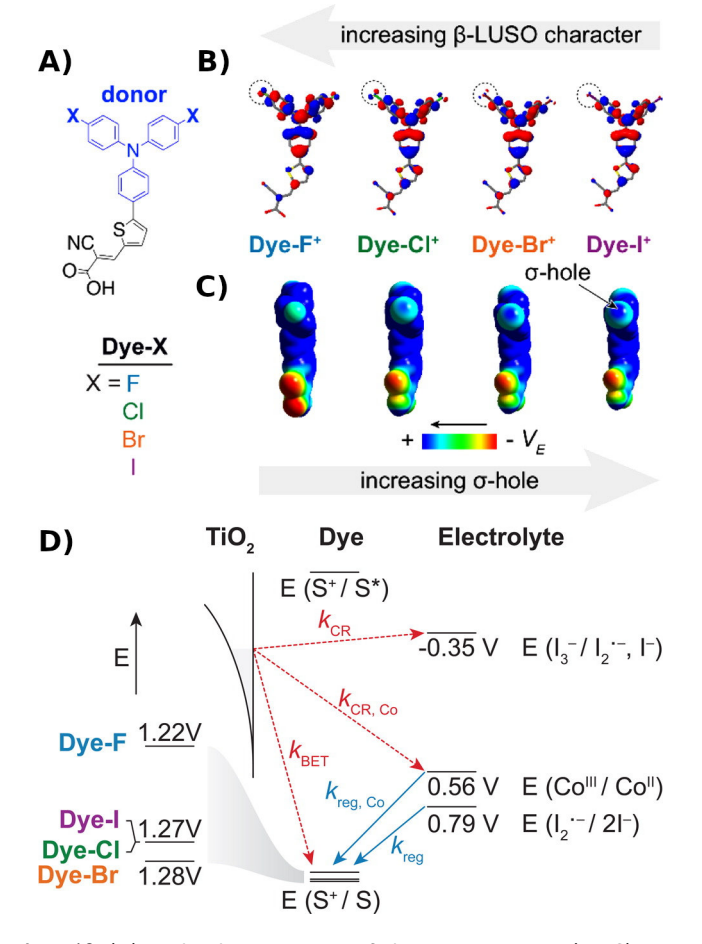


**Fig. 12** (A) Molecular structures of the Dye-X series. (B, C) DFT models of the singly oxidized forms of Dye-X showing (B) the  $\beta$ -LUSO and (C) the existence of  $\sigma$ -holes on the poles of the terminal halogen substituents for the series, with the exception of Dye-F. Adapted with permission from ref. 92. Copyright 2016 American Chemical Society.

kinetics. It has been less clear how "average" observed rate constants extracted from transient spectroscopic data are related to the fundamental electron transfer rate constant. An early model assumed that the oxidized sensitizer remained fixed at the injection site while the injected electron underwent thermallyactivated random walk between traps states prior to recombination. 104-106 When trapping-detrapping was rate-limiting, the observed rate constant reported only on this process. More recent studies with polarized light have shown that the oxidized sensitizer does not remain fixed at the injection site, but rather undergoes intermolecular self-exchange electron transfer between sensitizers that is often called "hole hopping". Polarized light creates an anisotropic population of interfacial states whose time dependent reactivity provided clear evidence that hole hopping followed excited-state injection under many experimental conditions. 107-109 Monte Carlo simulations revealed that an oxidized sensitizer could circumnavigate an entire anatase nanocrystal by hole-hopping before charge recombination occurred. 108

The discovery that hole-hopping rates were directly correlated with charge recombination kinetics represents an important finding.  $^{110}$  Sensitizers that undergo rapid S + S^+  $\rightarrow$  S^+ + S hole-

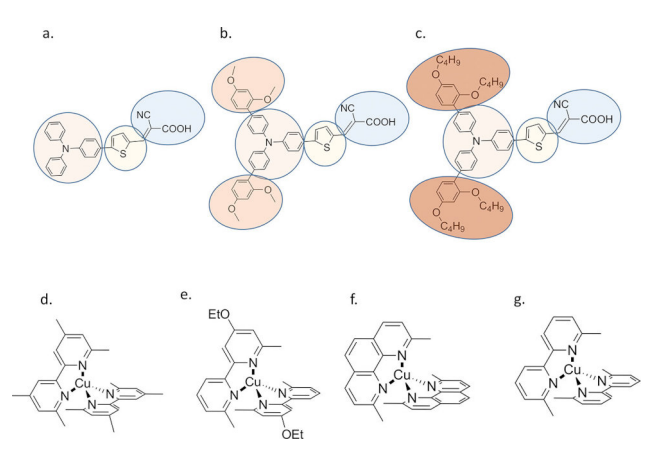


**Fig. 13** Molecular structures of (a) D5, (b) D45 and (c) D35 dyes, and (d)  $[Cu(tmby)_2]^{2+/+}$ , (e)  $[Cu(eto)_2]^{2+/+}$ , (f)  $[Cu(dmp)_2]^{2+/+}$  and (g)  $[Cu(dmby)_2]^{2+/+}$  complexes. Reprinted with permission from ref. 95. Copyright 2018 American Chemical Society.

hopping were shown to recombine more rapidly than those sensitizers that hop more slowly. An example is shown in Fig. 14, where the transient absorption data reports on the charge recombination reaction while the anisotropy reports on hole-hopping. For the D- $\pi$ -A sensitizer mp13, both hole-hopping and charge recombination responded in a similar fashion to changes in the solvent or external environment.

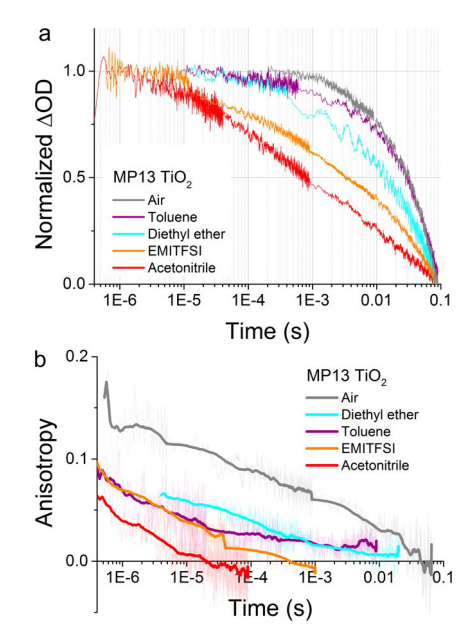


**Fig. 14** (a) Transient absorption and (b) transient absorption anisotropy spectroscopy on MP13 sensitized TiO2 films on glass immersed in different environments. The films were pumped with pulsed laser excitation at 430 nm while the oxidized dye signal was probed at 770 nm. The solid lines in (b) are obtained by calculating a moving average of the raw data (also displayed in background). Adapted with permission from ref. 110. Copyright 2016 American Chemical Society.

Studies of a homologous series of four sensitizers that maintain the cis-Ru(NCS) $_2$  coordination environment with one surface anchoring group show that they undergo rapid hole-hopping.  $^{111,112}$  The hole-hopping rate constants –  $k_{\rm hh}$  – measured electrochem-

ically spanned about a factor of seven and followed the same trend as did the charge recombination kinetic data. 112 Subsequent temperature and surface coverage-dependent kinetic studies with sensitizers that displayed very different hole-hopping rates also supported the conclusion that rapid hole-hopping promotes charge recombination. 113 Interestingly, no correlation between the activation energy for hole-hopping or charge recombination was evident with the solvent dielectric, but both dynamic processes could be tuned by the addition of inert salts to the solvent or by controlling access of electrolyte cations to the oxide surface. 114 Taken together, these findings indicate that unwanted charge recombination can be inhibited through control of lateral hole-hopping. This represents an unexpected finding that may indicate that sensitizer hole-hopping is more important to the charge recombination process than is transport of the injected electron. 110 Control of the intermolecular distance between sensitizers and the electrolyte tunes the charge recombination reaction and can favor conditions where the transient spectroscopic data reflects the true interfacial electron transfer event.

Absorption of a photon initiates the formation of one injected electron and one oxidized sensitizer. They are formed in equal numbers and a second-order recombination might be anticipated with the rate law as  $r = k[S^+][TiO_2(e^-)]$ . An Ostwald isolation type approach where an applied potential was used to control the number of electrons and oxidized sensitizers identified the rate law as  $r = k[S^+]^1[TiO_2(e^-)]^1$ . The Ostwald isolation conditions differ from that encountered in operational solar cells or in transient photovoltage measurements where alternative rate laws have been reported. 116 In all cases, the injected electrons reside in spherical nanocrystallites interconnected in a mesoporous thin film while the oxidized sensitizers are confined to the quasi-twodimensional oxide surface. Hence, charge recombination is an intriguing process where redox equivalents on opposite sides of an interface come into close proximity before electron transfer

For fundamental recombination studies, transparent conductive oxide (TCO) materials have some advantages. 117-119 Their metallic character allows potentiostatic control of the Fermi level  $(E_{\rm F})$  and thus of the driving force for charge recombination,  $-\Delta G^{\circ} = nF(E^{\circ \prime} - E_{\rm F})$ . Quantifying  $k_{\rm cr}$  as a function of  $-\Delta G^{\circ}$  allows analysis through Marcus-Gerischer theory and access to the total reorganization energy,  $\lambda$ , and the electronic coupling. Studies with acceptors positioned at variable distances from a TCO surface provided a remarkable result: λ decreases to near zero when the acceptor is most proximate to the oxide surface. 119 At distances greater than  $\sim$ 20 Å in the diffuse part of the electric double layer, happroximately equals the value expected for homogeneous reactions,  $\lambda \approx 0.9$  eV. Thus, dye-sensitization with transparent conductive oxides provides exciting opportunities to test interfacial electron transfer theories and to probe the impact of the electric double layer.

2.6.3.1 Recombination to solution species. It was recently shown that under some conditions electron transfer from TiO<sub>2</sub> to acceptors dissolved in fluid solution followed a first-order kinetic model. 120,121 Excited-state injection followed by sensitizer regeneration with triphenylamine donors dissolved in solution were used to quantify the reaction  $TiO_2(e^-) + TPA^+ \rightarrow TiO_2$ + TPA. Interestingly, when the thermodynamic driving force for this reaction was large, first-order kinetics were operative, a nonintuitive result that suggests the TPA+ acceptors are electrostatically bound to the oxide surface allowing a uni-molecular-type recombination reaction. When  $-\Delta G^{\circ}$  was small, dispersive kinetics were observed and attributed to electron transport to the oxidized TPA. Temperature-dependent studies analyzed through transition state theory indicated that recombination occurs with a highly unfavorable entropy of activation. 120 Activation energies were the same (within experimental error) – 12 kJ mol $^{-1}$  – for all interfacial electron transfer reactions, indicating that the barriers for electron transport and interfacial electron transfer were similar. Eyring analysis indicated a substantial entropy change to the activation barrier. 121

The  $TiO_2(e^-) + I_3^- \rightarrow$  reaction is known to be kinetically slow on a millisecond time scale, behavior that is typically attributed to an unfavorable positive  $\Delta G^{\circ}$ . The identity of Lewis acidic cations present in the electrolyte impacts the reaction kinetics.  $^{122-124}$  Alkaline and alkaline earth cations screen the electric field generated by the injected electrons and also influence charge recombination to organic acceptors.  $^{124}$  Interestingly, the  $SnO_2(e^-) + I_3^ \rightarrow$  reaction is much slower than for TiO<sub>2</sub> and extends to the seconds time scale, presumably by virtue of the more positive SnO<sub>2</sub> donor states. 90

2.6.3.2 Sensitizer-bridge-donor (S-B-D) acceptors. A successful approach for inhibiting unwanted charge recombination is to regenerate the oxidized sensitizer by intramolecular electron transfer. 125-128 In this approach, electron transfer occurs from a donor D covalently linked through a bridge unit B to the oxidized sensitizer. An interesting observation was that a relatively small structural change in the planarity of an aromatic Bridge altered the electron transfer mechanism from adiabatic to non-adiabatic. Interestingly, recombination to S<sup>+</sup> and D<sup>+</sup> were the same for adiabatic transfer, while non-adiabatic transfer to D<sup>+</sup> was markedly inhibited. The kinetic data revealed that recombination utilized a bridge orbital pathway. 125

In one study the  $S^{+/0}$  and  $D^{+/0}$  reduction potentials were very similar such that excited state injection created a quasiequilibrium  $K_{eq} = k_1/k_{-1}$  that was quantified over an 80 °C temperature range,  $TiO_2 | S^+-B-D \rightleftharpoons TiO_2 | S-B-D^+$ . A significant barrier was measured under all conditions indicating that a true redox equilibrium was operative. The magnitude of  $K_{eq}$  was closer to unity for the phenyl bridge and hence  $|\Delta G^{\circ}_{ad}| < |\Delta G^{\circ}|$ as had been predicted theoretically. The van't Hoff shown for the adiabatic equilibrium clearly indicate  $\Delta H^{\circ} = q_{\rm p} = 0$ , equilibrium constants determined solely by  $\Delta S^{\circ}.$  For non-adiabatic equilibrium  $\Delta H^{\circ} = \pm 7.0 \text{ kJ mol}^{-1}$ . The results show that the magnitude of  $\Delta G^{\circ}$  is decreased when adiabatic pathways are operative, a finding that should be considered in the design of S-B-D sensitizers for dye-sensitized solar cell applications. 127,128

# Theory and computational studies

DSCs offer a unique playground for fundamental studies of complex phenomena concerning sunlight harvesting, charge and mass diffusion across multi-layer heterogeneous interfaces, and electrochemistry. Theory and computation have been key players in providing the scientific foundation to understand and dissect DSC devices, starting from isolated components (e.g. dyes, electrodes) and elementary processes up to electron/ion transport properties at hybrid organic-inorganic and liquid-solid interfaces.  $^{129-132}$ This section presents a brief outline of the state-of-the-art theoretical methods addressing these systems and processes, with a particular focus on cutting-edge studies from the last ten years (Fig. 15).

#### 3.1 Theoretical background

Simulation of sunlight conversion to electricity in DSCs calls for the application of several theoretical methods to tackle complex materials and processes that span across several scales of space and time. Light harvesting, dye/electrode charge transfer, electron transport to the charge collector, oxidized dye regeneration, electrolyte diffusion, and reduction at the counter electrode are all processes that occur at different places and with different time frames, from femtoseconds to milliseconds. Therefore, the simulation approach must be multi-scale, starting from the elementary processes at the nano scale and adding step-by-step the effects coming from larger (longer) space (time) scales.

Initially, the quantum mechanical (QM) interactions among electromagnetic radiation, electrons, and nuclei need to be properly described. Within this framework, Density Functional Theory (DFT) is the current method of choice for the electronic structure of materials and interfaces, 136 and its extension to Time-Dependent DFT (TD-DFT) has also enabled the effective description of excited state properties. 137 However, the application of Kohn-Sham DFT and the related TD-DFT still suffers from the approximate nature of the unknown exchange-correlation (XC) density functional. <sup>138</sup> This flaw is very relevant for modeling within the context of DSCs as it can jeopardize DFT results reliability in predicting charge transfer processes involving strongly correlated materials (e.g. transition metal oxide-based electrodes) and noncovalent weak interactions (e.g. dispersion forces). 139 Recent theoretical advances in XC formulations and other effective approaches have been able to amend most of these drawbacks, but often only on a case-specific base. Moreover, DSC molecular and solid-state components have been traditionally studied within different numerical approximations, with no or little overlap, which has hindered an easy transferability of theoretical advancements from one DSC component to the other. For example, successful TD-DFT approaches for molecular dyes are not numerically feasible for solid-state electrodes. Vice versa, new approaches beyond DFT (e.g. GW 140,141 and RPA 142) for bulk extended materials are still not feasible for realistic hybrid interfaces. Thus, the following sections will discuss: (i) the best available approaches for each DSC component, (ii) the relevant physico-chemical properties to be computed, and (iii) how the results from first-principles calculations can be implemented in multi-scale models to predict the overall DSC power conversion efficiency.

# 3.2 Theoretical description of sensitizers and molecular

Since the earliest characterization of Ru-based 143,144 and organic 145 dyes, the computer power and theoretical machinery for modeling excited states of molecular species has considerably grown. 146 The advancements in XC functionals (long-range corrected hybrid 147 and double hybrid 148) and in TD-DFT algorithms (e.g. analytical first derivatives) allowed the molecular design of dyes with specific tailored properties for application in n-type  $^{149,150}$  and p-type  $^{151}$  photoelectrodes. The combination of long-range corrected density functionals like CAM-B3LYP or  $\omega$ -B97X and triple-z quality basis sets such as 6-311++G(d,p) and def2 TZVP have provided excellent results even for the challenging cases of intra-molecular charge-transfer excitations. 152 When TD-DFT fails, excited-state properties can still be obtained by means of wavefunction-based methods (e.g. CASPT2, 153 NEVPT2 154 and EOM-CCSD 155), whose major limit is the dye size, due to their high computational cost.

A key strategy to avoid undesired charge recombination is based on the development of push-pull dyes, where the excited electron is localized close to the electrode (for standard ntype DSCs<sup>156</sup>) or exposed to the solvent (in photocathodes<sup>157</sup>). The molecular design of new dyes with such characteristics has been greatly aided by the topological analysis of electron density changes upon photoexcitation, such as the combination of TD-DFT and density-based charge-transfer indexes. 158 This approach is based on the analysis of the difference between the charge densities of the excited and the ground state, and this approach has proven to be very effective for molecular dyes, <sup>159</sup> including metal-based ones. 160,161 Additionally, this approach has been recently updated to account for complex dye structures. 162

A significant novel contribution of the DFT-based quantum chemistry approach is related to the new transition metal complexes developed as redox shuttle substitutes to the I<sup>-</sup>/I<sub>3</sub><sup>-</sup> electrolyte. First-principles approaches have been exploited to assess the molecular parameters related to their redox potential (to be compared with the dye HOMO energy level) in order to evaluate the driving force for dye regeneration, 163 as well as to consider the reorganization energies upon oxidation within a diabatic charge transfer scheme based on Marcus theory. 164 The results of hybrid DFT on Co and Cu complexes present certain levels of inaccuracy in predicting the redox potentials, with errors usually around 0.2-0.5 eV with respect to experimental data. 15 This is due to the approximate nature of the XC density functional when comparing two systems with a different number of electrons. A much better agreement between theory and experiment is achieved in the computation of reorganization energies ( $\lambda$ ) and corresponding charge transfer kinetic parameters. 95,165

The accuracy in predicting such parameters (photoexcitation, redox potential, reorganization energies) largely depends on the approach used for modeling the chemical environment. A wellknown and effective strategy to model the structure and properties of solvated systems is represented by focused models, where

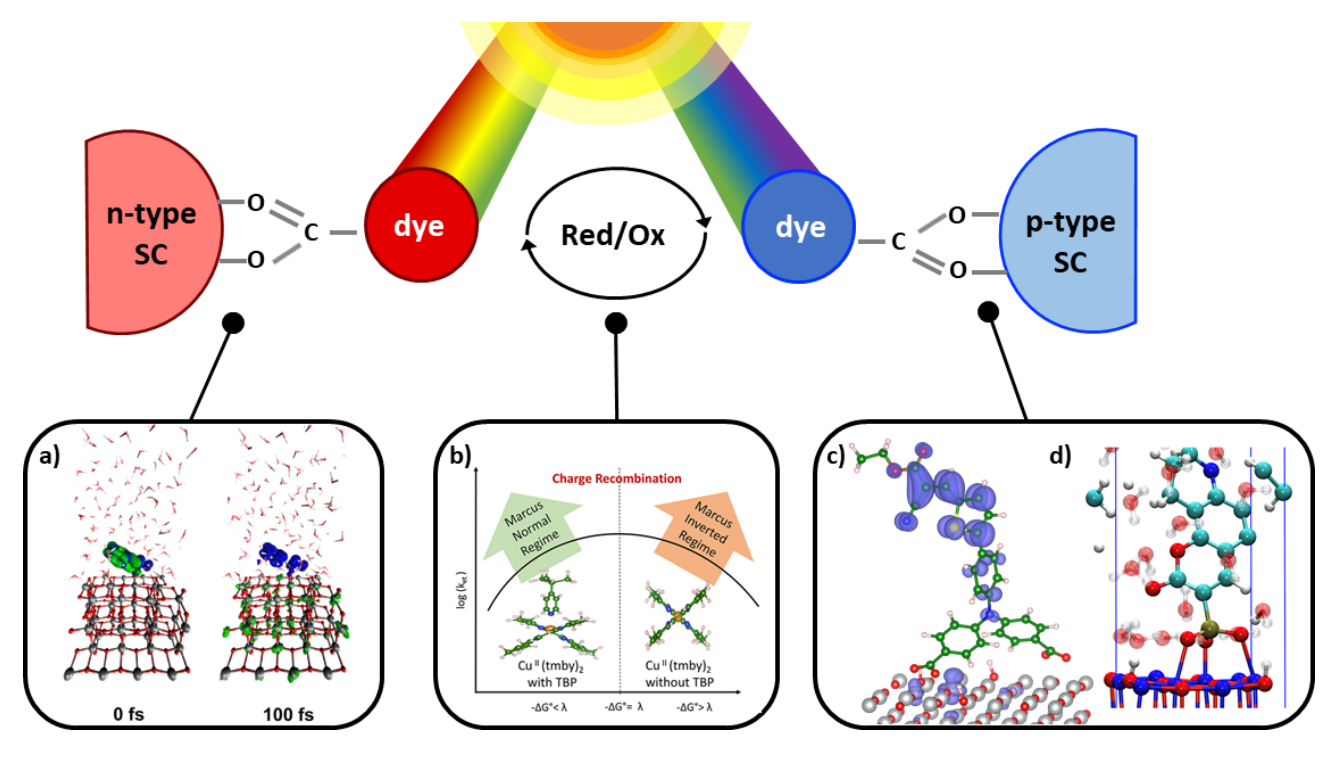


Fig. 15 Examples of recent computational studies on DSC components. (a) electron (green) and hole (blue) densities at the beginning of the simulation (t = 0 fs) and upon electron injection (t = 100 fs) for benzohydroxamic acid anchored on TiO<sub>2</sub> with full explicit water solvation. Adapted with permission from ref. 133. Copyright 2020 American Chemical Society. (b) Analysis of charge transfer parameters in Cu-based electrolytes. Adapted with permission from ref. 95. Copyright 2018 American Chemical Society. (c) Isosurfaces of band-decomposed charge density of the lowest unoccupied band of the push-pull dye T1/NiO system. Adapted with permission from ref. 134. Copyright 2019 American Chemical Society. (d) Anchoring geometry of C343 as a model dye on NiO during the molecular dynamics simulation in explicit water. Adapted with permission from ref. 135. Copyright 2017 American Chemical Society.

the system is partitioned into a chemically interesting core (e.g. the solute in a solution) and the environment, which perturbs the core, modifying its properties. While a level of theory as high as required is retained for the core, the environment is treated in a more approximate way. Two popular alternatives of such approaches are: (i) to consider the environment as a structure-less continuum as in the Polarizable Continuum Model (PCM), <sup>166</sup> or (ii) to retain its atomistic resolution within a molecular mechanics (MM) description. 167 Both alternative strategies can be effectively coupled to a QM description of the core, and can also be coupled together to overcome their respective limitations. <sup>168</sup> In the context of DSC, PCM and hybrid QM/MM approaches have been extensively applied to account for the solvent effects on the physico-chemical properties of dyes and redox shuttles. <sup>169</sup>

## Simulation of solid-state electrodes and heterogeneous 3.3

The first systematic computational studies on DSCs concerned the main components of the original Grätzel cell, focusing mostly on n-type semiconductor oxides (e.g. TiO2, ZnO, SnO2) and their interfaces with molecular dyes (e.g. dye anchoring groups). 129-132 In the last decade, the quest for tandem cells has spurred theoretical studies also on p-type DSC components 170 (p-type semiconductors, push-pull dyes, and their interfaces) that were barely studied in the first years of the modern DSC technology. In both cases, studies of electrode and counter electrode materials have relied on the periodic supercell DFT approach, mainly by employing plane-wave basis set and pseudo-potentials for replacing core electrons. 171-174 Standard local and semi-local XC functionals have been recently replaced mostly by DFT+U175 and hybrid HF-DFT <sup>176</sup> for modeling the strong correlated nature of the transition metal oxides that are commonly employed as electrodes in DSCs. The characterization of band structures with these methods can provide useful hints on the nature of the bandgap and the possible optical properties, and on electron/hole mobilities. 177 Within this framework, recent studies have explored several possible alternatives to NiO for p-type DSC and tandem cells. 178,179 While semi-local DFT (GGA) provides too low of a bandgap, the DFT+U approach strongly depends on the choice of the Hubbard-like U-J parameter. The hybrid HF-DFT approach tends to overestimate the bandgap, and the estimate is also affected by the choice of HF-like exact exchange percentage into the HF-DFT scheme. Methods based on Green function (GW) and on the Random Phase Approximation (RPA), as well as methods based on Bethe-Salpeter equation (BSE) and TD-DFT have the potential of providing results in quantitative agreement with experiments, but their feasibility is hindered by computational costs that are too high. 180 Besides these shortcomings, thanks to the relatively good accuracy in predicting bandgap centers by standard DFT and considering the Janak's theorem, it is possible to compute the absolute potentials vs. NHE of the electrode band edges within a surface slab approach.  $^{181}$  In particular, the conduction band (CB) is relevant for photoanodes, and the valence band (VB) is relevant for photocathodes. Comparing these values to the computed HOMO and LUMO energies of the dye provides a powerful tool to assess the quality of a dye/electrode combination. The dye LUMO must be higher in energy than the electrode CB in n-type DSCs and the dye HOMO must be lower than the electrode VB in the p-type counterpart to allow for convenient electron and hole injections, respectively.

In the last decade, the availability of more and more powerful computing facilities allowed the study of the dye-electrode interface at the full atomistic scale. From cluster-size electrodes with few atoms, <sup>182,183</sup> computational tools now have the capability of simulating the full electrode surfaces with periodic boundary conditions, including the attached dyes 184 and, in some cases, also the explicit solvent medium. 135 The characterization of dyeelectrode interfaces has provided great advancement in the understanding of the complex interfacial electronic processes. 185 For both n- and p-type DSCs, it has been possible to assess the strength of the dye-surface anchoring, 186-188 the role of dipole moment at the surface in tuning the electrode CB/VB edge potential, <sup>189</sup> and the effects of the polarizing surface <sup>190,191</sup> and the electrolyte solution <sup>192</sup> on the dye electronic structure. The results allowed for a better design of dyes, with specific anchoring groups and with electron-donor/acceptor moieties well distributed into the dye molecular architecture. 193

All these studies have paved the route to the recent implementation of real-time TD-DFT simulations of the dye/electrode interface after sunlight absorption and charge separation. 194-196 With these approaches, mostly focused on n-type DSCs, it has been possible to dissect the specific mechanism and kinetics of charge transfer between the excited dye and the electrode, as well as of the undesired charge recombination events. <sup>192</sup> These studies still retain some empiricism, for example in the choice of some parameters that need to be fitted to experiments, but they certainly represent a frontier in the theoretical modeling of DSC interfaces, and we can expect further developments of these tools in the near future.

Last but not least, the importance of using the results from atomistic simulations in macroscopic modelling approaches must be mentioned. For example, the computed charge transfer rates can be implemented in a kinetic Monte Carlo approach for the simulation and interpretation of complex electrochemical measures (e.g. impedance). 197 At the same time, computed parameters derived from the isolated dye, the pristine electrode, and the dye/electrode interface can be conveniently cast in empirical formula to obtain a realistic estimate of the photo-conversion efficiency. 198

#### 3.4 New horizons in modeling DSC devices

The great challenge of finding new materials and interfaces for DSCs requires further advancements in computational techniques. Although the atomistic description of complex materials and interfaces may still benefit from the accuracy and versatility of ab initio methods, new tools are emerging within the ongoing extraordinary revolution in computational sciences that involves Artificial Intelligence (AI) and Data Sciences. DSC development fits in these new approaches at different levels and, indeed, the first AI-based studies on DSC are now reality. 199 On one hand, AI under Machine Learning-based approaches has been applied for electrode materials and dyes, 200-202 tailoring specific structureproperty relationships with deep-learning neural networks rather than first-principles equations. On the other hand, several tools are already available for automated screening and analysis of large datasets, 203 compiled from experiments and/or advanced QM calculations, aimed at finding new, unexpected combinations of DSC components that maximize photo-conversion efficiencies, even at different light conditions. <sup>204–206</sup> The future of these tools looks bright, together with their further integration within the new promising quantum information technologies. 207

# Materials

#### 4.1 Nanostructured metal oxide electrodes

Nanostructured semiconductor electrodes provide a large surface area for dye adsorption, an essential feature for DSCs. The most commonly used type of nanostructured electrode in DSC is the mesoporous electrode, which is composed of 10 to 50 nm-sized nanocrystals and has a porosity of about 50%. Other types of metal oxide nanostructures that have been applied in DSC are nanotubes, nanorods, nanofibers, nanosheets, etc.

By far the most used material for mesoporous electrodes is TiO<sub>2</sub> with the anatase crystal structure (Fig. 16). This wide bandgap semiconductor has an indirect bandgap of 3.2 eV. The standard method for preparation of mesoporous TiO2 electrodes is by screen printing of suitable paste, followed by annealing in air at high temperature (400-500 °C) to burn out the organic additives required to make a paste with appropriate rheological properties and giving the required porosity. This heat treatment also gives a partial sintering of the TiO2 to make electronic connections between the particles and gives mechanical stability to the film. Depending on the precise composition, the mesoporous TiO2 film can be completely optically transparent, or have a slight white color. Several commercial suppliers offer suitable TiO<sub>2</sub> screen printing pastes.

A light scattering layer containing ~400 nm-sized TiO<sub>2</sub> particles is frequently deposited on top of the mesoporous layer. This layer reflects transmitted light back into the active film and usually improves the efficiency for DSC devices that are illuminated through the FTO/glass substrate. Light-scattering particles can also be added to the mesoporous film paste to obtain a similar effect; the latter method is more appropriate for DSC with illumination from the counter electrode side.

For best performance, it is common in research papers to apply a TiCl4 treatment: mesoporous TiO2 films are immersed in an aqueous TiCl<sub>4</sub> solution, leading to chemical bath deposition of an ultrathin layer of TiO2 (about 1 nm) onto the mesoporous electrode and the underlying conducting glass. <sup>208</sup> A further heat treatment is used to crystallize the material and to remove wa-

The porosity and pore size of mesoporous films are particularly important for the use of alternative redox mediators, such

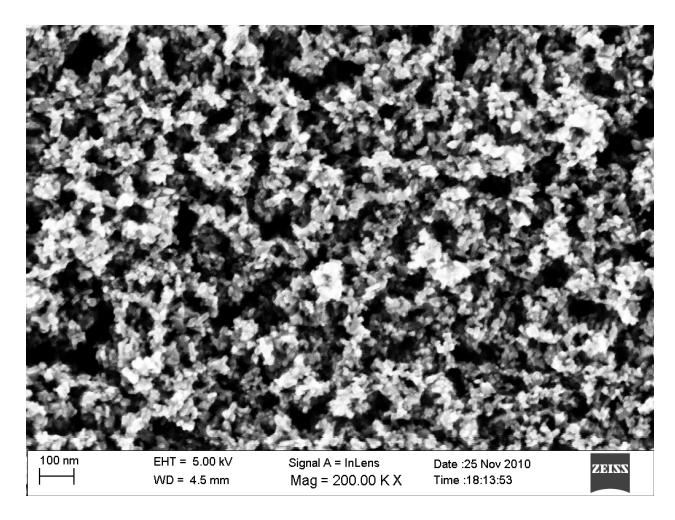


Fig. 16 SEM image of a mesoporous  ${\rm TiO_2}$  film made with the GreatCell Solar 18NR-T paste.

as cobalt bipyridine complexes. In this case, a marked improvement of DSC performance was found at one sun illumination, from 1.4% to 4.8%, when the porosity was increased from 52% to  $59\%.^{210}$  Deviations from linearity of photocurrent vs. light intensity plots, as well as photocurrent transients clearly demonstrated the occurrence of mass transport limitations of the redox mediator. Yella et al. demonstrated that best performing DSCs with cobalt bipyridine redox mediator should have a thinner added TiO<sub>2</sub> layer deposited by TiCl<sub>4</sub> after treatment. <sup>211</sup>

Doping of TiO2 can give some positive effects by adding or removing trap states, changing the band edge levels, improving dye adsorption, and by stabilizing the anatase phase, as recently reviewed by Roose et al.  $^{212}$  For instance, high  $V_{\rm OC}$  was obtained by Mg doping of TiO2, where 1.45 V was obtained with additional MgO/Al<sub>2</sub>O<sub>3</sub> surface treatment and bromide-based redox electrolyte. 213 In highly efficient DSCs, however, the state-of-the art mesoporous TiO2 electrodes are not doped.

A large variety of TiO2 nanostructures have been tested in DSC: one-dimensional structures such as nanotubes and oriented nanorod arrays, 214 mesoporous microbeads 215 and mesoporous single crystal. 216 Templating methods provide a route to ordered mesoporous TiO2 materials, with soft-templating methods using surfactants and hard-templating methods using silica or polystyrene spheres as templates. 217 None of these structures, however, outperform standard mesoporous TiO2 electrodes under optimized conditions.

In 1D structures (nanotubes and single crystalline nanorods) faster electron transport is often named as a potential advantage for these structures. In practice, however, the charge collection is sufficiently high in mesoporous films, so that no solar cell improvement can be expected on that basis. Mesoporous TiO2 microbeads are of potential interest for several reasons: first, a high PCE of 10.7% was achieved in a single printed layer; 215 secondly, they can be annealed at high temperature and sensitized before application onto a (flexible) substrate. Furthermore, this and other structures with hierarchical architecture can have an advantage with respect to mass transport in the electrolyte. Mesoporous microbead electrodes outperformed standard mesoporous electrodes when using a more viscous MPN-based cobalt electrolyte at 1 sun light intensity. 218 Microbead electrodes were also successfully applied in solid-state DSCs (Fig. 17). 219

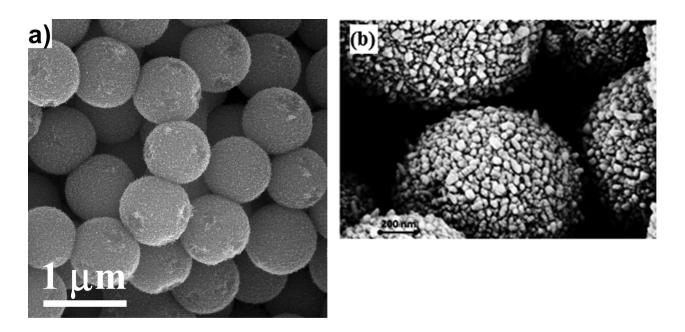


Fig. 17 SEM micrographs of mesoporous TiO<sub>2</sub> microbeads. (a) Adapted with permission from ref. 220. Copyright 2010 American Chemical Society. (b) Adapted from ref. 219 with permission from The Royal Society of Chemistry.

A disadvantage related to TiO2 as a material for the dyesensitized solar cell is its photocatalytic activity: 221 direct excitation of the semiconductor leads to highly energetic holes that can oxidize organic compounds. This will lower the long-term stability of DSC under illumination. Such degradation can be avoided by adding a UV-filter to the solar cell, but this will lead to additional cost. The UV-activity of TiO2 is one reason to look into alternatives.

There are many other metal oxides that can be applied in the working electrode of a DSC. ZnO it the most investigated alternative to TiO<sub>2</sub>, in a wide variety of nanostructures. <sup>222,223</sup> Its electron mobility is much higher than that of TiO2, but its (photo)chemical stability is lower. SnO2 is chemically very stable, has a higher bandgap than TiO2, but a lower conduction band edge energy, leading to a lower photovoltage in DSCs. 224 Both ZnO and SnO<sub>2</sub> are probably best applied in core-shell structures in DSCs, as discussed below. Table 1 lists alternative n-type semiconductor materials used in DSC that have obtained a PCE of more than 5%.

Combinations of metal oxides have also been evaluated for DSC in a large number of studies. Scientifically most interesting are the so-called core-shell structures, where a nanostructured electrode is covered by an ultra-thin layer of a different material, usually one with a higher bandgap. Deposition is performed by chemical bath deposition (using e.g., TiCl<sub>4</sub> for deposition of TiO<sub>2</sub>) or by atomic layer deposition (ALD). The shell material can be a semiconductor or an insulator such as Al<sub>2</sub>O<sub>3</sub> or SiO<sub>2</sub>: if sufficiently thin, adsorbed dyes can inject electrons into the core material through tunneling. Typically, rate constants for both electron injection and recombination are significantly reduced. This can lead to an improved solar cell efficiency if the injection efficiency is not significantly decreased. In addition, the shell can lead to added chemical stability (e.g. for Al<sub>2</sub>O<sub>3</sub>, SiO<sub>2</sub>, or TiO<sub>2</sub> on ZnO).

A few examples of core-shell structures will be given here: in ALD-deposited Al<sub>2</sub>O<sub>3</sub> on mesoporous TiO<sub>2</sub>, the PCE increased from 6.2% to 8.4% upon 20 ALD cycles. This was partly caused by a higher recombination resistance and partly by a higher dye

Table 1 Overview of different nanostructured metal oxide semiconductors used in DSC and their best performance in devices

Semiconductor	Bandgap (eV)	Nanostructure	Sensitizer – electrolyte	PCE (%)	Year	Ref.
TiO <sub>2</sub> (anatase)	3.2	Mesoporous	ADEKA-1/LEG4 – Co(phen) <sub>3</sub>	14.3	2015	25
TiO <sub>2</sub> (rutile)	3.0	Nanorod array	$N719 - I^-/I_3^-$	11.1	2019	225
TiO <sub>2</sub> (brookite)	3.2	Mesoporous	$N719 - I^-/I_3^-$	8.2	2020	226
ZnO	3.2	Aggregated nanoparticles	$N719 - I^-/I_3^-$	7.5	2011	227
$SnO_2$	3.5	Nanoparticles/	$N719 - I^-/I_3^-$	6.3	2013	228
$Nb_2O_5$	3.6	Nanorod array	$N719 - I^-/I_3^-$	6.0	2013	228
$Nb_3O_7(OH)$	3.0	Nanorod array	$N719 - I^-/I_3^-$	6.8	2013	228
$Zn_2SnO_4$	3.6	Aggregated nanoparticles	$X73 - Co(phen)_3$	8.1	2020	229
BaSnO <sub>3</sub>	2.9	Mesoporous	$N719 - I^{-}/I_{3}^{-}$	6.6	2019	230
$Ba_{0.8}Sr_{0.2}SnO_3$	3.0	Mesoporous	$N719 - I^{-}/I_{3}^{-}$	7.7	2019	230

adsorption of the modified electrode. <sup>231</sup> As another example, 3Dbicontinous SnO<sub>2</sub> inverse opal structures were synthesized using infiltration of a film of monodisperse polystyrene particles with SnCl<sub>2</sub> in ethanol, followed by heating, see Fig. 18. A TiO<sub>2</sub> shell was formed by chemical bath deposition using TiCl4. The resulting electrodes yielded an efficiency of 8.2% in DSCs, whereas TiO<sub>2</sub>/TiO<sub>2</sub> inverse opal/shell structures yielded 7.2%. <sup>232</sup>

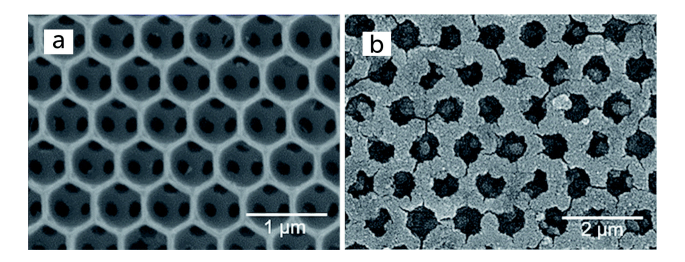


Fig. 18 (a) Inverse opal SnO<sub>2</sub> electrode; (b) after coating with a 170 nm shell of TiO2. Adapted from ref. 232 with permission from The Royal Society of Chemistry

#### 4.2 Sensitizers

Photoanodes based on molecular sensitizers at a semiconductor interface for DSCs require that the sensitizer absorbs solar energy and injects electrons into the semiconductor conduction band. Thus, the sensitizer controls the breadth of the solar spectrum used and the quantum yield for electron injection. Additionally, the sensitizer should promote long lived charge separated states at the interface, and the oxidized sensitizer should rapidly undergo electron transfer from a reducing redox shuttle (RS) to limit the competitive back electron transfer reaction from electrons in TiO2 to the oxidized dye. The sensitizer is also often tasked with providing insulating groups to protect electrons in TiO<sub>2</sub> from recombining with the electrolyte. Recent progress in dye design with respect to these design criteria has fueled much of the increase observed in performance metrics. The atomistic level control with respect to dye design allows for the precise tuning of dye properties. One strategy that has been explored intensely is related to the design of a dye capable of absorbing photons across the visible spectrum and into the near infra-red (NIR) region to maximize the power conversion efficiency (PCE) from a single photoanode-based device. Estimates of a practical efficiency limit at about 22% PCE are reported if driving forces for electron transfers to a semiconductor and from a redox shuttle to the oxidized dye can be kept to a combined 400 mV or less and the sensitizer can efficiently use photons as low in energy as~950 nm. <sup>233</sup> Alternatively, an increasingly popular approach is to tailor chromophores to a specific spectral region to be used in multiple photoanode-based devices. This second approach increases the complexity of the device, but allows for higher theoretical PCEs. Using similar approximations of 400 mV free energies for electron transfers with the spectrum divided into three equal parts (wide, medium, and narrow optical gaps) from 400-950 nm leads to a practically possible PCE of  $\sim$ 33%. Thus, significant gains in PCE are possible through research of multiple photoanode systems. Additionally, these materials are attractive for use with existing solar cell technologies as described below. For this strategy to work effectively, the sensitizer (and redox shuttle) needs to be custom tailored to each spectral region for minimal overpotential losses. Both single and multiple photoanode dye design approaches are discussed below with respect to both metal- and organic-based dyes. Notably, the literature with respect to dyes for DSCs is vast and growing rapidly with many exciting findings being reported weekly, which cannot all be highlighted (especially with regard to phthalocyanies, BODIPYs, DPP chromophores, multidonor systems, multiacceptor systems, dual anchor dyes, unique anchoring groups, and non-covalently bound dye-dye and dye-RS systems). The examples below serve to highlight recent select findings on high photocurrent, high photovoltage, deep NIR absorbing dyes, wide optical gap dyes, and high PCE dyes. Select design strategies being used within approximately the last decade are highlighted and should not be viewed as an exhaustive catalogue of dye design approaches.

### 4.2.1 Metal coordination complexes.

Transition metal-based complexes were critical to the early development of DSCs and were the highest performing materials in the field for more than a decade after the modern mesoporous metal oxide construct inception. Dyes such as N3, 143 N719, 209 CYC-B11, <sup>234</sup> and Black Dye <sup>235</sup> are commercial and remain common benchmarking materials in the DSC literature (Fig. 19). These dyes are used in a variety of DSC-based applications with many PCEs reported at >11%. Derivatives of these dyes such as TUS-38 - where a hexylthiophene replaces one of the three anchors of Black Dye - have shown further improved efficiencies (11.9% PCE).  $^{236}$  These dyes give excellent PCEs with the  $I^-/I_3^-$  redox shuttle; however, performances are generally diminished when the 1-electron metal-based redox shuttles (RSs) that have fueled the more recent increases in PCE to beyond 14% are paired with

metal-based dyes. 25 TiO2 surface protection is generally considered to be lower with metal-based dyes, which often incorporate relatively few alkyl chains. These insulating alkyl groups have proven to be critical to sensitizer design with respect to organic dyes since they provide an umbrella type effect that slows electron transfers from the TiO<sub>2</sub> surface to the electrolyte. Additional concerns about low metal-based sensitizer molar absorptivities arise due to reduced film thicknesses being used with transition metal-based RSs to limit TiO2 surface recombination sites and limit mass transport issues. Competitive electron transfer from the dye to the oxidizing RS directly rather than electron injection into the semiconductor conduction band (CB) have been noted as well. <sup>237</sup> However, given that ultrafast electron transfer is often observed with transition metal-based sensitizers and the exceptionally broad IPCE spectrum that these materials can generate, the design of transition metal-based sensitizers that are compatible with Co and Cu RSs capable of high efficiency systems is an attractive area of research. Cyclometalated Ru complexes Ru-1, SA246, and SA634 incorporate four alkyl chains to insulate electrons in TiO2 from the electrolyte. This design leads to an 8.2-9.4% PCE with the use of a  $Co^{3+/2+}$  redox shuttle. <sup>238–240</sup> The replacement of the NCS ligands commonly employed in the DSC literature on Ru complexes with the cyclometalated phenylpyridinederived ligand leads to broad absorbing dyes with an IPCE onset near 800 nm. The incorporation of a pyrazolate-derived ligand onto an Ru complex with 6 alkyl chains gives dye 51-57dht.1. 241 This complex was found to have good surface insulating properties leading to a PCE of 9.5% with a Co<sup>3+/2+</sup> redox shuttle, which improved on the up to 9.1% PCE from a similar dye design. 242 Given that the IPCE spectrum of many of these dyes is near 90% with the  $I^-/I_3^-$  RS and around 60-70% with  $Co^{3+/2+}$  RSs, systems that productively use the 20-30% of the IPCE spectrum not utilized with the  $Co^{3+/2+}$  shuttle are needed. The IPCE curve shape often resembles the absorption spectrum of the metal-based chromophore. This is typically only the case when regions of the absorption spectrum have a lower molar absorptivity and cannot efficiently absorb the available photons once the dye is anchored to a thin photoanode. Examples within the organic dye literature are discussed below where the IPCE does not resemble the absorption curve shape of these materials despite large valleys in the absorption spectrum. This is due to the absorption curve minima often sufficing to collect photons efficiently. However, metalfree dyes performing well with metal-based RSs have IPCE onsets that are 100-200 nm shifted to higher energies relative to broadly absorbing dyes such as N719. The blue-shift of organic sensitizers relative to transition metal-based systems which lowers the possible photocurrent output from organic dyes; thus, strategies to boost the molar absorptivity and broaden the spectrum of 1electron-compatible metal-based sensitizers are needed. Table 2 lists device parameters of DSCs fabricated with metal coordination complexes-based dyes referenced in this review, together with the electrolyte used.

Wide optical gap sensitizers are important for a number of applications and within DSC literature these systems are exceptionally valuable for use in multiple photoanode systems. With respect to these applications, generating a high photovoltage is critical from the high energy visible photons to avoid thermal free energy waste. The overall PCE of the system is typically not the metric being pursued in these systems since they are often designed with tandem or multiple photoanode systems as the larger goal. Wide optical gap metal-based sensitizers are relatively rarely used in the literature with RSs capable of generating high photovoltages. This may in part be due to the higher photovoltage generating redox shuttles often being 1-electron metalbased RSs. As described above, the design of metal-based dyes that undergo efficient electron transfers with good charge separation lifetimes with metal-based RSs remains a key research direction. However, recently a cyclometalated Ir complex (Ir-1) based on two phenylpyridine ligands and a 4,4'-bis(phosphonomethyl)-2,2'-bipyridine ligand has been used in high photovoltage DSCs with the  $Fe(bpy)_3^{3+/2+}$  redox shuttle to give a 1.06 V DSC device (Fig. 19). <sup>243</sup>

Narrow optical gap sensitizers are critical toward the use of lower energy photons in multiple photoanode-based devices (e.g. tandem solar cells). Within this region, the breadth of the IPCE spectrum (and  $J_{SC}$  generated) is a key performance metric with the goal being to combine these photoanodes into tandem-type systems. Metal-based sensitizers are exceptional in the >800 nm spectral region within DSC devices. Ru- and Os-based sensitizers specifically have shown exceptional deep NIR photon absorption and conversion properties. The ultrafast electron injection properties of these systems allows for efficient electron transfers prior to excited-state relaxation and likely allows for the use of relatively low energy photons efficiently with minimal driving force needed for charge injection. Os-1 is a similar structure to N3 which uses two bipyridine-based ligands and a  $\beta$ -diketone in place of the NCS ligands of N3 (Fig. 19.244 Os-1 is broadly absorbing with an IPCE onset near 1100 nm and in excess of 70% across the visible spectrum. A PCE of 2.7% is reported which is low due to a poor  $V_{\rm OC}$  (0.32 V) despite the high  $J_{\rm SC}$  value of 23.7 mA cm<sup>-2</sup>. Os dye TF-52 was one of the first sensitizers to reach 1000 nm with a high peak IPCE ( 75%).  $^{245}$  A photocurrent of 23.3 mA cm $^{-2}$  was reported with an efficiency of 8.85%. Light soaking at 60 °C with TF-52 reveals no significant change in PCE for this device over a 1000 hour measurement. Dye DX3 efficiently uses photons across the visible spectrum with an IPCE onset of  $\sim$ 1100 nm. The peak IPCE value observed with this system is >80% with the IPCE remaining in excess of 80% from approximately 450 to 900 nm. A  $J_{\rm SC}$  in excess of 30 mA cm<sup>-2</sup> is observed from DSC devices using this dye. The deep NIR photon use of DX3 lead to the use of a DSC device made from this material in tandem with a perovskite solar cell with the DSC device being used as the narrow bandgap material (21.5% PCE tandem efficiency). 246 These dyes are attractive for use in tandem type systems and illustrate the forefront of high percentage IPCE, broadly absorbing sensitizers. Design of sensitizers that retain high percentage IPCE values throughout the IPCE spectrum and extend IPCE wavelengths to beyond 1100 nm is an intriguing direction for this type of sensitizers that could have significant impact on tandem device designs.

 Table 2 Photovoltaic characteristics of DSCs based on metal coordination complex dyes

Sensitizer	Electrolyte	Additives	V <sub>OC</sub> (mV)	$J_{\rm SC}~({\rm mA~cm^{-2}})$	FF (%)	PCE (%)	Year	Ref.
N719	I <sub>2</sub> , BMII	GuSCN, tBP	789	18.2	70.4	10.1	2008	209
CYC-B11	I <sub>2</sub> , LiI, DMII	GuSCN, tBP	743	20.05	77	11.5	2009	234
Black dye	I <sub>2</sub> , LiI, DMPII	tBP	727	20.43	72.4	10.75	2012	235
TUS-38	I <sub>2</sub> , LiI, DMPII	tBP	674	23.88	68.8	11.07	2016	236
T7	I <sub>2</sub> , LiI, DMPII	tBP	760	16.7	70	8.9	2016	237
T7	Co(phen) <sub>3</sub>	LiClO <sub>4</sub> , tBP	800	10.1	70	5.7	2016	237
T5	I <sub>2</sub> , LiI, DMPII	tBP	680	19.5	67	8.9	2016	237
T5	Co(phen) <sub>3</sub>	LiClO <sub>4</sub> , tBP	670	4.05	52	1.4	2016	237
TF-1	I <sub>2</sub> , LiI, DMPII	tBP	670	16.7	68	7.7	2016	237
TF-1	Co(phen) <sub>3</sub>	LiClO <sub>4</sub> , tBP	570	6.85	39	1.5	2016	237
Ru-1	Co(phen) <sub>3</sub>	LiTFSI, tBP	837	13.2	78	8.6	2013	238
Ru-1	I <sub>2</sub> , LiI, PMII	GuSCN, tBP	715	16.3	75	8.7	2013	238
SA22	Co(phen) <sub>3</sub>	LiTFSI, NOP	827	12.25	75.5	7.9	2016	239
SA25	Co(phen) <sub>3</sub>	LiTFSI, NOP	810	10.68	77.9	6.9	2016	239
SA246	Co(phen) <sub>3</sub>	LiTFSI, NOP	845	14.55	74.7	9.4	2016	239
SA282	Co(phen) <sub>3</sub>	LiTFSI, NOP	794	9.89	78.5	6.3	2016	239
SA284	Co(phen) <sub>3</sub>	LiTFSI, NOP	794	11.28	76.9	7.0	2016	239
SA285	Co(phen) <sub>3</sub>	LiTFSI, NOP	807	11.85	73.6	7.2	2016	239
SA633	Co(phen) <sub>3</sub>	LiTFSI, tBP	819	13.68	71.5	8.0	2017	240
SA634	Co(phen) <sub>3</sub>	LiTFSI, tBP	845	13.89	70.0	8.2	2017	240
SA635	Co(phen) <sub>3</sub>	LiTFSI, tBP	809	13.03	72.1	7.6	2017	240
51-5ht	Co(bpy) <sub>3</sub>	LiTFSI, tBP	840	12.78	76.4	8.22	2016	241
51-5ht	Co(phen) <sub>3</sub>	LiTFSI, tBP	842	12.17	75.0	7.69	2016	241
51-5ht	I <sub>2</sub> , LiI, PMII	tBP	718	15.31	74.6	8.20	2016	241
51-57dht	$Co(bpy)_3$	LiTFSI, tBP	844	13.56	74.2	8.49	2016	241
51-57dht	Co(phen) <sub>3</sub>	LiTFSI, tBP	898	12.32	75.4	8.34	2016	241
51-57dht	I <sub>2</sub> , LiI, PMII	tBP	727	14.17	74.3	7.66	2016	241
51-57dht.1	$Co(bpy)_3$	LiTFSI, tBP	853	13.36	75.0	8.55	2016	241
51-57dht.1	Co(phen) <sub>3</sub>	LiTFSI, tBP	900	13.89	76.2	9.53	2016	241
51-57dht.1	I <sub>2</sub> , LiI, PMII	tBP	740	13.53	74.9	7.50	2016	241
TFRS-80a	Co(phen) <sub>3</sub>	LiTFSI, tBP	840	13.44	75.7	8.55	2014	242
TFRS-80a	I <sub>2</sub> , LiI, DMPII	tBP	780	14.49	66.8	7.55	2014	242
TFRS-80a	I <sub>2</sub> , EII, DIVII II I <sub>2</sub> , DMPII	tBP	890	12.93	72.7	8.37	2014	242
TFRS-80b	Co(phen) <sub>3</sub>	LiTFSI, tBP	820	13.30	72.7 76.6	8.36	2014	242
TFRS-80b	I <sub>2</sub> , LiI, DMPII	tBP	680	10.39	68.1	4.8	2014	242
TFRS-80b	I <sub>2</sub> , EII, DIVIFII I <sub>2</sub> , DMPII	tBP	780	9.81	72.5	5.55	2014	242
TFRS-80c	Co(phen) <sub>3</sub>	LiTFSI, tBP	840	14.32	72.3 75.4	9.06	2014	242 242
		tBP	730		65.1	7.06	2014	242 242
TFRS-80c	I <sub>2</sub> , LiI, DMPII	tBP		14.84	75.6			
TFRS-80c	I <sub>2</sub> , DMPII	tBP	880 870	12.41 0.014	/5.6 48	8.26 0.60	2014 2020	242 243
Ir-1	Fe(bpy) <sub>3</sub>							
Os-1	I <sub>2</sub> , LiI, DMPII	none	320	23.7	36	2.7	2010	244
TF-5	I <sub>2</sub> , LiI, DMPII	tBP	640	18.0	71.6	8.25	2012	245
TF-51	I <sub>2</sub> , LiI, DMPII	tBP	560	20.1	66.4	7.47	2012	245
TF-52	I <sub>2</sub> , LiI, DMPII	tBP	600	23.3	63.3	8.85	2012	245
DX3	I <sub>2</sub> , LiI, DMPII	tBP	552	30.3	60	10.0	2015	246

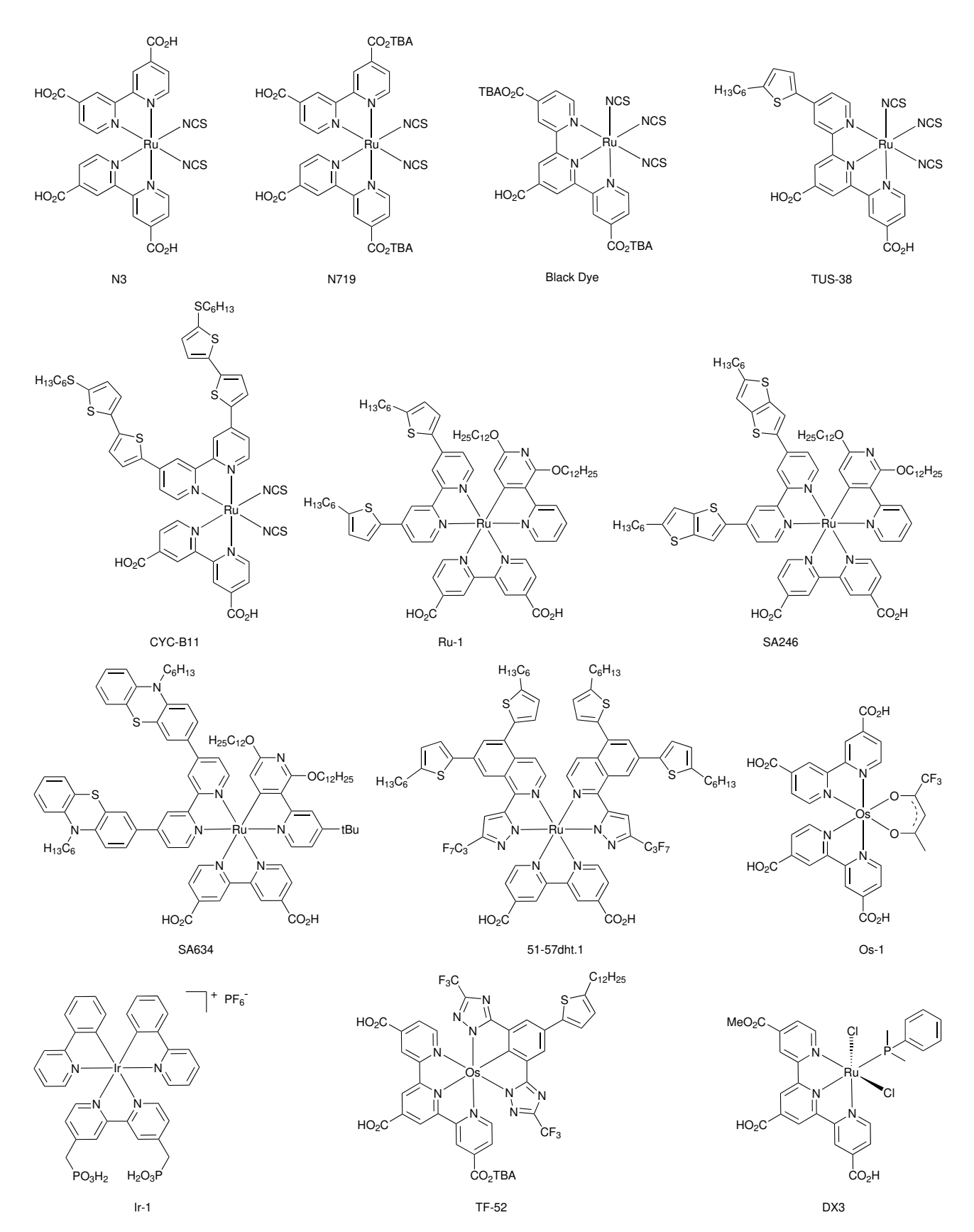


Fig. 19 Examples of metal complex-based sensitizers.

#### 4.2.2 Organic sensitizers.

Organic dyes have been intensely explored within DSC devices over the last decade with progressively sophisticated designs giving a variety of chromophores tailored to probe various metrics. The demand for higher performing dyes for a range of DSC applications has been assisted by several notable synthetic approaches focused on rapid dye diversification strategies based on onepot three-component couplings, 247 one-pot four-component couplings, <sup>248</sup> C-H activation-based cross couplings, <sup>249,250</sup> sequential C-H activations, <sup>251–256</sup> masked-halide approaches for sequential couplings, <sup>257</sup> and cross-dehydrogenative couplings (Fig. 20). <sup>258</sup> These types of contemporary routes in addition to traditional cross-couplings have in part fueled the rapid expansion of knowledge with regard to organic dyes in dye-sensitized systems. An infinite possibility for new dye designs exists that generally fall into two categories: intramolecular charge transfer (ICT) donoracceptor type systems and inherent chromophore tuned systems. The donor-acceptor approach typically relies on building blocks which have little or no visible light absorption, but when combined can generate broadly absorbing dyes due to ICT events. The tunability of ICT systems relies primarily on adjusting electron donor or acceptor building block strengths. The inherent chromophore direction selects a molecule with desirable optical properties (i.e. porphyrins, phthalocyanines, squaraines, diketopyrrolopyrrole, BODIPY, etc.) and tunes the dye photophysical properties with added functionality. Both approaches utilize  $\pi$ -systems with increased or decreased conjugation lengths to adjust optical energy gaps. Both design approaches have found widespread use in the design of dye-sensitized systems with intriguing properties. Table 3 lists device parameters of DSCs fabricated with organic dyes referenced in this review, together with the electrolyte used.

The highest performing DSC dyes are typically based on amine donors. These groups are tunable in donation strength, offer reversible oxidation potentials, and have multiple positions for addition of insulating groups. Indoline-based donor dyes have been a popular class of materials in the DSC literature. Relatively early success with indoline use in an organic dye was found when D205 demonstrated a PCE in excess of 9.5% as a donor-acceptor (D-A) dye design with a rhodanine acceptor (Fig. 21). <sup>259</sup> This PCE value was reported to be the highest observed for an organic dye at the time and fueled wide-spread use of the indoline donor with varied  $\pi$ -bridges and acceptors. WS-69 uses an indoline donor group with a benzoxydiazole (BOD), cyclopentadithiophene (CPDT), and phenyl-cyanoacrylic acid (CAA) to generate a device with an IPCE onset nearing 800 nm, which resulted in a  $J_{\rm SC}$  of 19.4 mA cm<sup>-2</sup> and a PCE of 9% as a single dye device. <sup>260</sup> The use of indoline in a donor- $\pi$ -bridge-acceptor (D- $\pi$ -A) design allowed expansion of the IPCE onset from 700 nm with D205 to 800 nm with WS-69. A PCE in excess of 10% could be obtained when co-sensitization strategies were employed with WS-69. Increasing the bulk of the indoline donor used with D205 and utilizing a D-A'- $\pi$ -A design with a quinoxaline auxiliary acceptor gives dye YA422. 261 The increased bulk of the donor group led to a dye compatible with a Co-based electrolyte for a PCE of 10.7% withone pot three component coupling  $H = (\Pi_1) + (\Pi_2) + (\Pi_3) + (\Pi_3) + (\Pi_4) + (\Pi_2) + (\Pi_3) + (\Pi_4) +$ 

Fig. 20 Contemporary rapid routes to complex organic dyes where X is a halide, M is a transmetallating reagent, and Y is a masked functionality such as a TMS group prior to halide conversion.

out an added co-sensitizer. The use of the same donor on YA422 on a diketopyrrolopyrrole (DPP)-based dye (DPP17) again lead to a >10% PCE device with a bright blue chromophore valuable for aesthetic applications.  $^{262}$ 

One of the most popular classes of amine donors used in dye design is based on triarylamines (TAAs). TAAs are typically stable and the symmetric aryl groups not in conjugation with the acceptor allow for ease of incorporation of alkyl chains in multiple dimensions. C218 is a TAA donor-based dye with a CPDT  $\pi\text{-bridge}$  and a CAA acceptor which demonstrated a  $\sim\!\!9.0\%$  PCE with an IPCE onset near 700 nm (Fig. 21). In ionic liquid-based devices, exceptional stabilities were noted with nearly no loss in performance under full sun soaking conditions at 60 °C. 263 A 3,4-thienothiophene (3,4-TT) group was inserted between the CPDT and CAA groups of C218 to give AP25. 264 The 3,4-TT building block is proaromatic by valence bond theory upon ICT, and excited-state aromaticity is observed computationally. 265 Proaromatic groups allow for lower energy excitations, which enables the use of lower energy NIR photons. An exceptional photocurrent ( $J_{SC} = 25 \text{ mA cm}^{-2}$ ) for an organic dye-based DSC device is reported when AP25 was co-sensitized with D35 (Fig. 21 and 22). AP25-based DSC devices have an IPCE onset of 900 nm with a peak value of near 90% and a PCE of 8.3%. The broad IPCE of the AP25-based DSC device is attractive for use as a narrow optical gap material in tandem and sequential series multijunction (SSM), <sup>266–268</sup> yielding DSC devices with PCEs exceeding 10% for both the two and three photoanode devices with an up to 2.1 V open circuit voltage. Replacing the CAA group of C218 with a BTD and a benzoic acid linked with an alkyne group gives C268, which has a red-shifted IPCE by 50 nm relative to C218. <sup>269</sup> C268 was shown to densely pack on the surface of TiO2 with a co-sensitizer, which enabled the fabrication of possibly the first >10% PCE ionic liquid-based DSC device. Exceptional stability of ionic liquid-based C268 DSC devices is reported during light soaking at 60 °C or at 85 °C when thermally stressed.

Amine donor group design has given rise to some of the highest performance DSC devices by enabling the use of 1-electron redox shuttles typically based on  $Co^{3+/2+}$  and  $Cu^{2+/+}$  in the highest performing devices. 95,270 For these positively charged 1-electron redox shuttles to facilitate productive electron transfers within the DSC device, exquisite surface protection is needed to slow the recombination reaction of electrons in TiO2 with the oxidized redox shuttle. The most common successful strategy employed with respect to dye design is the use of alkylated donor groups with alkyl chains extending in three dimensions to provide an "umbrella" of insulating groups to protect electrons at the TiO2 surface. One of the first and most widely used materials to demonstrate this concept is the dye D35, which illustrated the benefits of  $Co^{3+/2+}$ redox shuttles relative to  $I^-/I_3^-$  (Fig. 22). <sup>271</sup> The thiophene  $\pi$ bridge of D35 was expanded to a CPDT  $\pi$ -bridge to give Y123 with the same CAA acceptor.  $^{272,273}$  The expansion of the  $\pi$ -bridge conjugation length gave a red-shift of the absorption spectrum and allowed for an increase in PCE from 6.7% to 10.1%. Building from the D35/Y123 D- $\pi$ -A design, an auxiliary acceptor (A') strategy was employed with dye WS-72 by insertion of a quinoxaline group between the TAA donor and the CPDT bridge to give a D-A'-π-A design. <sup>274</sup> The D-A'-π-A dye design is reported to enable more favorable electron transfers with extended charge separation durations while red-shifting the absorption spectrum relative to the D- $\pi$ -A design. <sup>275</sup> The D-A'- $\pi$ -A design often shows modest effects on the ground state oxidation potential value despite extending conjugation, which allows for the use of RSs with more positive values in DSC devices for an increase in the theoretical  $V_{\rm OC}$ . WS-72 was found to minimize voltage losses when paired with a  $Cu^{2+/+}$  redox shuttle leading to an 11.6% PCE DSC device with a V<sub>OC</sub> in excess of 1.1 V. The same device and redox shuttle could be solidified to give a solid-state device operating at 11.7% PCE, which is claimed to be the highest known solid-state DSC PCE at the time of the report. L350 uses an indacenodithiophene (IDT)  $\pi$ -bridge with a similar donor group to Y123 and a benzothiadiazole (BTD)-benzoic acid acceptor. <sup>276</sup> This design led to a positive ground state oxidation potential (1.04 V versus NHE) which allowed for the use of the bis-(4,4',6,6'-tetramethyl-2,2'-bipyridine)copper ([Cu(tmby)<sub>2</sub>]<sup>2+/+</sup>) redox shuttle system to give a 1.14 V open-circuit voltage solar cell for a PCE of 11.2% under full sun conditions. Under low light conditions (1000 lux), an impressive PCE of 28.4% could be obtained. Interestingly, L350 has an optical energy gap of 1.82 eV as estimated from the IPCE onset, which indicates that only 680 mV of total absorbed energy was required to drive both the electron transfer to TiO<sub>2</sub> and the regeneration reaction from the redox shuttle. XY1b uses a similar design to that of dye WS-72 with a BTD group in place of the quinoxaline group and a phenyl spacer between the CPDT and CAA groups. Through the use of XY1b, co-sensitizer Y123, redox shuttle [Cu(tmby)<sub>2</sub>]<sup>2+/+</sup>, and a direct contact PE-DOT counter electrode, a PCE of 13.1% could be obtained under full sun conditions. A 32% PCE at 1000 lux was reported which exceeds the values reported to date with commonly used materials such as silicon and GaAs systems under low light conditions. 277 Very recently Zhang et al. have introduced a new dye – MS5 – with a particularly long *n*-dodecyl "umbrella" alkyl chain and a favorable ground state oxidation potential in respect to the  $Cu(tmby)_2$  redox couple, leading to a record device  $V_{OC}$  of 1.24 V for a copper redox shuttle-based device. 13 The co-sensitization of MS5 with the broader-absorbing XY1b dye resulted in a DSC with a certified PCE of 13.0%, the highest certified efficiency reported to date, while a batch of such devices reached an average 13.5% efficiency when measured in the laboratory. These devices also retained 93% of their initial efficiency after 1000 h of full sun light soaking at 45 °C.

The use of extended  $\pi$ -conjugation systems as donor groups has been an increasing popular strategy for increasing light absorption and improving device PCEs. SC-3 is a perylene-based dye with a bulky diarylamine donor substituted onto a phenanthrocarbazole group (Fig. 21). <sup>278</sup> A BTD-benzoic acid acceptor was used with SC-3 to give a dye reported to undergo electron injection from non-relaxed, hot excited states. The fast electron injection coupled with good surface protecting gave a dye with 11.5% PCE. Notably, replacing the diarylamine group on SC-3 with an arylether group planarized by a ring fusion strategy led to dye C275, with a higher PCE of 12.5% owing to a high voltage (>950 mV) when using the Co(phen) $_3^{3+/2+}$  RS system. <sup>279</sup> R6 is designed with a central thienothiophene component fused to two anthracene groups. <sup>280</sup> A diarylamine donor and a BTD group with a benzoic acid acceptor complete the conjugated system. Two tetra-substituted sp<sup>3</sup>-hybridized carbons provide alkyl groups extending above and below the dye conjugated plane to increase solubility and reduce aggregation. R6-based DSC devices have an IPCE onset near 800 nm and give a 12.6% PCE using a Co(bpy)<sub>3</sub><sup>3+/2+</sup>-based electrolyte. The devices show a remarkable stability and offer a blue dye for use in aesthetically-driven applications. Dye H2 incorporated a donor group with four alkyl chains with BTD as a  $\pi$ -bridge and benzoic acid as an anchoring group. <sup>281</sup> This arrangement led to a high photovoltage (900 mV) when paired with a cobalt redox shuttle, indicating minimal recombination losses due to transfer of an electron from the TiO2 surface to the oxidized redox shuttle. Exceptional stability was observed from a dye analogue during light soaking studies, but ultimately the DSC device PCE was limited by the absorption range of the dye which had an IPCE onset of ~750 nm. ZL003 was designed with a novel donor group with three alkylated nitrogens, a bisthiophene-substituted benzothiadiazole (BTD), and a benzoic acid anchoring group. This design resulted in exceptional surface protection with minimal recombination losses for a photovoltage loss of only 106 mV based on the theoretical obtainable photovoltage assuming no shift in the TiO2 conduction band taken as −0.5 V versus NHE. <sup>282</sup> Notably, ZL003 was found to up-shift the Fermi level of TiO<sub>2</sub> by approximately 600-700 mV, which likely contributed to the high photovoltage observed (956 mV) from the ZL003 device with the  $Co(bpy)_3^{3+/2+}$  RS.

Fig. 21 Examples of high-performing organic charge transfer dyes used in DSC devices.

MS5

Fig. 22 Examples of high-performing organic charge transfer dyes used in DSC devices with "umbrella" type donors.

L350

XY1b

The exceptional surface protections, rapid hot electron injection occurring out of locally excited states from the dye to TiO<sub>2</sub>, and the broad IPCE nearing 800 nm onset led to the highest performing single dye DSC device reported in the literature at 13.6% PCE. A large number of anchoring group strategies have been reported in the literature, with strategies often focused on finding strong binding groups which retain facile electron transfer from the photoexcited dye to TiO2. The use of carboxylic acid-based systems is the most popular strategy in the literature owing to their relative ease of preparation and exceptional performance with respect to electron injection. One of the most intriguing motivations for replacing carboxylic acid anchoring groups in DSCs is highlighted with the discovery of ADEKA-1 (Fig. 21).  $^{25,283,284}$ ADEKA-1 features a siloxane-based anchoring group as a tight binding group to TiO2. The siloxane anchoring group enabled the use of a co-sensitizer (LEG4, which is similar to Y123 with C<sub>4</sub>H<sub>9</sub> alkyl chains on the amine donor) and a tremendous number of surfaces protecting groups of varied shapes and sizes. This type of extensive co-sensitization is challenging unless a significant difference in anchor binding group strength is present. This strategy has led to the highest performing single DSC device reported in the literature at 14.3% PCE. It is noteworthy that since this discovery, siloxane anchoring groups remain underexplored with respect to incorporation into dye designs which may be due to challenges with identifying the composition of the anchoring group after purification. 285

4.2.2.1 Wide optical gap organic sensitizers. A growing body of work is focusing on the design of wide optical gap dyes which have applications in multijunction or tandem DSC devices as the initial photoactive layer and in photoelectrochemical cell systems. For SSM or tandem systems, the photovoltage output from the wide optical gap dye-based DSC is a critical parameter since higher V<sub>OC</sub> values allow for less free energy waste from high energy visible light (blue) photons. A common objective is to position the dye excited-state energy level near the CB energy of an n-type semiconductor to minimize free energy loss and to position the ground state oxidation potential of the dye positive enough to drive challenging electron transfer reactions. Initial high photovoltage DSCs focused on the use of the Br<sup>-</sup>/Br<sub>3</sub><sup>-</sup> RS system with wide optical gap dyes. Through the use of Mg-doped TiO2 to shift the CB to a more negative potential and the Br-/Br3- RS a theoretical photovoltage of 1.6 V can be obtained. 213 A wide optical gap dye with a siloxane-based anchor and a coumarin weak donor (ADEKA-3) was used to give a 1.45 V device at room temperature with 1.5 V observed at 5 °C. A PCE of 3.9% was observed for the room temperature DSC device (Fig. 23). AP14 is designed with an electron deficient thienopyrroledione bridging a benzene with an ether donor and a benzene with a CAA acceptor. <sup>286</sup> A 1.73 V versus NHE oxidation potential was measured for AP14 which is positive enough to drive the oxidation of Fe(bpy)<sub>3</sub><sup>2+</sup> in DSC devices to give a 1.32 V device. RR9 is comprised of a BTD  $\pi$ -bridge and a pentaalkylated aryl ether-based weak donor group. <sup>287</sup> While the ground state oxidation potential of RR9 is less positive (1.56 V versus NHE) than that reported for AP14, the DSC devices exhibited a higher V<sub>OC</sub> value of 1.42 V, which was the record high voltage for a room temperature DSC device without the use of  $TiO_2$  doping at the time of the report. This device was used in a three active layer SSM DSC device (6-terminal, series wired) as the top layer to give a 3.3 V device where the photovoltage output is >1 V per layer. These systems are inherently limited due to the light absorption of  $Fe(bpy)_3^{3+/2+}$ ; however, they provide proof of principle examples of the value of the dye design strategy and indicate the importance of finding a redox shuttle at  $\geq 1.4$  V oxidation potential versus NHE that does not absorb visible light for use in SSM or tandem device systems.

Fig. 23 Examples of high voltage dye-designs.

**4.2.2.2 Porphyrins.** Porphyrins are a primary focus of dye design research due in part to porphyrins being one of the first classes of dyes to show comparable and higher PCEs in DSC devices compared to ruthenium complexes. The donor-porphyrinacceptor construct is one of the most successful design strategies among researchers. In 2010, YD2 demonstrated an impressive precious metal-free 11% PCE using a diarylamine donor and benzoic acid acceptor at opposite meso positions of the zinc porphyrin core (Fig. 24). <sup>288</sup> Substitution of the remaining two meso positions with de-aggregating tert-butyl-substituted aryls is a key part of this design although dyes are known with these two meso position being differentiated with high performances. YD2-o-C8 is a derivative of YD2 with bis-ortho-substituted alkyl ether substituents on a benzene ring to better disrupt aggregation of the porphyrin dye. <sup>289</sup> This derivatization gave the highest performing DSC device at the time with a PCE of 12.3%. The landmark PCE was made possible by the use of a 1-electron-based cobalt RS which gave a  $V_{\rm OC}$  of near 1 V. Additionally, a complementary organic photosensitizer (Y123, Fig. 22) was used as a co-sensitizer to increase the performance of the YD2-o-C8 device in the 500-650 nm region where porphyrins are relatively weakly absorbing. The introduction of a BTD group near the benzoic acid anchor

led to GY50, which better absorbs photons in the 500-650 nm range and eliminated the need for the use of a co-sensitizer. <sup>290</sup> A 12.8% PCE was obtained from a single dye DSC device with a  $J_{SC}$ of 18.5 mA cm<sup>-2</sup> using a cobalt-based electrolyte. This high  $J_{SC}$ value was made possible by both red-shifting the Q-band when introducing the BTD group and increasing the absorptivity of the dye throughout the visible spectral region. Comparatively, GY50 with an iodine-based electrolyte system gave a PCE of only 8.9%, which highlights the critical importance of 1-electron-based RSs with regard to high power conversion efficiencies in DSCs. The diarylamine donor group of GY50 was expanded to include an additional aryl group with 4 total donor-group alkyl chains on SM315 for better TiO2 surface insulation, aimed to slow the recombination of electrons at the TiO2 surface with the cobalt-based electrolyte. This strategy led to a  $\sim$ 25 mV increase in  $V_{\rm OC}$  for SM315 relative to GY50 resulting in a similar PCE to GY50 and the first DSC device reported to reach 13.0% PCE. 291 A benzene group on the donor of SM315 was replaced with a fluorene group to give SGT-021.<sup>292</sup> When benchmarked against SM315, a higher photovoltage (20 mV increase) and photocurrent (1.1 mA cm<sup>-2</sup> increase) were obtained. When a non-porphyrin-based organic sensitizer was used as a top cell in a mechanically stacked tandem device, an impressive 14.6% PCE could be obtained. <sup>293</sup> Through the incorporation of a D- $\pi$ -A dye with an exceptionally effective amine donor design to promote favorable charge separation durations, a co-sensitized device with SGT-021 and SGT-149 gave a high PCE of 14.2

To improve further on the exceptional efficiencies described above, the use of lower energy photons (>750 nm) is needed. Numerous strategies have emerged with respect to porphyrin dye design aiming to reduce aggregation through novel constructs, improve spectral response both in the visible and NIR via building block incorporation, co-link chromophores, and design supramolecular assembly strategies (tailored aggregation) as referenced and discussed below. With respect to the linear donorporphyrin-acceptor design with meso-substituted de-aggregating groups, common general methods for extending the absorption range focus on adding donor groups 294-300, fusing non-amine donor groups for  $\pi$ -extended donor groups, or adding acceptor groups 301-306 as the D and A component to promote lower energy ICT events within the D-porphyrin-A structure. The use of a  $\pi$ extended donor group has shown promise for improving DSC device performances as well. Specifically, the introduction of an anthracene group between the amine donor and porphyrin (mJS3) resulted in a red shift of both the Soret and Q-band relative to no added anthracene group. 307,308 However, the PCE of mJS3 dropped significantly compared to a benchmark YD2-o-C8 DSC cell under identical conditions (9.8% versus 2.3%) primarily due to loss of photocurrent with possible aggregation-limited performance for mJS3. De-aggregating groups at the βpositions of the porphyrin were explored in the same study and termed a "double fence" porphyrin due to the use of two de-aggregating aryl groups on each side of the porphyrin (see dye bJS3). The double fence strategy shows minimal changes to the dye energetics in solution, and led to a 10.4% PCE cell, which was higher performing than YD2-o-C8 under identical conditions. The massive improvement from 2.3% to 10.4% based on the shift from meso to  $\beta$ -substituted de-aggregative aryls certainly warrants more investigation in this direction. An alternative strategy for red-shifting the porphyrin absorption spectrum has recently been presented which focuses on purposefully inducing aggregation of porphyrin-based dyes with a planarized indolizine donor to allow for an aggregate induced red-shifting of the absorption spectrum. 309 This approach allowed for the shifting of the absorption spectrum substantially on TiO2 versus solution (710 nm onset in solution, 875 nm onset on TiO<sub>2</sub>) and provided an under-explored method of absorbing deeper into the NIR spectral region post-synthesis. Bacteriochlorins are a related class of materials to porphyrins and are known as a type of hydroporphyrin. These building blocks have been used as DSC dyes (see LS-11) with exceptional NIR photon use until 870 nm in DSC devices. 310 LS-11 shows a relatively intense Q-band (112 000 M<sup>-1</sup>cm<sup>-1</sup>) compared to many porphyrin-based dyes and multiple absorption features throughout the visible spectral region. However, due to a peak IPCE response of ~60% and a modest open circuit voltage (0.52 V), the PCE was limited to 5.4%. Further exploration of this class of materials is intriguing given the rare use of NIR photons beyond 800 nm.

Doubly-strapped porphyrins have also shown promise in DSC devices by minimizing aggregate formation thorough the introduction of carbon chains bridging the meso positions such as with dye XW51. 311,312 This strategy leads to a high PCE of 11.1% with the I<sup>-</sup>/I<sub>3</sub><sup>-</sup> RS system. XW51 has demonstrated exceptional stabilities over the course of 1000 hours of aging. 311 XW51 was covalently linked to a "companion" D-A'- $\pi$ -A organic dye with a complementary absorption spectrum for a 12.4% PCE from an I<sup>-</sup>/I<sub>3</sub><sup>-</sup> RS-based cell generating 21.4 mA cm<sup>-2</sup> of photocurrent with a remarkable photostability to light soaking. <sup>313</sup> Significantly diminished performances were reported with a cobalt electrolyte (10.7% PCE), likely due to recombination of electrons in TiO<sub>2</sub> with the oxidizing electrolyte remaining problematic. Strategies aimed at complete aggregation mitigation and shifting the absorption spectrum onset of porphyrins to lower energy remain intriguing directions for this class of materials.

**4.2.2.3 Squaraines.** Squaraine dyes are a popular class of materials in dye-sensitized systems owing to their strong absorption into the NIR spectral region. Squaraine-based dyes have shown some of the deepest NIR photon use in DSC devices known.  $^{314}$  Squaraines typically absorb intensely in the NIR region often between 600-900 nm with molar absorptivities often above 100 000  $\rm M^{-1}cm^{-1}$ ; however, absorption is typically weak in the higher energy spectral region. The literature surrounding this class of materials is expanding dramatically since high performing NIR absorbing chromophores are urgently needed to improve DSC devices. Select examples of squaraine dyes are discussed below (Fig. 25).

A series of squaraines with systematically varied alkyl groups in and out of the  $\pi\text{-system}$  plane were evaluated with alkyl group positions both near and far from the  $\text{TiO}_2$  surface.  $^{315}$  Extending the out of plane alkyl groups on the indoline building block furthest from the surface was found to have a dramatic effect on overall DSC device performance. Under identical conditions, the PCE

increased from 3.4% with methyl groups in place of long alkyl chains to 7.7% PCE for SQ5 (Fig. 25). Including alkyl chains at the indoline near the  $\mathrm{TiO}_2$  anchor led to a decrease in PCE to 6.8% which was attributed to lower dye loading.

Fig. 24 Select porphyrin examples discussed in this review.

Fig. 25 Examples of squaraine-based dyes.

Under fully optimized conditions with reduced CDCA loadings, SQ5 reached a PCE of 8.9%. These findings are notably recent, and many of the examples discussed below utilize much shorter alkyl chains on the indoline portion of the dye far from the TiO2 surface. Addition of  $\pi$ -conjugated groups extending from the squaraine chromophore have been used to increase the absorption of dyes in the high energy region and to red-shift the strong NIR absorption further. A series of 8  $\pi$ -bridges were examined with the indoline-based squaraine core showing 4,4-dihexyl-4Hcyclopenta[2,1-b:3,4-b']dithiophene (CPDT) as the highest efficiency system studied as dye JD10.316 Part of the high performance is attributed to the alkyl chains on CPDT out of the  $\pi$ system plane leading to reduced aggregation and the introduction of a high energy absorption band upon incorporation of CPDT. Squaraine dyes in general benefit from co-sensitization with visible light-absorbing dyes and when JD10 was co-sensitized with D35 the efficiency could be improved to 7.9% PCE from 7.3% PCE without D35. Upon replacing the alkylated carbon of CPDT with an alkylated silicon atom to give a 4,4-bis(2-ethylhexyl)-4Hsilolo[3,2-b:4,5-b']dithiophene (DTS) group for dye DTS-CA, the PCE improved to 8.9%. 317 DTS-CA was found to have low recombination rates and reduced aggregation, which contributed to the observed high performance. The high energy bands introduced by the CPDT and DTS groups in the 400-550 nm region were modest in intensity with a strong effect on the IPCE curve in this region. To balance the high energy absorption intensity with the low energy absorption intensity, a porphyrin ring was added to the the DTS-CA structure to give PSil-SC12-DTS, which absorbs strongly from 400-550 nm due to the porphyrin core. 318 However, despite the balancing of the absorption bands, the peak percent IPCE of the devices with PSil-SC12-DTS dropped from ∼90% with DTS-CA to ~70%, which was attributed to a lower charge injection efficiency.

DSCs are thought to reach a theoretical maximum practical PCE from a single active layer device near 950 nm. 233 Very few dye designs have reached this value. The NIR absorption of squaraine chromophores places them relatively near to this value with IPCE onsets routinely near 800 nm. One approach aimed at a further red-shifting of the squaraine chromophore is based on the use of multiple squaraine building blocks on a single dye such as with TSQa. 319 The common bis-indoline-squaraine chromophore has a solution absorption onset of approximately 700 nm. Through the introduction of multiple squaraine building blocks onto the bis-indoline-squaraine chromophore, a solution absorption onset >900 nm could be reached. An IPCE onset of near 1000 nm was obtained with TSQa; however, the peak IPCE was limited to <20%. The addition of multiple squaraine building blocks was found to dramatically lower the dye LUMO energy resulting in a low driving force for electron transfer to TiO<sub>2</sub>. A second approach to red-shifting squaraine-derived dyes focuses on the desymmetrization of the commonly used bis-indoline chromophore to allow for the use of a donor- $\pi$ -bridge group (triarylaminethiophene-pyrrole based) with a single indoline-squaraine building block as with dyes JK-216 and JK-217. 320 An IPCE onset of near 850 nm was obtained with the more red-shifted JK-217. The higher  $V_{\rm OC}$  (610 mV) and FF (74%) with JK-216 led to a higher PCE of 6.3% than is observed with JK-217 ( $V_{\rm OC}=583~{\rm mV}$ , FF = 70%, PCE = 5.5%). Importantly, both dyes were shown to be stable to prolonged light soaking (1000 h at 60 °C) and function well in solid-state devices. WCH-SQ10 is comprised of a triaryl amine-3,4-ethylenedioxythiophene donor- $\pi$ -bridge with a squaraine-quinoline-based structure. <sup>321</sup> This design lead to an IPCE onset beyond 1000 nm to give one of the deepest NIR photon accessing organic dyes known. Interestingly, a symmetric core bis-quinoline squaraine dye (ISQ3) shows appreciable light harvesting efficiency on TiO<sub>2</sub> reaching 1000 nm, but an IPCE onset near 850 nm. <sup>314</sup> This suggests significant influence of the electrolyte on the dye absorbance energy with quinoline-squaraine based materials.

Dicyanomethylene-based squaraine materials show significant red shifts of the absorption spectrum onset relative to the keto squaraine core. Dye PSQ 9 has a broad IPCE spectrum reaching  $\sim$ 850 nm and generating >17 mA cm $^{-2}$  of photocurrent. Due to a modest photovoltage (577 mV) - as is common in the NIR region with dye sensitized solar cells – the overall power conversion efficiency was limited to 6.9% PCE. 322 An ethyl cyanoacetatederived squaraine dye (HSQ4) with dual anchors was shown to have a substantially increased stability relative to mono-anchored squaraine dyes with no change in PCE after 1000 hours. 323 In this same study, the ethyl cyanoacetate group was found to give a dye with a significantly higher excited state oxidation potential than a dicyanomethylene derived dye, which correlated to a higher IPCE peak value (80% versus 70%). Dicyanomethylene squaraines without a conjugated anchoring group have also been shown to function well within co-sensitized DSC device. 324 SPSQ2 was found to increase the performance of N3-based devices by red-shifting the IPCE onset leading to an improved  $J_{SC}$ (14.9 mA cm<sup>-2</sup> without SPSQ2 and 17.1 mA cm<sup>-2</sup> with SPSQ2) and improved PCE (7.1% versus 8.2%). With substantial recent progress having been shown in co-sensitized DSC devices and in deep NIR photon absorption, continued vigorous research within the area of squaraine dyes is likely and warranted.

Notably, the majority of squaraine dye-based DSC devices in the literature rely on the 2-electron  $I^-/I_3^-$  RS system, which inherently limits the PCEs of DSC devices. Progressive improvements have been observed with squaraine dyes reaching  $\sim\!\!9\%$  PCE to date with the  $I^-/I_3^-$  RS. Similar to the breakthrough performances enabled with porphyrin-based sensitizers, a squaraine dye design that functions well with 1-electron RSs such as Co-and Cu-based systems is needed. This advance in porphyrin designs shifted the PCE from  $\sim\!\!9\%$  to  $\sim\!\!13\%$  when Co RS-compatible dyes were discovered. A similar discovery would greatly benefit squaraine research.

Table 3 Photovoltaic characteristics of DSCs based on organic dyes

Sensitizer	Electrolyte	Additives	V <sub>OC</sub> (mV)	$J_{\rm SC}~({ m mA~cm^{-2}})$	FF (%)	PCE (%)	Year	Ref.
D149	I <sub>2</sub> , LiI, BMII	tBP	644	19.86	69.4	8.85	2008	259
D205	I <sub>2</sub> , LiI, BMII	tBP	710	18.68	70.7	9.40	2008	259
WS-66	I <sub>2</sub> , LiI, DPMII	tBP	757	12.97	71	7.01	2017	260
WS-67	I <sub>2</sub> , LiI, DPMII	tBP	711	15.91	73	8.25	2017	260
WS-68	I <sub>2</sub> , LiI, DPMII	tBP	705	17.73	67	8.42	2017	260
WS-69	I <sub>2</sub> , LiI, DPMII	tBP	696	19.39	67	9.03	2017	260
IQ4	Co(bpy) <sub>3</sub>	LiClO <sub>4</sub> , tBP	771	14.69	68.8	7.79	2014	261
IQ4	I <sub>2</sub> , LiI, DMII	GuSCN, tBP	737	15.33	75.5	8.53	2014	261
YA421	Co(bpy) <sub>3</sub>	LiClO <sub>4</sub> , tBP	803	15.76	71.2	9.00	2014	261
YA421	I <sub>2</sub> , LiI, DMII	GuSCN, tBP	741	15.41	71.1	8.12	2014	261
YA422	Co(bpy) <sub>3</sub>	LiClO <sub>4</sub> , tBP	876	15.26	68.9	9.22	2014	261
YA422	I <sub>2</sub> , LiI, DMII	GuSCN, tBP	741	14.40	68.2	7.28	2014	261
DPP13	I <sub>2</sub> , LiI, DMII	GuSCN, tBP	705	16.2	67	7.60	2013	262
DPP13	$Co(bpy)_3$	LiClO <sub>4</sub> , tBP	743	15.6	78	8.97	2013	262
DPP14	I <sub>2</sub> , LiI, DMII	GuSCN, tBP	680	16.6	68	7.73	262	
DPP14	$Co(bpy)_3$	LiClO <sub>4</sub> , tBP	716	15.2	76	8.23	2013	262
DPP15	I <sub>2</sub> , LiI, DMII	GuSCN, tBP	684	16.9	65	7.44	2013	262
DPP15	Co(bpy) <sub>3</sub>	LiClO <sub>4</sub> , tBP	745	17.6	75	9.81	2013	262
DPP17	I <sub>2</sub> , LiI, DMII	GuSCN, tBP	700	16.3	63	7.13	2013	262
DPP17	Co(bpy) <sub>3</sub>	LiClO <sub>4</sub> , tBP	761	17.9	74	10.1	2013	262
D21L6	Со(Бру) <sub>3</sub> I <sub>2</sub> , LiI, DMII	GuSCN, tBP	701	13.81	74 72.1	7.11	2013	263
C218	I <sub>2</sub> , LiI, DMII I <sub>2</sub> , LiI, DMII		714 768	15.84	73.5		2010	263
		GuSCN, tBP				8.95		
AP25	I <sub>2</sub> , LiI, DMII	GuSCN, tBP	527	19.0	65	6.8	2020	264
PB1	I <sub>2</sub> , LiI, DMII	GuSCN, tBP	704	12.1	75 75	6.50	2016	265
PB2	I <sub>2</sub> , LiI, DMII	GuSCN, tBP	648	12.7	75 75	6.24	2016	265
DP1	I <sub>2</sub> , LiI, DMII	GuSCN, tBP	680	10.9	75 <b>-</b> 6	5.61	2016	265
DP2	I <sub>2</sub> , LiI, DMII	GuSCN, tBP	697	13.7	76	7.41	2016	265
C268	I <sub>2</sub> , DMII, EMII	sulfolane, NBB, GuSCN	718	16.76	72.3	8.7	2018	269
D35	$Co(bpy)_3$	LiClO <sub>4</sub> , tBP	920	10.7	68	6.7	2010	271
D35	I <sub>2</sub> , LiI, TBAI	tBP	910	9.38	65	5.5	2010	271
Y123	I <sub>2</sub> , LiI, DMII	GuSCN, tBP	757	13.6	70	7.2	2011	272
Y123	Co(bpy) <sub>3</sub>	LiClO <sub>4</sub> , tBP	855	14.6	70	8.8	2011	272
Y123	Co(bpy-pz) <sub>2</sub>	LiClO <sub>4</sub> , tBP	1020	12.54	69.4	8.87	2012	273
Y123	$Cu(tmby)_2$	LiTFSI, tBP	1030	13.6	74	10.3	2018	274
WS-70	$Cu(tmby)_2$	LiTFSI, tBP	1060	13.2	77	11.0	2018	274
WS-72	$Cu(tmby)_2$	LiTFSI, tBP	1100	13.3	78	11.6	2018	274
L348	Cu(tmby) <sub>2</sub>	LiTFSI	1170	6.4	72.0	5.3	2018	276
L349	$Cu(tmby)_2$	LiTFSI	1160	11.0	71.7	9.2	2018	276
L350	Cu(tmby) <sub>2</sub>	LiTFSI	1140	13.0	76.0	11.2	2018	276
L351	Cu(tmby) <sub>2</sub>	LiTFSI	1060	11.2	76.3	9.1	2018	276
NT35	$Cu(tmby)_2$	LiTFSI, MBI	950	5.96	79.1	4.5	2021	13
MS4	$Cu(tmby)_2$	LiTFSI, MBI	1170	8.86	73.0	7.6	2021	13
MS5	Cu(tmby) <sub>2</sub>	LiTFSI, MBI	1240	8.87	73.3	8.0	2021	13
XY1b	Cu(tmby) <sub>2</sub>	LiTFSI, MBI	1010	15.26	76.3	11.8	2021	13
SC-1	Co(bpy) <sub>3</sub>	LiTFSI, tBP	828	14.70	76.2	9.3	2017	278
SC-2	Co(bpy) <sub>3</sub>	LiTFSI, tBP	856	16.62	74.5	10.6	2017	278
SC-3	Co(bpy) <sub>3</sub>	LiTFSI, tBP	920	16.50	75.8	11.5	2017	278
C272	Co(phen) <sub>3</sub>	LiTFSI, tBP	897	15.81	74.4	10.6	2015	279
C275	Co(phen) <sub>3</sub>	LiTFSI, tBP	956	17.03	77.0	12.5	2015	279
R4	$Co(bpy)_3$	LiTFSI, tBP	852	17.25	75.4	11.1	2018	280
R6	$Co(bpy)_3$	LiTFSI, tBP	850	19.69	75.4	12.6	2018	280
H1	$Co(bpy)_3$	LiTFSI, tBP	931	14.33	72.3	9.7	2019	281

H <sub>2</sub>	Co(bpy) <sub>3</sub>	LiTFSI, tBP	903	15.47	74.0	10.3	2019	281
ZL001	Co(bpy) <sub>3</sub>	LiClO <sub>4</sub> , tBP	887	20.57	70.0	12.8	2019	282
ZL003	Co(bpy) <sub>3</sub>	LiClO <sub>4</sub> , tBP	956	20.73	68.5	13.6	2019	282
ADEKA-2	Co(bpy) <sub>3</sub>	LiClO <sub>4</sub> , tBP	821	15.1	75.2	9.32	2014	284
ADEKA-1	Co(bpy) <sub>3</sub>	LiClO <sub>4</sub> , tBP LiClO <sub>4</sub> , tBP, NaClO <sub>4</sub> ,	848	16.1	76.2	10.4	2014	284
ADEKA-1	Co(Cl-phen) <sub>3</sub>	TBAPF <sub>6</sub> , TBPPF <sub>6</sub> , HMIPF <sub>6</sub> , TMSP, MP	1036	15.6	77.4	12.5	2014	284
SFD-5	Br <sub>2</sub> , BMIBr, TPABr	GuSCN, tBP	960	6.16	53	3.1	2016	213
ADEKA-3	Br <sub>2</sub> , BMIBr, TPABr	GuSCN, tBP, TMSP, MP, H <sub>2</sub> O	1450	4.77	56	3.9	2016	213
AP11	Fe(bpy) <sub>3</sub>	LiTFSI, tBP	1260	3.50	63	2.9	2019	286
AP14	$Fe(bpy)_3$	LiTFSI, tBP	1320	3.40	63	2.7	2019	286
AP16	$Fe(bpy)_3$	LiTFSI, tBP	1290	3.10	65	2.6	2019	286
AP17	Fe(bpy) <sub>3</sub>	LiTFSI, tBP	1270	2.90	58	2.2	2019	286
RR9	Fe(bpy) <sub>3</sub>	LiTFSI, tBP	1420	2.8	47	1.9	2018	287
YD2	I <sub>2</sub> , LiI, DMII	GuSCN, tBP	735	16.7	71.5	8.8	2010	288
YD2	$Co(bpy)_3$	LiClO <sub>4</sub> , tBP	825	14.9	69	8.4	2011	289
YD2-o-C8	$Co(bpy)_3$	LiClO <sub>4</sub> , tBP	965	17.3	71	11.9	2011	289
GY21	Co(bpy) <sub>3</sub>	not specified	615	5.03	79.8	2.52	2014	290
GY21	I <sub>2</sub> , PMII	LiTFSI, tBP	552	11.50	75.1	4.84	2014	290
GY50	Co(bpy) <sub>3</sub>	not specified	885	18.53	77.3	12.75	2014	290
GY50	I <sub>2</sub> , PMII	LiTFSI, tBP	732	18.45	65.7	8.90	2014	290
SM371	$Co(bpy)_3$	LiTFSI, tBP	960	15.9	79	12.0	2014	291
SM315	Co(bpy) <sub>3</sub>	LiTFSI, tBP	910	18.1	78	13.0	2014	291
SGT-020	Co(bpy) <sub>3</sub>	LiClO <sub>4</sub> , tBP	864	15.8	76.6	10.5	2017	292
SGT-020	Co(bpy) <sub>3</sub>	LiClO <sub>4</sub> , tBP	910	17.5	75.3	12.0	2017	292
SGT-130		LiClO <sub>4</sub> , tBP	810	16.84	72.08	9.83	2017	293
	Co(bpy) <sub>3</sub>	LiClO <sub>4</sub> , tBP	804	18.35				293
SGT-136 SGT-137	Co(bpy) <sub>3</sub>				74.84	11.04	2017 2017	
	Co(bpy) <sub>3</sub>	LiClO <sub>4</sub> , tBP	825	19.39	73.98	11.84		293
SM63	I <sub>2</sub> , LiI, DMII	GuSCN, tBP	700	14.43	73	7.35	2016	294
LD14-C8	I <sub>2</sub> , LiI, DMII	GuSCN, tBP	730	15.72	74	8.45	2016	294
WW-3	Co(bpy) <sub>3</sub>	LiTFSI, tBP	744	9.81	76.7	5.6	2014	295
WW-4	Co(bpy) <sub>3</sub>	LiTFSI, tBP	500	3.00	29.9	0.3	2014	295
WW-5	Co(bpy) <sub>3</sub>	LiTFSI, tBP	766	181.43	73.3	10.3	2014	295
WW-6	$Co(bpy)_3$	LiTFSI, tBP	840	17.16	73.8	10.6	2016	296
WW-7	$Co(bpy)_3$	LiTFSI, tBP	708	8.05	77.7	4.4	2016	296
WW-8	$Co(bpy)_3$	LiTFSI, tBP	733	8.27	78.6	4.8	2016	296
WW-9	$Co(bpy)_3$	LiTFSI, tBP	770	15.93	75.2	9.2	2016	296
YD22	I <sub>2</sub> , LiI, PMII	tBP	700	14.92	72.43	7.56	2016	297
YD23	I <sub>2</sub> , LiI, PMII	tBP	740	17.10	71.41	9.00	2016	297
YD24	I <sub>2</sub> , LiI, PMII	tBP	730	17.29	72.46	9.19	2016	297
YD25	I <sub>2</sub> , LiI, PMII	tBP	720	15.22	72.66	7.93	2016	297
YD26	I <sub>2</sub> , LiI, PMII	tBP	790	15.26	73.24	8.79	2016	297
YD27	I <sub>2</sub> , LiI, PMII	tBP	790	15.45	73.07	8.92	2016	297
YD28	I <sub>2</sub> , LiI, PMII	tBP	760	14.07	70.60	7.58	2016	297
XW1	I <sub>2</sub> , LiI, PMII	tBP	716	14.99	66	7.13	2014	298
XW2	I <sub>2</sub> , LiI, PMII	tBP	680	15.73	64	6.84	2014	298
XW3	I <sub>2</sub> , LiI, PMII	tBP	694	15.60	68	7.32	2014	298
XW4	I <sub>2</sub> , LiI, PMII	tBP	702	16.22	70	7.94	2014	298
C1	I <sub>2</sub> , LiI, PMII	tBP	780	11.21	65	5.67	2014	298
XW9	I <sub>2</sub> , LiI, I WIII I <sub>2</sub> , LiI, PMII	tBP	740	16.17	68.9	8.2	2015	299
XW10	I <sub>2</sub> , LiI, PMII	tBP	740	17.51	68.0	8.8	2015	299
XW10 XW11	I <sub>2</sub> , LiI, PMII I <sub>2</sub> , LiI, PMII	tBP	739 727	18.26	70.1	9.3	2015	299
XW11 XW14	I <sub>2</sub> , LiI, PMII I <sub>2</sub> , LiI, PMII	tBP	727	17.07	70.1	9.3 8.6	2015	300
VANTA	17, 111, 11111	(DI	/ 4.0	1/.0/	/ 0	0.0	2013	300

XW15									
XM17	XW15	I <sub>2</sub> , LiI, PMII	tBP	720	18.02	67	8.7	2015	300
SGF1021   Cofbybys   LITFSI, IBP   849   19.2   76.8   12.6   2019   301     SGF10225   Ca(bpy)s   LITFSI, IBP   761   9.2   77.9   5.6   10.0   2019   301     SGF10225   Ca(bpy)s   LITFSI, IBP   837   17.3   76.0   11.0   2019   301     XW26		_							
SCF1023		_							
SCHOOLS   Co(phy)s   LiTESI, HP   837   17.3   76.0   51.0   2019   301   302   3									
XW26         Is, Isi, PMI         tBP         708         11.37         69.13         5.57         2017         302           XW27         Is, Isi, PMI         tBP         715         19.38         72.96         10.14         2017         302           LG1         Is, Isi, DMII         tBP         710         17.43         71         8.89         20.96         10.14         2017         303           LG2         Is, Isi, DMII         tBP         710         15.45         72         7.87         2017         303           LG3         Is, Isi, DMII         tBP         710         15.02         68         7.30         107         303           LG5         Is, Isi, DMII         tBP         690         21.01         71         10.20         2017         303           LG6         Is, Isi, DMII         dBP         690         19.55         71         9.62         2012         2017         303           LG7         Is, Isi, DMII         GBSCN, tBP         732         15.33         69.97         7.78         2015         304           ZZX-N8         Is, Isi, DMII         GBSCN, tBP         730         17.3         65         8.8         20	SGT-023		LiTFSI, tBP	761			5.6	2019	301
XW27	SGT-025	$Co(bpy)_3$	LiTFSI, tBP	837	17.3	76.0	11.0	2019	301
NUMBER   Tall, PMII   IBP   715   19.38   72,06   10.14   20.17   30.2   10.2	XW26	I <sub>2</sub> , LiI, PMII	tBP	708	11.37	69.13	5.57	2017	302
In   In   In   In   In   In   In   In	XW27	I <sub>2</sub> , LiI, PMII	tBP	710	14.08	72.26	7.17	2017	302
LG2         I <sub>2</sub> , LiI, DMII         tBP         710         15.45         72         7.87         2017         303           LG3         I <sub>2</sub> , LiI, DMIII         tBP         710         12.10         72         6.17         2017         303           LG4         I <sub>2</sub> , LiI, DMIII         tBP         680         21.01         71         10.20         2017         303           LG6         I <sub>2</sub> , LiI, DMIII         tBP         690         19.55         71         19.64         2017         303           LG7         I <sub>2</sub> , LiI, DMIII         tBP         660         13.38         69         6.21         2017         303           ZZX-N7         I <sub>2</sub> , LiI, DMIII         GuSCN, tBP         732         15.36         69.9         7.78         2015         304           ZZX-N8         I <sub>2</sub> , LiI, DMII         GuSCN, tBP         656         15.46         70.57         7.53         2015         304           ZZX-N8         I <sub>2</sub> , LII, DMII         GuSCN, tBP         730         15.6         68         7.7         2015         305           YB2-o-C8         I <sub>2</sub> , LII, DMII         GuSCN, tBP         780         17.3         65         8.8         2015         305 </td <td>XW28</td> <td>I<sub>2</sub>, LiI, PMII</td> <td>tBP</td> <td>715</td> <td>19.38</td> <td>72.96</td> <td>10.14</td> <td>2017</td> <td>302</td>	XW28	I <sub>2</sub> , LiI, PMII	tBP	715	19.38	72.96	10.14	2017	302
LG3	LG1	I <sub>2</sub> , LiI, DMII	tBP	710	17.43	71	8.89	2017	303
IG-64   12, I, I, DMII	LG2	I <sub>2</sub> , LiI, DMII	tBP	710	15.45	72	7.87	2017	303
IG-64   12, I, II, DMII	LG3	I <sub>2</sub> , LiI, DMII	tBP	710	12.10	72	6.17	2017	303
IGS	LG4	I <sub>2</sub> , LiI, DMII	tBP	710	15.02	68	7.30	2017	303
Incide	LG5	I <sub>2</sub> , LiI, DMII	tBP	680	21.01	71	10.20	2017	303
LG7		=							
ZZX-N8									
ZZX-N8									
ZZXN9									
VD2-o-C8T         I <sub>2</sub> , LiI, DMII         GuSCN, tBP         730         1.5         68         7.7         2015         305           YD2-o-C8         I <sub>2</sub> , LiI, DMIII         GuSCN, tBP         780         17.3         65         8.8         2014         306           PZn-HOQ         I <sub>2</sub> , LiI, DPMIII         GuSCN, tBP         595         7.81         66.4         3.09         2014         306           DPZn-HOQ         I <sub>2</sub> , LiI, DPMIII         GuSCN, tBP         692         4.22         69.4         1.76         2014         306           DPZn-HOQ         I <sub>2</sub> , LiI, DPMIII         GuSCN, tBP         602         4.22         69.4         1.76         2014         306           mJS1         Co(bpy) <sub>3</sub> LiTFSI, tBP         833         10.55         76.2         7.92         2021         307           mJS2         Co(bpy) <sub>3</sub> LiTFSI, tBP         814         3.73         76.8         7.74         2021         307           MJS1         Co(bpy) <sub>3</sub> LiTFSI, tBP         849         16.59         75.9         4.93         2021         307           MS2         Co(bpy) <sub>3</sub> LiTFSI, tBP         836         16.48         75.5         4.0									
YD2-o-C8         I2, LiI, DMIII         GuSCN, tBP         780         17.3         65         8.8         2015         305           PZH-HOQ         I2, LiI, DPMIII         GuSCN, tBP         576         6.48         67.8         2.53         2014         306           DPZH-HOQ         I2, LiI, DPMIII         GuSCN, tBP         692         4.22         69.4         1.76         2014         306           mJS1         Co(bpy)3         LiTFSI, tBP         833         10.55         76.2         7.59         2021         307           mJS2         Co(bpy)3         LiTFSI, tBP         845         5.47         75.2         7.22         2021         307           mJS3         Co(bpy)3         LiTFSI, tBP         814         3.73         76.8         7.74         2021         307           MJS3         Co(bpy)3         LiTFSI, tBP         823         12.52         77.9         4.81         2021         307           MJS3         Co(bpy)3         LiTFSI, tBP         836         16.48         75.5         4.70         2021         307           LWP12         Co(bpy)3         LiTFSI, tBP         731         12.07         73.8         6.5         2016 <th< td=""><td></td><td></td><td>=</td><td></td><td></td><td></td><td></td><td></td><td></td></th<>			=						
PZn-HOQ         I2, LiI, DPMII         GuSCN, tBP         576         6.48         67.8         2.53         2014         306           DPZn-HOQ         I2, LiI, DPMII         GuSCN, tBP         595         7.81         66.4         3.09         2014         306           DPZn-COOH         I2, LiI, DPMII         GuSCN, tBP         602         4.22         66.4         3.09         2014         306           mJS1         Co(bpy)3         LiTFSI, tBP         833         10.55         76.2         7.59         2021         307           mJS3         Co(bpy)2         LiTFSI, tBP         845         5.47         75.2         7.22         2021         307           bJS1         Co(bpy)3         LiTFSI, tBP         814         3.73         76.8         7.74         2021         307           bJS3         Co(bpy)3         LiTFSI, tBP         836         16.68         75.5         4.70         2021         307           bJS3         Co(bpy)3         LiTFSI, tBP         731         12.07         73.8         6.5         2016         308           LWP12         Co(bpy)3         LiTFSI, tBP         706         10.06         78.0         5.5         2016 <td< td=""><td></td><td></td><td>-</td><td></td><td></td><td></td><td></td><td></td><td></td></td<>			-						
DPZn-HOQ         I2, LiI, DPMII         GuSCN, tBP         595         7.81         66.4         3.09         2014         306           DPZn-COOH         I2, LiI, DPMIII         GuSCN, tBP         602         4.22         69.4         1.76         2014         306           mJS1         Co(bpy)3         LiTFSI, tBP         833         10.55         76.2         7.59         2021         307           mJS2         Co(bpy)3         LiTFSI, tBP         814         3.73         76.8         7.74         2021         307           bJS1         Co(bpy)3         LiTFSI, tBP         814         3.73         76.8         7.74         2021         307           bJS2         Co(bpy)3         LiTFSI, tBP         884         16.59         75.9         4.93         2021         307           bJS3         Co(bpy)3         LiTFSI, tBP         836         16.48         75.5         4.70         2021         307           LWP12         Co(bpy)3         LiTFSI, tBP         731         12.07         73.8         6.5         2016         308           LWP14         Co(bpy)3         LiTFSI, tBP         706         10.06         78.0         5.5         2016         308<									
DPZn-COOH         I <sub>2</sub> , LiI, DPMII         GuSCN, tBP         602         4.22         69.4         1.76         2014         306           mJS1         Co(bpy) <sub>3</sub> LiTFSI, tBP         833         10.55         76.2         7.59         2021         307           mJS2         Co(bpy) <sub>3</sub> LiTFSI, tBP         845         5.47         75.2         2021         307           MJS3         Co(bpy) <sub>3</sub> LiTFSI, tBP         814         3.73         76.8         7.74         2021         307           MJS3         Co(bpy) <sub>3</sub> LiTFSI, tBP         823         12.52         77.9         4.81         2021         307           MJS3         Co(bpy) <sub>3</sub> LiTFSI, tBP         849         16.59         75.5         4.70         2021         307           LWP12         Co(bpy) <sub>3</sub> LiTFSI, tBP         836         16.48         75.5         4.70         2016         308           LWP13         Co(bpy) <sub>3</sub> LiTFSI, tBP         706         10.06         78.0         5.5         2016         308           LWP14         Co(bpy) <sub>3</sub> LiTFSI, tBP         805         71.22         74.1         10.3         2017         310 </td <td></td> <td></td> <td></td> <td></td> <td></td> <td></td> <td></td> <td></td> <td></td>									
mJS1         Co(bpy)3         LiTFSI, tBP         833         10.55         76.2         7.59         2021         307           mJS2         Co(bpy)3         LiTFSI, tBP         845         5.47         75.2         7.22         2021         307           mJS3         Co(bpy)3         LiTFSI, tBP         814         3.73         76.8         7.74         2021         307           bJS1         Co(bpy)3         LiTFSI, tBP         823         12.52         77.9         4.81         2021         307           bJS3         Co(bpy)3         LiTFSI, tBP         849         16.59         75.9         4.93         2021         307           bJS3         Co(bpy)3         LiTFSI, tBP         836         16.48         75.5         4.70         2021         307           LWP13         Co(bpy)3         LiTFSI, tBP         706         10.06         78.0         5.5         2016         308           LWP14         Co(bpy)3         LiTFSI, tBP         805         17.22         74.1         10.3         2016         308           SM85         L2, LiI, PMII         tBP         540         5.26         73         2.06         2017         310									
mJS2         Co(bpy)3         LiTFSI, tBP         845         5.47         75.2         7.22         2021         307           mJS3         Co(bpy)3         LiTFSI, tBP         814         3.73         76.8         7.74         2021         307           bJS1         Co(bpy)3         LiTFSI, tBP         823         12.52         77.9         4.81         2021         307           bJS2         Co(bpy)3         LiTFSI, tBP         849         16.59         75.9         4.93         2021         307           bJS3         Co(bpy)3         LiTFSI, tBP         836         16.48         75.5         4.70         2021         307           LWP12         Co(bpy)3         LiTFSI, tBP         706         10.06         78.0         5.5         2016         308           LWP14         Co(bpy)3         LiTFSI, tBP         706         10.06         78.0         5.5         2016         308           LWP14         Co(bpy)3         LiTFSI, tBP         805         17.22         74.1         10.3         2016         308           LWP14         Co(bpy)3         LiTFSI, tBP         50         12.2         74.1         10.3         2016         310									
mJS3         Co(bpy)3         LiTFSI, tBP         814         3.73         76.8         7.74         2021         307           bJS1         Co(bpy)3         LiTFSI, tBP         823         12.52         77.9         4.81         2021         307           bJS2         Co(bpy)3         LiTFSI, tBP         849         16.59         75.9         4.93         2021         307           bJS3         Co(bpy)3         LiTFSI, tBP         836         16.48         75.5         4.70         2021         307           LWP12         Co(bpy)3         LiTFSI, tBP         731         12.07         73.8         6.5         2016         308           LWP14         Co(bpy)3         LiTFSI, tBP         706         10.06         78.0         5.5         2016         308           SM85         12, LiI, DMII         GuSCN, tBP         805         17.22         74.1         10.3         2016         308           SM85         12, LiI, PMII         tBP         540         5.26         73         2.06         2017         310           LS-01         12, LiI, PMII         tBP         530         12.58         70         4.67         2017         310									
bJS1         Co(bpy)3         LiTFSI, BP         823         12.52         77.9         4.81         2021         307           bJS2         Co(bpy)3         LiTFSI, BP         849         16.59         75.9         4.93         2021         307           bJS3         Co(bpy)3         LiTFSI, BP         836         16.48         75.5         4.70         2021         308           LWP12         Co(bpy)3         LiTFSI, BP         731         12.07         73.8         6.5         2016         308           LWP13         Co(bpy)3         LiTFSI, BP         706         10.06         78.0         5.5         2016         308           LWP14         Co(bpy)3         LiTFSI, BP         805         17.22         74.1         10.3         2016         308           SM85         12, LiI, PMII         BP         540         5.26         73         2.06         2017         310           LS-01         12, LiI, PMII         BP         530         12.58         70         4.67         2017         310           LS-11         12, LiI, PMII         BP         730         18.67         68.3         9.3 <t>2019         311           XW</t>									
bJS2         Co(bpy)3         LiTFSI, tBP         849         16.59         75.9         4.93         2021         307           bJS3         Co(bpy)3         LiTFSI, tBP         836         16.48         75.5         4.70         2021         307           LWP12         Co(bpy)3         LiTFSI, tBP         731         12.07         73.8         6.5         2016         308           LWP14         Co(bpy)3         LiTFSI, tBP         805         17.22         74.1         10.3         2016         308           SM85         I2, LiI, DMII         GuSCN, tBP         578         13.4         71         5.7         2019         309           H2PE1         I2, LiI, PMII         tBP         540         5.26         73         2.06         2017         310           LS-01         I2, LiI, PMII         tBP         530         12.58         70         4.67         2017         310           LW40         I2, LiI, PMII         tBP         730         18.67         68.3         9.3         2019         311           XW48         Co(bpy)3         LiTFSI, tBP         803         15.20         73.2         8.9         2019         311									
D.									
LWP12         Co(bpy) <sub>3</sub> LiTFSI, tBP         731         12.07         73.8         6.5         2016         308           LWP13         Co(bpy) <sub>3</sub> LiTFSI, tBP         706         10.06         78.0         5.5         2016         308           LWP14         Co(bpy) <sub>3</sub> LiTFSI, tBP         805         17.22         74.1         10.3         2016         308           SM85         12, LiI, DMII         GuSCN, tBP         578         13.4         71         5.7         2019         309           LS-01         12, LiI, PMII         tBP         540         5.26         73         2.06         2017         310           LS-01         12, LiI, PMII         tBP         530         12.58         70         4.67         2017         310           LS-11         12, LiI, PMII         tBP         520         16.13         64         5.36         2017         310           XW48         12, LiI, PMII         tBP         755         18.34         70.2         9.7         2019         311           XW49         Co(bpy) <sub>3</sub> LiTFSI, tBP         803         15.60         72.9         9.5         2019         311									
LWP13         Co(bpy)3         LiTFSI, tBP         706         10.06         78.0         5.5         2016         308           LWP14         Co(bpy)3         LiTFSI, tBP         805         17.22         74.1         10.3         2016         308           SM85         12, LiI, DMII         GuSCN, tBP         578         13.4         71         5.7         2019         309           H2PE1         12, LiI, PMII         tBP         540         5.26         73         2.06         2017         310           LS-01         12, LiI, PMII         tBP         530         12.58         70         4.67         2017         310           LS-11         12, LiI, PMII         tBP         520         16.13         64         5.36         2017         310           XW40         12, LiI, PMII         tBP         755         18.34         70.2         9.7         2019         311           XW48         Co(bpy)3         LiTFSI, tBP         803         15.20         73.2         8.9         2019         311           XW49         12, LiI, PMII         tBP         753         18.0         72.9         9.5         2019         311           XW									
LWP14         Co(bpy)3         LiTFSI, tBP         805         17.22         74.1         10.3         2016         308           SM85         I2, LiI, DMII         GuSCN, tBP         578         13.4         71         5.7         2019         309           H2PE1         I2, LiI, PMII         tBP         540         5.26         73         2.06         2017         310           LS-01         I2, LiI, PMII         tBP         530         12.58         70         4.67         2017         310           LS-11         I2, LiI, PMII         tBP         520         16.13         64         5.36         2017         310           LS-11         I2, LiI, PMII         tBP         750         18.36         68.3         9.3         2019         311           XW40         I2, LiI, PMII         tBP         755         18.34         70.2         9.7         2019         311           XW48         Co(bpy)3         LiTFSI, tBP         803         15.20         73.2         8.9         2019         311           XW49         Co(bpy)3         LiTFSI, tBP         837         15.60         72.9         9.5         2019         311           X									
SM85         I2, LII, DMII         GuSCN, tBP         578         13.4         71         5.7         2019         309           H2PE1         I2, LiI, PMII         tBP         540         5.26         73         2.06         2017         310           LS-01         I2, LiI, PMII         tBP         530         12.58         70         4.67         2017         310           LS-11         I2, LiI, PMII         tBP         520         16.13         64         5.36         2017         310           XW40         I2, LiI, PMII         tBP         730         18.67         68.3         9.3         2019         311           XW48         I2, LiI, PMII         tBP         755         18.34         70.2         9.7         2019         311           XW49         I2, LiI, PMII         tBP         753         18.09         69.6         9.5         2019         311           XW50         I2, LiI, PMII         tBP         761         18.96         70.2         10.1         2019         311           XW51         I2, LiI, PMII         tBP         781         20.07         70.2         11.1         2019         311           XW51									
H2PE1         I2, LiI, PMII         tBP         540         5.26         73         2.06         2017         310           LS-01         I2, LiI, PMII         tBP         530         12.58         70         4.67         2017         310           LS-11         I2, LiI, PMII         tBP         520         16.13         64         5.36         2017         310           XW40         I2, LiI, PMII         tBP         730         18.67         68.3         9.3         2019         311           XW48         I2, LiI, PMII         tBP         755         18.34         70.2         9.7         2019         311           XW48         Co(bpy)3         LiTFSI, tBP         803         15.20         73.2         8.9         2019         311           XW49         Co(bpy)3         LiTFSI, tBP         837         15.60         72.2         9.5         2019         311           XW50         I2, Li, PMII         tBP         761         18.96         70.2         10.1         2019         311           XW51         I2, Li, PMII         tBP         781         20.07         70.2         11.1         2019         311           XW51									
LS-01         I2, LiI, PMII         tBP         530         12.58         70         4.67         2017         310           LS-11         I2, LiI, PMII         tBP         520         16.13         64         5.36         2017         310           XW40         I2, LiI, PMII         tBP         730         18.67         68.3         9.3         2019         311           XW48         I2, LiI, PMII         tBP         755         18.34         70.2         9.7         2019         311           XW48         Co(bpy)3         LiTFSI, tBP         803         15.20         73.2         8.9         2019         311           XW49         I2, LiI, PMII         tBP         753         18.09         69.6         9.5         2019         311           XW50         I2, LiI, PMII         tBP         761         18.96         70.2         10.1         2019         311           XW51         I2, LiI, PMII         tBP         781         20.07         70.2         11.1         2019         311           XW51         Co(bpy)3         LiTFSI, tBP         844         15.24         75.6         9.7         2019         311           XW51 <td></td> <td><del>-</del>: :</td> <td></td> <td></td> <td></td> <td></td> <td></td> <td></td> <td></td>		<del>-</del> : :							
LS-11       I2, LiI, PMII       tBP       520       16.13       64       5.36       2017       310         XW40       I2, LiI, PMII       tBP       730       18.67       68.3       9.3       2019       311         XW48       I2, LiI, PMII       tBP       755       18.34       70.2       9.7       2019       311         XW48       Co(bpy)3       LiTFSI, tBP       803       15.20       73.2       8.9       2019       311         XW49       I2, LiI, PMII       tBP       753       18.09       69.6       9.5       2019       311         XW49       Co(bpy)3       LiTFSI, tBP       837       15.60       72.9       9.5       2019       311         XW50       I2, LiI, PMII       tBP       761       18.96       70.2       10.1       2019       311         XW51       I2, LiI, PMII       tBP       781       20.07       70.2       11.1       2019       311         XW51       Co(bpy)3       LiTFSI, tBP       844       15.24       75.6       9.7       2019       311         XW51       Co(bpy)3       LiTFSI, tBP       844       15.24       75.6       9.7       2019		=							
XW40       I2, LiI, PMII       tBP       730       18.67       68.3       9.3       2019       311         XW48       I2, LiI, PMII       tBP       755       18.34       70.2       9.7       2019       311         XW48       Co(bpy)3       LiTFSI, tBP       803       15.20       73.2       8.9       2019       311         XW49       I2, LiI, PMII       tBP       753       18.09       69.6       9.5       2019       311         XW49       Co(bpy)3       LiTFSI, tBP       837       15.60       72.9       9.5       2019       311         XW50       I2, LiI, PMII       tBP       761       18.96       70.2       10.1       2019       311         XW50       Co(bpy)3       LiTFSI, tBP       843       16.24       73.9       10.1       2019       311         XW51       I2, LiI, PMII       tBP       781       20.07       70.2       11.1       2019       311         XW41       I2, LiI, PMII       tBP       695       16.77       70.1       8.16       2019       312         XW60       I2, LiI, PMII       tBP       763       20.75       73.9       11.7       2020									
XW48       I2, LiI, PMII       tBP       755       18.34       70.2       9.7       2019       311         XW48       Co(bpy)3       LiTFSI, tBP       803       15.20       73.2       8.9       2019       311         XW49       I2, LiI, PMII       tBP       753       18.09       69.6       9.5       2019       311         XW49       Co(bpy)3       LiTFSI, tBP       837       15.60       72.9       9.5       2019       311         XW50       I2, LiI, PMII       tBP       761       18.96       70.2       10.1       2019       311         XW50       Co(bpy)3       LiTFSI, tBP       843       16.24       73.9       10.1       2019       311         XW51       I2, LiI, PMII       tBP       781       20.07       70.2       11.1       2019       311         XW51       Co(bpy)3       LiTFSI, tBP       844       15.24       75.6       9.7       2019       311         XW41       I2, LiI, PMII       tBP       695       16.77       70.1       8.16       2019       312         XW60       I2, LiI, PMII       tBP       763       20.75       73.9       11.7       2020 </td <td></td> <td></td> <td></td> <td></td> <td></td> <td></td> <td></td> <td></td> <td></td>									
XW48       Co(bpy)3       LiTFSI, tBP       803       15.20       73.2       8.9       2019       311         XW49       I2, LiI, PMII       tBP       753       18.09       69.6       9.5       2019       311         XW49       Co(bpy)3       LiTFSI, tBP       837       15.60       72.9       9.5       2019       311         XW50       I2, LiI, PMII       tBP       761       18.96       70.2       10.1       2019       311         XW50       Co(bpy)3       LiTFSI, tBP       843       16.24       73.9       10.1       2019       311         XW51       I2, LiI, PMII       tBP       781       20.07       70.2       11.1       2019       311         XW51       Co(bpy)3       LiTFSI, tBP       844       15.24       75.6       9.7       2019       311         XW41       I2, LiI, PMII       tBP       695       16.77       70.1       8.16       2019       312         XW60       I2, LiI, PMII       tBP       763       20.75       73.9       11.7       2020       313         XW62       I2, LiI, PMII       tBP       762       20.70       73.2       11.6       2020<									
XW49       I2, LiI, PMII       tBP       753       18.09       69.6       9.5       2019       311         XW49       Co(bpy)3       LiTFSI, tBP       837       15.60       72.9       9.5       2019       311         XW50       I2, LiI, PMII       tBP       761       18.96       70.2       10.1       2019       311         XW50       Co(bpy)3       LiTFSI, tBP       843       16.24       73.9       10.1       2019       311         XW51       I2, LiI, PMII       tBP       781       20.07       70.2       11.1       2019       311         XW51       Co(bpy)3       LiTFSI, tBP       844       15.24       75.6       9.7       2019       311         XW41       I2, LiI, PMII       tBP       695       16.77       70.1       8.16       2019       312         XW60       I2, LiI, PMII       tBP       715       16.77       73.1       8.8       2020       313         XW61       I2, LiI, PMII       tBP       763       20.75       73.9       11.7       2020       313         XW62       I2, LiI, PMII       tBP       763       20.63       73.7       11.6       2020 <td></td> <td></td> <td></td> <td></td> <td></td> <td></td> <td></td> <td></td> <td></td>									
XW49       Co(bpy)3       LiTFSI, tBP       837       15.60       72.9       9.5       2019       311         XW50       I2, LiI, PMII       tBP       761       18.96       70.2       10.1       2019       311         XW50       Co(bpy)3       LiTFSI, tBP       843       16.24       73.9       10.1       2019       311         XW51       I2, LiI, PMII       tBP       781       20.07       70.2       11.1       2019       311         XW51       Co(bpy)3       LiTFSI, tBP       844       15.24       75.6       9.7       2019       311         XW41       I2, LiI, PMII       tBP       695       16.77       70.1       8.16       2019       312         XW60       I2, LiI, PMII       tBP       715       16.77       73.1       8.8       2020       313         XW61       I2, LiI, PMII       tBP       763       20.75       73.9       11.7       2020       313         XW62       I2, LiI, PMII       tBP       763       20.63       73.7       11.6       2020       313         ISQ1       Iodolyte Z-50       544       8.99       68.4       3.34       2018       314 <td></td> <td></td> <td></td> <td></td> <td></td> <td></td> <td></td> <td></td> <td></td>									
XW50       I2, LiI, PMII       tBP       761       18.96       70.2       10.1       2019       311         XW50       Co(bpy)3       LiTFSI, tBP       843       16.24       73.9       10.1       2019       311         XW51       I2, LiI, PMII       tBP       781       20.07       70.2       11.1       2019       311         XW51       Co(bpy)3       LiTFSI, tBP       844       15.24       75.6       9.7       2019       311         XW41       I2, LiI, PMII       tBP       695       16.77       70.1       8.16       2019       312         XW60       I2, LiI, PMII       tBP       715       16.77       73.1       8.8       2020       313         XW61       I2, LiI, PMII       tBP       763       20.75       73.9       11.7       2020       313         XW62       I2, LiI, PMII       tBP       762       20.70       73.2       11.6       2020       313         XW63       I2, LiI, PMII       tBP       763       20.63       73.7       11.6       2020       313         ISQ1       Iodolyte Z-50       544       8.99       68.4       3.34       2018       314									
XW50         Co(bpy) <sub>3</sub> LiTFSI, tBP         843         16.24         73.9         10.1         2019         311           XW51         I <sub>2</sub> , LiI, PMII         tBP         781         20.07         70.2         11.1         2019         311           XW51         Co(bpy) <sub>3</sub> LiTFSI, tBP         844         15.24         75.6         9.7         2019         311           XW41         I <sub>2</sub> , LiI, PMII         tBP         695         16.77         70.1         8.16         2019         312           XW60         I <sub>2</sub> , LiI, PMII         tBP         715         16.77         73.1         8.8         2020         313           XW61         I <sub>2</sub> , LiI, PMII         tBP         763         20.75         73.9         11.7         2020         313           XW62         I <sub>2</sub> , LiI, PMII         tBP         762         20.70         73.2         11.6         2020         313           XW63         I <sub>2</sub> , LiI, PMII         tBP         763         20.63         73.7         11.6         2020         313           ISQ1         Iodolyte Z-50         544         8.99         68.4         3.34         2018         314           ISQ2									
XW51       I2, LiI, PMII       tBP       781       20.07       70.2       11.1       2019       311         XW51       Co(bpy)3       LiTFSI, tBP       844       15.24       75.6       9.7       2019       311         XW41       I2, LiI, PMII       tBP       695       16.77       70.1       8.16       2019       312         XW60       I2, LiI, PMII       tBP       715       16.77       73.1       8.8       2020       313         XW61       I2, LiI, PMII       tBP       763       20.75       73.9       11.7       2020       313         XW62       I2, LiI, PMII       tBP       762       20.70       73.2       11.6       2020       313         XW63       I2, LiI, PMII       tBP       763       20.63       73.7       11.6       2020       313         ISQ1       Iodolyte Z-50       544       8.99       68.4       3.34       2018       314         ISQ2       Iodolyte Z-50       558       9.62       68.7       3.68       2018       314         ISQ3       Iodolyte Z-50       576       10.02       72.0       4.15       2018       314									
XW51       Co(bpy) <sub>3</sub> LiTFSI, tBP       844       15.24       75.6       9.7       2019       311         XW41       I <sub>2</sub> , LiI, PMII       tBP       695       16.77       70.1       8.16       2019       312         XW60       I <sub>2</sub> , LiI, PMII       tBP       715       16.77       73.1       8.8       2020       313         XW61       I <sub>2</sub> , LiI, PMII       tBP       763       20.75       73.9       11.7       2020       313         XW62       I <sub>2</sub> , LiI, PMII       tBP       762       20.70       73.2       11.6       2020       313         XW63       I <sub>2</sub> , LiI, PMII       tBP       763       20.63       73.7       11.6       2020       313         ISQ1       Iodolyte Z-50       544       8.99       68.4       3.34       2018       314         ISQ2       Iodolyte Z-50       558       9.62       68.7       3.68       2018       314         ISQ3       Iodolyte Z-50       576       10.02       72.0       4.15       2018       314									
XW41       I2, LiI, PMII       tBP       695       16.77       70.1       8.16       2019       312         XW60       I2, LiI, PMII       tBP       715       16.77       73.1       8.8       2020       313         XW61       I2, LiI, PMII       tBP       763       20.75       73.9       11.7       2020       313         XW62       I2, LiI, PMII       tBP       762       20.70       73.2       11.6       2020       313         XW63       I2, LiI, PMII       tBP       763       20.63       73.7       11.6       2020       313         ISQ1       Iodolyte Z-50       544       8.99       68.4       3.34       2018       314         ISQ2       Iodolyte Z-50       558       9.62       68.7       3.68       2018       314         ISQ3       Iodolyte Z-50       576       10.02       72.0       4.15       2018       314		<del>-</del> : :							
XW60       I <sub>2</sub> , LiI, PMII       tBP       715       16.77       73.1       8.8       2020       313         XW61       I <sub>2</sub> , LiI, PMII       tBP       763       20.75       73.9       11.7       2020       313         XW62       I <sub>2</sub> , LiI, PMII       tBP       762       20.70       73.2       11.6       2020       313         XW63       I <sub>2</sub> , LiI, PMII       tBP       763       20.63       73.7       11.6       2020       313         ISQ1       Iodolyte Z-50       544       8.99       68.4       3.34       2018       314         ISQ2       Iodolyte Z-50       558       9.62       68.7       3.68       2018       314         ISQ3       Iodolyte Z-50       576       10.02       72.0       4.15       2018       314									
XW61       I2, LiI, PMII       tBP       763       20.75       73.9       11.7       2020       313         XW62       I2, LiI, PMII       tBP       762       20.70       73.2       11.6       2020       313         XW63       I2, LiI, PMII       tBP       763       20.63       73.7       11.6       2020       313         ISQ1       Iodolyte Z-50       544       8.99       68.4       3.34       2018       314         ISQ2       Iodolyte Z-50       558       9.62       68.7       3.68       2018       314         ISQ3       Iodolyte Z-50       576       10.02       72.0       4.15       2018       314									
XW62     I <sub>2</sub> , LiI, PMII     tBP     762     20.70     73.2     11.6     2020     313       XW63     I <sub>2</sub> , LiI, PMII     tBP     763     20.63     73.7     11.6     2020     313       ISQ1     Iodolyte Z-50     544     8.99     68.4     3.34     2018     314       ISQ2     Iodolyte Z-50     558     9.62     68.7     3.68     2018     314       ISQ3     Iodolyte Z-50     576     10.02     72.0     4.15     2018     314								2020	
XW63     I <sub>2</sub> , LiI, PMII     tBP     763     20.63     73.7     11.6     2020     313       ISQ1     Iodolyte Z-50     544     8.99     68.4     3.34     2018     314       ISQ2     Iodolyte Z-50     558     9.62     68.7     3.68     2018     314       ISQ3     Iodolyte Z-50     576     10.02     72.0     4.15     2018     314									
ISQ1     Iodolyte Z-50     544     8.99     68.4     3.34     2018     314       ISQ2     Iodolyte Z-50     558     9.62     68.7     3.68     2018     314       ISQ3     Iodolyte Z-50     576     10.02     72.0     4.15     2018     314		I <sub>2</sub> , LiI, PMII					11.6	2020	
ISQ2     Iodolyte Z-50     558     9.62     68.7     3.68     2018     314       ISQ3     Iodolyte Z-50     576     10.02     72.0     4.15     2018     314	XW63	I <sub>2</sub> , LiI, PMII	tBP	763	20.63	73.7	11.6	2020	313
ISQ3 Iodolyte Z-50 576 10.02 72.0 4.15 2018 314	ISQ1	Iodolyte Z-50		544	8.99	68.4	3.34	2018	314
ISQ3 Iodolyte Z-50 576 10.02 72.0 4.15 2018 314	ISQ2	Iodolyte Z-50		558	9.62	68.7	3.68	2018	314
	ISQ3	Iodolyte Z-50		576	10.02	72.0	4.15	2018	314
		Iodolyte Z-50		579	8.33	71.1	3.43	2016	315

sQ2	Iodolyte Z-50		647	12.49	70.7	5.71	2016	315
SQ3	Iodolyte Z-50		601	8.97	70.1	3.78	2016	315
SQ4	Iodolyte Z-50		636	9.31	70.1	4.15	2016	315
SQ5	Iodolyte Z-50		637	17.97	67.3	7.70	2016	315
SQ6	Iodolyte Z-50		633	12.35	67.6	5.28	2016	315
SQ7	Iodolyte Z-50		654	14.67	70.4	6.75	2016	315
YR1	I <sub>2</sub> , LiI, DMII	GuSCN, tBP	524	2.88	69	1.04	2013	316
YR2	I <sub>2</sub> , LiI, DMII	GuSCN, tBP	563	2.77	73	1.14	2013	316
YR3	I <sub>2</sub> , LiI, DMII	GuSCN, tBP	604	7.26	74	3.27	2013	316
YR4	I <sub>2</sub> , LiI, DMII	GuSCN, tBP	613	8.53	74	3.85	2013	316
YR5	I <sub>2</sub> , LiI, DMII	GuSCN, tBP	605	7.80	74	3.49	2013	316
YR6	I <sub>2</sub> , LiI, DMII	GuSCN, tBP	642	14.8	71	6.74	2013	316
TS3	I <sub>2</sub> , LiI, DMII	GuSCN, tBP	622	13.1	73	5.95	2013	316
JD10	I <sub>2</sub> , LiI, DMII	GuSCN, tBP	635	16.4	70	7.30	2013	316
T-PA	I <sub>2</sub> , LiI, DMII	GuSCN, tBP	644	9.6	72.2	4.6	2015	317
DTP-PA	I <sub>2</sub> , LiI, DMII	GuSCN, tBP	642	5.9	73.5	2.8	2015	317
DTT-CA	I <sub>2</sub> , LiI, DMII	GuSCN, tBP	644	13.1	71.6	6.0	2015	317
DTT-PA	I <sub>2</sub> , LiI, DMII	GuSCN, tBP	621	3.7	76.3	1.8	2015	317
DTS-CA	I <sub>2</sub> , LiI, DMII	GuSCN, tBP	682	19.1	68.3	8.9	2015	317
DTS-PA	I <sub>2</sub> , LiI, DMII	GuSCN, tBP	676	10.4	70.5	5.0	2015	317
PBut-SC2-T	I <sub>2</sub> , LiI, DMII	GuSCN, tBP	650	13.4	70.4	6.1	2015	318
PBut-SC12-T	I <sub>2</sub> , LiI, DMII	GuSCN, tBP	660	16.3	70.1	7.5	2015	318
PSil-SC12-T	I <sub>2</sub> , LiI, DMII	GuSCN, tBP	650	15.2	71.2	7.1	2015	318
PSil-SC12-DTS	I <sub>2</sub> , LiI, DMII	GuSCN, tBP	690	16.0	69.6	7.6	2015	318
TSQa	I <sub>2</sub> , LiI, DMPII	none	450	8.05	59	2.13	2013	319
TSQb	I <sub>2</sub> , LiI, DMPII	none	450	8.89	61	2.43	2013	319
MSQ	I <sub>2</sub> , LiI, DMPII	none	520	5.25	69	1.88	2013	319
МЗQ JK-216	I <sub>2</sub> , LiI, DMPII I <sub>2</sub> , LiI, DMPII	tBP	610	13.92	77.4	6.29	2013	320
JK-217	I <sub>2</sub> , LiI, DMPII	tBP	583	13.73	70.2	5.54	2011	320
	_		363 374	9.25	70.2 51		2011	321
WCH-SQ10	I <sub>2</sub> , LiI	none		9.25 9.06	51 55	1.77 1.96	2012	
WCH-SQ11 PSQ9	I <sub>2</sub> , LiI	none	391 577	9.00 17.07	70.35	6.93	2012	321 322
	Iodolyte Z-50 Iodolyte Z-50		577 579	16.93			2019	
PSQ10	•				69.83	6.84		322
HSQ2	I <sub>2</sub> , LiI, DMPII	none	584	11.55	61 57	4.11	2014	323
HSQ3	I <sub>2</sub> , LiI, DMPII	none	581	13.95	57	4.60	2014	323
HSQ4	I <sub>2</sub> , LiI, DMPII	none	558	15.61	65	5.66	2014	323
SPSQ1	I <sub>2</sub> , LiI, DMPII	tBP	627	6.51	73	2.98	2016	324
SPSQ2	I <sub>2</sub> , LiI, DMPII	tBP	670	7.94	74 71	3.95	2016	324
L1	Cu(tmby) <sub>2</sub>	LiTFSI, tBP	910	9.4	71	6.1	2020	33
WS-68/WS-5	I <sub>2</sub> , LiI, DPMII	tBP	746	14.08	67	7.67	2017	260
WS-5/WS-69	I <sub>2</sub> , LiI, DPMII	tBP	753	19.56	68	10.09	2017	260
AP25/D35	I <sub>2</sub> , LiI, DMII	GuSCN, tBP	551	24.5	63	8.4	2020	264
C268/SC-4	I <sub>2</sub> , DMII, EMII	sulfolane, NBB, GuSCN	779	18.10	71.0	10.0	2018	269
XY1b/Y123	Cu(tmby) <sub>2</sub>	LiTFSI, MBI	1050	15.74	79	13.1	2018	277
MS5/XY1b	Cu(tmby) <sub>2</sub>	LiTFSI, MBI	1050	15.84	81.3	13.5	2021	13
		LiClO <sub>4</sub> , NaClO <sub>4</sub> , TBAPF <sub>6</sub> ,						
ADEKA-1/LEG4	Co(phen) <sub>3</sub>	TBPPF <sub>6</sub> , HMIPF <sub>6</sub> , tBP,	1014	18.27	77.1	14.3	2015	25
		TMSP, MP, CPrBP,						
		CPeBP, COcBP						
ADEKA 1 (CED =	0 (1 )	LiClO <sub>4</sub> , NaClO <sub>4</sub> , TBAPF <sub>6</sub> ,	1005	16.05	<b>55</b> 0	10.00	0015	000
ADEKA-1/SFD-5	Co(phen) <sub>3</sub>	TBPPF <sub>6</sub> , HMIPF <sub>6</sub> , tBP,	1035	16.07	77.3	12.86	2015	283
0.000.000.000	0.4	TMSP, MP	06:	4		46 -	001-	0.5.
SGT-020/HC-A4	Co(bpy) <sub>3</sub>	LiClO <sub>4</sub> , tBP	864	15.8	76.6	10.5	2017	292
SM315/HC-A4	Co(bpy) <sub>3</sub>	LiClO <sub>4</sub> , tBP	893	16.4	79.4	11.6	2017	292
SGT-021/HC-A4	Co(bpy) <sub>3</sub>	LiClO <sub>4</sub> , tBP	910	17.5	75.3	12.0	2017	292

SGT-137/HC-A1	$Co(bpy)_3$	LiClO <sub>4</sub> , tBP	884	18.37	76.7	12.45	2017	293
XW1/C1	I <sub>2</sub> , LiI, PMII	tBP	746	17.53	71	9.24	2014	298
XW2/C1	I <sub>2</sub> , LiI, PMII	tBP	697	18.22	70	8.96	2014	298
XW3/C1	I <sub>2</sub> , LiI, PMII	tBP	705	18.42	70	9.05	2014	298
XW4/C1	I <sub>2</sub> , LiI, PMII	tBP	736	20.15	71	10.45	2014	298
XW9/C1	I <sub>2</sub> , LiI, PMII	tBP	764	17.01	71.8	9.3	2015	299
XW10/C1	I <sub>2</sub> , LiI, PMII	tBP	753	18.24	74.2	10.1	2015	299
XW11/C1	I <sub>2</sub> , LiI, PMII	tBP	746	19.52	74.0	10.6	2015	299
XW9/WS-5	I <sub>2</sub> , LiI, PMII	tBP	770	17.70	74.1	10.1	2015	299
XW10/WS-5	I <sub>2</sub> , LiI, PMII	tBP	765	19.01	76.4	11.0	2015	299
XW11/WS-5	I <sub>2</sub> , LiI, PMII	tBP	760	20.33	74.4	11.5	2015	299
XW14/WS-5	I <sub>2</sub> , LiI, PMII	tBP	765	18.54	70	9.9	2015	300
XW15/WS-5	I <sub>2</sub> , LiI, PMII	tBP	763	18.88	71	10.1	2015	300
XW16/WS-5	I <sub>2</sub> , LiI, PMII	tBP	773	19.01	72	10.4	2015	300
XW17/WS-5	I <sub>2</sub> , LiI, PMII	tBP	748	20.30	72	10.9	2015	300
SGT-021/HC-A1	$Co(bpy)_3$	LiTFSI, tBP	849	19.2	76.8	12.6	2019	301
SGT-023/HC-A1	$Co(bpy)_3$	LiTFSI, tBP	761	9.2	79.9	5.6	2019	301
SGT-025/HC-A1	$Co(bpy)_3$	LiTFSI, tBP	837	17.3	76.0	11.0	2019	301
PZn-HOQ/BET	I <sub>2</sub> , LiI, DPMII	GuSCN, tBP	573	6.87	66.8	2.63	2014	306
PZn-HOQ/BET	I <sub>2</sub> , LiI, DPMII	GuSCN, tBP	605	8.33	67.7	3.41	2014	306
XW40/Z1	I <sub>2</sub> , LiI, PMII	tBP	748	19.59	71.9	10.55	2019	312
XW41/Z1	I <sub>2</sub> , LiI, PMII	tBP	726	19.63	71.5	10.19	2019	312
XW51/Z2	$Co(bpy)_3$	LiTFSI, tBP	822	14.72	79.8	9.7	2020	313
TSQa/MSQ	I <sub>2</sub> , LiI, DMPII	none	440	11.57	56	2.82	2013	319
SPSQ1/N3	I <sub>2</sub> , LiI, DMPII	tBP	635	15.60	73	7.20	2016	324
SPSQ2/N3	I <sub>2</sub> , LiI, DMPII	tBP	656	17.10	73	8.20	2016	324
XY1/L1	Cu(tmby) <sub>2</sub>	LiTFSI, tBP	1080	15.9	67	11.5	2020	33
XY1/D35	Cu(tmby) <sub>2</sub>	LiTFSI, tBP	1070	15.3	67	11.0	2020	33

4.2.2.4 Multifunctional DSCs. DSCs have shown exceptional performances as described above in terms of low light intensity use and in tandem of SSM device designs. Additionally, DSCs are intriguing materials for aesthetically important devices owing to the wider range of colors available from the dyes used in these devices. Given the molecular nature of the chromophores being used, photochromic dyes offer a possible strategy for accessing materials with dynamic optical properties and electricity production. DSCs have been shown to operate as photo-chromovoltaic solar cells that can be converted from transparent states to visible light absorbing states with the NPI dye (Fig. 26). The use of photochromic dyes is intriguing for building-integrated photovoltaics which can exist in semi-transparent states at night and as visible light absorbing states in the daytime. A key challenge with this approach consists in synthesizing dyes with reasonable power conversion efficiencies in the visible light absorbing state since visible light is competitively used within the devices to both drive electron transfers to the metal oxide semiconductor, and to convert the dye back to the non-visible light absorbing state. The use of diphenyl-naphthopyran has shown exceptional promise in allowing for a PCE >4% with good device stability (50 days tested). 197 Interestingly, the diphenylnaphthopyran building block also allows for thermal conversion or light intensity-based conversion back to a transparent state giving a self-adjusting transmission. Continued research in this area is promising with regard to building integrated photovoltaic markets.

$$C_6H_{13}$$
 $C_6H_{13}$ 
 $C_6H$ 

Fig. 26 Photoresponsive NPI in a non-visible light absorbing state (left) and a visible light absorbing state (right).

# 4.3 Charge transport materials

Although they had been neglected in the early stages of DSC development, charge transport materials (CTMs) are an essential part of this technology and therefore some of the biggest advances in the field in the past decade were made through progress on this cell component. <sup>24,325-331</sup> Research on CTMs branched into the development of materials, the study of their properties and the fundamental understanding of charge transport within the materials and devices. CTMs are responsible for electron transfer between the electrodes and they must be able to regenerate the oxidized dye following light absorption and to be reduced at the counter electrode. Charge transport materials are not only essential for the solar cell efficiency, but also determine its overall stability. All parameters defining the efficiency of solar cells including the short-circuit photocurrent density  $(J_{SC})$ , open-circuit photovoltage  $(V_{OC})$  and the fill factor (FF) are influenced by the properties of charge transport materials and their interface interaction with the electrodes. 16,329,332-334 Photocurrent, even if largely determined by the photon-to-electron conversion abilities of dyes, 335,336 is still influenced by the charge transport abilities and recombination pathways of the CTM.  $^{337}$   $V_{\rm OC}$  depends on the energy level alignment between the Fermi level of the TiO<sub>2</sub>, ground state of the dye and overpotential to the CTM.

CTMs can be integrated in DSCs in the liquid, quasi-solid and solid state. 11 Liquid CTMs or electrolytes in solar cells are comprised of an organic, aqueous or ionic solvent with a redox couple, for example  $I^-/I_3^-$ , 338–340 copper 15,95,96,339,341–346 or cobalt <sup>271</sup>,289,291,330,347–349 coordination complexes or organic molecules <sup>350</sup>. For DSCs to become commercially viable, significant efforts are being made to develop quasi-solid- and solidstate charge transport materials to ensure sustainability and stability. These CTMs are usually based on organic molecules and polymers 326,351,352 or on inorganic and coordination metal complexes. The fundamental contrast between the different charge transport materials are the charge mobility and mechanism characteristics. 11 While in liquid electrolytes there is a prevalence of ionic conductivity, in polymeric and solid-state CTMs the mechanism can be a combination of ionic and electronic or there is a prevalence of the electronic process. 353

### 4.3.1 Liquid electrolytes and redox mediators.

Liquid electrolytes are a significant component not only of DSCs, but also of all electrochemical devices including capacitors, fuel cells and batteries (e.g. lithium-ion batteries). Liquid electrolytes typically consist of a redox couple and additives dissolved in a liquid solvent. The photovoltaic properties of DSCs can be optimized by employing additives: the redox couple potential, semiconductor surface state, semiconductor conduction band edge, recombination kinetics, as well as the photovoltaic parameters of DSCs can all be improved by adding a small number of dopants/additives.

In order to transport charges between the electrodes efficiently, charge transport materials in DSCs must fulfill several requirements: 354-356 (i) a redox potential that provides the minimal overpotential, but with a driving force high enough to efficiently regenerate the dye, (ii) low recombination rates with the metal oxide semiconductor and the conductive substrate, (iii) minimal mass transport limitations for fast diffusion through the mesoporous semiconductor towards the counter electrode, (iv) absence or minimization of unwanted chemical and physical interactions of the electrolyte with the components of the solar cell to improve overall stability, (v) no or minimal competitive light absorption with respect to the dye.

Currently, there is no ideal electrolyte system that fulfills all the requirements, but there are several successful systems that have been discovered and their advantages and drawbacks will be outlined. Fast dye regeneration and slow charge recombination are prerequisites for selecting superior redox couples for electrolytes to obtain highly efficient DSCs. <sup>11</sup> Table 4 lists device parameters of DSCs employing various liquid electrolytes referenced in this review, together with the dye used.

4.3.1.1 Halide redox mediators. Initially, successful and efficient DSCs implemented the iodide/triiodide redox mediator.  $^{87,143,357,358}$  The  $I^-/I_3^-$  redox couple shows remarkable performance up to its record PCE of 11.9% (certified, 12.4% noncertified).  $^{3\bar{1}3,359}$  The I $^-/$ I $_3$  $^-$  redox couple fulfills several requirements for an ideal electrolyte and it was for several decades the benchmark for research and industry applications. Advantages of the  $I^-/I_3^-$  redox couple include a suitable redox potential, small molecular size for high diffusion, good solubility in a wide range of solvents at high concentration for high conductivity, and good stability. However, it also has several drawbacks, which have initiated the search for alternative redox mediators: (i) substantial light absorption of the triiodide and other possible polyiodide species in the 400-500 nm range of the solar spectrum, (ii) corrosivity towards several components of DSCs including the materials used for counter electrodes and sealing, (iii) possible iodine diffusion out of the electrolyte stemming from its high vapor pressure, and especially (iv) the very large driving force of over 0.5 V for dye regeneration due to the 2-electron oxidation steps from I to  $I_{3-}$ . Consequently, the  $V_{OC}$  attainable from a DSC containing the iodide/triiodide electrolyte is smaller than what is theoretically possible given the choice of dye. Since the overall efficiency of a solar cell scales directly with V<sub>OC</sub>, this large driving force constitutes a significant limitation of the  $I^-/I_3^-$  redox couple. <sup>357</sup>

The step towards iodide-free redox mediators begins with bromide/tribromide, which has a more positive potential of an additional 0.35 V, a two-electron transfer, and high solubility in many solvents. Thus, the electrolyte containing the bromide/tribromide redox system can improve greatly the photovoltage, but shows lower  $J_{\rm SC}$  values. Hanaya and co-workers successfully implemented the Br $^-/{\rm Br_3}^-$  electrolyte with the organic dye ADEKA-3 and a Mg $^{2+}$ -doped anatase TiO $_2$  electrode reaching a photovoltage over 1.4 V and a conversion efficiency close to 4%.  $^{213}$  The development bottleneck for the Br $^-/{\rm Br_3}^-$ -based electrolyte remains the search for a suitable dye. Bi-interhalogen redox systems, such as I $^-/{\rm IBr_2}^-$  and I $^-/{\rm I_2Br}^-$  were also tested in combination with ruthenium-based sensitizing dyes and reached conversion efficiencies up to 6.4%.  $^{355,360}$ 

Furthermore, pseudohalogen-based redox couples  $SCN^-/(SCN)_2$  and  $SeCN^-/(SeCN)_2$  have been studied with the hope to enhance  $V_{OC}$  in DSCs, because their redox potentials are 0.19 and 0.43 V more positive than that of the  $I^-/I_3^-$  redox couple, respectively. However, since dye regeneration efficiency with these systems is low, it only resulted in low photocurrents.  $SeCN^-$  has ambivalent reactivity and can interact with the dye

from the Se and N side. 361

4.3.1.2 Transition metal coordination complexes. Cobalt-, iron-, copper-, nickel-, manganese- and vanadium-based complexes as 1-electron outer-sphere redox couples are currently the most promising and successful candidates to replace the I-/I3system in DSCs. 12 Their characteristics are favorable for the commercialization of DSCs, as they show reversible electrochemical properties, structural tunability, higher positive Fermi level values, and lower absorption of visible light and better stability compared to I<sup>-</sup>/I<sub>3</sub><sup>-</sup>. The Fermi level of metal complexes can be easily tuned by changing the central metal cation or ligands. According to Marcus theory, a driving force of 0.2 eV is sufficient for outer-sphere single-electron-transfer reactions to ensure a fast dye regeneration rate, opening the opportunity to increase the  $V_{\rm OC}$ . 95,164 Most importantly, the electronic properties and redox chemistry can be tuned by varying the ligand environment. The development of novel redox mediators has fallen far behind that of sensitizing dyes and other materials for different DSC components, but recent developments have renewed the attention to this aspect of DSCs. 362

## Cobalt coordination complexes

Most prominent Co-based redox mediators form octahedral coordination complexes with either two tridentate ligands (such as terpyridines) or three bidentate ligands (such as 2,2'-bipyridyl or 1,10-phenanthroline). 164,363-365 First breakthroughs with high efficiency DSCs incorporating transition metal complexes were introduced in 2010 by the Hagfeldt group, with a new Co complexbased electrolyte in combination with the organic dye D35. 271 The authors introduced a series of complexes with various ligands creating a library of redox mediators with a variety of redox potentials. The highest efficiency of 7% under 1 sun (V<sub>OC</sub> of 0.92 V and  $J_{SC}$  of 10.7 mA cm<sup>-2</sup>) was reached with the  $[Co(bpy)_3]^{3+/2+}$ redox couple (Fig. 27). In 2012, Mosconi et al. were able to show that the formation of an ion pair between the negatively-charged Ru dye and the positively-charged Co complex was responsible for the increase in recombination processes and consequent poor performance of DSCs implementing these systems. This was improved later with addition of larger blocking groups on the Ru dyes. 163

A follow-up study by Feldt et al. on fundamental aspects of the regeneration and recombination processes of cobalt redox mediators also confirmed that a driving force of 0.25 eV was sufficient to ensure 84% dye regeneration.  $^{164,336}$  The introduction of this new redox mediator system led to a surge in dye development. In 2011 Tsao et al. increased the efficiency with the organic dye Y123, which had a high extinction coefficient thanks to the cyclopentadithiophene (CPDT)  $\pi$ -bridge. DSCs reaching a PCE of 8.8% ( $V_{\rm OC}=0.855$  V,  $J_{\rm SC}=14.6$  mA cm $^{-2}$ ) under full sun were obtained in conjunction with a platinized FTO counter electrode.  $^{272}$  A new family of porphyrin-based dyes was introduced by Yella et al., YD2 and YD2-o-C8, leading to an impressive PCE of 11.9% under full sun ( $V_{\rm OC}=0.965$  V,  $J_{\rm SC}=17.3$  mA cm $^{-2}$ ).  $^{289}$ 

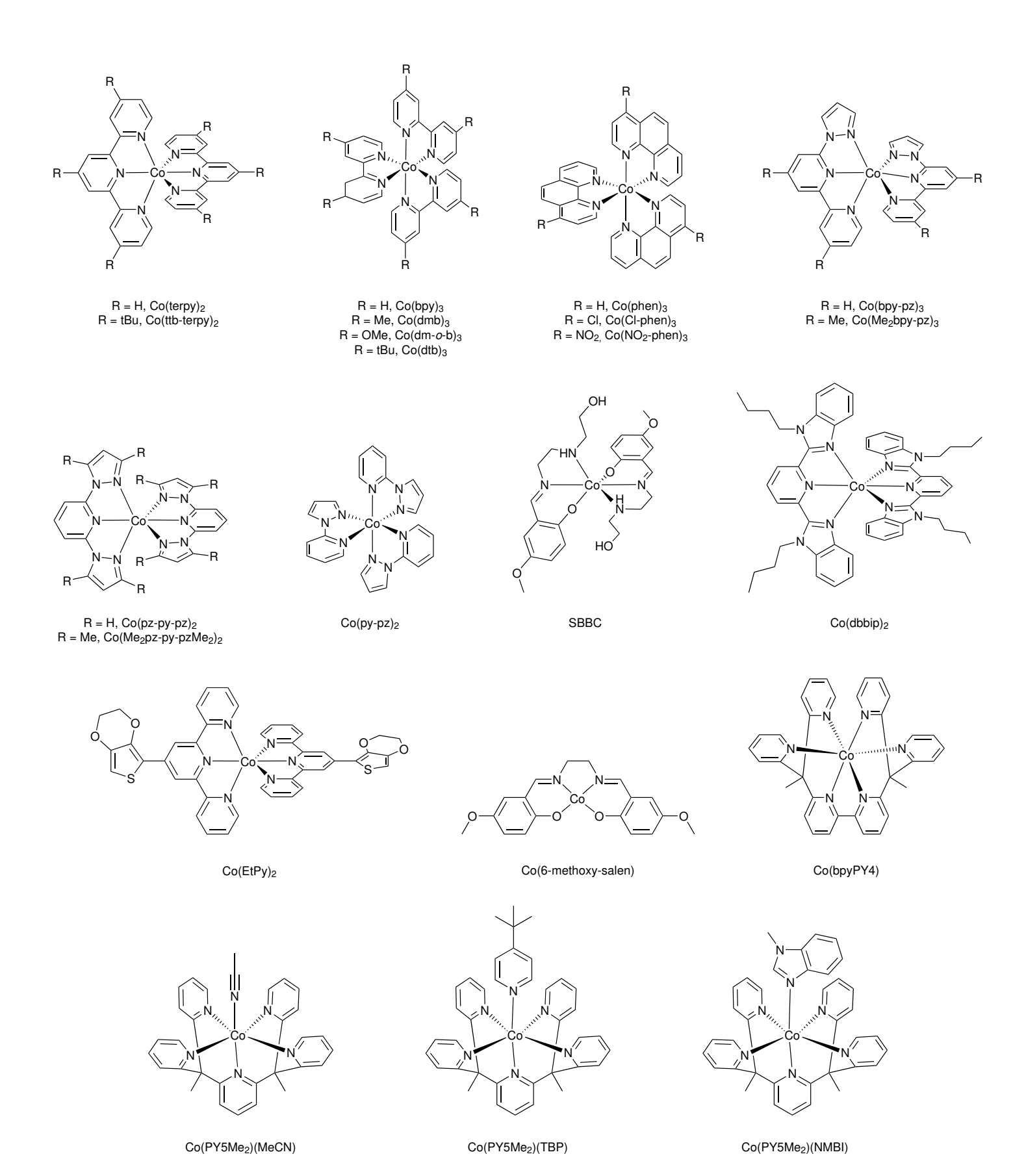


Fig. 27 Chemical structures of cobalt coordination complexes-based redox mediators implemented in DSCs.

The PCE mark of 13% was passed by Mathew et al. with porphyrins improved through a triphenylamine-type hydrophobic donor, leading to dyes SM315 and SM371.291 The highest efficiency reported for DSCs to date is still that obtained with the  $Co(phen)_3$ ]<sup>3+/2+</sup> redox mediator by Kakiage et al., who reached a PCE of 14.3% under full sun ( $V_{OC} = 1.01 \text{ V}$ ,  $J_{\rm SC} = 18.2 \text{ mA cm}^{-2}$ ) by cosensitizing the ADEKA-1 (MK2 dye variant with an alkoxysilyl binding group) and LEG4 dyes. 25 A series of 2,2'-ethylenebis(nitrolomethylidene)diphenol-N,N'ethylenebis(salicylimine) (salen)-based cobalt complexes was introduced by Nasr-Esfahani et al. in 2014 and reached a PCE of only 2.53% under full sun illumination. 366 New complexes were developed by Koussi-Daoud et al. a cobalt coordination complex featuring a terpyridine functionalized with 3,4-ethylenedioxythiophene (EDOT). 367 This combination of an electron cascade to the PEDOT counter electrode lead to an enhanced cell efficiency of 5.1% with The group of U. Bach also introduced D35 at 1 sun. new cobalt-based redox mediators with 4-tert-butylpyridine (tBP) and N-methylbenzimidazole (NMBI). The tested complexes  $[Co(PY5Me2)(tBP)]^{3+/2+}$ ,  $[Co(PY5Me2)(NMBI)]^{3+/2+}$ and [Co(PY5Me2)(MeCN)]<sup>3+/2+</sup> reached an efficiency of 8.4% under full sun ( $V_{OC} = 0.940 \text{ V}, J_{SC} = 11.8 \text{ mA cm}^{-2}$ ). <sup>330</sup> They further introduced a hexadendate ligand in 2015 to increase the overall stability of cobalt redox mediators. Devices fabricated with this new Co complex, and MK2 or Y123 as dye produced a PCE up to 8.3% under full sun. 368,369 In 2016, Freitag et al. introduced the new supramolecular, hemicage cobalt-based mediator  $[Co(ttb)]^{3+/2+}$  with the highly pre-organized hexadentate ligand 5,5",5""-((2,4,6-triethyl benzene-1,3,5-triyl) tris(ethane-2,1diyl))tri-2,2'-bipyridine (ttb) reaching the same performance as with  $[Co(bpy)_3]^{3+/2+}$  (bpy=2,2'-bipyridine) redox mediator and the LEG4 dye. 348 Both hexadendate systems exhibit exceptional stability under thermal and light stress.

The addition of aqueous electrolytes aided in the advancement of stabilization and sustainability, which also required the development and use of appropriate hydrophobic dyes. In 2013 Xiang and co-workers used the combination of MK2 and [Co(bpy)<sub>3</sub>]<sup>3+/2+</sup>. 370 Ultimately, they obtained aqueous-based devices with a PCE of 5.0% at 1 sun illumination ( $V_{OC} = 0.687 \text{ V}$ ,  $J_{SC} = 9.8 \text{ mA cm}^{-2}$ ). Dong et al. used the common strategy of introducing surfactants in DSCs and reached a PCE of 5.6% under full sun ( $V_{\rm OC} = 0.821 \text{ V}, J_{\rm SC} = 10.17 \text{ mA cm}^{-2}$ ) with the MK2 dye. <sup>371</sup> In 2016, Ellis et al. introduced two complexes with high solubility in water, [Co(bpy)3](NO3)2 and [Co(phen)3]Cl2, and the new dye D51, with a shorter blocking group to allow better wetting in comparison to the organic dye D35. The initial performance reported was 1.4% and 3.4%, respectively, both under 1000 W m<sup>-2</sup> illumination. <sup>372</sup> In the same study, optimization of [Co(phen)3]Cl3 concentration allowed further performance enhancements to 4.8% and the use of [Co(bpy-pz)<sub>3</sub>]<sub>3</sub>]<sup>3+/2+</sup> featuring chloride counter ions lead to a 5.5% PCE ( $V_{OC} = 0.9 \text{ V}$ ,  $J_{\rm SC}=8.1~{\rm mA~cm^{-2}})$  under full sun. <sup>372</sup>

Some disadvantages of cobalt complexes remain. They have a large molecular size leading to slow mass transport and diffusion, large reorganization energies between the oxidation states Co(II)

and Co(III) increase the overall energy required to regenerate the dye, and their long-term stability is in question as the complexes in solution will likely undergo ligand exchange, which has to be structurally controlled.

### Copper coordination complexes

As alternative redox mediators,  $Cu^{2+/+}$  complexes outperform both iodine- and Co-based electrolytes in combination with various dyes, which was made possible due to lower reorganization energy and minimized overpotential losses. 373,374

The large differences in coordination complex geometries between Cu(I) and Cu(II) species, four-coordinate with tetrahedral geometry vs. four- to six-coordinate (square planar to tetragonal), were expected to lead to high reorganization energies. However, successful copper coordination complexes employed in DSCs were implemented with sterically-hindered ligands to minimize the reorganization energy. For the first time, Hattori et al. obtained a maximum PCE of 1.4% with bis(2,9-dimethyl-1,10-phenantroline)copper(II/I) complexes ( $[Cu(dmp)_2]^{2+/+}$ ), Fig. 28. 373 This result was later improved by Bai et al., 339 who reached 7% PCE with the C218 organic dye followed by Freitag et al. in 2016, who reported 8.3% PCE with a remarkably high open-circuit voltage above 1.0 V with the D- $\pi$ -A LEG4 organic dye. It was reported that the  $[Cu(dmp)_2]^{2+/+}$ complex with a redox potential of 0.93 V vs. NHE can sufficiently regenerate the oxidized dye molecules with a small driving force (0.2 eV) by minimizing internal energy losses. 96 Cong et al. reported a novel Cu mediator –  $[Cu(bpye)_2]^{2+/+}$ - with the 1,1-bis(2-pyridyl)ethane ligand. They achieved a PCE of 9.0% ( $V_{OC} = 0.90 \text{ V}$ ,  $J_{SC} = 14.1 \text{ mA cm}^{-2}$ ) under full sun, however the efficiency declined from 9% to 6% after a short light ageing period. 375 In 2017, Freitag and co-workers introduced two Cu bipyridyl-based complexes,  $[Cu(dmby)_2]^{2+/+}$ (0.97 V vs. NHE, dmby = 6,6'-dimethyl-2,2'-bipyridine) and  $[Cu(tmby)_2]^{2+/+}$  (0.87 V vs. NHE, tmby = 4,4',6,6'-tetramethyl-2,2'-bipyridine) as new redox couples showing efficient organic Y123 dye regeneration at very low driving forces of 0.1 eV. 15 The efficiency exceeded 10% under 1000 W m<sup>-2</sup> AM1.5G illumination. In their follow-up work Saygili et al. examined the recombination processes and regeneration behavior of  $Cu[(dmby)_2]^{2+/+}$ ,  $Cu[(tmby)_2]^{2+/+}$ ,  $Cu[(eto)_2]^{2+/+}$  (eto = 4ethoxy-6,6'-dimethyl-2,2'-bipyridine), and  $Cu[(dmp)_2]^{2+/+}$  in conjunction with organic dyes having various degrees of blocking groups: D5, D35, and D45.95 They showed that DSCs employing the D35 dye with  $Cu[(dmp)_2]^{2+/+}$  reached a record value for the open-circuit voltage of 1.14 V without compromising the short-circuit current density value. In addition, with the D5 dye, which lacks recombination-preventing steric units, VOC values as high as 1.13 V were possible with  $Cu[(dmp)_2]^{2+/+}$  and  $Cu[(dmby)_2]^{2+/+}$  electrolytes. Liu et al. introduced a series of indacenodithiophene (IDT)-based D-π-A organic dyes reaching high open-circuit voltage values (>1.1 V) and PCE values of 11.2% at 1 sun. <sup>276</sup> Zhang et al. also employed  $[Cu(tmby)_2]^{2+/+}$ in conjunction with the novel WS-72 dye, which reduced interfacial electron recombination.

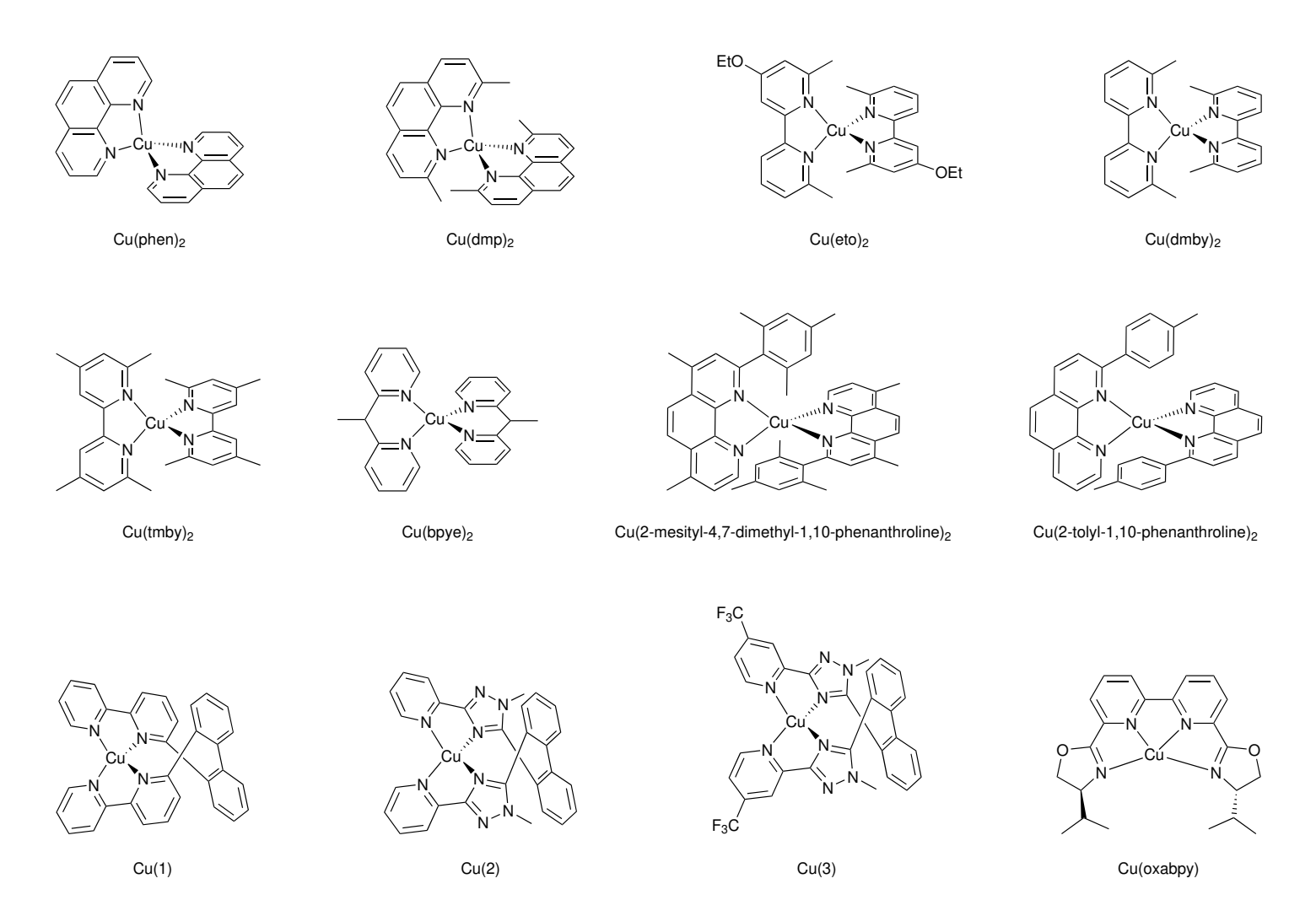


Fig. 28 Chemical structures of copper coordination complexes-based redox mediators implemented in DSCs.

Liquid-junction devices generated a notable V<sub>OC</sub> of 1.1 V along with an excellent PCE of 11.6% under simulated AM1.5G illumination. The solidification of the liquid-junction devices lead to an even higher PCE of 11.7% ( $J_{SC} = 13.8 \text{ mA cm}^{-2}$ ,  $V_{OC} = 1.07 \text{ V}$ and FF = 79%). <sup>274</sup>

In 2017, the field of DSCs experienced a significant push towards indoor applications. Indoor illumination is very different to sun illumination, with an emission spectrum only in the visible and light intensities that are three orders of magnitude lower. With high power conversion efficiencies of indoor photovoltaics, the power output obtained under low light illumination is sufficient to power a range of wireless devices belonging to the family of Internet of Things (IoT). Freitag et al. developed a cosensitized DSC with D35 and XY1 dyes employing the  $[Cu(tmby)_2]^{2+/+}$  redox couple with TiO2 films. The PCE was reported as 28.9% and 11.3% under light provided by a 1000 lx fluorescent light tube and at full sun, respectively. 341 Cao, et al. reported the record PCE of 13.1% under full sun by employing XY1 and Y123 dye blends with the [Cu(tmby)<sub>2</sub>]<sup>2+/+</sup> redox mediator. <sup>277</sup> In 2020, Michaels et al. presented co-sensitized DSCs, where the small organic dye L1 was combined with the XY1 dye to provide  $V_{\rm OC}$ and performance values of 910 mV and 34.0%, respectively, at 1000 lx (11.5% at 1 sun). These DSCs were able to power IoT devices capable of machine learning under ambient light. 33

Phenathroline complexes were further developed by Magni et al. They studied the redox couple [Cu(2-mesityl-4,7-dimethyl-1,10-phenanthroline)<sub>2</sub> $]^{2+/+}$  in comparison to  $[Cu(dmp)_2]^+$  and its penta-coordinated oxidized form [Cu(dmp)<sub>2</sub>Cl]<sup>+</sup>. With these redox couples, they reported an overall 4.4% solar energy conversion efficiency with a  $\pi$ -extended benzothiadiazole dye (G3). They also reported that the steric hindrance effects of the methyl groups in  $[Cu(dmp)_2]^+$  and the two mesityl rings of [Cu(2mesityl-4,7-dimethyl-1,10-phenanthroline)<sub>2</sub>](PF<sub>6</sub>)<sub>2</sub> are different. They speculated that the mesityl rings may induce a smaller conformational modification upon redox reaction, acting as a "kiss-lock enclosure" that causes a more negative redox potential. 344,376

Colombo et al. developed novel [Cu(2-mesityl-4,7-dimethyl-1,10-phenanthroline)<sub>2</sub>]PF<sub>6</sub> and [Cu(2,9-dimethyl-4,7-diphenyl-1,10-phenanthroline)<sub>2</sub>]PF<sub>6</sub> redox couples with a Fe(II) comediator for DSC applications<sup>376</sup> and later introduced a series of Cu complexes with different substituents in the α-positions of phenanthroline, with appropriate redox potentials and a distorted tetragonal geometry. 377 Dragonetti

studied a heteroleptic Cu dye with [Cu(2-n-butyl-1,10-phenanthroline)<sub>2</sub>]<sup>2+/+</sup> and  $[Cu(dmp)_2]^{2+/+}$ Due to a higher molar absorption coefficient, [Cu(dmp)<sub>2</sub>]<sup>2+/+</sup> showed lower short-circuit photocurrents compared to  $[Cu(2-n-butyl-1,10-phenanthroline)_2]^{2+/+}$ , which is in agreement with a lower IPCE value at 475 nm for  $[Cu(dmp)_2]^{2+/+}$ . The highest PCE value is reported as 2% with  $[Cu(2-n-butyl-1,10-phenanthroline)_2]^{2+/+}$  and the new copper dye D ( $J_{SC} = 6.3 \text{ mA cm}^{-2}$ ,  $V_{OC} = 0.61 \text{ V}$  and FF = 0.53). Colombo et al. studied [Cu(2-mesityl-1,10phenanthroline)<sub>2</sub>] $^{2+/+}$  and [Cu(2-mesityl-4,7-dimethyl-1,10phenanthroline)<sub>2</sub>]<sup>2+/+</sup> in conjunction with Zn(II) porphyrin dyes D1 and D2. The best performance was reported for the new [Cu(2-mesityl-1,10-phenanthroline)<sub>2</sub>]<sup>2+/+</sup> redox couple at a PCE of 3.7% under full sun ( $J_{SC} = 5.9 \text{ mA cm}^{-2}$ ,  $V_{\rm OC} = 0.81$  V and FF = 0.77) with the D1 dye. <sup>379</sup> Benazzi et al. developed homoleptic Cu complexes redox couples with low molar absorption coefficient with substituted 1,10- $([Cu(2-tolyl-1,10-phenanthroline)_2]^{2+/+},$  $[Cu(2-phenyl-1,10-phenanthroline)_2]^{2+/+}$ , and [Cu(2-n-butyl-n-b1,10-phenanthroline)<sub>2</sub>]<sup>2+/+</sup>.<sup>380</sup>

Another polypyridyl complex was presented by Hoffeditz et al., a Cu redox shuttle with the 1,8-bis(2'-pyridyl)-3,6-dithiaoctane (PDTO) ligand. This work showed the ligand exchange processes in the electrolyte upon oxidation from Cu(I) to Cu(II) with the common additive tBP. 381 Wang et al. also studied the effect of tBP substitution of the bidentate ligands on the Cu(II) species to form a poor electron acceptor [Cu(tBP)<sub>4</sub>]<sup>2+</sup> responsible for high voltages and charge collection efficiencies. 382 Karpacheva et al. studied heteroleptic Cu(I)-based dyes in conjunction with homoleptic Cu(II/I) redox shuttles. They obtained a DSC PCE of 2.06%. The introduction of electron-donating methoxy groups in Cu(4,4'-dimethoxy-6,6'-dimethyl-2,2'-bipyridine)<sub>2</sub> resulted in a lower oxidation potential with respect to Cu(dmby)2. It was reported that the PCE improvement with the [Cu(4,4'-dimethoxy-6,6'-dimethyl-2,2'-bipyridine)<sub>2</sub>]<sup>2+/+</sup> redox couple was achieved by a  $J_{SC}$  increase despite a  $V_{OC}$  decrease. <sup>383</sup>

Michaels et al. introduced new copper complexes with the tetradentate ligand 6,6'-bis(4-(S)-isopropyl-2-oxazolinyl)-2,2'-bipyridine – Cu[(oxabpy)] $^{2+/+}$  – as redox mediators. With this ligand, the copper complexes exhibit "sterically frozen" square-planar geometry providing minimized reorganization energies. The gel-like  $Cu[(oxabpy)]^{2+/+}$  complexes showed considerable enhancement of charge transport performance. 346 In 2020 Rodrigues et al. introduced a series of three copper redox shuttles with pre-organized tetradentate ligands, which were tested computationally, electrochemically, and in solar cell devices for performance. The rigid tetradentate ligand design achieved a high  $J_{\rm SC}$  (14.1 mA cm<sup>-2</sup>) and more effective electron transfer reactions, which lead to an improved  $V_{OC}$  value for one of the copper redox shuttle-based devices. 345

#### Iron coordination complexes

An electrolyte based on iron complexes is of high interest as it would represent a sustainable, low cost and non toxic option. In 2012 Daeneke introduced an aqueous electrolyte hexacyanoferrate for DSC. With a high extinction coefficient organic dye, MK2, the assembled solar cells reached  $V_{\rm OC}=0.761~\rm V$ ,  $J_{SC} = 7.21 \text{ mA cm}^{-2}$ , FF = 75% and PCE = 4.1%. <sup>384</sup> Previously, in 2011 Rutkowska et al. successfully implemented a polynuclear electronically/ionically (redox) conducting mixed-valent inorganic material such as nickel(II) hexacyanoferrate(III/II) - $([NiFe(CN)_6]^{2-/-}$  – with a redox potential of approximately 0.84 V vs. NHE, resulting in DSCs of  $V_{OC} = 0.790$  V,  $J_{SC} = 8 \text{ mA cm}^{-2}$ , FF = 70% and PCE = 4%. <sup>385</sup>

The bipyridine equivalents to cobalt complexes - $[Fe(bpy)_3]^{3+/2+}$  (Fig. 29) - have weaker Fe(II)-N bonds than Co(II)-N, resulting in a high redox potential of 1.37 V as the Fe center stabilizes the bipyridyl radical cation less. Furthermore, the  $[Fe(bpy)_3]^{3+/2+}$  redox couple is well known to be a stable, highly reversible redox system. The RR9 dye, with a low HOMO energy level, was judiciously synthesized to match the redox potential of  $[Fe(bpy)_3]^{3+/2+}$  by Delcamp and co-workers. With a driving force of 0.190 eV the DSCs reached a record  $V_{\rm OC}$  of over 1.4 V and PCE of 1.9%. 287

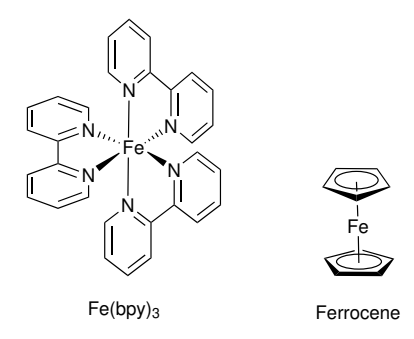


Fig. 29 Chemical structures of iron coordination complexes-based redox mediators implemented in DSCs.

The 1-electron, outer-sphere iron-based redox shuttle ferrocenium/ferrocene (Fc<sup>+</sup>/Fc) couple has been intensively investigated in the DSC field due to its favourable kinetics property, it has a more positive redox potential fast electron exchange and low toxicity in comparison to the Iodide redox couple. Initial results disclosed that the Fc<sup>+</sup>/Fc couple is not a suitable electrolyte for DSC application due to a facile back transfer of electrons from the TiO2 and the substrate. Suppression was achieved by surface passivation, including spray pyrolysis, atomic layer deposition (ALD), and silane treatment. In a later study by Daeneke et al., the aim was to suppress mass-transport limitations in the Fc<sup>+</sup>/Fc-containing electrolyte as well as to decrease the active area for recombination by using thin films of TiO2 (2.2 µm of mesoporous layer with an 18 nm underlayer and a 4.4 µm scattering layer) sensitized with the organic dye Carbz-PAHTDTT; Pt was used as counter electrode. Moreover, the electrolyte contained the base tBP to passivate TiO2 surface states. The device performance exhibited enhanced parameters ( $V_{OC} = 0.842 \text{ V}$ ,  $J_{SC} = 12.2 \text{ mA cm}^{-2}$ , FF = 73%, and PCE = 7.5%), which are the highest values hitherto reported for Fc-based electrolytes and can be favourably compared to reference cells ( $V_{OC} = 0.735 \text{ V}$ ,  $J_{SC} = 13.3 \text{ mA cm}^{-2}$ , FF = 62%, and PCE = 6.1%) with iodidebased electrolyte. Further work with this material could poten-

tially lead to efficiencies higher than 8% with Fc-containing electrolytes. 384,386

# Nickel coordination complexes

Nickel bipyridyl complexes have been tested in battery applications and showed a high cell potential of over 2.25 V, and the anodic and cathodic half-cell reactions appeared to be highly stable and electrochemically pseudo-reversible. 387,388 Ni-bis(dicarbollide), featuring two η5-coordinated deboronated (nido-2) o-carborane ligands, readily undergoes multiple redox transformations involving net charges of -2, -1, and 0, with Ni(II-IV) oxidation states (Fig. 30). Li et al. introduced a promising new class of Ni(IV/III) bis(dicarbollide) complexes as a fast, non-corrosive redox shuttle for DSC applications, creating a framework with electron donating and electron withdrawing groups through chemical modification of the Ni-bis(dicarbollide) moiety in the B(9/12) positions. These  $Ni^{4+/3+}$ -dicarbollide mediators exhibit low electron exchange rates since the electron transfer process requires a cis-to-trans conformational rotation resulting in high reorganization energies. 389 Spokoyny et al. created a series of redox mediators ranging in redox potentials from 0.37 V to 0.55 V vs. NHE and the highest  $V_{\rm OC}$  was obtained for the 3,5-bis(trifluoromethyl)phenyl group, with  $V_{OC} = 0.850 \text{ V}$ ; PCEs were in the range between 0.7% and 2%. In DSCs with the N719 photosensitizer, the Ni redox couple with potential 0.77 V vs. NHE rendered a 1.5% efficiency, which was further improved up to  $J_{SC} = 6.3 \text{ mA cm}^{-2}$  by electrode modification using a nanoparticle-and-aerogel framework with high surface area and thickness of 13.6  $\mu m$  to reach a PCE = 2.1% ( $V_{OC}$  = 0.628 V,  $J_{SC} = 5.3 \text{ mA cm}^{-2}$ , FF = 60%). Further investigations were focused on modification of Ni complexes and the search for an appropriate sensitizer to match this kind of redox couples. 387

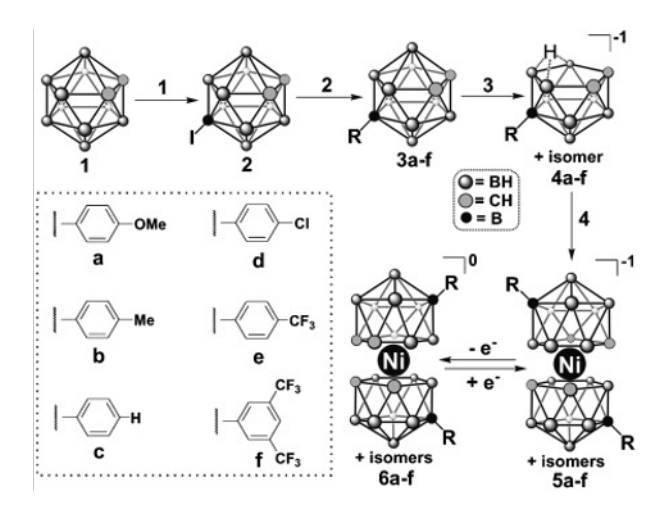


Fig. 30 Starting with commercially available o-carborane, a five-step, high-yield synthetic strategy is used to create bis(dicarbollide) species from B(9)-functionalized derivatives of the parent carborane. Reprinted with permission from ref 387. Copyright 2010 WILEY-VCH Verlag GmbH & Co. KGaA, Weinheim.

# Manganese coordination complexes

The search for more sustainable and less toxic redox mediators based on coordination complexes for DSCs was extended to Mn(IV/III) complexes. Manganese can be considered as an interesting 1-electron outer-sphere redox shuttle candidate because of its variety of accessible redox states (from +2 to +7), low toxicity and abundance. Ideally, the oxidized redox mediator species Mnox, present at the TiO2 surface, should not significantly reduce the lifetime of TiO<sub>2</sub> conduction band electrons before Mn<sub>ox</sub> diffuses to the counter electrode. The undesired recombination reaction between electrons at the TiO2 surface and Mnox limits charge collection, as with the ferrocene/ferrocenium couple, and constrains the choice of alternative mediators, which require surface passivation. Some Mn(III) complexes are known to undergo a spin change upon reduction (d<sup>4</sup> to d<sup>5</sup>) that can slow the undesired recombination.

The first example of application was reported in 2014 by Spiccia et al., who focused on DSCs containing the commercially available  $[Mn(acac)_3]^{+/0}$  (acac = acetylacetonate) (Fig. 31) with a redox potential of 0.49 V vs. NHE and the MK2 dye, reporting an energy conversion efficiency of 4.4% under AM1.5G,  $100 \text{ mW cm}^{-2} \text{ conditions.}^{390} \text{ Carli et al. followed up}$ by developing the derivatives  $[Mn(CF2)_3]$  (CF2 = 4,4-difluoro-1phenylbutanate-1,3-dione) and [Mn(DBM)<sub>3</sub>] (dbm = dibenzoylmethanate). <sup>391</sup> This series showed redox potentials in the range between 0.41 V and 0.69 V vs. NHE for  $[Mn(CF2)_3]^{3+/2+}$  and  $[Mn(DBM)_3]^{3+/2+}$ .

Fig. 31 Chemical structures of manganese coordination complexes-based redox mediators implemented in DSCs.

### Vanadium coordination complexes

Fundamental electrochemical research on the kinetics and mechanisms of vanadium(V/IV) redox couple reactions in a range of electrolytes especially for redox flow batteries is ongoing. For DSCs, in 2013 Nishide and co-workers featured an electrochemically-reversible and fast redox mediator VO(salen) (salen = N, N'-ethylene-bis(salicylideneiminate)), Fig. 32, reaching a conversion efficiency of 5.4% ( $V_{OC} = 0.74$  V and  $J_{SC} = 12.3 \text{ mA cm}^{-2}$ ) in a co-sensitized DSC with D205/D131. <sup>392</sup> In 2015 Apostolopoulou et al. introduced the oxidovanadium(IV) reversible redox couple  $[VO(hybeb)]^{2-/-}$  (where hybeb<sup>4-</sup> is a tetradentate diaminodiphenolate ligand) with a very low redox potential of -0.047 V vs. NHE. The electrolyte was tested in DSCs with the N719 dye reaching a performance of 2% ( $V_{OC} = 0.66$  V,  $J_{SC} = 5.2 \text{ mA cm}^{-2}$ ) under 1 sun illumination. <sup>393</sup>

4.3.1.3 Small organic molecules Various organic redox active molecules such as TEMPO+/TEMPO, AZA (2-azaadamantan-

Fig. 32 Chemical structures of vanadium coordination complexes-based redox mediators implemented in DSCs.

N-oxyl) Quinone or  $T^-/T_2$  (T for 1-methyl-1-H-tetrazole-5thiolate, T2 for the dimer) were tried to circumvent the limitations that still exist with coordination complex redox couples, including inefficient dye regeneration, mass transport limitations of large metal complexes or high electron recombination with the fast outer-sphere redox systems (Fig. 33).

In 2012 Burschka et al. reached a power conversion efficiency of 7.9% with a DSC based on the T-/T2 redox couple together with PEDOT counter electrode. 350 In the same year, Li et al. introduced a new thiolate/disulfide redox couple AT-/BAT, <sup>394</sup> an analogue to T-/T2 with more positive redox potential and slower charge recombination reaching promising efficiencies of 6.07%. A year later supramolecular lithium cation assemblies of crown ether have been used to replace conventional tetraalkylammonium counter-ions in thiolate/disulfide (ET-/BET)-mediated dyesensitized solar cells, which exhibited high stability and efficiency of 6.61% under 1 sun illumination. <sup>395</sup>

The redox-active TEMPO was successfully implemented into DSCs as a redox mediator by Grätzel et al. and it improved the  $V_{\rm OC}$  over the  $I^-/I_3^-$  electrolyte. <sup>396</sup> Nitroxide derivatives were also studied as DSC mediators by other groups. However, the  $V_{\rm OC}$ was enhanced at the expense of the short-circuit current density of the cell. 349,397

Another organic radical - 2-azaadamantan-N-oxyl (AZA) - was used as a stable and highly reactive redox mediator in a DSC. AZA exhibited both an appropriate redox potential and significantly high values of diffusivity, heterogeneous electron-transfer rate, and electron self-exchange reaction rate. These properties gave rise to an enhanced electron-transfer mediation, which lead to a high fill factor and thus excellent photovoltaic performance to achieve a conversion efficiency of 8.6%. 398

The organic redox couple tetramethylthiourea/tetramethylformaminium disulfide (TMTU/TMFDS<sup>2+</sup>) was evaluated in dye-sensitized solar cells in conjunction with a series of indoline- and ruthenium-based dyes. Of these, devices with indoline dye D205 showed the best performance, with an optimized power conversion efficiency of 7.6% under AM1.5G 1 sun illumination. Charge collection and injection were highly efficient in all TMTU-based DSCs studied. Regeneration of indoline dyes was highly efficient, whereas regeneration of ruthenium dyes by TMTU was less efficient, accounting for their inferior performance. 399

The hydroquinone/benzoquinone (HQ/BQ) redox pair has in-

creased interest in research as the electron transfer of the redox couple is a thermodynamically reversible process. 400 In previous reports, the anionic hydroquinone species (TMAHQ/BQ) was used as a redox mediator in DSCs with the N719 dye as sensitizer and Pt as CE; these systems showed promising photovoltaic characteristics ( $V_{OC} = 750 \text{ mV}, J_{SC} = 17.2 \text{ mA cm}^{-2},$ FF = 066.3%, and PCE = 8.4%). With the same redox mediator but with PEDOT as counter electrode and the organic dye CM-309, the following parameters were achieved:  $V_{OC} = 755 \text{ mV}$ ,  $J_{SC} = 12.10 \text{ mA cm}^{-2}$ , FF 67.8%, and PCE = 6.2%. <sup>401</sup>

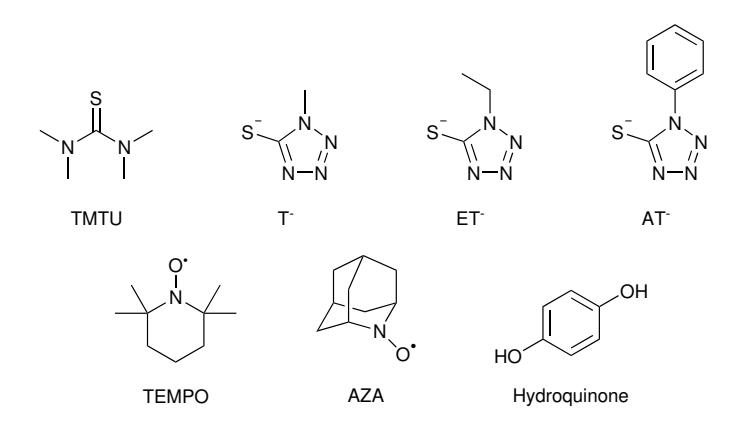


Fig. 33 Chemical structures of small organic molecules-based redox mediators implemented in DSCs.

 Table 4 Photovoltaic characteristics of DSCs employing various redox mediator couples

Mediator	Sensitizer	V <sub>OC</sub> (mV)	$J_{\rm SC}~({\rm mA~cm^{-2}})$	FF (%)	PCE (%)	Year	Ref.
I <sup>-</sup> /I <sub>3</sub> <sup>-</sup>	N719	846	17.73	75	11.18	2005	143
Br <sup>-</sup> /Br <sub>3</sub> <sup>-</sup>	ADEKA-3	1450	4.77	56	3.9	2016	213
$I^-/IBr_2^-$	N3	790	12.8	64	6.4	2007	360
$I^-/I_2Br^-$	N3	640	9.2	41	2.4	2007	360
Co(bpy) <sub>3</sub>	D35	936	12.05	69.1	7.80	2018	95
Co(bpy) <sub>3</sub>	D45	810	13.40	73.0	7.93	2018	95
Co(bpy) <sub>3</sub>	D5	713	9.45	72.8	4.91	2018	95
Co(bpy) <sub>3</sub>	N719	620	3.8	76	1.8	2011	363
Co(bpy) <sub>3</sub>	Z907	744	14.0	62	6.5	2011	363
Co(bpy) <sub>3</sub>	D9L6	688	10.7	72	5.32	2012	163
Co(bpy) <sub>3</sub>	D21L6	852	12.3	63	6.63	2012	163
Co(bpy) <sub>3</sub>	D25L6	854	10.8	63	5.51	2012	163
Co(bpy) <sub>3</sub>	Y123	855	14.6	70	8.8	2011	272
Co(bpy) <sub>3</sub>	YD2	825	14.9	69	8.4	2011	289
Co(bpy) <sub>3</sub>	YD2-o-C8	965	17.3	71	11.9	2011	289
Co(bpy) <sub>3</sub>	SM371	960	15.9	79	12.0	2014	291
Co(bpy) <sub>3</sub>	SM315	910	18.1	78	13.0	2014	291
Co(bpy) <sub>3</sub>	MK2	826	13.7	69	7.8	2013	368
Co(bpy) <sub>3</sub>	LEG1	815	8.80	60	4.3	2013	364
Co(bpy) <sub>3</sub>	LEG1	830	11.2	51	4.7	2013	364
Co(bpy) <sub>3</sub>	LEG2	915	8.9	68	5.5	2013	364
Co(bpy) <sub>3</sub>	LEG4	805	12.1	68	6.6	2015	348
	C218/MKA253	810	12.1	69	6.9	2016	348
Co(bpy) <sub>3</sub> Co(phen) <sub>3</sub>	D35	910	7.3	62	4.2	2015	3 <del>4</del> 6
Co(phen) <sub>3</sub>	ADEKA-1/LEG4	1014	7.3 18.27	77.1	4.2 14.3	2015	25
	Z907	700	3.6	56	1.4	2015	2 <i>3</i> 367
Co(Mo, hwy ng)	D35	1020	6.1	61	3.7	2013	367 164
Co(Me <sub>2</sub> bpy-pz) <sub>2</sub>	D35	1020	5.3	68	3. <i>7</i> 3.6	2013	164
Co(bpy-pz) <sub>2</sub>	D35 D35	900	2.5	66	3.6 1.5	2013	164 164
Co(py-pz) <sub>3</sub>							
Co(Mepy-pz) <sub>3</sub>	D35	880	0.78	58	0.4	2013	164
SBCC	D35	905	5.19	53.8	2.53	2014	366
Co(phen) <sub>3</sub> /Co(EtPy) <sub>2</sub>	Z907	750	5.1	58	2.2	2015	367
Co(phen) <sub>3</sub> /Co(EtPy) <sub>2</sub>	D35	920	8.4	67	5.1	2015	367
Co(PY5Me <sub>2</sub> )(tBP)	MK2	993	8.1	76	6.1	2012	330
Co(PY5Me <sub>2</sub> )(NMBI)	MK2	940	11.8	77	8.4	2012	330
Co(bpyPY4)	MK2	757	14.7	75 	8.3	2013	368
Co(ttb)	LEG4	810	11.6	57	5.4	2016	348
Co(ttb)	C218/MKA253	805	13.0	60	6.6	2016	348
Cu(SP)(mnt)	N719	660	4.4	44	1.3	2005	373
Cu(dmp) <sub>2</sub>	N719	790	3.2	55	1.4	2005	373
Cu(dmp) <sub>2</sub>	C218	932	11.29	66	7.0	2011	339
Cu(dmp) <sub>2</sub>	LEG4	1020	12.6	62	8.3	2016	96
Cu(dmp) <sub>2</sub>	Y123	1060	13.61	69.2	10.3	2016	15
Cu(dmp) <sub>2</sub>	D5	1130	9.02	73.6	7.53	2018	95
Cu(dmp) <sub>2</sub>	D45	1020	9.90	74.1	7.48	2018	95
Cu(dmp) <sub>2</sub>	D35	1140	11.40	70.6	9.22	2018	95
Cu(dmp) <sub>2</sub>	G3	860	3.8	59	1.9	2016	344
Cu(dmp) <sub>2</sub>	D	750	4.7	36	1.3	2018	378
Cu(phen) <sub>2</sub>	N719	570	0.48	43	0.12	2005	373
Cu(bpye) <sub>2</sub>	LEG4	904	13.8	71.8	9.0	2016	375
Cu(bpye) <sub>2</sub>	Y123	627	13.2	65	5.6	2020	345
Cu(dmby) <sub>2</sub>	Y123	1070	14.15	68.7	10.0	2016	15

Cu(dmby) <sub>2</sub>	D5	1070	9.85	71.2	7.53	2018	95
Cu(dmby) <sub>2</sub>	D45	956	11.85	68.0	7.71	2018	95
Cu(dmby) <sub>2</sub>	D35	1130	11.53	60.2	7.84	2018	95
Cu(tmby) <sub>2</sub>	Y123	1040	15.53	64.0	10.3	2016	15
Cu(tmby) <sub>2</sub>	D5	837	10.79	67.4	6.10	2018	95
Cu(tmby) <sub>2</sub>	D45	984	12.52	67.3	8.30	2018	95
Cu(tmby) <sub>2</sub>	D35	1110	12.81	66.1	9.44	2018	95
Cu(tmby) <sub>2</sub>	L348	1170	6.4	72.0	5.3	2018	276
Cu(tmby) <sub>2</sub>	L349	1160	11.0	71.7	9.2	2018	276
Cu(tmby) <sub>2</sub>	L350	1140	13.0	76.0	11.2	2018	276
Cu(tmby) <sub>2</sub>	L351	1060	11.2	76.3	9.1	2018	276
Cu(tmby) <sub>2</sub>	WS-70	1060	13.2	77	11.0	2018	274
Cu(tmby) <sub>2</sub>	WS-72	1100	13.3	78	11.6	2018	274
Cu(tmby) <sub>2</sub>	D35/XY1	1030	16.19	68	11.3	2017	341
Cu(tmby) <sub>2</sub>	Y123/XY1b	1050	13.1	79	13.1	2018	277
$Cu(tmby)_2$	XY1	1000	13.3	67	8.9	2020	33
$Cu(tmby)_2$	L1	910	9.4	71	6.1	2020	33
$Cu(tmby)_2$	XY1/L1	1080	15.9	67	11.5	2020	33
$Cu(eto)_2$	D5	828	10.12	71.5	6.00	2018	95
Cu(eto) <sub>2</sub>	D45	978	12.59	66.7	8.21	2018	95
$Cu(eto)_2$	D35	1120	11.93	66.3	8.84	2018	95
Cu(2-mesityl-4,7-dimethyl-1,10-phenanthroline) <sub>2</sub>	G3	720	9.3	66	4.4	2016	344
$Cu(2-n-butyl-1,10-phenanthroline)_2$	D	610	6.3	53	2.0	2018	378
$Cu(2-n-butyl-1,10-phenanthroline)_2$	G3	860	10.1	66	5.7	2018	380
$Cu(2-n-butyl-1,10-phenanthroline)_2$	G4	780	10.1	63	4.9	2018	380
Cu(2-mesityl-1,10-phenanthroline) <sub>2</sub>	G3	830	11.4	59	5.6	2018	380
Cu(2-mesityl-1,10-phenanthroline) <sub>2</sub>	G4	840	11.7	54	5.3	2018	380
Cu(2-tolyl-1,10-phenanthroline) <sub>2</sub>	G3	870	11.1	62	6.0	2018	380
Cu(2-tolyl-1,10-phenanthroline) <sub>2</sub>	G4	870	11.1	62	6.0	2018	380
Cu(2-phenyl-1,10-phenanthroline) <sub>2</sub>	G3	880	8.0	69	4.9	2018	380
Cu(2-phenyl-1,10-phenanthroline) <sub>2</sub>	G4	810	10.2	58	4.8	2018	380
Cu(oxabpy)	Y123	920	9.75	69	6.2	2018	346
Cu(1)	Y123	689	5.7	77	3.1	2020	345
Cu(2)	Y123	693	10.2	72	4.7	2020	345
Cu(3)	Y123	792	7.9	75	4.3	2020	345
Ferrocene	Carbz-PAHTDTT	842	12.2	73	7.5	2011	384
K <sub>4</sub> Ni[Fe(CN) <sub>6</sub> ]	N3	790	8	0.7	4	2011	385
Fe(bpy) <sub>3</sub>	RR9	1420	2.8	47	1.9	2018	287
Me <sub>10</sub> Fc	Carbz-PAHTDTT	437	6.6	40	1.1	2012	386
Et <sub>2</sub> Fc	Carbz-PAHTDTT	641	13.3	50	4.2	2012	386
EtFc	Carbz-PAHTDTT	669	12.8	56	4.8	2012	386
BrFc	Carbz-PAHTDTT	671	9.3	48	3.0	2012	386
Br <sub>2</sub> Fc	Carbz-PAHTDTT	599	4.4	46	1.2	2012	386
$Mn(acac)_3$	K4	765	7.8	73	3.9	2014	390
Mn(acac) <sub>3</sub>	MK2	733	8.6	69	4.4	2014	390
Mn(acac) <sub>3</sub>	N719	771	7.9	73	4.4	2014	390
Mn(CF <sub>2</sub> ) <sub>3</sub>	MK2	800	4.95	69	2.72	2016	391
VO(salen)	D205/D131	740	12.3	59	5.4	2013	392
VO(hybeb)	N719	660	5.2	58	2	2015	393
$T^{-}/T_{2}$	Z907	687	15.9	72	7.9	2013	350
$T^{-}/T_{2}$	N719	630	14.25	68	6.10	2012	394
AT <sup>-</sup> /BAT	N719	670	13.76	68	6.27	2012	394
ET <sup>-</sup> /BET	N719 N719	632	9.3	71	4.2	2012	395
TEMPO	D-149	830	9.3 9.4	71 70	5.4	2013	396
TEMPO	LEG4	965	7.74	70 73	5.43	2015	349

TEMPO	D205	880	9.88	75	6.5	2012	398
TEMPO	D205/D131	780	13.5	66	7.0	2012	398
AZA	D205	820	12.9	76	8.1	2012	398
AZA	D205/D131	850	13.3	75	8.6	2012	398
TMTU	D205	777	16.6	49	6.32	2013	399
TMTU	D102	770	13.8	54	5.74	2013	399
TMTU	D131	825	11.0	61	5.53	2013	399
TMTU	N719	626	10.3	50	3.22	2013	399
TMTU	Z907	642	8.3	53	2.82	2013	399
HQ/BQ	N719	755	10.28	66.7	5.2	2013	401
HQ/BQ	CM309	755	12.10	67.8	6.2	2013	401
HQ/BQ	Y123	533	6.5	30	1.08	2018	400
PhHQ/PhBQ	Y123	528	6.3	39	1.3	2018	400
DTHQ/DTBQ	Y123	542	12.6	36	2.5	2018	400
ThymHQ/ThymBQ	Y123	455	10	44	2.0	2018	400

**4.3.1.4 Ionic liquids.** One of the key parameters of DSC is the selection of electrolytes, which provide the internal electrical conductivity. The use of liquid electrolytes demands perfect sealing of the device to avoid leakage and evaporation of the solvents. To eliminate electrolyte leakage issues in traditional DSCs (i.e. cells with organic solvent-based electrolytes), ionic liquids are used as the electrolyte to improve cell durability. An ionic liquid (IL) is a salt in liquid state; ionic liquids or molten salts are generally defined as liquid electrolytes composed entirely of ions. 326,402-404 More in detail, the melting point criterion was proposed to distinguish between molten salts with high melting point and high viscosity, and ionic liquids with low melting point below 100 °C and relatively low viscosity. Whithin the latter category are free-flowing liquids at room temperature; thus, they are often called room temperature ionic liquids (RTILs). Ionic liquids (Fig. 34) have been widely used as electrolytes in DSCs, which is due to their unique features, such as good chemical and thermal stability, tunable viscosity, relative non-flammability, high ionic conductivity and broad electrochemical potential window, and, more importantly, extremely low vapor pressure, greatly reducing evaporation and leakage. Ionic liquids have two applications within electrolytes in DSCs. One is acting as solvents in liquid electrolytes, and the other is functioning as organic salts in quasisolid-state electrolytes. These excellent properties have made ILs a sustainable solution to the problematic use organic solvents, and ILs with different substituents and ions were prepared and used as redox mediators in dye-sensitized solar cells.

Cations: 
$$R_1$$
 $R_1$ 
 $R_2$ 
 $R_3$ 
 $R_4$ 
 $R_3$ 
 $R_4$ 
 $R_3$ 
Anions:

Cl<sup>-</sup>, Br<sup>-</sup>, l<sup>-</sup>, CN<sup>-</sup>, SCN<sup>-</sup>, [N(CN)<sub>2</sub>]<sup>-</sup>, PF<sub>6</sub><sup>-</sup>, BF<sub>4</sub><sup>-</sup>, CF<sub>3</sub>COO<sup>-</sup>, CF<sub>3</sub>SO<sub>3</sub><sup>-</sup>, etc.

Fig. 34 Examples of cations and anions used in ionic liquids.

Best performances with ILs were reached with imidazoliumbased ionic electrolytes. Other IL cations employed are sulfonium, guanidinium, ammonium, pyridinium, or phosphonium, which were also tested as solvent-free electrolytes. The limitations in low diffusion and charge mobility of ILs in comparison to redox mediators in organic solvents remain. Several strategies were employed to improve the mass transport limitations by diluting the ionic liquid with organic solvents, compromising the system with the high volatility of organic solvents. Even in the low-viscosity imidazolium dicyanamide ionic liquids, triiodide diffusion is a limiting factor at low temperature, whereas recombination reactions limit the performance at high temperatures. For example, an ionic liquid electrolyte composed of EMImSCN and PMImI had a triiodide diffusion coefficient of  $2.95 \times 10^{-7} \text{ cm}^2 \text{ s}^{-1}$ , which was 1.6 times higher than that in the pure PMImI electrolyte. The cell using this electrolyte together with Z907 dye achieved an efficiency of 7%. ILs' potential advantage over organic solvents remains to be explored, and the main drawbacks of high viscosity and low ion mobility must be overcome. 405

**4.3.1.5 Quasi-solid and solid polymer electrolytes.** Depending on fabrication strategies, the inclusion of polymers can lead to either quasi-solid (gel) or solid electrolytes. In the former case, the polymer acts as a host matrix for a liquid electrolyte, and it swells to accommodate the liquid inside, forming a gelatinous material that prevents solvent leakage. In the latter case, the redox active components of the charge transport layer are embedded directly within the polymeric structure, without the presence of a solvent.

#### Gels, quasi-solid polymers

Gel polymer electrolytes (GPEs) can hold large amounts of the electrolyte (tens to hundreds of times that of the polymer itself). Their excellent contacting and filling properties between the electrodes result in fast dye regeneration, while their high conductivity ensures fast charge transport to the counter electrode. 326,331,404,406-409 Polyacrylonitrile (PAN), poly(ethylene oxide) (PEO) derivatives and conducting polymers that include polypyrrole (PPy), polyaniline (PAni) and other polymers are the typical host materials (Fig. 35). Dimethyl carbonate (DMC), propylene carbonate (PC) and ethylene carbonate (EC) can be used as organic plasticizers with a large variety of polar solvents, ionic liquids and salts. 410,411 A good proportion of GPE work in DSCs can be credited to Bella and co-workers, as they showed long-term stability and efficiency of gel electrolytes. The specific approach to create an in-situ electrolyte comprises the expansion of a monomer - bisphenol-A-ethoxylate dimethacrylate (BEMA) or poly(ethylene glycol) methyl ether methacrylate (PEGMA) as well as a photoinitiator into the electrolyte and UV exposure of the assembled solar cell. To prove long-term stability, a DSC fabricated using this method with the LEG4 dye and an electrolyte containing the [Co(bpy)<sub>3</sub>]<sup>3+/2+</sup> redox mediator was subjected at first to dark soaking at 60 °C for 1500 h, followed by fullsun irradiation for 300 h at 40 °C. At the end of this treatment, the DSC retained 90% of the initial PCE of 6%. 352,412-414 Using polyethylene glycol diacrylate (PEGDA) and PEGMA as copolymers, power conversion efficiencies of up to 4.41% (Table 5) were recorded. 415 After inserting fillers based on metal organic frameworks (MOFs) or micro-fibrillated cellulose (MFC) into BEMA or PEGDA and PEGMA polymer blends, a dramatic increase in PCE (up to 7.03%) was observed. 333,416,417

The classic conductivity and diffusivity of the iodine/1-butyl-3-methylimidazolium iodide (BMII) redox system was similar to that of liquid electrolytes and, relative to conventional liquid DSCs, the resulting cells displayed increased stability. <sup>351</sup> For devices filled with liquid electrolyte and directed dissolution of polystyrene nanobeads on the counter electrode, resulting in a gel electrolyte, PCEs of 7.54% were registered. The PCE of those devices is close to that of DSCs based on liquid electrolytes (7.59%). <sup>418</sup> Finally, when polyurethane was used as gelation matrix, a PCE up to 6.1% was obtained. <sup>419</sup>

# Solid polymers

Polymer electrolytes (PEs) retain the beneficial aspects of liquid electrolytes (high ionic conductivity, diffusive transport and interfacial contact properties) in combination with the mechanical

advantages of a polymer's durability and versatility. 326,331,420,421 The majority of inorganic conductors in a host polymer consist of lithium salts (LiI, NaI, LiClO<sub>4</sub>, LiCF<sub>3</sub>SO<sub>3</sub>, LiSCN, NaSCN, NaClO<sub>4</sub>,  $LiPF_6$ , etc).

The selection of polymer hosts for PEs is based on the following characteristics: sufficiently polar and/or groups to form strong cation coordination and display low impediment to bond rotation. Poly(ethylene oxide) (PEO) is the host polymer most widely used, 402,422 although these systems typically exhibit poor conductivity  $(10^{-8} \text{ S cm}^{-1})$ ,  $^{326}$  which can be increased with the use of blends of various polymers or copolymers and synthetically adapted monomers (Fig. 35). 326,423,424

Li et al. introduced functionalized hydroxyethyl and ester cofunctionalized imidazolium iodide (HEII) as a solid-state electrolyte, and investigated the effect of imidazolium ring substitutes on ionic conductivity and solid-state DSC efficiency. 425 Bella et al. contributed by constructing biodegradable polymers derived from seaweed as green chemistry-based PE. Carboxymethyl-dacaraageenan (CkC) and NaI/I2-based DSCs display high efficiency of power conversion up to 2.06%. 426 Limitations associated with PEs are connected to insufficient pore filling and ionic conduction, resulting in a low rate of dye regeneration and high kinetics of electron recombination in solid polymer electrolytes and dye and metal oxide semiconductor interfaces.

### 4.3.2 Hole transport materials.

Hole transporting materials (HTMs) transport charges locally within the materials themselves, not via ions. 427,428 In this case, it is more correct to talk about electronic (or charge) diffusion. Due to the lack of molecular movement, solid-state DSCs (ssD-SCs) based on an HTM layer can work similarly to liquid DSCs while also maintaining the advantages of a solid-state system. For efficient DSC, rapid carrier transport with low recombination rate is always necessary. Apart from electronic and optical properties, stability is also a vital requirement for PV technology. The choice of the HTM has shown significant impact on the stability of ssDSCs. During operation, the HTM has to facilitate the energy conversion process via: (i) Compatible valance band (VB) level between HTM and dye. The purpose of this criterion is to minimize the energy barrier during charge (hole) transfer. For the reduction of the recombination rate, a large bandgap or low electron affinity would also enable the HTM to efficiently block electrons. (ii) High carrier mobility, long diffusion length, and long carrier lifetime. These can prevent carrier loss during extraction and transport. (iii) Stability during processing and various working conditions along with resistance against heat, moisture, oxygen, and UV light. (iv) Low material and processing cost.

New limitations emerge in the manufacturing of dye-sensitized solar cells due to solid-state hole transporting materials, for example poor pore filling of the mesoporous oxide layer. If large molecules with long molecular chains are introduced to mesoporous materials, they are unable to completely penetrate the mesoporous network. 429-432 However, in 2011, Burschka et al. presented a ssDSC featuring spiro-OMeTAD with a PCE of 7.2%, thanks to a careful HTM layer optimization with the addition of p-dopants into the precursor solution. 433 Given the high perfor-

Fig. 35 Chemical structures of polymer electrolytes used in DSCs.

mance reached by Burschka, spiro-OMeTAD is often used as a benchmark HTM when presenting new ones, and it has therefore been used in combination with a large number of dyes. 434-438 Nevertheless, this material poses many issues and a consensus has been established that an affordable, new material must be sought before ssDSC commercial feasibility can be achieved. In more depth, spiro-OMeTAD suffers from poor conductivity and hole mobility in its pristine form, and it is not stable over time. 437,439,440

4.3.2.1 Organic hole transport materials. Many organic compounds have been investigated as hole transfer materials for ssDSCs. The variety in synthesis helps researchers to develop new materials with the desired properties. New compounds allow the fine-tuning of energy levels, electronic properties, filmforming properties, and solubility in different solvents. Organic hole transport materials have very well-defined composition and molecular weight that ensures consistent properties in different batches. Compared to other compounds, these smaller molecules are better in penetrating the mesoporous layer of the photoanode. 441,442

Organic small molecules are the most common class of novel HTMs for ssDSCs. Most of the compounds referenced in this re-

Table 5 Photovoltaic characteristics of DSCs based on polymer electrolytes

Matrix/polymer	Salt	Sensitizer	V <sub>OC</sub> (mV)	$J_{\rm SC}~({ m mA~cm^{-2}})$	FF (%)	PCE (%)	Year	Ref.
PPVII	none	N719	637	13.61	71	6.18	2014	404
MPII:SiO $_2$	I <sub>2</sub> , NMBI	Z907	700	13.67	73.1	7.0	2003	406
PVP	I <sub>2</sub> , KI, BMII	N3	626	15.72	55	5.41	2010	407
PVDF-HFP	I <sub>2</sub> , NMBI, DMPII	Z907	730	12.5	67	6.1	2003	408
BEMA:PEGMA	Co(bpy) <sub>3</sub>	LEG4	880	10.5	68	6.4	2015	409
BEMA:PEGMA	I <sub>2</sub> , NaI	N719	580	16.0	58	5.41	2013	413
P(EO-EPI)	I <sub>2</sub> , LiI	N3	670	9.1	54	3.3	2008	410
Gelator 1	I <sub>2</sub> , LiI, DMPII	N719	670	12.8	67	5.91	2001	411
Gelator 2	I <sub>2</sub> , LiI, DMPII	N719	632	11.1	65.8	4.62	2001	411
Gelator 3	I <sub>2</sub> , LiI, DMPII	N719	640	11.1	63.4	4.49	2001	411
Gelator 4	I <sub>2</sub> , LiI, DMPII	N719	623	11.2	66.4	4.67	2001	411
PEO:CMC	I <sub>2</sub> , NaI, MPII	N719	750	10.03	69	5.18	2013	412
PEGDA:PEGMA	I <sub>2</sub> , NaI	N719	499	17.46	52	4.41	2014	415
Cellulose	I <sub>2</sub> , LiI, MPII	N719	590	8.39	67	3.33	2014	333
PEGDA:PEGMA:Mg-MOF	I <sub>2</sub> , NaI, MPII	N719	690	12.6	55	4.80	2013	416
BEMA:PEGMA:MFC	I <sub>2</sub> , NaI	N719	760	15.2	61	7.03	2014	417
PMMA	I <sub>2</sub> , BMII	N719	750	15.53	69	8.03	2013	351
Polystyrene beads	I <sub>2</sub> , BMII	N719	770	15.3	64	7.54	2012	418
Polyurethane	I <sub>2</sub> , LiI, BMII	N719	740	14.97	55	6.1	2011	419
PEO:TiO <sub>2</sub>	I <sub>2</sub> , LiI	N3	664	7.2	57.5	4.19	2002	422
HEII	I <sub>2</sub> , LiI, NMBI, MPII	MK2	733	14.66	69.3	7.45	2013	425
CkC	I <sub>2</sub> , NaI	N719	510	7.60	53	2.06	2015	426

view have a triphenylamine component in their composition: the nitrogen atom is a strong electron acceptor due to its lone electron pair and it is aided by the presence of three extra phenyl groups. The energy levels of the molecules containing such moiety are tuned by inserting substituents – most commonly the electrondonating group methoxy – on the phenyls that are not linked to the rest of the molecule, to destabilize the electronic cloud in the rings. <sup>443</sup> A list of small molecular HTMs is reported along with their related dye and conversion efficiency in Table 6, and their chemical structures are represented in Fig. 36-37.

Debia et al. and Xu et al. both reported on a carbazole featuring a p-methoxyphenyl group attached to the nitrogen atom and a di(p-methoxyphenyl)amino group in para to each benzene ring, 3b444 and X19,445 respectively. Devices with the 3b HTM were sensitized with the D102 dye, while those with X19 employed LEG4. This comparison allows to understand how important a good dye-HTM combination is in terms of charge transfer efficiency. The champion device with the 3b HTM had a  $V_{\rm OC}$  of 680 mV,  $J_{\rm SC}$  of 6.32 mA cm<sup>-2</sup>, FF of 41% and PCE of 1.75%. The best device with X19 featured a  $V_{\rm OC}$  of 750 mV,  $J_{\rm SC}$ of 9.62 mA cm<sup>-2</sup>, FF of 62% and PCE of 4.5%. While a higher current might be due to differences in light absorption profiles between the two dyes, the higher  $V_{\rm OC}$  and FF in the latter case is the result of a reduced series resistance in the device based on X19. In their later work, Xu et al. reported on a second carbazolebased HTM, X51. 445 The constituents of X51 were similar to those of X19 but in this case two carbazole units were linked together by the two nitrogen atoms through a biphenyl linker, creating a molecule of almost double molecular weight compared to X19. The higher conductivity of X51 lead to a lower  $R_s$  in the final device, as it can be inferred by cell parameters resulting in a VOC of 920 mV,  $J_{SC}$  of 9.27 mA cm<sup>-2</sup>, FF of 70% and PCE of 6.0%. Similar to the work performed for X51, Benhattab et al. also linked two carbazole units with alkyl chains, namely propyl (TCz-C3), hexyl (TCz-C6), and dodecyl (TCz-T12). 434 Unlike X51, alkyl chains electronically isolated the two carbazole units, which behaved as single molecules for what concerned charge transfer. The presence of the alkyl linker was instead an attempt to tune the morphology of the solid-state film in the device reaching a  $V_{\rm OC}$  of 690 mV,  $J_{\rm SC}$  of 6.27 mA cm<sup>-2</sup>, FF of 51% and PCE of 2.21%.

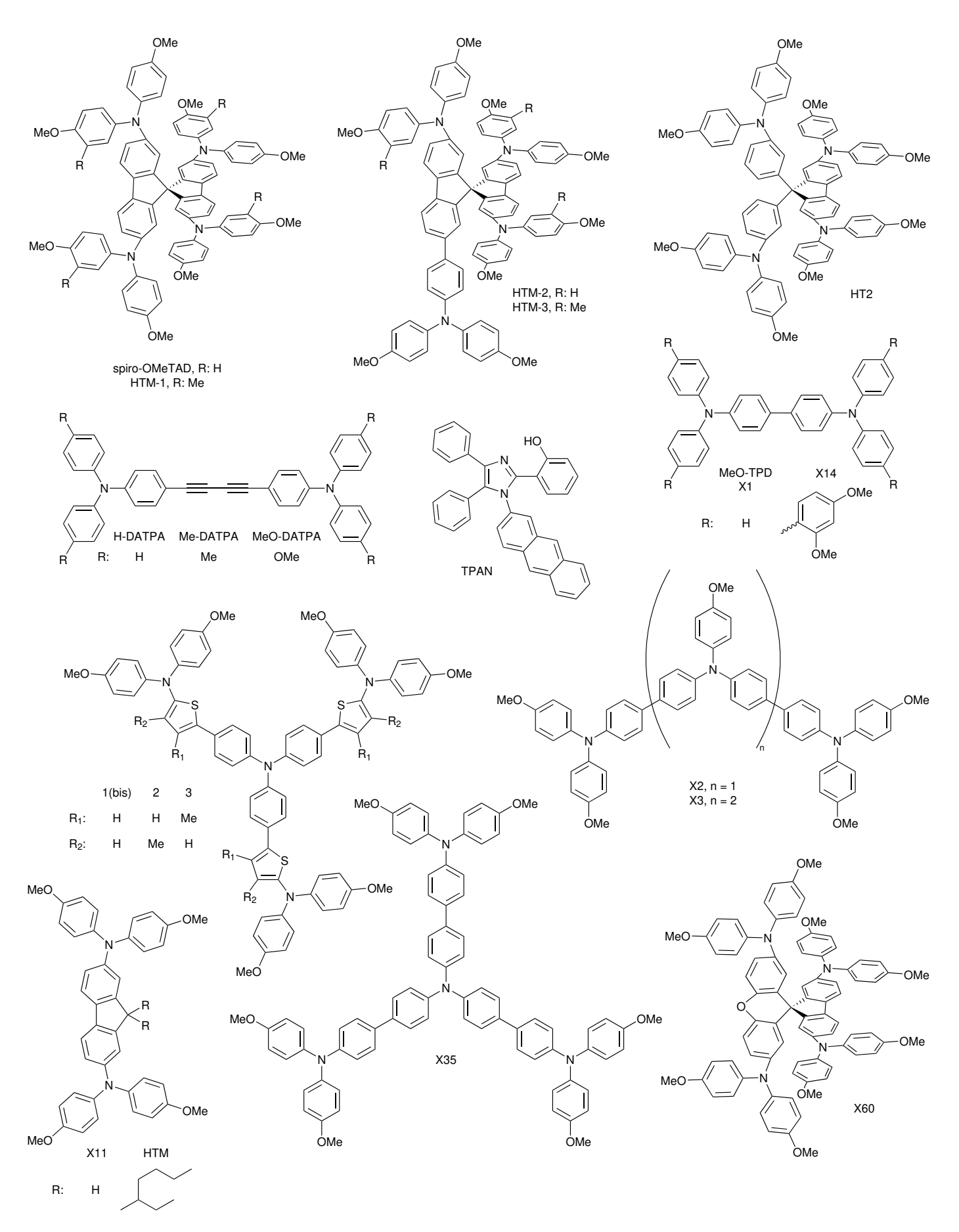
Snaith, Robertson and co-workers developed a series of rodshaped HTMs based on two triphenylamine groups linked by a highly linear diacetylene core, namely H-DATPA, Me-DATPA, MeS-DATPA and MeO-DATPA (Fig. 37). 446 The device fabricated with the first one achieved a  $V_{\rm OC}$  of 620 mV,  $J_{\rm SC}$  of 0.67 mA cm<sup>-2</sup>, FF of 37% and PCE of 0.15%, while for the other two cell parameters were  $V_{\rm OC}$  of 700 mV,  $J_{\rm SC}$  of 1.13 mA cm<sup>-2</sup>, FF of 43% and PCE of 0.34%, and  $V_{\rm OC}$  of 890 mV,  $J_{\rm SC}$  of 1.93 mA cm<sup>-2</sup>, FF of 67% and PCE of 1.16%, respectively. Johansson and co-workers demonstrated that light soaking of full DSCs dramatically improves the efficiency of the solar cell, indicating that ion migration occurs in the solid-state layer. The PCE of a solar cell improved from 1.1% to 4.9% after light soaking. 447 Yuan et al. and Liu et al. introduced new HTMs – HTM 448 and X11 435 – featuring a fluorene center and p-methoxyphenylamino groups connected to each benzene ring. A ssDSC with HTM reached a PCE of 3.3%, while one with X11 reached a PCE of 1.7% with the MKA253 sensitizer and of 3.0% with the LEG4 sensitizer.

Sun and co-workers designed a series of p-methoxy-substituted triphenylamine oligomers, which they used to make X1, X2, X3 and X35.  $^{436,449}$  Optimized devices showed that there was an increase in performance with increasing number of repeating units (see Table 6 for champion device details, for X3-based devices

Fig. 36 Examples of carbazole-based organic hole conductors.

 $V_{\rm OC}$  was 880 mV,  $J_{\rm SC}$  was 9.23 mA cm<sup>-2</sup>, FF was 62% and PCE was 5.4%). Another effective hole conductor, X14, was created by Sun, Kloo and co-workers. This molecule also featured an expanded aromatic conjugation, as each of X14's methoxy groups were replaced with an o,p-dimethoxy-substituted phenyl moiety. This substitution pushed the HOMO level about 200 meV away from vacuum and gave to X14 a hole mobility value double that of X1 when both compounds were doped with LiTFSI. In the experiments, solar cell efficiency was comparable between the two hole transporting materials. The best X1 samples were the ones that had a PCE of 5.8%, while those with X14 had a PCE of 6.1%. For comparison, the best spiro-OMeTAD-based system displayed a PCE of 5.9%. 450 Malinauskas et al. have conducted a study on the long-term stability of spiro-OMeTAD-derived DSCs. They noticed that crystalline domains formed in the originally amorphous spiro-OMeTAD film when the devices were held at 60 °C, which proved the cause of the poor performance of those devices. 437 In order to circumvent this limitation they changed spiro-OMeTAD's molecular structure to incorporate asymmetry, reaching high performances with a  $V_{\rm OC}$  of 820 mV,  $J_{\rm SC}$  of 9.34 mA cm<sup>-2</sup>, FF of 63% and PCE of 4.8%. The more heavily substituted HTM-2 and HTM-3 proved less efficient with a  $V_{\rm OC}$  of 800 mV,  $J_{\rm SC}$  of  $7.08 \text{ mA cm}^{-2}$ , FF of 38% and PCE of 2.2%; and a  $V_{OC}$  of 800 mV,  $J_{\rm SC}$  of 7.00 mA cm<sup>-2</sup>, FF of 38% and PCE of 2.1%; respectively.

Xu et al. synthesized X60, the only HTM able to rival with Burschka's benchmark system. X60 is based on a spiro[fluorene-9,9'-xanthene] core with p-methoxy substituted diphenylamine side groups, and the core moiety costs less than 30 times that of spiro-OMeTAD. They did not have a spiro-OMeTAD-based reference cell, but an X60-based one featured a  $V_{\rm OC}$  of 890 mV,  $J_{\rm SC}$ of 11.38 mA cm $^{-2}$ , FF of 72% and PCE of 7.30%.  $^{451}$ 



 $\textbf{Fig.} \ \ \textbf{37} \ \ \textbf{Examples of triphenylamine-based organic hole conductors}.$ 

**4.3.2.2 Polymeric hole transporting materials.** Using polymers in ssDSCs is more complex than using small molecules. In fact, it is not enough for a compound to be highly performing, it is also important to engineer the constructed device so that the compound can infiltrate the TiO2 mesoporous structure and thus regenerate the dye over the entire device thickness. Most of the studied polymers are capable of in-situ polymerization; thanks to this processing, monomer molecules will wet and infiltrate the system and after polymerization the usually higher conductivity of macromolecules can be exploited. In each article, the polymerization mechanism is studied in depth and also referred to the general structure and properties of the monomer itself.

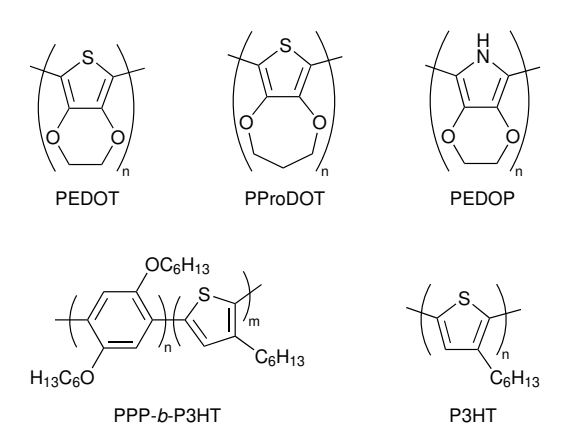


Fig. 38 Examples of polymeric hole conductors.

Kim and co-workers introduced a polymer based on a propylenedioxythiophene monomer, ProDOT (Fig. 38). 452 PProDOT is similar in structure to PEDOT, but it contains a propylene chain rather than an ethylene one. They employed a solid-state polymerization method in which a dibrominated ProDOT monomer was the starting material. This method is sluggish, but also very inexpensive. A solution of monomers was sprayed onto the photoanode. The solid monomer was put in an oven that was heated at 25 °C and allowed for polymerization to occur with the evaporation of Br2 as a side product. Via coupling with a Pt-coated FTO counter electrode,  $V_{\rm OC}$  of 630 mV,  $J_{\rm SC}$  of 10.0 mA cm<sup>-2</sup>, FF of 56% and PCE of 3.5% were achieved in the complete device. Zhang et al. demonstrated the efficiency of PEDOP (poly(ethylenedioxypyrrole)) combined with three separate dyes in suppressing electron recombination, essentially demonstrating the importance of the dye in the system. <sup>453</sup> The ssDSCs with D35 dye reached a PCE of 4.34%. The other organic dye, D21L6, was slightly less performing with a PCE of 3.05%. Later, Zhang et al. also showed that the dye DPP07 is as efficient in combination with PEDOT as LEG4, when they fabricated a device a with a  $V_{\rm OC}$  of 770 mV,  $J_{SC}$  of 11.13 mA cm<sup>-2</sup>, FF of 65% and PCE of 5.54%. <sup>454</sup>

Wang et al. studied the properties of a pre-polymerized block copolymer of poly(3-hexylthiophene) and poly(2,5-dihexyloxyp-phenylene) 455 and a PPP-b-P3HT-based solar cell achieved a  $V_{\rm OC}$  of 810 mV,  $J_{\rm SC}$  of 8.81 mA cm<sup>-2</sup>, FF of 65% and PCE of 4.65%; while those employing poly(3-hexylthiophene) (P3HT) could only display a  $V_{\rm OC}$  of 750 mV,  $J_{\rm SC}$  of 7.71 mA cm $^{-2}$ , FF of 61% and PCE of 3.53%.

Liu et al. probed the performance of P3HT with two different dyes.  $^{456}$  Solar cells reached a  $V_{\rm OC}$  of 880 mV,  $J_{\rm SC}$  of 8.22 mA cm<sup>-2</sup>, FF of 44% and PCE of 3.21% when sensitized with BzTCA, showing that organic dyes are better-suited to work with polymeric HTMs. The best P3HT-based ssDSCs were fabricated by Clément and co-workers. 457 They overcame the typical pore filling issues of P3HT by synthesizing a highly regioregular polymer with medium-range molecular weight and narrow dispersity. When P3HT with such characteristics was employed in a system with a 2 µm thick TiO2 sheet, performance increased. After HTM deposition and an annealing step at 150 °C to improve film morphology, devices displayed a  $V_{\rm OC}$  of 720 mV,  $J_{\rm SC}$  of  $11.37 \text{ mA cm}^{-2}$ , FF of 58% and PCE of 4.78%. For comparison, a device fabricated with spiro-OMeTAD reached a PCE of 3.99%.

4.3.2.3 Inorganic hole transporting materials. Organic HTMs are less stable in water and oxygen than inorganic materials. Generally, inorganic HTMs possess good electronic properties, good conductivity and high temperature stability. 458-460 Although these inorganic HTMs already provide good stability in photovoltaic devices, their promise of efficiency remains unfulfilled. Table 7 lists device parameters of DSCs employing various inorganic HTMs referenced in this review, together with the dye used.

Chung et al. used the tin-based perovskite compound CsSnI<sub>3</sub> in a N719-sensitized ssDSC. 22 With tin fluoride doped into semiconductors, the solar cell developed  $V_{\rm OC}$  of 732 mV,  $J_{\rm SC}$  of  $19.2 \text{ mA cm}^{-2}$ , FFs of 72%, and a PCE of 10.2%. Due to the volatility of Sn(II)-based perovskites, the Cs<sub>2</sub>SnI<sub>6</sub> compound was implemented as hole transport material in solar cells, enabling them to harvest holes from different photoanodes with different dyes. 461 The ssDSC sensitized with Z907 yielded a PCE of 4.63%, while that sensitized with N719 yielded a PCE of 6.32%. The best results were achieved with a combination of dyes, N719, YD2-o-c8 and RLC5. Such a system had a  $V_{\rm OC}$  of 623 mV,  $J_{\rm SC}$ of 16.9 mA  $\rm cm^{-2}$ , FF of 66% and PCE of 6.94%. The output with these dyes was further improved after engineering the solar cell with ZnO photonic crystals, achieving a  $V_{\rm OC}$  of 618 mV,  $J_{\rm SC}$  of  $18.6 \text{ mA cm}^{-2}$ , FF of 68% and PCE of 7.80%. A Z907-sensitized cell was found to be stable for 800 hours.

Sakamoto et al. worked on copper iodide, a well-known HTM in the solar cell field. In their analysis, the researchers discovered how the interface materials affect the formation of CuI layers. The degree of thiocyanate groups in both the dye and counter electrode was crucial for obtaining high efficiency. The variance of the SCN groups in the PEDOT:PSS-based counter electrode resulted in the systems having a greater than 2-fold performance compared to those without SCN groups. The successful DSCs showed a  $V_{\rm OC}$  of 739 mV,  $J_{\rm SC}$  of 14.5 mA cm<sup>-2</sup>, FF of 69% and PCE of 7.4%.462

Table 6 Photovoltaic characteristics of DSCs implementing organic (small molecular and polymeric) hole transporting materials

HTM	Sensitizer	V <sub>OC</sub> (mV)	$J_{\rm SC}~({ m mA~cm^{-2}})$	FF (%)	PCE (%)	Year	Ref.
Spiro-OMeTAD	Y123	986	9.5	76	7.2	2011	433
Spiro-OMeTAD	D102	710	8.06	53	3.03	2018	434
Spiro-OMeTAD	MKA253	780	12.4	63	6.1	2015	435
Spiro-OMeTAD	Z907	750	7.28	64	3.5	2013	436
Spiro-OMeTAD	ID504	760	9.76	64	4.8	2015	437
Spiro-OMeTAD	LEG4	900	10.10	70	6.36	2016	438
3a	D102	860	0.32	44	0.12	2014	444
3b	D102	680	6.32	41	1.75	2014	444
X19	LEG4	750	9.62	62	4.5	2014	445
X51	LEG4	920	9.27	70	6.0	2014	445
TCz-C3	D102	690	6.27	51	2.21	2018	434
TCz-C6	D102	590	0.86	38	0.20	2018	434
TCz-C12	D102	660	0.21	34	0.05	2018	434
H-DATPA	D102	620	0.67	37	0.15	2013	446
Me-DATPA	D102	700	1.13	43	0.34	2013	446
MeO-DATPA	D102	890	1.93	67	1.16	2013	446
MeO-TPD	LEG4	800	9.5	65	4.9	2013	447
HTM	Z907	750	8.5	51	3.3	2014	448
X1	MKA253	680	5.8	58	2.3	2015	435
X1	LEG4	880	9.44	69	5.8	2017	450
X11	MKA253	580	4.7	62	1.7	2015	435
X11	LEG4	655	8.2	55	3.0	2015	435
X2	LEG4	810	9.79	63	5.0	2015	449
X35	LEG4	890	9.81	63	5.5	2015	449
Х3	LEG4	900	9.70	66	5.8	2013	436
Х3	Z907	720	8.10	63	3.7	2013	436
X14	LEG4	910	9.71	71	6.1	2017	450
HTM1	ID504	820	9.34	63	4.8	2015	437
HTM2	ID504	800	7.08	38	2.2	2015	437
HTM3	ID504	800	7.00	38	2.1	2015	437
X60	LEG4	890	11.38	72	7.30	2016	451
PProDOT	N719	630	10.0	56	3.5	2012	452
PEDOP	D35	825	7.99	66	4.34	2014	453
PEDOP	D21L6	645	7.92	59	3.05	2014	453
PEDOP	Z907	440	1.97	53	0.46	2014	453
PEDOT	DPP07	770	11.13	65	5.54	2016	454
PPP-b-P3HT	CYC-B11	810	8.81	65.2	4.65	2014	455
P3HT	CYC-B11	750	7.71	61.1	3.53	2014	455
P3HT	N3	628	6.29	43	1.70	2014	456
P3HT	BzTCA	880	8.22	44	3.21	2014	456
P3HT	D102	720	11.37	0.58	4.78	2017	457

Out of the several p-type semiconductors examined for use as hole conductors, the chemical robustness of CuSCN is of particular interest owing to it being a polymeric semiconductor. The solar cells fabricated by Premalal et al. with this HTM included doped p-type copper sulphide nanoparticles and were coated onto a transparent conducting oxide base. 463 They doped CuSCN with triethylamine hydrothiocyanate to further improve the p-type conductivity of the inorganic material and the resulting ssDSC reached a  $V_{OC}$  of 578 mV,  $J_{SC}$  of 10.52 mA cm<sup>-2</sup>, FF of 55% and PCE of 3.4%.

#### 4.3.2.4 Metal coordination complex hole transporting mate-

rials. Transition metal coordination complexes are a category of materials that incorporates the advantages and disadvantages of both organic and inorganic compounds. As organic compounds they retain an ease-of-processing, but with the high conductivities typical of inorganic compounds, which eliminate the need of p-dopants. The p-dopant is found in the compound itself, and it consists of a complex of the same metal with a higher oxidation state. Energy levels can be varied by modifying the ligand or metal center. 464-467 Metal complexes have already contributed greatly to the advancement of liquid DSC as they are a far more efficient electrolyte than iodide/triiodide and are far less corrosive than the latter. Only few transition metal coordination complexes have been implemented as redox mediators in liquid junction DSCs. 277,289,291 Coordination complexes in solid-state dyesensitized solar cells have only recently begun to be studied, however, and there are only a few examples of their use as of present. Despite this, the best-performing ssDSCs are those employing a metal complex as the hole conductor (see Table 7).

Freitag et al. were the first researchers to publish a work on solid-state dye-sensitized solar cells based on a metal complex hole conductor. They used a mix of Cu(I) and Cu(II) coordinated with a phenanthroline-based ligand ([Cu(dmp)<sub>2</sub>]). 467 The device fabrication method was similar to that of liquid devices, but instead of sealing the cell after electrolyte injection the solvent was allowed to evaporate in air and then a new injection was performed until the space between the photoanode and the counter electrode was filled with solid HTM. Their best solar cell achieved a  $V_{\rm OC}$  of 1010 mV,  $J_{\rm SC}$  of 13.8 mA cm<sup>-2</sup>, FF of 59% and PCE of 8.2%, making it more efficient than the spiro-OMeTAD-based reference device (5.6%) and even more efficient than a liquid DSC based on the same electrolyte (6.0%).

Kashif et al. published a similar device based on a Co(III/II) metal center and a polypyridyl hexadentate ligand ([Co(bpyPY<sub>4</sub>)](OTf)<sub>2.33</sub>).<sup>369</sup> As inferred by the counter ion nomenclature, the Co(II) to Co(III) ratio was 2:1. The device fabrication method was similar to that of Freitag et al. but in this case the HTM solvent was removed under vacuum rather than by natural evaporation in air. Kashif's best device exhibited a  $V_{\rm OC}$  of 768 mV,  $J_{\rm SC}$  of 12.12 mA cm $^{-2}$ , FF of 62% and PCE of 5.68%. In this same work, Kashif tried to fabricate ssDSCs with the [Co(bpy)<sub>3</sub>] metal complex, which is known to yield high efficiency in liquid DSCs. <sup>368</sup> However, in the solid state charge transport issues due to poor conductivity severely limited the output current, yielding a device with a PCE of 0.21%. This demonstrated that not all metal complexes, not even those with a common metal centre, can be employed as hole conductors in ssDSCs.

Building on the work on Cu complexes by Freitag, Grätzel and co-workers have further improved the performance of ssD-SCs.  $^{274,468}$  In their first work the authors coupled [Cu(tmby)<sub>2</sub>] with the Y123 dye to achieve a  $V_{\rm OC}$  of 1080 mV,  $J_{\rm SC}$  of  $13.87 \text{ mA cm}^{-2}$ , FF of 73% and PCE of 11.0%. In their more recent study, they created a new dye intended to improve the performance of solar cells by properly matching components and reducing electrons that recombine. Indeed, in liquid DSCs a voltage enhancement of 70 mV and a relative performance difference of 11% were observed while switching from Y123 to the WS-72 dye. An experiment was performed to fabricate a [Cu(tmby)<sub>2</sub>] and WS-72 centered solid-state system with a  $V_{\rm OC}$  of 1070 mV,  $J_{SC}$  of 13.8 mA cm<sup>-2</sup>, FF of 79% and PCE of 11.7%. Most recently, Michaels et al. developed a novel co-sensitization technique, with organic dyes XY1 and L1 sensitized solar cells based on the Cu(II/I) hole transfer materials [Cu(tmby)<sub>2</sub>] for ambient light conversion with unparalleled conversion efficiency (34% at 1000 lx, 33% at 500 lx and 32% at 200 lx from a fluorescent lamp).33

### 4.3.3 Dopants and additives.

Adding suitable chemical species to the electrolyte to finetune the semiconductor-electrolyte interface is the simplest way to increase photovoltaic performance. For the desired Fermi level upshift, nitrogen heterocyclic compounds such as 4-tertbutylpyridine (tBP) and N-methylbenzimidazole (NMBI) are typically used to inhibit electron recombination and thus to improve the V<sub>OC</sub>. 469,470 Consequently, as a regular additive, tBP is present in almost every electrolyte solution for liquid-junction DSCs. With iodine- and cobalt complexes-based electrolytes tBP addition does not greatly affect ionic diffusion in solution, while in case of other coordination complex redox mediators it can have a negative effect. Saygili and co-workers introduced new bases -2,6-bis-tert-butylpyridine (BtBP), 4-methoxypyridine (MOP) and 4-(5-nonyl)pyridine (NOP) - to copper-based redox mediator  $[Cu(tmby)_2]^{2+/+}$ , with significant effects on electrolyte properties.  $^{471}$  Guanidinium thiocyanate (GuNCS) has been found to increase both  $V_{\rm OC}$  and  $J_{\rm SC}$ , as it accumulates its positive charge on the semiconductor surface, causing a positive conduction band edge shift, thus improving the efficiency of electron injection and at the same time slowing down recombination under open-circuit conditions.

Similar to liquid electrolytes, additives in solid-state electrolytes and hole transport materials are compounds dissolved in the precursor solution to be deposited on the device after dye sensitization. For example, additives like LiTFSI and 4-tertbutylpyridine (or other similarly substituted pyridines) are known to migrate to the TiO<sub>2</sub> surface to shift energy levels and passivate exposed surface, in order to enable better charge injection and to reduce charge recombination at the TiO<sub>2</sub>/HTM interface. 472-478 In the solid state they may have the added effect of changing the HTM film morphology. Additionally, certain dopants can directly influence the material. Studies demonstrate that the partial oxidation of the hole conducting substrate facilitates increased

Table 7 Photovoltaic characteristics of DSCs implementing inorganic and metal complexes-based hole transporting materials

HTM	Sensitizer	V <sub>OC</sub> (mV)	$J_{\rm SC}~({ m mA~cm^{-2}})$	FF (%)	PCE (%)	Year	Ref.
CsSnI <sub>3</sub>	N719	732	19.2	72.7	10.2	2012	22
$Cs_2SnI_6$	Z907	571	13.2	61.3	4.63	2014	461
$Cs_2SnI_6$	N719	631	14.7	68.1	6.32	2014	461
$Cs_2SnI_6$	mix	623	16.9	66.1	6.94	2014	461
$Cs_2SnI_6$	mix + PC	618	18.6	68.0	7.80	2014	461
CuI	N3	739	14.5	69	7.40	2012	462
CuSCN	N719	578	10.52	55.6	3.39	2012	463
$Cu(dmp)_2$	LEG4	1010	13.8	59	8.2	2015	467
Co(bpyPY4)	Y123	768	12.12	62	5.68	2016	369
Co(bpy) <sub>3</sub>	Y123	877	0.66	73	0.21	2016	369
Cu(tmby) <sub>2</sub>	Y123	1090	13.65	78	11.6	2018	277
Cu(tmby) <sub>2</sub>	Y123/XY1b	1050	15.74	79	13.1	2018	277
Cu(tmby) <sub>2</sub>	WS-72	1070	13.8	79	11.7	2018	274
Cu(tmby) <sub>2</sub>	XY1:L1	1020	14.5	72	10.7	2020	33

hole mobility across the layer and, finally, conductivity. Oxidizing dopants are necessary for organic compounds and small molecules in particular (see Table 8 for differences in efficiency of DSCs with pristine and doped HTMs), and as an example they must be applied to the spiro-OMeTAD molecule to make it the ideal reference material for ssDSCs.  $^{451,479,480}$  Cappel et al. studied the p-doping properties of LiTFSI in the presence of light and air or  $\rm N_2$  atmosphere and Snaith and co-workers continued the work providing a complete description of the doping properties of LiTFSI.  $^{440,481}$ 

The combined results of these studies showed that LiTFSI enabled molecular oxygen to oxidize spiro-OMeTAD regardless of light exposure, while LiTFSI alone was not able to oxidize the hole conductor. The redox reaction in air consumes Li<sup>+</sup> ions due to the formation of lithium oxides, but Li<sup>+</sup> also plays a significant role as additive on the titania surface in DSCs. For this reason, the authors recommended the use of a different p-dopant.

A Co(III) complex (FK102) has been used as oxidizing dopant in solar cells, which allowed them to attain relatively high efficiencies (Fig. 39).  $^{433}$  The Co(III)-based metal complex was soluble in the HTM precursor solution, making deposition simpler. The complex was able to oxidize spiro-OMeTAD and the resulting Co(II) species had a low molar extinction coefficient. The film's conductivity rose from 4.4  $\times$  10 $^{-5}$  to 5.3  $\times$  10 $^{-4}$  S cm $^{-1}$ , which boosted the overall performance from 2.3 to 5.6%. Two years later Burschka et al. proposed two new Co complexes with better performance, FK209 and FK269.  $^{482}$ 

Chen et al. combined spiro-OMeTAD with the Lewis acid 2,3,5,6-tetrafluoro-7,7,8,8-tetracyanoquinodimethane (F4TCNQ), a strong electron acceptor. 483 When they added 1.1 wt.% dopant to the HTM solution a UV-Vis measurement confirmed the formation of the spiro-OMeTAD+ species. They applied pristine and doped hole transporter solutions (without LiTFSI) to ssDSCs obtaining a 3300% increase in efficiency from 0.01 to 0.33%. However, the presence of LiTFSI was required to achieve high efficiency and the two solutions with the added Li salt led to device efficiencies of 4.55 and 5.44%, without and with dopant respectively, confirming the beneficial effect of F4TCNQ doping. Han and colleagues also worked on a Lewis

Fig. 39 Examples of dopants for hole transporting materials.

acid, SnCl<sub>4</sub> leading to a 4-fold improvement in conductivity. When 0.8%-doped spiro-OMeTAD was used in a solar cell, a 3.4% efficiency was obtained. <sup>484</sup> McGehee and co-workers eliminated the p-dopant from the HTM solution by pre-oxidizing the hole conductor itself. They reacted spiro-OMeTAD with two equivalents of AgTFSI to obtain Spiro(TFSI)<sub>2</sub> and metallic silver. Devices fabricated with tBP showed a significant improvement in efficiency from 0 to 4.67%. <sup>439</sup>

Xu et al. reported on 1,1,2,2-tetrachloroethane (TeCA), which they described as a co-solvent, not a proper p-dopant. The reason for this is that it is important to keep the TeCA-containing solution under UV light for one minute to allow the spiro-OMeTAD oxidation to take place. System efficiencies increased from 5.8% to 7.7%; for comparison, devices fabricated with FK209 yielded only 6.8% performance. 485 TEMPO, already mentioned as a redox mediator, has been used as a dopant as well. Yang et al.

Table 8 Photovoltaic efficiencies of DSCs with pristine and doped hole transporting materials

Dopant	Pristine efficiency (%)	Doped efficiency (%)	Year	Ref.
T'mpor . O		•	0010	110
LiTFSI + $O_2$	0	3	2013	440
FK102	2.3	5.6	2011	433
FK209	2.3	6.0	2013	482
FK269	2.3	6.0	2013	482
F4TCQN	4.55	5.44	2012	483
SnCl <sub>4</sub>	2.52	3.40	2013	484
Spiro(TFSI) <sub>2</sub>	2.34	4.89	2014	439
TeCA	5.8	7.7	2015	485
TEMPO-Br	3.99	6.83	2018	486
DDQ	3.50	6.37	2018	487

have used the bromide salt of the oxidized TEMPO to improve the efficiency of their cells from 3.99 to 6.83%. 486 The most recent work on p-dopants in ssDSCs was reported by Sun and co-workers, who researched the effects on spiro-OMeTAD of 2,3dichloro-5,6-dicyano-1,4-benzoquinone (DDQ), another oxidant commonly used in organic synthesis. Conductivity of the oxidized HTM film improved from  $5.31 \times 10^{-5}$  to  $2.22 \times 10^{-4}$  S cm<sup>-1</sup>, and device efficiency was boosted from 3.50 to 6.37% with a rather insignificant amount of the dopant. 487

#### 4.4 Counter electrodes

The counter electrode (CE) has a major impact on the overall efficiency of DSCs and it performs two main functions: it receives electrons from the external circuit and transmits them into the cell - which necessitates a low resistance - and it acts as a catalyst for the reduction of the oxidized species of the redox mediator. A good CE for DSCs should have the following qualities: high catalytic activity towards the redox mediator, high conductivity, high reflectance, low cost, high surface area, high porosity, low charge-transfer resistance, high exchange current density, chemical resistance to corrosion, energy alignment meeting the potential of the electrolyte's redox couple and good processability for deposition. 488,489 In DSCs there is a great variety of CE preparation recipes, including thermal and photo-decomposition, <sup>490–493</sup> electrochemical deposition, 494–496 chemical vapor deposition, 497 and sputter deposition. 498-500 The preparation methods greatly affect particle size, surface, morphology, and catalytic and electrochemical characteristics of the electrodes. Smaller particles and larger electrode surface areas provide more catalytic active sites and facilitate improved electrode operation. 501

Platinum has traditionally been the most common counter electrode active material for DSCs, due to its excellent conductivity and catalytic activity, with PCEs of over 12%. 289 Nevertheless, Pt still has certain drawbacks to solve, including the high price and rarity of the raw material, poor stability over longer periods, migration towards the photoanode and deposition on the TiO<sub>2</sub> layer leading to cell shortage. 502-506 Furthermore, due to energy level misalignment, Pt is not very effective in regenerating alternative redox couples such as coordination complexes, T2/T- or polysulfide electrolytes. 332 Fortunately, many other materials can be used as CE in DSCs.

Carbon compounds (Fig. 40) 507 are appealing candidates to replace Pt as CE material in DSCs, due to benefits such as low cost, high surface area, high catalytic activity, high electrical conductivity, high thermal stability, good iodine corrosion resistance and high reactivity for triiodide reduction. 357 A FTO/Au/GNP (graphene nanoplatelets) stack was used as CE to reach a PCE of 14.3%. <sup>25,508</sup> The inexpensive and easy preparation, and good stability improve the competitiveness of carbon materials. The key downsides of CEs based on carbon compounds are an overall worse performance compared to platinized electrodes – in terms of conductivity and catalytic activity - when coupled with the I<sup>-</sup>/I<sub>3</sub><sup>-</sup> redox couple and poor adhesion to the FTO substrate, which leads to electrode degradation. 509

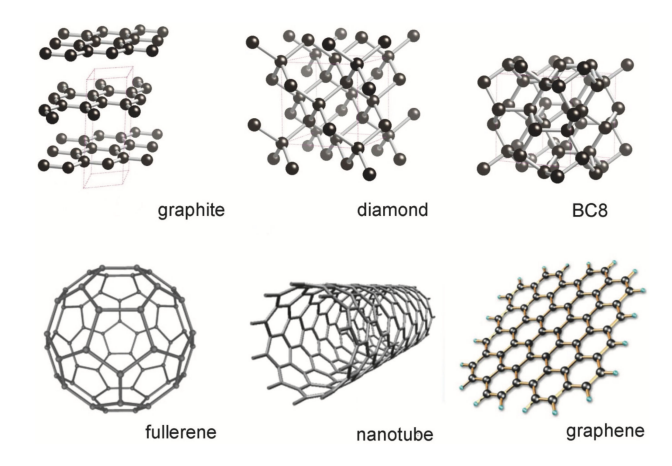


Fig. 40 Structures of various carbon allotropes. Reprinted with permission from ref. 507. Copyright 2013 Mineralogical Society of America.

Flexibility, translucency, and facile processing and tuning are all properties of conductive polymers that make them prime candidates as CE materials in DSCs (Fig. 41). 171,510 PEDOT (poly(3,4ethyleneedioxythiophene)), first discovered by the Bayer Lab in the 1980s, is a promising substrate for antistatic and optoelectronic applications due to its high conductivity, outstanding visible light transmittance and extraordinary stability. 494 Although PEDOT is an insoluble polymer, it can be easily electrodeposited from its monomer in solution, resulting in excellent conductivity, much higher than that of polyaniline (PAni), polypyrrole (PPy) and polythiophene (PT). 510-512 Moreover, the solution to PEDOT's insolubility problem was later solved by copolymerization with poly(styrene sulfonate) (PSS). PEDOT:PSS is the market pioneer in transparent conductive polymers, it is water-soluble and allows fast manufacturing. Saito et al. investigated for the first time in 2002 PEDOT-based materials specifically PEDOT:PSS and p-toluenesulfonate (TsO)-doped PE-DOT – as CE for DSCs, deposited on FTO via chemical polymerization. 513 The PCE of the cell with the PEDOT:TsO CE was almost the same as that with the Pt CE, while in the case of the PE-DOT:PSS electrode it was shown that I<sup>-</sup>/I<sub>3</sub><sup>-</sup> oxidation/reduction processes occurred at higher potentials compared to the other two electrodes, which was attributed to a steric hindrance effect of the PSS component of the polymer. <sup>513</sup> By using electrodeposition techniques PEDOT is now being deployed in the most efficient DSCs, especially due to its high performance in combination with alternative redox mediators and hole transport materials. Tsao et al. showed how electropolymerized PEDOT CEs are much better performing with Co-based redox mediators compared to their Pt counterparts. 514 Their best PEDOT-based cell reached a PCE of 10.3%, compared to 7.9% of a Pt-based one. The performance improvement was attributed to a much lower charge transfer resistance of PEDOT towards the Co complex compared to Pt. Freitag et al. achieved a PCE of 11.3% with a copper-mediated DSCs featuring a PEDOT CE, 341 recently surpassed by Grätzel et al. with a 13.5% PCE cell. 13 One more advantage of PEDOT over Pt is that the former is a hole-selecting material. As such, it is possible to fabricate PEDOT-based sandwich-type solar cells without any spacing between the two electrodes without the risk of cell shortage. 277,341

Fig. 41 Repeating units of polymers used as counter electrode materials in DSCs.

DSCs incorporating hybrid/mixed CEs outperform devices with single component CEs, thanks to the synergistic effects of the hybrid composite. However, the exact mechanism behind this success is still not fully understood on a fundamental level. Examples of efficient hybrid CEs include platinized PEDOT and a combination of graphene with PEDOT, PAni or Pt. 492,496,502,515,516

#### P-type DSCs 5

### 5.1 Photocathodes

During the last 20 years increasing attention has been paid to the development of more efficient p-type DSCs with the goal of combining both photocathodes and the more widely studied ntype TiO2-based photoanodes in tandem DSCs. 517,518 Such tandem architectures offer an opportunity to collect more light more efficiently by overcoming the thermodynamic limits of singlejunction devices. In principle, tandem DSC devices (p-n DSCs) could surpass the Shockley-Queisser limit (theoretically 43%) 519 by increasing the spectral response of the device without sacrificing photovoltage. 520,521 P-type devices operate in a similar fashion to n-DSCs; however, as the majority charge carriers in the mesoporous NiO layer are positive holes (h<sup>+</sup>), the electron flow occurs in the reverse direction. Electron transfer occurs from the valence band of the semiconductor to the photoexcited dye. A schematic representation of a NiO-based p-DSC is provided in Fig. 42 and the individual components are discussed in more detail in Section 5.5.

The first p-DSC was reported in 1999 by Lindquist and coworkers. 522 The cell was made using the same components as for an n-DSC (Fig. 42), but the TiO<sub>2</sub> semiconductor was replaced with a layer of NiO; a p-type semiconductor. An overall PCE of 0.0076% was obtained using erythrosin B as a sensitizer. By 2010,

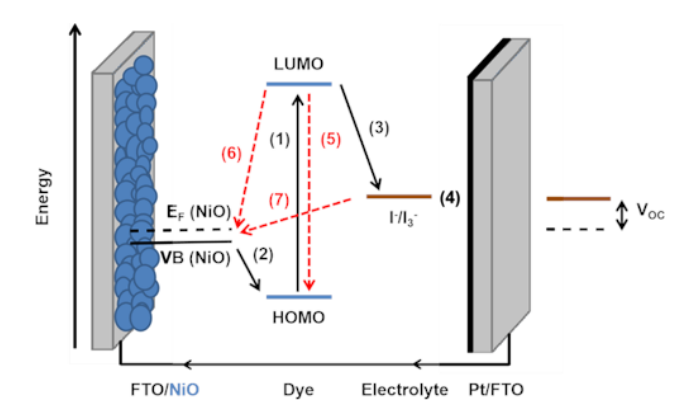


Fig. 42 Schematic representation of the charge transfer processes occurring within a NiO-based p-DSC. Recombination processes shown in red. Processes 1-6 defined in the text. Adapted from ref. 517 with permission from The Royal Society of Chemistry.

this had been improved to 0.41% efficiency by improving the quality of the NiO and engineering a dye specifically for NiO. 523 However, since the p-DSC efficiency was well below that of n-type devices, the tandem cell efficiency was severely limited (1.91%). The development of sensitizers which permit a long-lived charge separated state at the dye/semiconductor interface is imperative to reduce parasitic charge recombination. Furthermore, their coupling with new electron mediators can dramatically improve device efficiencies. Further research into the mechanism, electron transfer dynamics and surface characterisation has enabled further improvements to be made over the following decade, which are summarised in the following sections. By the end of 2020 the highest tandem cell efficiency had reached 4.1%. 521

#### 5.2 Semiconductors

NiO is the most widely researched p-type semiconductor, with a valence band edge of 0.3 V vs. SCE at pH 7 and a bandgap of 3.6-4.0 eV. 524 There have been extensive articles and reviews on the various synthetic techniques and the challenges of applying NiO in p-DSCs. 525-530 A comparison by Gibson et al. of different mesoporous NiO electrodes concluded that a crystallite size of at least 20 nm, a film thickness of 1-2 µm and a specific surface area above 40 m<sup>2</sup> g<sup>-1</sup> is most appropriate for photoelectrochemical devices using NiO. 531 The most commonly used synthetic technique is the sol-gel method, due to its simplicity and reproducibility, and pluronic triblock copolymer-templated NiO films satisfy these criteria, giving thicknesses of 1-2 µm and crystal sizes of 15-20 nm. 532 Typically, these films are applied in the laboratory by the doctor blade technique, but Jousselme et al. attained promising results ( $J_{SC} = 3.42 \text{ mA cm}^{-2}$ ) by inkjet printing a sol-gel precursor. 533

Despite being straightforward to synthesize and deposit, there are several unfavourable characteristics of NiO. Firstly, whereas  $TiO_2$  is non-toxic, NiO is a group 1 carcinogen. The  $V_{OC}$  of NiObased DSCs is limited to 100-200 mV because NiO has a highlying valence band (0.54 V vs. NHE), which is advantageous in terms of electron transfer to photosensitizers, but leads to a small difference between the Fermi level in the NiO and the redox potential of the electrolyte. NiO also has a low charge diffusion coefficient (  $\sim\!10^{-8}~\text{cm}^2~\text{s}^{-1})^{532,534,535}$  and the presence of high valence states (e.g. Ni<sup>III</sup> and Ni<sup>IV</sup>) leads to rapid recombination at the dye/semiconductor and semiconductor/electrolyte interfaces. 536,537 This leads to a small diffusion length for holes (2-3 µm), which means thin NiO films must be used. 537 Strategies applied over the last 10 years to reduce recombination include applying compact blocking layers on the FTO substrate, <sup>538</sup> chemical reduction of the NiO surface, 539 surface treatment with an aqueous nickel salt, 540 applying a thin, surface layer of Al<sub>2</sub>O<sub>3</sub>, B or TiO<sub>2</sub>, <sup>541–543</sup> or adding organic surfactants such as chenodeoxycholic acid. 544 Other approaches to improving the electronic properties (either by increasing the hole mobility or lowering the Fermi level) include doping or forming solid solutions with alkali or transition metals such as Li, Co, Mg. 545-548 However, a competition between increasing  $V_{OC}$  and decreasing  $J_{SC}$  is frequently observed, possibly as a result of decreasing the driving force for electron injection if the valence band edge is shifted to more positive potential. The porosity, dye loading and hole transport can be improved by adding graphene or reduced graphene oxide to NiO.549,550 However, despite these modest improvements, the small built-in potential and poor fill factors (typically 30-40%) limit the solar cell efficiency to <1%.

To match the built-in potential of TiO2 devices, the valence band of the p-type semiconductor needs to be about 0.5 V more positive than that of NiO. This means completely replacing NiO with an alternative material, but this is difficult due to the tradeoff between conductivity and transparency. Binary or ternary oxides and oxysulfides have been tested in p-type DSCs, but in each case, if the  $V_{\rm OC}$  was improved, the current was sacrificed. The potential reasons for this could be physical (insufficient surface area for the dye to adsorb or insufficient porosity for the electrolyte to diffuse), electronic (low dielectric constant or hole mobility) or surface properties such as the presence of high-valence Ni.

K-doped ZnO thin films, which have high optical transparency (>85%) and smaller hole diffusion coefficient ( $10^{-6}$  cm<sup>2</sup> s<sup>-1</sup>) than NiO, show some promise for p-DSCs ( $J_{SC} = 0.408 \text{ mA cm}^{-2}$ ,  $V_{\rm OC} = 82$  mV, and PCE = 0.0012% with C343). 551 More encouraging results have been achieved with tin-doped indium oxide (ITO) reaching PCEs of ca. 2%. 552,553 Promising results have been obtained with CuO-based DSCs by applying nanoparticles, nanorods or nanowires. 554 One dimensional materials could overcome the shorter transport time for CuO compared to NiO. CuO electrodes are unstable towards I<sup>-</sup>/I<sub>3</sub><sup>-</sup> so alternative redox mediators such as cobalt coordination complexes are required. 555 An efficiency of 0.19% was reached in combination with zinc phthalocyanine sensitizers and cobalt-based redox mediators. 556,557 However, CuO is not optically transparent ( $E_g = 1.4 \text{ eV}^{555}$ ). Cu<sub>2</sub>O is more transparent but less stable than CuO. An open-circuit voltage of 0.71 V, a short-circuit current density of  $1.3 \text{ mA cm}^{-2}$ , a fill factor of 46%, and a PCE of 0.42% has been attained with the commercial C343 dye. 558 Cu<sub>2</sub>O@CuO core-shell structures have been applied to improve the stability, but this has not yet improved the solar cell characteristics ( $V_{OC} = 315 \text{ mV}, J_{SC} = 0.14 \text{ mA cm}^{-2}, PCE = 0.017\%$ ). <sup>559</sup> Cu-based delafossites (CuAlO<sub>2</sub>, CuGaO<sub>2</sub>, CuFeO<sub>2</sub>, CuBO<sub>2</sub>, AgCrO<sub>2</sub> and CuCrO<sub>2</sub>) have been highlighted as potential p-type TCOs. 560,561 During the last 10 years, attempts have been made to exploit the deeper lying valence band and high hole mobility of these materials compared to NiO in p-DSCs. 555,562-566 Efficiencies of 0.04% have been recorded with CuAlO2, but with delafossites, as with doped NiO, a trade-off between  $J_{SC}$  (<1 mA cm<sup>-2</sup>) and  $V_{\rm OC}$  (333 mV) has been found. 555,562,567 Better efficiencies of up to 0.18% have been obtained with CuGaO2 in combination with P1 and  $I^-/I_3^-$ . 568,569 Doping with Mg, Fe and Al improves the specific surface area of CuGaO2 photocathodes and conversion efficiencies comparable with NiO have been reached with Mg:CuGaO<sub>2</sub>. 563,570,571 The best results so far have been with CuCrO2, which reached 0.4% PCE with PMI-6T-TPA and the  $[Co(en)_3]^{2+/3+}$  electrolyte, but although the  $V_{OC}$  (734 mV) was better than the equivalent NiO device, the  $J_{SC}$  (1.23 mA cm<sup>-2</sup>) was much lower. Successful attempts to improve the current include adding plasmonic Au nanoparicles, <sup>572</sup> and doping with Mg, Ga and Co, but solar cell efficiencies with delafossites are yet to surpass NiO. 573-575

Other proposed alternatives to NiO include mixed chalcogens. LaCuOS has been applied in p-DSCs with PMI-NDI dye but a low PCE (0.002%) was recorded, which the authors attribute to similar valence band edge energies of NiO and LaCuOS, rapid charge recombination and weak binding affinity for the dye on the surface. 576 More encouraging results have been reported with spinel cobaltites (MCo<sub>2</sub>O<sub>4</sub>; M = Ni, Zn). NiCo<sub>2</sub>O<sub>4</sub> nanowire-woven nanosheet arrays with N719 dye produced a PCE = 0.785%  $(V_{OC} = 189 \text{ mV}, J_{SC} = 8.35 \text{ mA cm}^{-2}, \text{ FF} = 50\%), \text{ which is}$ exceptionally high compared to most p-DSCs fabricated using the standard I<sup>-</sup>/I<sub>3</sub><sup>-</sup> electrolyte. <sup>577,578</sup> Table 9 lists the electrochemical properties of the referenced p-type semiconductors, together with the best cell efficiency obtained with them.

#### 5.3 Sensitizers

In p-DSCs, the HOMO of the dye must be more positive than the valence band edge of the semiconductor and the LUMO of the dye needs to be more negative than the redox potential of the electrolyte. 591-595 Because the film thickness is limited by the diffusion length in NiO devices (see above), high extinction coefficients are required to capture all the incident light. If the photocathode is to be positioned on the bottom of the cell, the dye needs to absorb red-NIR photons. In the first 10 years of p-type DSC development commercial dyes were applied but the first breakthroughs came from developing bespoke "push-pull" systems specifically designed for photocathodes. <sup>523,535,596</sup> D-π-A systems where the electron density is pushed away from the NiO surface on excitation of the dye improve the charge-separated state lifetime and quantum efficiency. Over the last 10 years, a substantial number of different dye-systems have been developed and tested in p-DSCs, typically with NiO. 517,579,597-599 Metal complexes such as N719 and N3 generally give poor results in p-DSCs. 525 There are a few examples of Ru-based dyes giving promising results with NiO, where there is some charge-transfer character directed away from the semiconductor surface (e.g. an anchoring group is positioned on the electron donating part of the

Table 9 Properties and characteristics of p-type metal oxides

Semiconductor	bandgap (eV)	Valence band energy (eV vs. vacuum)	Dielectric constant	Max cell efficiency (%)  – Electrolyte used	Refs.
NiO	4.7 – 4	-4.944.7	9.7	2.51 – Fe(acac) <sub>3</sub>	526, 542, 544, 579, 103
K:ZnO	3.23	-5.7	not reported	$0.012 - I^-/I_3^-$	551
Sn:In <sub>2</sub> O <sub>5</sub> (ITO)	4.1	-4.8	not reported	$1.96 - Fe(acac)_3$	580, 553
CuO	1.41 - 1.82	-4.955.09	18.1	$0.11 - I^-/I_3^-$	554, 581, 555
Cu <sub>2</sub> O	2.4	-5.20	12	$0.42 - I^{-}/I_{3}^{-}$	582, 583, 584, 558
CuAlO <sub>2</sub>	3.5	-5.68	10	$0.037 - I^-/I_3^-$	560, 561, 585, 562
CuCrO <sub>2</sub>	3.11	-5.44	not reported	$0.17 - T^{-}/T_{2}$	572, 575
Au@SiO <sub>2</sub> :CuCrO <sub>2</sub>	3.11	not reported	not reported	$0.31 - T^{-}/T_{2}$	572
Mg:CuCrO <sub>2</sub>	not reported	not reported	not reported	$0.132 - I^-/I_3^-$	573
Ga:CuCrO <sub>2</sub>	3.25 - 3.30	-5.39	not reported	$0.100 - I^{-}/I_{3}^{-}$	575
AgCrO <sub>2</sub>	3.32	not reported	not reported	$0.0145 - I^{-}/I_{3}^{-}$	565
CuGaO <sub>2</sub>	3.6 - 3.8	-5.29	0.96	$0.182 - I^{-}/I_{3}^{-}$	568, 586, 569
CuFeO <sub>2</sub>	2.03 - 3.35	-4.95.13	not reported	$0.0103 - I^-/I_3^-$	587, 567
LaOCuS	3.1	-4.94	4	$0.002 - Co(dtb-bpy)_3$	588, 589, 576
NiCo <sub>2</sub> O <sub>4</sub>	2.06 - 3.63	-5.00	not reported	$0.785 - I^{-}/I_{3}^{-}$	590, 577

molecule), see Table 10.  $^{600-605}$  Ir complexes (Fig. 43) have also been applied in p-DSCs due to their long lived and strongly oxidizing triplet excited states which favour hole injection into the semiconductor valence band.  $^{606-609}$  The  $J_{\rm SC}$  of iridium photosensitizers is generally low due to the narrow absorption spectrum.

Better results have been reported with metal-free systems (see Table 11). One of the first metal-free push-pull dyes to achieve a significant JSC was the triphenylamine-based dye P1 and its design has heavily influenced the development of many subsequent dyes for p-DSCs. 534,610 Optimised devices with P1 and  $I^-/I_3^-$  give IPCE = ca. 63%, and PCE of 0.15%, and P1 has become a benchmark dye for optimising new materials in p-DSCs. 523,535,611 In the last decade since these breakthroughs, numerous arylamine-containing molecules have been designed for p-DSCs (Fig. 44), mostly with different acceptor or linker groups, 612-618 and a few reports of modified anchoring structure. 595,619 Dyes with two acceptor groups per triarylamine unit tend to have a higher absorption coefficient and produce a higher  $J_{SC}$ . The highest  $J_{SC}$  reported for a p-DSC was produced using CAD3 with two cationic indolium groups as electron acceptors ( $J_{SC} = 8.21 \text{ mA cm}^{-2}$ ,  $\lambda_{max} = 614 \text{ nm}$ ,  $\varepsilon = 95\,000\,\mathrm{M}^{-1}\,\mathrm{cm}^{-1}).^{612,620}$ 

The  $\pi$ -linker (e.g. oligothiophenes, fluorenes) length can also be optimized to maximize the absorption coefficient, the breadth of the spectral response, the energy offset at the interfaces with the semiconductor and electrolyte, the dye loading, the charge-transfer efficiency and recombination rate.  $^{621-625}$  PMI-nT-TPA series with oligothiophene bridges of different lengths greatly increased device performances (PCE = 0.09%, 0.19% and 0.41% for n = 1, 2 and 3 respectively) by further extending the charge separated state lifetime (Fig. 45).  $^{523}$  Other examples include PMI-4T-TPA ( $J_{SC}$  = 3.40 mA cm $^{-2}$ ),  $^{624}$  PMI-6T-NDI ( $J_{SC}$  = 6.26 mA cm $^{-2}$ ),  $^{522}$  BH4 ( $J_{SC}$  = 7.40 mA cm $^{-2}$ ),  $^{624}$  PMI-6T-NDI ( $J_{SC}$  = 6.26 mA cm $^{-2}$ ),  $^{22}$  cm $^{2}$  = 4.36 mA cm $^{-2}$ ),  $^{22}$  = 7.57 mA cm $^{-2}$ ).  $^{614}$  Fairly small structural changes to the dye seem to have a big impact, for example

O2  $(J_{\rm SC}=1.43~{\rm mA~cm^{-2}},~V_{\rm OC}=94~{\rm mV},~{\rm FF}=37\%,~{\rm PCE}=0.05\%)^{626}$  compared to a thienoquinoidal dye  $(J_{\rm SC}=8.20~{\rm mA~cm^{-2}},V_{\rm OC}=120~{\rm mV},~{\rm FF}=34\%,~{\rm PCE}=0.33\%)$  when tested with the I $^-/{\rm I_3}^-$  electrolyte and when used with a Co(II/III)-based electrolyte  $(J_{\rm SC}=6.5~{\rm mA~cm^{-2}},V_{\rm OC}=226~{\rm mV},~{\rm FF}=34\%,~{\rm PCE}=0.50\%).^{613}$  The EH series of p-type sensitizers with a D–A– $\pi$ –A framework were prepared containing triphenylamine (TPA) as a donor, an electron deficient 2,3-diphenylquinoxaline as the auxiliary acceptor, various thiophene derivatives as the  $\pi$ -linkers, methylene malonitrile as the electron acceptor, and carboxylic acid as the anchoring group.  $^{627}$  The p-DSC sensitized by EH174 with a bithiophene  $\pi$ -linker and with one anchoring group performed best (PCE = 0.207%,  $J_{\rm SC}=4.84~{\rm mA~cm^{-2}},V_{\rm OC}=137~{\rm mV},~{\rm FF}=31.2\%)$  and EH162 with an EDOT  $\pi$ -linker and double anchoring groups performed worst in the series.

The importance of the push-pull structure and the influence of the thiophene  $\pi$ -spacer have been demonstrated with bodipy dyes (Fig. 46). These are relatively straightforward to synthesize and simple modifications to the structure can be made to tune the absorption and emission wavelengths across the visible spectrum. 628 The performance of bodipy dyes anchored through benzoic acid at the meso position is quite low, but push-pull bodipy dyes with a triphenylamine donor linked through a thiophene spacer to the bodipy chromophore perform much better (e.g. bodipy-6 PCE = ca. 0.3% and  $J_{SC} = 3.15 \text{ mA cm}^{-2}$ ). <sup>629</sup> The electronic coupling between the donor and the chromophore is important and bodipy dyes with methyl pyrrole groups give a lower photocurrent compared to the pyrrole analogues (IPCE bodipy-4 = 27%, bodipy-7 = 53%,  $J_{SC}$  = 5.87 mA cm<sup>-2</sup>), which is attributed to better electronic communication with the NiO substrate.  $^{630}$  Kubo et al. reported a NIR absorbing  $\pi$ -extended dibenzo-bodipy dye applied in p-type DSCs with a  $I^-/I_3^-$  electrolyte. 631 Despite the push-pull structure – arising from the triphenylamine donor units and nitrothiophene acceptor - and the broad spectral response (up to 850 nm) the performance was still limited by rapid recombination at the dye/NiO interface

Table 10 Photovoltaic characteristics of p-type DSCs implementing metal coordination complexes-based sensitizers. IPCE values with the approximation sign are a visual estimate taken from the plotted data

Sensitizer	Electrolyte	V <sub>OC</sub> (mV)	$J_{\rm SC}~({ m mA~cm^{-2}})$	FF (%)	PCE (%)	IPCE max (%)	Year	Ref.
K1	I <sub>2</sub> , LiI	96	2.91	32	0.09	14	2014	600
K2	I <sub>2</sub> , LiI	93	1.96	39	0.07	9	2014	600
O3	I <sub>2</sub> , LiI	93	3.04	35	0.099	${\sim}20$	2013	601
O13	I <sub>2</sub> , LiI	89	2.66	31	0.074	$\sim 19$	2013	601
017	I <sub>2</sub> , LiI	92	2.69	34	0.085	$\sim 16$	2013	601
08	I <sub>2</sub> , LiI	63	0.44	36	0.009	2.02	2012	602
011	I <sub>2</sub> , LiI	79	1.16	36	0.033	5.49	2012	602
O12	I <sub>2</sub> , LiI	82	1.84	34	0.051	9.08	2012	602
O18	I <sub>2</sub> , LiI	93	3.43	33	0.10	not reported	2014	605
SL1	I <sub>2</sub> , DMBII	104	2.25	34	0.079	18	2016	603
SL2	I <sub>2</sub> , DMBII	77	1.5	33	0.038	10	2016	603
$[Ru(bpy)_2(H1)]$	I <sub>2</sub> , LiI	95	4.06	36	0.14	not reported	2017	604
IrPhen	$Co(dtb-bpy)_3$	345	0.14	44	0.021	$\sim$ 4	2014	606
IrDPQCN2	$Co(dtb-bpy)_3$	508	0.25	54	0.068	$\sim$ 6.2	2014	606
IrBpystyryl	$Co(dtb-bpy)_3$	383	0.37	44	0.061	$\sim 10.5$	2014	606
1	I <sub>2</sub> , LiI	58	0.076	27	0.0012	2	2017	607
AS16	I <sub>2</sub> , LiI	94	0.69	42	0.028	17	2017	607
2	I <sub>2</sub> , LiI	134	0.069	40	0.0037	3	2017	607
AS17	I <sub>2</sub> , LiI	89	0.14	42	0.0052	5	2017	607
3	I <sub>2</sub> , LiI	77	0.16	45	0.0056	6	2017	607
AS18	I <sub>2</sub> , LiI	79	0.15	46	0.0055	6	2017	607
AS19	I <sub>2</sub> , LiI	104	0.45	42	0.02	${\sim}28$	2016	608
AS9	I <sub>2</sub> , LiI	90	0.68	36.6	0.022	$\sim 15$	2017	609
AS10	I <sub>2</sub> , LiI	90	0.66	37.6	0.022	$\sim$ 21.5	2017	609
AS11	I <sub>2</sub> , LiI	70	0.45	38.1	0.013	~11	2017	609
AS12	I <sub>2</sub> , LiI	90	0.36	40.1	0.013	${\sim}13$	2017	609
AS13	I <sub>2</sub> , LiI	100	0.82	38.7	0.032	${\sim}26$	2017	609
AS14	I <sub>2</sub> , LiI	100	1.12	36.8	0.043	${\sim}21.5$	2017	609

 $(V_{OC} = 79 \text{ mV}, J_{SC} = 0.61 \text{ mA cm}^{-2}, \text{ FF} = 25\%, \text{ PCE} = 0.012\%).$ 

Generally, having two anchoring groups per triphenylamine unit is less favourable than having two acceptors because the extinction coefficient tends to be higher with two acceptors and the dye loading may be more compact. 627 There have been some exceptions, such as the zzx-op series of fluorene-bridged biphenylamine-perylenemonoimide dyes, where the fluorene bridge was directly appended to biphenylamine to ensure good donor/acceptor coupling. W2 with an electron-withdrawing, 1,3benzothiadiazole bridge and an octyl 2-cyanoacrylate acceptor also performed well ( $J_{SC}=4.16~{\rm mA~cm^{-2}},~V_{OC}=121~{\rm mV},$  FF = 33%, PCE = 0.166%). <sup>632</sup> In certain cases, such as dye 3 vs. dye 5633 and p-SQ1 vs p-SQ2,634 a double anchoring group can improve the solar cell performance through enhancing the binding strength between the dye and the semiconductor, thereby facilitating more efficient charge transfer, or by suppressing the dark current. 633,634

Typically, carboxylic acid anchoring groups are used; however, until recently, there has been little research into whether or not this is the best choice. 635 Alternative anchoring groups have been proposed, including pyridine, 542,595,619,636,637 di(carboxylic acid)pyrrole, 638,639 hydroxamic acid, 640 di(carboxylic acid)triazole, 607 catechol, 591 carbodithioic acid, 591 methyl phosphonic acid, 591 acetylacetone (acac), 637,641 alkoxysilane, 186 coumarin, 642 aniline, 637 phosphonic acid, 637 hydroxyqinoline, 637 and dipicolinic acid. 637 Phosphonic acid is one of the strongest binding groups and is resistant to both acid and base, but can present some synthetic challenges. 637,642 Odobel et al. and Gibson et al. compared the charge-transfer dynamics at the dye/NiO interface for a number of anchoring groups and found that the anchoring group did not significantly influence the rates. 637,642 This finding is consistent with the work of Housecroft et al. who compared the benchmark dye P1 with the phosphonic acid derivative PP1. 643 The solar cell performance of both dyes was similar, PP1: PCE = 0.054-0.069%, IPCE = 10% at  $\lambda_{max} = \sim 500$  nm; P1: PCE = 0.065–0.079%, IPCE = 13.5% at  $\lambda_{max}$  = 500 nm.

Recombination at the dye/semiconductor surface appears to be a limiting factor to achieving high quantum efficiencies, unlike the analogous  ${\rm TiO_2}$  devices.  ${}^{644,645}$  Perylene-based donoracceptor dyads with varying acceptor units (such as either perylene itself coupled to a triarylamine donor, or NDI or C60 appended to a perylene) led to one of the most important breakthroughs in terms of extending the lifetime of the chargeseparated state long enough to enable alternative redox mediators to be used (see below).  $^{596}$  The  $J_{\rm SC}$  for PMI-6T-TPA and P1 were similar when  $I^-/I_3^-$  was used as the electrolyte ( $J_{SC} = 5.35$ vs. 5.48mA cm<sup>-2</sup>), the  $V_{\rm OC}$  was larger (218 vs. 84 mV), possibly due to reduced charge recombination at the electrolyte/electrode interface. 535

Fig. 43 Examples of metal complex-based sensitizers for p-type DSCs.

Fig. 44 Examples of triphenylamine-based sensitizers for p-type DSCs.

Fig. 45 Examples of PMI- and NDI-based sensitizers for p-type DSCs.

Fig. 46 Examples of different sensitizers for p-type DSCs.

 $\textbf{Table 11} \ \ \textbf{Photovoltaic characteristics of p-type DSCs implementing organic sensitizers}$ 

Sensitizer	Electrolyte	V <sub>OC</sub> (mV)	$J_{\rm SC}~({ m mA~cm^{-2}})$	FF (%)	PCE (%)	IPCE max (%)	Year	Ref.
1	I <sub>2</sub> , MBII	153	2.06	29	0.09	${\sim}10$	2010	523
2	I <sub>2</sub> , MBII	176	3.40	32	0.19	${\sim}20$	2010	523
3	I <sub>2</sub> , MBII	218	5.35	35	0.41	$\sim$ 50	2010	523
P1	I <sub>2</sub> , LiI	89	5.37	33	0.16	54	2015	612
P1	Co(dtb-bpy) <sub>3</sub>	280	1.18	30	0.10	${\sim}20$	2016	625
C343	I <sub>2</sub> , LiI	208	0.951	32.4	0.064	7.1	2019	646
C343	Co(dtb-bpy) <sub>3</sub>	190	0.25	32	0.015	${\sim}2$	2009	596
PI	Co(dtb-bpy) <sub>3</sub>	80	0.26	26	0.006	${\sim}3$	2009	596
PINDI	Co(dtb-bpy) <sub>3</sub>	350	1.66	34	0.20	31	2009	596
Eosin B	I <sub>2</sub> , LiI	77	0.14	29	0.0032	not reported	2008	525
Erythrosin J	I <sub>2</sub> , LiI	122	0.36	26	0.011	not reported	2008	525
Rhodamine 101	I <sub>2</sub> , LiI	69	0.12	21	0.0022	not reported	2008	525
Rhodamine 110	I <sub>2</sub> , LiI	80	0.15	25	0.0031	not reported	2008	525
P4	I <sub>2</sub> , LiI	100	2.48	36	0.09	44	2009	610
P2	I <sub>2</sub> , LiI	63	3.37	31	0.07	32	2010	611
P3	I <sub>2</sub> , LiI	55	1.36	34	0.03	6	2010	611
P7	I <sub>2</sub> , LiI I <sub>2</sub> , LiI	80	3.37	35	0.09	26	2010	611
CAD3	I <sub>2</sub> , LiI I <sub>2</sub> , LiI	101	8.21	31	0.09	50	2015	612
GS1				31	0.23	53		
	I <sub>2</sub> , LiI	106	5.87				2015	612
QT-1	I <sub>2</sub> , LiI, DMII	120	8.2	34	0.33	60	2015	613
QT-1	Co(pz-py) <sub>3</sub>	226	6.5	34	0.50	not reported	2015	613
zzx-op1	I <sub>2</sub> , LiI	96	5.70	38	0.21	50.1	2014	614
zzx-op1-2	I <sub>2</sub> , LiI	117	7.57	40	0.35	70.2	2014	614
zzx-op1-3	I <sub>2</sub> , LiI	115	6.68	40	0.31	${\sim}57$	2014	614
zzx-op2	I <sub>2</sub> , LiI	111	4.00	36	0.16	${\sim}27$	2014	615
zzx-op3	I <sub>2</sub> , LiI	109	3.80	36	0.15	${\sim}20$	2014	615
C1	I <sub>2</sub> , LiI	40	1.63	27	0.016	${\sim}24$	2017	616
C2	I <sub>2</sub> , LiI	59	2.41	29	0.040	${\sim}22$	2017	616
C3	I <sub>2</sub> , LiI	17	1.00	17	0.001	$\sim \! 36$	2017	616
SK2	I <sub>2</sub> , LiI	81	0.51	33	0.014	${\sim}14$	2016	617
SK3	I <sub>2</sub> , LiI	82	0.54	33	0.015	$\sim 11.5$	2016	617
SK4	I <sub>2</sub> , LiI	134	0.43	32	0.018	$\sim$ 5.6	2016	617
RBG-174	I <sub>2</sub> , LiI	90	2.88	36.7	0.096	not reported	2018	618
COCO	I <sub>2</sub> , LiI	91	2.45	35.9	0.080	not reported	2018	618
BBTX	I <sub>2</sub> , LiI	88	4.32	33.0	0.126	not reported	2018	618
COCN	I <sub>2</sub> , LiI	77	1.53	32.3	0.038	not reported	2018	618
CW1	I <sub>2</sub> , LiI	93	3.54	35	0.114	~36	2014	595
CW2	I <sub>2</sub> , LiI	118	4.05	34	0.160	${\sim}42$	2014	595
1	I <sub>2</sub> , LiI	50	0.83	43	0.018	~25	2019	619
2	I <sub>2</sub> , LiI	103	1.6	36	0.060	$\sim$ 25	2019	619
3	I <sub>2</sub> , LiI	49	0.87	32	0.014	~22.5	2019	619
4	I <sub>2</sub> , LiI	66	0.83	33	0.014	~25	2019	619
5	I <sub>2</sub> , LiI I <sub>2</sub> , LiI	86	1.11	37	0.016	$\sim$ 25	2019	619
6	=	70						
	I <sub>2</sub> , LiI		0.84	23	0.014	$\sim$ 21.3	2019	619
CAD2	I <sub>2</sub> , LiI	87	3.32	33	0.09	25	2014	620
CAD2	I <sub>2</sub> , LiI	96	3.25	33	0.10	17	2014	620
T3	I <sub>2</sub> , LiI	121	5.01	30.3	0.184	~30	2015	621
T4	I <sub>2</sub> , LiI	119	5.31	32.9	0.208	$\sim$ 32	2015	621
T5	I <sub>2</sub> , LiI	124	4.51	33.3	0.186	${\sim}27$	2015	621
Т6	I <sub>2</sub> , LiI	133	4.02	33.3	0.178	$\sim$ 23	2015	621
T3H	I <sub>2</sub> , LiI	133	5.56	30.5	0.226	${\sim}32$	2016	622
T4H	I <sub>2</sub> , LiI	152	6.74	31.0	0.317	${\sim}38$	2016	622

T1	I <sub>2</sub> , LiI	125	2.82	31	0.11	$\sim$ 37	2014	623
T3	I <sub>2</sub> , LiI	144	4.01	33	0.19	$\sim$ 45	2014	623
T4	I <sub>2</sub> , LiI	123	1.69	29	0.06	$\sim \! 26$	2014	623
$BH_2$	I <sub>2</sub> , DMII	97	4.3	31	0.13	not reported	2014	624
BH4	I <sub>2</sub> , DMII	128	7.4	30	0.28	not reported	2014	624
ВН6	I <sub>2</sub> , DMII	95	4.4	31	0.13	not reported	2014	624
E1	Co(dtb-bpy) <sub>3</sub>	320	0.93	44	0.13	$\sim 13$	2016	625
E2	Co(dtb-bpy) <sub>3</sub>	320	0.78	41	0.10	$\sim 9$	2016	625
O2	I <sub>2</sub> , LiI	94	1.43	37	0.050	12.3	2011	626
06	I <sub>2</sub> , LiI	97	1.04	37	0.037	13.5	2011	626
07	I <sub>2</sub> , LiI	90	1.74	38	0.060	17.9	2011	626
QT-1	I <sub>2</sub> , LiI, DMII	120	8.2	34	0.33	60	2015	613
QT-1	Co(pz-py) <sub>3</sub>	226	6.5	34	0.50	not reported	2015	613
EH122	I <sub>2</sub> , LiI, DMPII	134	4.39	30.3	0.178	~28	2019	627
EH126	I <sub>2</sub> , LiI, DMPII	122	3.93	30.4	0.146	$\sim$ 25.5	2019	627
EH166	I <sub>2</sub> , LiI, DMPII	131	3.47	28.4	0.129	$\sim$ 20.5	2019	627
EH162	I <sub>2</sub> , LiI, DMPII	115	1.79	30.4	0.062	~16	2019	627
EH174	I <sub>2</sub> , LiI, DMPII	137	4.84	31.2	0.207	$\sim$ 28.5	2019	627
EH170	I <sub>2</sub> , Lii, DMPII	139	3.47	31.5	0.152	~20	2019	627
BOD1		70	0.56	31.3	0.132		2019	628
BOD1 BOD2	I <sub>2</sub> , LiI	70 40		36 29	0.015	not reported	2020	628
	I <sub>2</sub> , LiI		0.48			not reported		
BOD3	I <sub>2</sub> , LiI	60	0.21	29	0.003	not reported	2020	628
1	I <sub>2</sub> , LiI	79 05	3.15	31	0.08	28	2014	629
Bodipy-CO <sub>2</sub> H	I <sub>2</sub> , LiI	95 97	1.48	36	0.05	20	2015	630
4	I <sub>2</sub> , LiI	97	1.60	38	0.06	27	2015	630
5	I <sub>2</sub> , LiI	109	3.70	35	0.14	44	2015	630
6	I <sub>2</sub> , LiI	95	1.58	35	0.05	23	2015	630
7	I <sub>2</sub> , LiI	106	5.87	31	0.20	53	2015	630
1	I <sub>2</sub> , LiI, BMII	79	0.61	25	0.012	3.2	2019	631
W1	I <sub>2</sub> , LiI	131	2.83	34.0	0.126	$\sim 14$	2015	632
W2	I <sub>2</sub> , LiI	121	4.16	33.0	0.166	${\sim}17$	2015	632
W3	I <sub>2</sub> , LiI	134	2.32	33.1	0.103	~9	2015	632
1	I <sub>2</sub> , LiI	105	1.59	35.9	0.060	$\sim 17$	2011	633
2	I <sub>2</sub> , LiI	115	1.39	36.3	0.058	${\sim}15$	2011	633
3	I <sub>2</sub> , LiI	113	1.38	34.0	0.053	$\sim 14$	2011	633
4	I <sub>2</sub> , LiI	125	2.25	33.1	0.093	$\sim$ 27.5	2011	633
5	I <sub>2</sub> , LiI	122	2.18	34.6	0.092	$\sim \! 17$	2011	633
6	I <sub>2</sub> , LiI	131	2.05	32.4	0.087	${\sim}24$	2011	633
S	I <sub>2</sub> , LiI	132	2.31	33.1	0.101	${\sim}22.5$	2011	633
p-SQ1	I <sub>2</sub> , LiI	117	1.22	37.1	0.053	$\sim$ 6	2012	634
p-SQ2	I <sub>2</sub> , LiI	140	1.92	42.0	0.113	$\sim 19$	2012	634
BQI	I <sub>2</sub> , BMII	140	3.00	33	0.140	$\sim$ 37	2017	542
BQII	I <sub>2</sub> , BMII	137	2.17	34	0.102	${\sim}25$	2017	542
I	I <sub>2</sub> , LiI	124	2.36	37	0.11	${\sim}20$	2013	636
II	<sub>-2</sub> , I <sub>2</sub> , LiI	130	2.97	35	0.14	~29	2013	636
PMI-CO <sub>2</sub> H	$T^-/T_2$	161	1.52	25.4	0.062	$\sim$ 20	2020	637
PMI-HQ	$T^-/T_2$	164	2.21	23.8	0.086	~21.5	2020	637
PMI-DPA	$T^{-}/T_{2}$	168	1.33	24.6	0.055	~26	2020	637
PMI-acac	$T^{-}/T_{2}$	169	2.08	27.9	0.033	$\sim$ 20 $\sim$ 32	2020	637
PMI-PO <sub>3</sub> H <sub>2</sub>	$T^{-}/T_{2}$	181	2.08 1.27	27.9 17.7	0.098	${\sim}32$ ${\sim}20$	2020	637
CAD4								
	I <sub>2</sub> , LiI	84	3.96	31.6	0.105	not reported	2017	638
1	I <sub>2</sub> , LiI	41 52	0.31	31	0.004	10	2017	639
2	I <sub>2</sub> , LiI	53	0.53	30	0.009	5	2017	639
3	I <sub>2</sub> , LiI	61	1.17	32	0.023	11	2017	639
YK-1	I <sub>2</sub> , BMII	102	2.33	27.9	0.064	~13	2018	640

YK-2	I <sub>2</sub> , BMII	93	1.95	29.5	0.054	~11	2018	640
JW44	I <sub>2</sub> , LiI	75	1.29	31	0.030	${\sim}21$	2014	641
1	I <sub>2</sub> , LiI	57	0.28	35	0.006	5.4	2019	642
2	I <sub>2</sub> , LiI	74	0.45	35	0.012	8.2	2019	642
3	I <sub>2</sub> , LiI	76	0.51	37	0.014	9.8	2019	642
$ZnP_{ref}$	I <sub>2</sub> , LiI	98	0.19	35	0.006	not reported	2019	642
PP1	I <sub>2</sub> , LiI	132	1.45	36	0.069	10	2018	643
SQ	I <sub>2</sub> , LiI	85	1.18	34	0.034	${\sim}24$	2014	647
SQ	Co(dtb-bpy) <sub>3</sub>	85	0.12	30	0.0041	${\sim}2$	2014	647
PMI-NDI	I <sub>2</sub> , LiI	135	0.69	35	0.033	${\sim}15$	2014	647
PMI-NDI	Co(dtb-bpy) <sub>3</sub>	315	1.06	31	0.10	$\sim \! 17$	2014	647
SQ-PMI	I <sub>2</sub> , LiI	65	1.31	31	0.0026	${\sim}24$	2014	647
SQ-PMI	Co(dtb-bpy) <sub>3</sub>	95	0.34	28	0.009	$\sim$ 4	2014	647
SQ-PMI-NDI	I <sub>2</sub> , LiI	95	2.73	32	0.083	${\sim}25$	2014	647
SQ-PMI-NDI	Co(dtb-bpy) <sub>3</sub>	175	1.17	27	0.055	${\sim}22$	2014	647
1	I <sub>2</sub> , LiI	100	1.89	33	0.063	$\sim\!\!26$	2016	648
1	$Co(dtb-bpy)_3$	198	0.49	24	0.024	$\sim$ 11	2016	648
2	I <sub>2</sub> , LiI	84	1.44	33	0.040	$\sim$ 23	2016	648
2	Co(dtb-bpy) <sub>3</sub>	134	0.41	24	0.040	~7	2016	648
DPP-Br	I <sub>2</sub> , LiI	70	0.41	33	0.013	~21	2016	648
DPP-Br	Co(dtb-bpy) <sub>3</sub>	103	0.26	28	0.020	~5	2016	648
3	I <sub>2</sub> , LiI	90	2.03	33	0.062	~35	2016	648
3	Co(dtb-bpy) <sub>3</sub>	330	2.06	30	0.205	~26	2016	648
4	Со(цтр-рру) <sub>3</sub> I <sub>2</sub> , LiI	76	1.72	32	0.203	$^{\sim20}$	2016	648
4	Co(dtb-bpy) <sub>3</sub>	370	1.72	32 29	0.041	$^{\sim 24}$ $^{\sim 25}$	2016	648
				34				
DPP-NDI	I <sub>2</sub> , LiI	81	1.79		0.048	~30	2016	648
DPP-NDI	Co(dtb-bpy) <sub>3</sub>	292	1.56	29	0.13	${\sim}28$	2016	648
ISO-Br	I <sub>2</sub> , LiI	87	0.82	34	0.025	~5	2015	649
ISO-Br	Co(dtb-bpy) <sub>3</sub>	182	0.80	23	0.033	$\sim$ 8	2015	649
ISO-NDI	I <sub>2</sub> , LiI	96	1.27	33	0.040	~7	2015	649
ISO-NDI	Co(dtb-bpy) <sub>3</sub>	260	1.54	25	0.100	~13	2015	649
ZnP <sub>ref</sub>	I <sub>2</sub> , LiI, DMBII	98	0.19	35	0.006	not reported	2016	650
ZnP-NDI	I <sub>2</sub> , LiI, DMBII	127	1.38	32	0.056	not reported	2016	650
ZnP-TPA-NO <sub>2</sub>	I <sub>2</sub> , LiI, DMBII	107	0.29	38	0.012	not reported	2016	650
TCPP	I <sub>2</sub> , LiI	128	0.8	39	0.04	not reported	2014	651
ZnTCPP	I <sub>2</sub> , LiI	158	1.5	38	0.09	${\sim}33$	2014	651
ZnP-CO <sub>2</sub> H-NO <sub>2</sub>	I <sub>2</sub> , LiI, DMBII	113	0.49	36	0.020	$\sim \! 16$	2015	652
ZnP-eCO <sub>2</sub> H-NO <sub>2</sub>	I <sub>2</sub> , LiI, DMBII	114	0.48	35	0.019	$\sim 16$	2015	652
$ZnP-CO_2H-eNO_2$	I <sub>2</sub> , LiI, DMBII	98	0.43	32	0.013	${\sim}14$	2015	652
ZnP-eCO <sub>2</sub> H-eNO <sub>2</sub>	I <sub>2</sub> , LiI, DMBII	115	0.55	34	0.022	${\sim}10$	2015	652
ZnP-CO <sub>2</sub> H-eNDI	I <sub>2</sub> , LiI, DMBII	127	1.38	32	0.056	${\sim}20$	2015	652
ZnP-CO <sub>2</sub> H-eNDI	$Co(dtb-bpy)_3$	195	0.5	31	0.03	not reported	2015	652
ZnP-CO <sub>2</sub> H-BV <sup>2+</sup>	I <sub>2</sub> , LiI, DMBII	125	0.44	33	0.018	$\sim 11.5$	2015	652
3	I <sub>2</sub> , LiI	134	0.956	28.9	0.037	24.3	2019	646
3(Ni)	I <sub>2</sub> , LiI	206	1.199	33.2	0.082	26.0	2019	646
4	I <sub>2</sub> , LiI	195	1.353	33.0	0.087	23.0	2019	646
C <sub>60</sub> trZnPCOOH	I <sub>2</sub> , LiI	109	1.86	37	0.076	not reported	2018	653
C <sub>60</sub> trZnPCOOH	Co(dtb-bpy) <sub>3</sub>	244	0.63	35	0.054	not reported	2018	653
C <sub>60</sub> trZnPtrCOOH	I <sub>2</sub> , LiI	84	1.82	33	0.050	not reported	2018	653
C <sub>60</sub> trZnPtrCOOH	Co(dtb-bpy) <sub>3</sub>	269	0.76	36	0.074	not reported	2018	653
C <sub>60</sub> ZnPCOOH	I <sub>2</sub> , LiI	103	1.68	37	0.063	not reported	2018	653
C <sub>60</sub> ZnPCOOH	Co(dtb-bpy) <sub>3</sub>	175	0.71	28	0.035	not reported	2018	653
Ph <i>tr</i> ZnPCOOH	I <sub>2</sub> , LiI	68	0.69	33	0.015	not reported	2018	653
Ph <i>tr</i> ZnPCOOH	$Co(dtb-bpy)_3$	48	0.22	24	0.002	not reported	2018	653
PMI-6T-TPA	Fe(acac) <sub>3</sub>	568	6.4	52	1.90	~60	2018	654

ZnP0	Fe(acac) <sub>3</sub>	327	1.9	48	0.26	not reported	2018	654
ZnP1	Fe(acac) <sub>3</sub>	465	4.4	45	0.92	$\sim$ 43	2018	654
VG1-C8	Iodolyte Z-150	87	0.577	37.2	0.018	$\sim$ 7	2016	655
VG10-C8	Iodolyte Z-150	102	0.435	40.9	0.018	$\sim$ 7	2016	655
VG11-C8	Iodolyte Z-150	93	1.160	36.1	0.043	${\sim}10$	2016	655
Erythrosine B	Iodolyte Z-150	88	1.019	36.0	0.032	$\sim$ 5.5	2016	655
BAI-COOH	I <sub>2</sub> , LiI	79	1.13	33	0.029	7.8	2018	656
CB5	EL-HSE	115	1.516	34.1	0.059	$\sim 16$	2018	657
CB6	EL-HSE	117	1.135	31.4	0.044	$\sim$ 7	2018	657
CB7	EL-HSE	117	2.001	32.6	0.076	$\sim 13$	2018	657
CB8	EL-HSE	117	1.717	32.9	0.066	$\sim 11$	2018	657

Subsequently, there have been a number of reported dye series showing the benefits of the auxiliary acceptor on reducing charge recombination and, consequently, improving the device performance. These include Warnan et al.'s iodo-squaraines (SQ), the PMI-appended dyad (SQ-PMI), and the NDI-appended triad (SQ-PMI-NDI). 647 The PCE of the systems steadily increased in the order of:  $SQ < SQ-PMI < PMI-NDI \ll SQ-PMI-NDI$ . (SQ-PMI-NDI with  $I^{-}/I_{3}^{-}$ :  $J_{SC} = 2.73 \text{ mA cm}^{-2}$ ,  $V_{OC} = 95 \text{ mV}$ , FF = 32%, PCE = 0.083%; with Co(II/III):  $J_{SC} = 1.17 \text{ mA cm}^{-2}$ ,  $V_{\rm OC} = 175$  mV, FF = 27%, PCE = 0.055%). Odobel et al.'s diketopyrrolopyrrole (DPP) and isoindigo series demonstrate the necessity for an appended NDI acceptor group to deliver good solar cell performance.  $^{648,649}$  NiO/Th-DPP-NDI produced a  $J_{SC}$  of 8.2 mA cm<sup>-2</sup>, which is comparable to the record dyes CAD3 and

Porphyrin dyes have been applied in state-of-the-art ntype DSCs, providing record efficiencies. However, rapid electron-hole recombination has limited their application in p-type DSCs. 650,651,658 Odobel et al. attempted to improve their performance by covalently attaching methyl viologen and NDI acceptors at the meso position (ZnP-NDI dye), but these systems were limited by inefficient regeneration by I<sup>-</sup>/I<sub>3</sub><sup>-</sup>. 652 Chernick et al. developed a series of free base and nickel asymmetric push-pull porphyrins with alternating meso subsitutuents, electron-withdrawing pentafluorobenzene, electron-donating/coordinating 4-pyridyl ligand, and an electron withdrawing/synthetically modifiable 4-cyanophenyl unit. 646 The porphyrins performed similarly to C343 (IPCE = 26%, PCE = 0.082% for the nickel porphyrin). Coordinating an electron acceptor such as C<sub>60</sub>PPy through the metal centre of zinc porphyrins improves the p-DSC performance. <sup>642,651</sup> Better p-DSC results were reported by Coutsolelos et al. who applied three covalently linked donor-acceptor zinc porphyrin-fullerene (ZnP-C<sub>60</sub>) dyads (C60trZnPCOOH, C60trZnPtrCOOH and C60ZnPCOOH) with a triazole ring spacer between the porphyrin and C<sub>60</sub> or anchoring group. 653 Long-lived charge-separated states were observed in all three cases, due to the shift in electron density from the chromophore to the acceptor. The lifetime was enhanced by the presence of the triazole spacer for the dyads in solution, but it made only a moderate impact on the rate of charge separation and recombination when the dyads were adsorbed on NiO. However, the triazole ring did improve the photovoltaic performance. The presence of the C60 acceptor improved the solar cell performance compared to the C<sub>60</sub>-free reference compound PhtrZnPCOOH. The best performing dyad in  $I^-/I_3^-$  was  $C_{60}trZnPCOOH$  (PCE = 0.076%); in Co(III/II), the best performing dyad was C<sub>60</sub>trZnPtrCOOH (PCE = 0.074%). The best performance for a porphyrin photosensitizer in a NiO device so far was reported by Spiccia et al. 654 ZnP1 contained a perylenemonoimide (PMI) electron acceptor linked through a fluorene and a Zn(II) porphyrin with alkyl chains as a  $\pi$ conjugated bridge to a di(p-carboxyphenyl)amine (DCPA) electron donor. The configuration led to a red-shifted absorption onset to the near-IR region (~800 nm) compared to the PMI-free reference dye ZnP0 (~650 nm) and the benchmark PMI-6T-TPA (~700 nm). With the tris(acetylacetonato)iron(III/II) redox mediator, ZnP1 (PCE = 0.92%) out-performed the ZnP0 sensitiser (PCE of 0.29%) but despite the broader spectral response, it did not perform better that the benchmark PMI-6T-TPA dye (2.0% PCE), possibly due to aggregation on the NiO surface.

To complement the state-of-the-art dyes for n-DSCs, red-NIR absorbing dyes have been developed. This is important for tandem devices, where the aim is to increase the spectral response and the  $V_{\rm OC}$ . A well-known class of red-NIR absorbing dyes are squaraines such as the VG and p-SQ series. 634,655 Indigo is a naturally occurring red-absorbing dye, but its poor solubility makes it challenging to apply in solar cells. A bay-annulated indigo (BAI) was applied in p-DSCs producing a promising photocurrent  $(J_{SC} = 1.14 \text{ mA cm}^{-2})$ , but the performance was limited by aggregation and charge recombination. 656 Using a strong electron acceptor to lower the LUMO level in triphenylamine-based pushpull dyes also shifts the absorption towards the red. 612 Example are COCO and COCN, 618 the pyran-based dyes CB7 and CB8, 657 and the CAD series. 618,620

### 5.4 Electrolytes

The I-/I3- liquid electrolyte is most frequently chosen for ptype DSCs for compatibility with n-type DSCs. 612 The composition can be optimized for the p-type system by the choice of solvent, typically acetonitrile, and the additives, for example using lithium salts to lower the valence band potential, promote charge transport, limit charge recombination and increase  $V_{\rm OC}$ . 544,557,597,659,660 Ionic liquid iodide sources such as 1-butyl-3-methylimidazolium iodide (BMII), 1-ethyl-3-methylimidazolium (EMII) and dimethylpropylimidazolium (DMPII) have also been shown to give good performance. 557 Drawbacks to the I<sup>-</sup>/I<sub>3</sub><sup>-</sup> redox mediator include strong light absorption in the blue region, its corrosivity and the small difference between the redox potential of this electrolyte (315 mV vs. NHE) and the Fermi level of NiO, which limits the  $V_{\rm OC}$  of these devices to 100-200 mV.  $^{597,661}$  Exchanging  $I^-/I_3^-$  for a transparent alternative with a more negative redox potential can increase the  $V_{\rm OC}$  of p-type DSCs. For example, the 5,5'-dithiobis(1-phenyl-1H-tetrazole) and sodium 1-phenyl-1H-tetrazole-5-thiolate couple has a redox potential of 245 mV vs. NHE, about 70 mV more negative than that of the iodide electrolyte. <sup>637,662</sup> With optimised dyes this electrolyte improved the  $V_{\rm OC}$  compared to  $I^-/I_3^-$  and maintained a good  $J_{SC}$ . <sup>663,664</sup>

Coordination complexes have given the most encouraging improvement to device efficiency (see Table 12). Co(II/III) complexes (Fig. 47) offer better optical transparency and tunable redox potentials compared to  $I^-/I_3^-$ . Slower recombination at the electrolyte/electrode interface and more negative redox potentials than  $I^-/I_3^-$  frequently translate to higher  $V_{OC}$  (ca. 200-300 mV). 666,667 However, not all dyes can be used with transition metal-based electrolytes, as a long-lived charge-separated state is necessary for dye regeneration to compete with charge recombination at the dye<sup>-</sup>/NiO<sup>+</sup> interface. As mentioned above, a secondary electron acceptor, such as PMI or NDI, is required to generate long-lived dye radical anions. 665,666 PMI-NDI sensitized NiO and a [Co(dtb-bpy)<sub>3</sub>]<sup>2+/3+</sup> redox electrolyte led to a high  $V_{\rm OC}$  of 350 mV and an overall PCE of 0.20%. <sup>596</sup> Modification of the peripheral ligands leads to differences in recombination rate and redox potential, leading to efficiencies ranging from 0.04 to 0.24%. <sup>665</sup> The first example of a p-type DSC with an efficiency exceeding 1% was with PMI-6T-TPA and Co(III/II) tris(1,2-diaminoethane) ([Co(en)<sub>3</sub>]<sup>2+/3+</sup>). <sup>666</sup> Interestingly, this redox mediator also performs well in aqueous electrolytes (PCE = 2%, IPCE<sub>max</sub> = ~40% between pH 8-11). <sup>668</sup> The device efficiency was raised from 1.3% to 2.51% by substituting Co(en)<sub>3</sub> for [Fe(acac)<sub>3</sub>]<sup>0/-</sup>. <sup>103</sup> This is the highest reported efficiency to date for a p-type DSC.

Fig. 47 Structures of different redox mediators applied in p-DSCs.

Fe(acac)<sub>3</sub>

Co(en)<sub>3</sub>

In addition to metal complex-based electrolytes, anionic metal oxide clusters polyoxometalates (POMs) are versatile and transparent electron reservoirs. <sup>669</sup> POMs have been applied as coadsorbents on the surface of NiO electrodes in p-type DSCs to decrease the recombination rate and increase the  $V_{\rm OC}$ . <sup>670</sup> Lindqvist POMs (M<sub>6</sub>O<sub>19</sub><sup>2-</sup>) have directly been applied as redox mediators in p-DSCs, giving a 4 to 5-fold increase in  $V_{\rm OC}$  compared to  $I^-/I_3^-$ . <sup>671</sup> Increasing the solubility of the POMs could increase

the short-circuit current of these cells to deliver competitive efficiencies.

Recently, a few solid-state p-DSCs have been reported. 672 Phenyl-C<sub>61</sub>-butyric acid methyl ester (PCBM) is a well-known solid electron-transfer material used in organic photovoltaics. Tian et al. reported the first example of a p-type solid-state dye-sensitized solar cell (p-ssDSC), but the PCE of the device was low due to slow dye (P1) regeneration from PCBM. 672 Applying molecular dyads such as DPP (diketopyrrolopyrrole)pyromellitimide (PYRO) can improve the performance. 673 However, much improvement is required to deliver an efficient solidstate p-type DSC. Tian et al. followed up their work with organic electron transport mediators by completely removing the electrolyte/organic charge transport component and directly putting TiO<sub>2</sub> or ZnO on the NiO, so that the dye injects electrons directly into the n-type semiconductor and holes directly into the p-type semiconductor. 674-677 This concept was first introduced by Bandara et al. but incomplete pore filling by the n-type semiconductor limited the cell performance. 561,678 Tian et al. have optimised the interface between the dye and the semiconductors by engineering the structure of the dye and the deposition of the ntype semiconductor. Solar cells based on the TIP dye, containing an indacenodithieno[3,2-b]thiophene linker, gave PCE = 0.18%,  $J_{SC} = 0.86 \text{mA cm}^{-2}$ ,  $V_{OC} = 535 \text{ mV}$ , FF = 40% and max IPCE of 5%.674

#### 5.5 Photoelectrochemistry and photovoltaic performance

The key charge transfer processes that occur in a p-DSC under operation are summarised in Fig. 42 and the reactions important to photocathodes are:

Electron transfer from the valence band of NiO to the excited dye D\* (or hole transfer from the dye to NiO):

$$D^* + NiO \rightarrow D^- + NiO|h^+$$

Regeneration of the ground state of the dye by the oxidized species in the electrolyte, which involves radical species:

$$D^- + I_3^- \to D + I_2^- + I$$

The reduced dye is first regenerated by triiodide to form the diiodide radical. <sup>661</sup> This undergoes disproportionation to form triiodide and iodide:

$$2I_{2}^{-} \rightarrow I_{3}^{-} + I^{-}$$

Recombination between the reduced dye and a hole in NiO:

$$D^- + NiO|h^+ \rightarrow D + NiO$$

Recombination of a hole in NiO with the reduced species in the electrolyte:

$$2 \text{NiO} | \text{h}^+ + 3 \text{I}^- \rightarrow 2 \text{NiO} + \text{I}_3^-$$

Over the last ten years, there have been extensive studies into the dynamics of each process. Charge injection is typically a fast process, between 100 femtoseconds to 100 picoseconds according

Table 12 Photovoltaic characteristics of p-type DSCs employing various redox mediators. IPCE values with the approximation sign are a visual estimate taken from the plotted data

Mediator/HTM	Sensitizer	V <sub>OC</sub> (mV)	$J_{\rm SC}~({ m mA~cm^{-2}})$	FF (%)	PCE (%)	IPCE max (%)	Year	Ref.
Co(dtb-bpy) <sub>3</sub>	DPP-NDI	379	1.52	29	0.17	not reported	2017	544
$Co(dtb-bpy)_3$	PP2-NDI	342	1.72	39.7	0.31	$\sim$ 21	2018	664
Co(dtb-bpy) <sub>3</sub>	PMI-NDI	340	2.00	35	0.24	33	2011	665
$Co(dtb-bpy)_3$	PMI-PhNDI	210	0.78	29.3	0.048	${\sim}14$	2011	667
$Co(dtb-bpy)_3$	PMI-PhC <sub>60</sub>	180	0.58	38.8	0.040	${\sim}23$	2011	667
$Co(dtb-bpy)_3$	18	85	0.342	23.6	0.007	not reported	2011	667
$Co(dtb-bpy)_3$	19	85	0.250	28.9	0.006	not reported	2011	667
$Co(dtb-bpy)_3$	C343	190	0.25	32	0.015	${\sim}2$	2009	596
$Co(dtb-bpy)_3$	PI	80	0.26	26	0.006	${\sim}3$	2009	596
$Co(dtb-bpy)_3$	PINDI	350	1.66	34	0.20	31	2009	596
$T^-/T_2$	PMI-CO <sub>2</sub> H	161	1.52	25.4	0.062	${\sim}20$	2020	637
$T^-/T_2$	PMI-HQ	164	2.21	23.8	0.086	$\sim$ 21.5	2020	637
$T^-/T_2$	PMI-DPA	168	1.33	24.6	0.055	${\sim}26$	2020	637
$T^-/T_2$	PMI-acac	169	2.08	27.9	0.098	${\sim}32$	2020	637
$T^-/T_2$	$PMI-PO_3H_2$	181	1.27	17.7	0.041	${\sim}20$	2020	637
$T^-/T_2$	P1	304	1.73	44	0.23	${\sim}19$	2013	662
$T^-/T_2$	PMI-6T-TPA	285	5.3	34	0.51	$\sim$ 50	2015	663
$T^-/T_2$	PP1	169	1.60	30.5	0.082	${\sim}17$	2018	664
$T^-/T_2$	PP2	158	1.82	31.5	0.090	${\sim}17$	2018	664
$T^-/T_2$	PP2-NDI	212	4.31	33.9	0.23	$\sim \! \! 30$	2018	664
Co(dm-bpy) <sub>3</sub>	PMI-NDI	125	2.32	29	0.08	28	2011	665
$Co(dMeO-bpy)_3$	PMI-NDI	200	2.42	34	0.17	30	2011	665
Co(ttb-tpy) <sub>2</sub>	PMI-NDI	240	1.61	33	0.13	31	2011	665
Co(en) <sub>3</sub>	PMI-6T-TPA	654	5.23	43	1.48	not reported	2016	668
Fe(acac) <sub>3</sub>	PMI-6T-TPA	645	7.65	51	2.51	57	2015	103
PCBM	DPP-PYRO	228	0.32	32	0.023	${\sim}3$	2017	673
PCBM	DPP-Br	198	0.45	32	0.028	$\sim$ 4.5	2017	673
ZnO	BH4	480	0.346	39.4	0.07	${\sim}3$	2019	674
ZnO	TIP	535	0.855	39.8	0.18	${\sim}5$	2019	674
ZnO	PB6	440	0.68	45	0.135	$\sim$ 4	2019	677
TiO <sub>2</sub>	PB6	480	0.020	66	0.006	~0.08	2018	676

to transient absorption spectroscopy and time-resolved infrared spectroscopy. <sup>637,644</sup> The surface electronic states at the interface between NiO and a series of bodipy dyes have been studied by hard and soft XPS and the good overlap between the dye HOMO and semiconductor valence states was consistent with rapid light-induced charge transfer. <sup>628</sup> Recombination at the dye<sup>-</sup>/NiO<sup>+</sup> interface, however, is also fast, occurring on a picosecond to nanosecond time scale in simple dye systems such as bodipy and perylene. <sup>628,679,680</sup> Regeneration occurs from a nanosecond up to microsecond time scale. Competition between recombination and regeneration is responsible for the poor efficiency for p-type DSCs. <sup>611,629,667</sup> Recombination between holes in NiO with the reduced dyes contributes to the low FFs. <sup>681,682</sup> A hole-hopping charge-transport mechanism has been proposed for NiO, arising from "trap states" such as Ni<sup>3+</sup> and Ni<sup>4+</sup>. <sup>539,579,683</sup>

The Ni<sup>3+</sup> states are important for charge transport and charge recombination at the NiO/electrolyte and NiO/dye interfaces. <sup>536,537,548,684</sup> Competition between these processes leads to the short diffusion length and low fill factors observed in NiO-based DSCs. <sup>685</sup> Unlike TiO<sub>2</sub>, the charge transport lifetime is independent of light intensity or charge density and a charge hopping process, regulated by ions in the electrolyte, takes place at the NiO surface. <sup>686</sup> The NiO preparation and deposition route af-

fects both the charge lifetime and transport time. 531,535,536 Small amplitude light-modulated transient photocurrent and photovoltage decay measurements and electrochemical impedance spectroscopy (EIS) have also been used to study the effect of doping, of applying an insulating blocking layer and of varying the redox mediator and dye structure on the hole lifetime and transport time. 547,665,667,687,688 Application of a NiO blocking layer to suppress charge recombination led to a higher photocurrent and fill factor. 689 A Ni(CH<sub>3</sub>COO)<sub>2</sub> treatment to the NiO film was also shown to suppress the hole recombination and led to a 31.3% improvement in the photovoltaic performance. <sup>690</sup> Insulating coatings of Al<sub>2</sub>O<sub>3</sub> and TiO<sub>2</sub> on the NiO surface increase the recombination resistance and increase the  $V_{\rm OC}$  and efficiency of the device. 541,542 Chemical treatments such as immersing in  $NaBH_4$  or NaOH have also been used to improve the  $V_{OC}$  and FF by addressing the Ni<sup>3+</sup> surface states and decreasing recombination. 539,691,692

Developing new semiconductors, such as alternative metal oxides with better hole mobility compared to NiO or reducing electronic vacancies present above the valence band edge could favour charge transport over recombination. 683 Lithium has been well-characterized as a dopant for NiO and improves the electrical properties of the films, shifting the valence band position to

more positive potential, altering the density of states, narrowing the trap energy distribution and increasing the energy barrier for charge recombination. 548 Doping NiO with Co has been shown to increase the charge transport lifetime from  ${\sim}5$  ms for pure NiO to more than 2-fold for 2% and 6% Co-doped NiO films. The  $V_{\rm OC}$ increased from 122 mV up to a maximum of 158 mV with >6% cobalt doping due to a lowering of the flat-band potential of the NiO by a few tens of mV and also to higher hole lifetimes for the Co-doped cells than those for pure NiO cells. 547 Guldi et al. studied the charge transfer processes in CuO photocathodes with I<sup>-</sup>/I<sub>3</sub><sup>-</sup> using electrochemical impedance spectroscopy. <sup>556</sup> They probed the effect of calcination temperature, electrode thickness, and electrolyte ratio on the charge transfer resistance  $R_{CT}$ , charge collection efficiency  $\eta_{cc}$ , diffusion coefficient D and hole lifetime  $\tau_h$  and determined that a 300 °C calcination temperature, a film thickness of 5.0  $\mu$ m and an  $I^-/I_3^-$  electrolyte ratio of 2.5:1 gave the optimum balance of dynamics and best device performance. The experiments also revealed less recombination at the electrode/electrolyte interface for CuO compared to NiO.

The dye structure has been shown to affect the charge transfer dynamics. Push-pull donor-acceptor dyes and molecular dyad and triad structures have been developed to extend the chargeseparated state lifetimes from tens of picoseconds into the microsecond to millisecond regime. 606,634,642,651,667,679,693-695 By extending the linker it is possible to increase the charge-separated state lifetime without decelerating the rate of charge separation. 523,624 Varying the coupling between the chromophore and the linker has been shown to increase the charge-separated state lifetime, but this comes with a sacrifice to the charge injection yield so a balance must be struck to optimize the performance. <sup>603</sup> Adding bulky alkyl chains to the dye, or forming a compact arrangement of dye molecules at the electrode surface inhibit charge recombination at the semiconductor/electrolyte interface, leading to longer charge lifetimes. 614,615,689 A surprise came from exploring the charge transfer dynamics of P1 and CAD3, 616 which - despite having relatively short charge-separated state lifetimes (ca. <10 ns) – still generate relatively high photocurrents in NiO DSCs. When iodine and lithium iodide were added, the charge-separated state decayed over an order of magnitude longer time scale than in the presence of an inert electrolyte. This suggests that species in the electrolyte associate with either or both the cationic dyes adsorbed on NiO or high valence states on the surface of NiO. It has also been demonstrated that I- in the electrolyte reduces the Ni3+ states, which are thought to be responsible for rapid charge recombination, so a dual effect might be responsible for the increased charge-separated state lifetime in the presence of the redox electrolyte. 537,539,659

With electrolytes based on cobalt polypyridyl complexes, the hole lifetimes were shown to be – like  $I^-/I_3^-$  – strongly dependent on light intensity, whereas the hole transport times were largely independent of light intensity. Charge transport times have been found to be almost independent from the structure of the cobalt complexes, but charge lifetimes depend on the steric bulk of the cobalt polypyridyl complex. Most importantly, charge lifetimes were shown to be longer with cobalt complexes (particularly with bulky ligands) compared to I<sup>-</sup>/I<sub>3</sub><sup>-</sup>. <sup>667</sup> Electrolyte additives, such as chenodeoxycholic acid, have also been shown to slow recombination at the electrode/electrolyte interface. 544 In these examples, the longer charge lifetimes corresponded with higher open circuit voltage.

#### 5.6 Tandem devices

Tandem DSCs offer an opportunity to increase the solar cell efficiency beyond what can be attained by a single photoelectrode. The top electrode captures the higher energy photons and the transmitted lower energy photons are captured by the bottom electrode. However, the low performance of the photocathodes limits the performance of tandem DSCs. Early studies focused on proving the principle that the  $V_{\rm OC}$  of the tandem DSC is the sum of the individual n-type and p-type DSCs, but the devices suffered from very low photocurrents and poor fill factors. 520 These first tandem DSCs typically contained I-/I3- as the redox mediator, but substituting it for metal complexes and commercial photosensitizers for dyes designed specifically for photocathodes has led to an improved performance. 596 In particular, advances have been made in developing dyes which absorb in the red to NIR region of the solar spectrum to complement state of the art photosensitizers for TiO2 devices. For example, Gibson et al. reported a tandem cell with up to 5.2 mA cm<sup>-2</sup> employing the cationic chargetransfer dye CAD3 on NiO and a benchmark charge-transfer dye D35 on TiO2.612 Guldi et al. incorporated Zn(II) phthalocyanines (ZnPc) in photocathodes based on CuO and assembled them in tandem devices with N719 on TiO2, giving a light harvesting range from 300 nm to 800 nm ( $J_{SC} = 1.28 \text{ mA cm}^{-2}$ ,  $V_{\rm OC} = 860$  mV, FF = 63%, PCE = 0.69%). 696 A more encouraging efficiency of 2.42% was reported by Bach et al. with PMI-6T-TPA as the dye and Fe(acac)<sub>3</sub> as the electrolyte. <sup>523</sup> The most efficient dye-sensitized tandem cell to date has been reported by Odobel et al. with a diketopyrrolopyrrole (DPP)-based sensitizer at the photocathode (NiO/Th-DPP-NDI) and a TiO<sub>2</sub>/D35 photoanode. The tandem DSC efficiency was greater than that of the individual p-type and n-type devices ( $J_{SC} = 6.73 \text{ mA cm}^{-2}$ ;  $V_{\rm OC} = 910 \text{ mV}; \text{ PCE} = 4.1\%).^{521}$ 

Deepa et al. reported a tandem cell efficiency of 9.76% for a device which included a photocathode with a nickel pthalocyanine dye (NiPcTs) on NiO supported over carbon fabric. 697 The photoanode was assembled from conducting core/shell copper@carbon dots anchored to CdS quantum dots on TiO2 and a polysulfide electrolyte was used for compatibility with the CdS. The efficiency of the photocathode half-cell was quite low (0.039%) but when incorporated into the hybrid tandem device it improved the efficiency by almost 3% compared to the photoanode device with carbon fabric only as the counter electrode (6.69%). Most of the improvement came from the higher photocurrent.

The key issue with tandem devices is that, although great steps have been made in improving the photocurrent density by developing new photosensitizers and improving the photovoltage through developing new redox mediators, the efficiency is still limited by the valence band position of the p-type semiconductor. A semiconductor with a lower valence band than NiO or replac-

ing TiO2 with a material with a higher lying conduction band is needed to improve the built-in potential of tandem devices. Other than the tandem device by Guldi et al. described above, <sup>696</sup> a tandem cell by Kaya et al. assembled from a photocathode of CuCrO<sub>2</sub> with a coumarin 6 organic dye, iodide-based redox mediator and N719-sensitized TiO<sub>2</sub> photoanode gave a PCE of 2.33% with V<sub>OC</sub> of 813 mV,  $J_{SC}$  of 4.83 mA cm<sup>-2</sup>, and fill factor of 59%.<sup>698</sup> If an alternative p-type transparent semiconductor with a valence band 0.5 V deeper than NiO could be found, an efficiency above 20% would be possible. However, as described above, there is no obvious choice to replace NiO yet.

#### 6 DSCs for solar fuel

The diffused and intermittent nature of solar energy dictates the requirement for energy storage in solar energy conversion strategies. Chemical bonds are arguably the most appealing choice for this goal. For over two billion years nature's photosynthesis has been converting solar energy into chemical potential, while also sequestering CO2 and producing most of the oxygen in our planet. All fossil fuels we use today are derived from the natural photosynthetic process. Artificial photosynthesis aims to emulate natural photosynthesis to generate solar fuels and commodity chemicals from sunlight using H2O, CO2 and N2 as feedstocks. In the last decade, DSCs have played key roles in one of the fastestgrowing artificial photosynthetic approaches, Dye-Sensitized Photoelectrosynthesis Cells (DSPECs). A DSPEC is a modified DSC in which the reduced form of the redox shuttle in the anode compartment is replaced with an oxidation catalyst (e.g. a water oxidation catalyst), while the oxidized form of the redox shuttle in the cathode compartment is replaced with a reducing catalyst (e.g. a proton reduction catalyst). In a DSC the goal is to convert sunlight into electricity to power a device or to charge a battery. In a DSPEC the goal is to convert and store sunlight into chemical bonds, producing O2 or a commodity chemical at the anode and a fuel at the cathode.

Fig. 48 shows a schematic representation of a DSPEC for water splitting. Light-driven water oxidation takes place at the photoanode, composed of a chromophore-catalyst assembly on a mesoporous n-type semiconductor film, and proton/water reduction occurs at a dark Pt cathode. At the photoanode, light absorption by the chromophore in the chromophore-catalyst assembly is followed by electron injection from the excited state(s) of the chromophore into the conduction band of the semiconductor. The injected electrons are transported to a transparent conducting oxide (TCO) electrode and delivered to the cathode for proton/water reduction. Electron transfer from the water oxidation catalyst in the assembly to the oxidized chromophore initiates the activation of the water oxidation catalyst and regenerates the chromophore. This process is repeated four times leading to  $O_2$  evolution at the photoanode and H<sub>2</sub> evolution at the dark cathode, ideally in a 1:2 O2/H2 ratio, returning the chromophore-catalyst assembly to its initial state.

Meyer and co-workers reported the first DSPEC in 1999, 700 almost a decade after the pioneering DSC work of O'Regan and Grätzel. 6 The DSPEC carried out light-driven dehydrogenation of isopropanol to acetone at the photoanode with H2 generation at

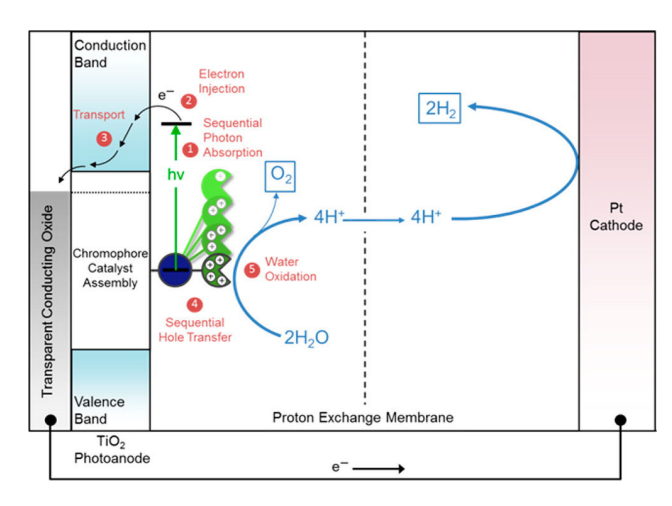


Fig. 48 Schematic diagram of a DSPEC for light-driven water splitting with an assembly-derived TiO2 photoanode for water oxidation to O2 and a dark Pt cathode for proton/water reduction to H<sub>2</sub>. Reprinted with permission from ref. 699. Copyright 2015 American Chemical Society.

the dark Pt cathode. It took yet another decade for the development of the first DSPEC for water splitting by Mallouk and coworkers in 2009. 701 Nevertheless, the last 12 years have seen an impressive development in this area. 699,702-739 The first DSPEC for water splitting reported by Mallouk and co-workers generated a photocurrent of 12.7  $\mu A~cm^{-2}$  at pH 5.8 under 450 nm light irradiation (7.8 mW cm<sup>2</sup>) with an internal quantum yield of 0.9% and a faradaic efficiency for O<sub>2</sub> generation of 20%.<sup>701</sup> Just a decade later, DSPECs are reaching photocurrent densities of  $\sim$ 2.2 mA cm<sup>-2</sup> at pH 7.0 under 1 sun illumination with an incident photon to current efficiency (IPCE) of 29% at 450 nm and faradaic efficiencies for O2 generation over 70%. Correcting for the injection yield of only  $\sim$ 42% for the chromophore at pH 7.0, the efficiency of the cell, excluding the losses at the core/shell interface, is a remarkable 67%. 738

### 6.1 Photoanodes and photocathodes

In theory, a tandem DSPEC (discussed in Section 6.5) with both a photoanode and a photocathode could provide significant advantages over a DSPEC with just a photoanode and a dark cathode. Absorption of one photon at the photoanode and one photon at the photocathode by two complementary dyes would emulate the Z-scheme in natural photosynthesis and enable coverage of a wider range of the solar spectrum. In addition, a photocathode would provide additional voltage that could eliminate the need for an applied bias to generate H<sub>2</sub> at the photocathode or enable access to fuels from CO2 using catalysts with higher overpotentials than those used to produce H2 as the fuel. Unfortunately, as in the case of DSCs, the development of tandem DSPECs has been hampered by the lack of suitable p-type photocathode materials.

#### 6.1.1 Photoanodes.

Most DSPECs reported to date function as a photoanode to drive oxidation reactions with a dark cathode to generate H<sub>2</sub>. The photoanode consists of a mesoporous 5-15 µm thick nanoparticle film of an n-type wide bandgap semiconductor deposited on a TCO and a combination of a chromophore or sensitizer and an oxidation catalyst. DSPEC photoanodes have greatly benefited from prior developments of DSCs photoanodes, both in terms of the n-type semiconductor materials as well as in terms of the photosensitizer or chromophore.

In a typical DSC the photosensitizer or chromophore is anchored to the semiconductor material, while the redox shuttle is free to diffuse from the anode to the cathode and back. In a DSPEC, on the other hand, the oxidation catalyst must be immobilized on the photoanode and it must undergo multiple, successive oxidations to complete one cycle or turnover. For this reason, the position and distance of the oxidation catalyst with respect to the photosensitizer and the semiconductor are key aspects in determining the overall cell performance. This has led to many approaches in the assembly of chromophores and catalysts on the nanoparticles' surfaces of the semiconductor.

The first DSPEC reported used a chromophore-catalyst assembly, in which the two were chemically linked through a bridge prior to loading on the semiconductor surface. 700 This design allows precise control of the distance between chromophore and catalyst and positions the catalyst away from the semiconductor surface to inhibit recombination reactions between injected electrons and oxidized catalyst molecules. However, it requires cumbersome synthetic procedures for each chromophore-catalyst assembly design. The first chromophore-catalyst assembly for water splitting was not suitable for a DSPEC. 740 In the excited state of the chromophore, the excited electron was localized in the bridging ligand and the injection yield into the conduction band of TiO<sub>2</sub> was less than 5%. Other chromophore-catalyst assembly designs failed to perform in a DSPEC configuration because the oxidized chromophore did not have enough oxidizing power to generate the RuV=O form of the catalyst, key intermediate for the initial O-O bond formation step. <sup>699,741,742</sup>

Introduction of carbene-based water oxidation catalysts in chromophore-catalyst assemblies enabled access to O-O bond formation at the  $\mathrm{Ru^{IV}}\!=\!\mathrm{O}$  form of the catalyst with additional redox power available from the weakly-coupled Ru(III) chromophore. Water-splitting DSPECs involving a single-site water oxidation catalyst in the chromophore-catalyst assembly were successfully developed.  $^{706,713,733}$ 

The discovery of the [Ru(bda)(L)<sub>2</sub>] (Ru-bda; bda is 2,2'bipyridine-6,6'-dicarboxylate; L is a monodentate ligand) water oxidation catalysts by Sun and co-workers 743,744 and their incorporation into chromophore-catalyst assemblies led to significant improvements on DSPEC performance because of their low overpotential and high rates for water oxidation. 727,730 This type of catalysts was first used on a DSPEC configuration by loading the catalyst into a Nafion overlayer deposited on top of a Ru(bpy)<sub>3</sub>-sensitized TiO<sub>2</sub> mesoporous film. <sup>702</sup> Nevertheless, the first significant DSPEC breakthrough was achieved by co-loading a Ru(bpy)<sub>3</sub>-type chromophore and a Ru-bda catalyst on TiO<sub>2</sub>. <sup>707</sup> Photocurrent densities up to 1.7 mA cm<sup>-2</sup> at pH 6.8 were obtained with a 14% IPCE at 450 nm and 83% faradaic efficiency for O2 generation. This co-loading strategy has been successfully used in DSPEC photoanodes with a variety of chromophorecatalyst combinations. 712,717,723,729,732

Mallouk and co-workers introduced a layer-by-layer approach to load chromophores and catalysts on the surface of the semiconductor. <sup>701</sup> The authors prepared a Ru(bpy)<sub>3</sub>-type chromophore containing one phosphonated bpy ligand for TiO2-anchoring and another bpy ligand functionalized with a malonate group that was selective for binding and stabilizing the colloidal IrO<sub>2</sub> · nH<sub>2</sub>O water oxidation catalyst nanoparticles. A related layer-by-layer strategy for nanostructured metal oxides films was developed by Meyer and co-workers 745 based on previous studies on Si and Au planar electrodes. 746,747 This strategy takes advantage of the strong affinity of phosphonate groups for high valent cations such as Zr(IV) and it has been successfully applied in a variety of DSPEC photoanode designs as well as in photocathodes, discussed below. 705,709,723,748 In yet another layer-by-layer strategy, a thin film of an oxide (TiO2, Al2O3, etc.) a few nm thick is deposited by atomic layer deposition (ALD) on top of the preloaded chromophore. The water oxidation catalyst is then loaded onto this oxide layer using typical metal-oxide anchoring groups. In addition to enabling loading of the catalyst, the ALD overlayer stabilizes and protects the chromophore. The ALD layerby-layer approach has been extensively used in DSPEC photoanodes. 728,731,749

Electropolymerization techniques have also been used to prepare DSPEC photoanodes. In this approach, electropolymerizable groups (e.g. vinyl groups) are introduced in both chromophore and catalysts which end up chemically linked during the electropolymerization process. <sup>714,718,725</sup> A variation of this strategy simply electropolymerizes a film of the catalyst on top of a dyefunctionalized electrode. The low water solubility of the polymer retains the catalyst molecules on the pores of the mesoporous electrode. <sup>716</sup>

A recent development for the assembly of chromophores and catalysts on an electrode surface takes advantage of hydrophobic interactions between long alkyl chains to build self-assembled bilayers (SAB, Fig. 49). To this approach, a chromophore containing both anchoring groups and long alkyl chains is loaded onto an electrode surface and the resulting chromophore-functionalized electrode is then immersed in a solution of the water oxidation catalyst which has also been functionalized with long alkyl chains. The long alkyl chains in the catalyst molecules self-assemble with the long alkyl chains in the chromophore to create a SAB. This approach allows easy combination of various chromophores and catalysts with the distance between them controlled by the length of the alkyl chains.

A water splitting DSPEC built using this strategy reached photocurrent densities of  $\sim$ 2.2 mA cm<sup>-2</sup> under 1 sun illumination at pH 7.0 with an IPCE of 29% at 450 nm and faradaic efficiencies for O<sub>2</sub> generation over 70%. Correcting for the injection yield of only  $\sim$ 42% for the chromophore at pH 7.0, the efficiency of the cell – excluding the losses at the core/shell interface – is a remarkable 67%. At pH 4.7, the cell was operated over a 3 hour period with an 86% faradaic efficiency for O<sub>2</sub> generation. <sup>738</sup>

### 6.1.2 Photocathodes.

The development of photocathodes for DSCs and DSPECs has been hampered by the lack of suitable p-type semiconductor ma-

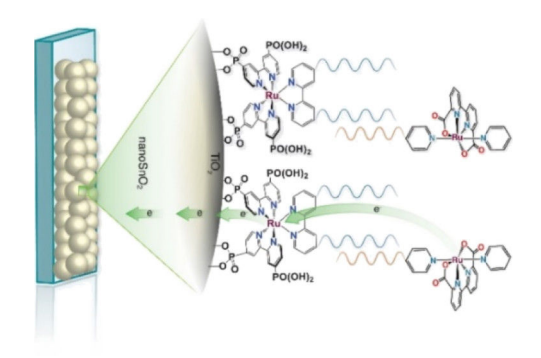


Fig. 49 Self-assembled bilayer of a chromophore-catalyst assembly on a metal oxide. Reprinted with permission from ref. 738. Copyright 2019 American Chemical Society.

terials. As it is the case for photoanodes, a DSPEC photocathode comprises a semiconductor material deposited on a TCO glass, a chromophore and a catalyst. For the last two decades, NiO has been the dominant wide bandgap p-type semiconductor material for sensitized photocathodes since its first report as a photocathode in a DSC. 522 Problems associated with the high density of traps and the low hole mobility have been identified as the main limitations of this material. 537 Target atomic deposition (TAD) has been used as a method to passivate defect states and improve the optical and electronic properties of NiO. 543,751,752 For example, TAD of Al increases the  $V_{\rm OC}$  of NiO in DSCs, leading to a  $\sim$ 3-fold improvement in their performance. <sup>543</sup> DSPECs operate in aqueous solutions and this introduces additional complications due to the appearance of localized electronic states centered on surface -OH groups associated with Ni vacancies. This enables proton-coupled charge transfer processes that are deleterious to the performance of aqueous NiO photocathodes. 753

The first sensitized photocathode for light-driven hydrogen generation was reported by Sun and co-workers. 754 It consisted of a cobaloxime molecular catalyst in solution and an organic triphenylamine-type dye anchored on nanostructured NiO. An analogous photocathode, but with the cobaloxime catalyst also anchored to the NiO, was used to prepare an organic dye tandem water splitting DSPEC. 717 The cell reached photocurrent densities of 300  $\mu A$  cm<sup>-2</sup> at pH 7 with an IPCE of 25% at 380 nm. Wu and co-workers reported a dye-sensitized photocathode that displayed high stability in strongly acidic solutions. 755 The organic dye consisted of a triphenylamine (TPA) donor moiety connected to two perylenemonoimide (PMI) acceptor groups by head-totail oligo-3-hexylthiophene-conjugated  $\pi$ -linker groups, Fig. 50. Carboxylic acid groups on the TPA donors enabled anchoring on NiO while the hydrophobic hexyl groups in the thiophene linkers provided protection for both the anchors and the NiO from the strongly acidic environment. An acid-stable cubane molybdenum sulphide cluster - [Mo<sub>3</sub>S<sub>4</sub>]<sup>4+</sup> - was chosen as the proton reduction catalyst. The cell sustained photocurrents above 180  $\mu A$  cm<sup>-2</sup> for more than 16 hours at pH 0 in 1.0 M HCl with a 49% faradaic efficiency for H2 generation. Artero and co-workers also reported a NiO-based photocathode using a TPA chromophore covalently linked to a cobaloxime catalyst. <sup>756</sup>

Wasielewski and co-workers used ALD to deposit a thick Al<sub>2</sub>O<sub>3</sub>

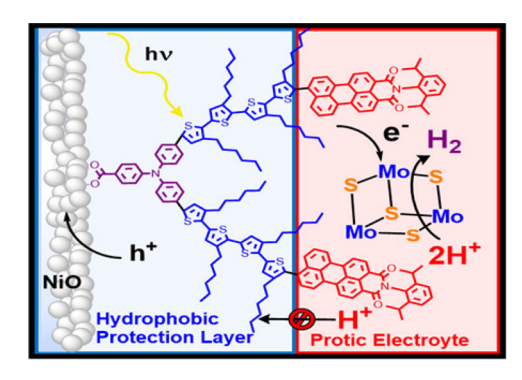


Fig. 50 Photocathode for hydrogen generation. Reprinted with permission from ref. 755. Copyright 2016 American Chemical Society.

layer on top of the NiO film with a modified perylene-3,4dicarboximide chromophore (PMI). In addition to providing protection for the NiO from the aqueous solution, the Al<sub>2</sub>O<sub>3</sub> layer films resulted in longer charge separated lifetimes as characterized via femtosecond transient absorption spectroscopy and photoelectrochemical techniques. Light-driven H2 generation was demonstrated with both cobaloxime and Dubois' Ni(L)2-type catalysts (L is a diphosphine). 757 Meyer and co-workers also used an ALD layer of Al<sub>2</sub>O<sub>3</sub> on NiO as a bridge between a Ru(bpy)<sub>3</sub>type chromophore and a Ni(L)2 proton reduction catalyst, an assembly strategy similar to that reported above for photoanodes. 728,731,749

The shortcomings of NiO as a p-type material for photocathodes has prompted scientists to look for new alternatives. Reisner and co-workers have used the delafossite-type material CuCrO2 as a suitable p-type semiconductor for visible light-driven H2 generation. 758 The semiconductor was functionalized by co-loading a phosphonated diketopyrrolopyrrole dye with a Ni(L)2 proton reduction catalyst. The hybrid CuCrO2 photocathode displayed a photocurrent of 15  $\mu A$  cm $^{-2}$  at 0.0 V vs. RHE in pH 3 aqueous electrolyte solution under UV-filtered simulated solar irradiation. The photocathode displayed good stability and yielded a Ni(L)<sub>2</sub> catalyst-based turnover number of 126 for H2 production during a 2 hour operation. The CuCrO2-based system outperformed an analogous NiO-based photocathode, but low dye and catalyst loadings limited product generation. In a follow-up study, macropore architectures of inverse opal CuCrO2 led to a 5-fold increase in loading. 759

More recently, Meyer and co-workers used boron-doped Si as the p-type material.  $^{748}$  Si nanowires  ${\sim}18~\mu m$  long were modified by physical vapor deposition of a thin Ti layer (~10 nm), followed by ALD of a  ${\sim}3.0$  nm TiO<sub>2</sub> layer. The latter protected the p-type Si electrode from photodegradation and allowed anchoring of phosphonate-functionalized perylene-diimide (PDI) chromophores. Ni(L)<sub>2</sub> proton reduction catalysts were introduced using the Zr-bridged layer-by-layer approach.  $^{745}$  The integrated photocathode was capable of delivering a photocurrent density of  $\sim -1.0$  mA cm<sup>-2</sup> under zero applied bias (vs. NHE).

Photocathodes for CO<sub>2</sub> reduction are even more challenging due to the larger overpotentials of CO2 reduction catalysts compared to proton reduction catalysts. Nevertheless, significant progress has been made on this front in recent years. Ishitani and co-workers reported a photocathode for reduction of  $\rm CO_2$  to CO using a NiO electrode functionalized with a Ru(II)-Re(I) supramolecular complex. The photocathode carried out 32 turnovers with a faradaic efficiency of 65% for CO, although the experiments were carried out in a DMF:triethanolamine (5:1) mixture with an applied bias of  $-1.2~\rm V$  vs. Ag/AgNO3. The same Ru(II)-Re(I) supramolecular complex on a CuGaO2 p-type semiconductor displayed photoelectrochemical activity for the conversion of CO2 to CO with 68% faradaic efficiency in an aqueous electrolyte solution with an applied bias of  $-0.7~\rm V$  vs. Ag/AgCl. The photocathode for reduction of CO3 with 68% faradaic efficiency in an aqueous electrolyte solution with an applied bias of  $-0.7~\rm V$  vs. Ag/AgCl.

More recently, Meyer and co-workers reported a binary p–n junction strategy to prepare photocathodes that convert sunlight into high-energy electrons for efficient  ${\rm CO_2}$  reduction to formate. The photocathodes integrate a semiconductor p–n junction comprising GaN nanowire arrays on silicon and surface-bound molecular assemblies for light absorption and catalysis. The photocathodes reduce  ${\rm CO_2}$  to formate at stable photocurrent densities of around -1.1 mA cm<sup>-2</sup> during 20 h of irradiation with faradaic efficiencies of up to 64%.

#### 6.2 Photosensitizers

The photosensitizers (or chromophores) used in DSPECs must meet additional demands compared to those used in DSCs. In the photoanode, the oxidized photosensitizer must be capable of oxidizing the water oxidation catalyst through a series of increasingly demanding oxidation states during the water oxidation cycle. In addition to the thermodynamic requirements for such a task, some (or all) the oxidation steps of the catalysts are protoncoupled in nature and this adds to the kinetic barriers for these oxidations. Because of this, in a DSPEC the photosensitizer remains for longer times in its oxidized form compared to DSCs, which leads to significantly faster decomposition of the photosensitizer. Another important issue is that injection efficiency into the conduction band of the semiconductor is pH dependent due to the pH dependence of the latter. 763,764 In addition, in the aqueous environment where DSPECs operate, long-term stability of the anchoring groups of the photosensitizer remains a challenge. Phosphonic acid groups have been the dominant choice in this regard for both photoanodes and photocathodes, although recent studies include the use of significantly more robust silanes. <sup>765–768</sup>

 $[Ru(bpy)_3]^{2+}$ -type chromophores have photoanode nated the DSPEC literature the side 701,702,705,707,709,712,714,716,718,723,725,729-731,738,748 with a few other examples including zinc porphyrins 727 and triphenylamine derivatives. 717,726,728 Recent efforts have been made on developing new chromophores with higher oxidation potentials that could enable faster oxidation of the water oxidation catalyst, use of water oxidation catalysts with higher overpotentials and DSPEC operation at low pH. Unfortunately, tuning the ground state redox potential of the chromophore also affects their excited state energy levels. Brudvig and co-workers developed a series of CF3-substituted free-base and metalated porphyrins that displayed redox potentials in the 1.25-1.56 V vs. NHE range, higher than the unsubstituted analogues.<sup>82</sup> The new porphyrins showed high efficiency for injection into SnO2 but poor injection into TiO2. Meyer and co-workers prepared a series of complexes of the type [Ru(bpy)2(N-N)]2+ (N-N is a polypyridyl ligand with low-lying  $\pi^*$  levels). With this approach, the absorption spectra of the new chromophores could be red-shifted up to  $\lambda_{max} = 564$  nm for the lowest MLCT compared to 449 nm for the parent  $[Ru(bpy)_3]^{2+}$  complex. In addition, the redox potentials for the Ru<sup>3+/2+</sup> couples could be enhanced by more than 250 mV. However, these improvements came at the expense of the excited state energy becoming more positive than the conduction band of TiO2, rendering these chromophores unsuitable for excited state electron injection. <sup>769</sup> In a follow-up work, introduction of electron-withdrawing groups on the bpy ligands enabled a  $\sim$ 200 mV increase in the Ru<sup>3+/2+</sup> couple for surface-bound chromophores. But once again, this improvement resulted in more positive excited state energies and smaller driving forces for electron injection. 770 More recently, the introduction of -CF3 and/or -PO3H2 groups on all bpy ligands in tris-homoleptic [Ru(bpy)<sub>3</sub>]<sup>2+</sup>-type chromophores resulted in increases of the Ru<sup>3+/2+</sup> couple up to 1.6 V vs. NHE while retaining similar absorption profile and photophysical properties compared to the  $[Ru(bpy)_3]^{2+}$  complex. 771 These chromophores enabled photochemical water oxidation to be carried out at pH 1 for the first time.

Significant efforts have been also made on developing organic chromophores for both photoanodes and photocathodes. This subject has been recently reviewed by Abbotto and co-workers and it is beyond the scope of this review. <sup>772</sup> A recent review on chromophores/sensitizers for photocathodes for both DSCs and DSPECs has been published by Odobel and co-workers. <sup>773</sup>

# 6.3 Catalysts

Most studies reported to date in DSPECs have used only a handful of catalysts for both photoanodes and photocathodes. After the first DSPEC for water splitting reported by Mallouk and co-workers  $^{701}$  that used  $\rm IrO_x$  nanoparticles as water oxidation catalyst in the photoanode, the majority of the reports that followed used either [Ru(tpy)(Mebim-py)(OH\_2)]^2+ (tpy is 2,2':6',2''-terpyridine; Mebim-py is 1-methyl-3-(pyridin-2-yl)-1H-benzo[d]imidazol-3-ium-2-ide)  $^{774-777}$  or [Ru(bda)(L)\_2], Fig. 51,  $^{743,744}$ 

[Ru(tpy)(Mebim-py)(OH<sub>2</sub>)]<sup>2+</sup> is a single-site water oxidation catalyst and retains its homogeneous catalytic performance when immobilized on the surface of photoanode materials. Nevertheless, its high overpotential and low rates for water oxidation resulted in poor performances for DSPECs using this catalyst. [Ru(bda)(L)<sub>2</sub>]-type catalysts, on the other hand, follow a bimolecular pathway for water oxidation and do not retain their impressive homogeneous catalytic performance when heterogenized, generating  $\mu$ -oxo bridged, blue dimer-like structures on the surface of the electrode. <sup>778,779</sup> These structures are the true water oxidation catalysts on the surface and their number is only a fraction of all the heterogenized monomeric catalysts that have the proper distance and orientation to generate  $\mu$ -oxo bridged

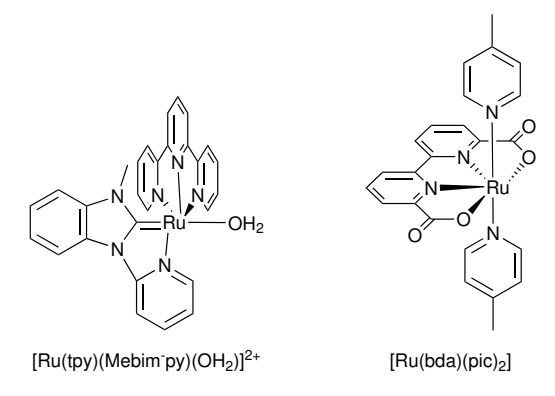


Fig. 51 Structures of Ru-based water oxidation catalysts.

species. Nevertheless, their high water oxidation activity and low overpotential enable DSPECs using these catalysts to display remarkable performance.

Single-site water oxidation catalysts capable of oxidizing water at high rates and low overpotentials, and which retain their homogeneous catalytic activity when heterogenized could potentially lead to significant improvements in DSPEC performance. Llobet and co-workers have reported single-site water oxidation catalysts with impressive rates although at neutral and basic pH values. 780,781 Combining the features of single-site bisphosphonate catalysts ([Ru(bpaH<sub>2</sub>)(L)<sub>2</sub>], bpaH<sub>2</sub> is 2,2'-bipyridine-6,6'-diphosphonic acid) 782 and fast bimolecular [Ru(bda)(L)2]type catalysts, Concepcion and co-workers have developed hybrid water oxidation catalysts ([Ru(bpHc)(L)<sub>2</sub>], bpHc is 6'-(hydroxyoxidophosphoryl)-[2,2'-bipyridine]-6-carboxylate) that are faster than the parent catalysts under identical conditions in both chemical and photochemical water oxidation. 779,783 Nevertheless, the performance of these catalysts in DSPEC configurations has not been reported to date.

On the photocathode side, catalysts can be separated into two groups: catalysts for proton/water reduction (other than platinum) and catalysts for CO2 reduction. Most studies where a molecular catalyst was used to carry out proton/water reduction at the photocathode used either cobaloxime-type catalysts 717,756,757 or the Ni(II) bis(diphosphine) complexes developed by DuBois and co-workers. 748,757-759,784-787 A cubane molybdenum-sulfide cluster was also successfully used for proton reduction in extremely acidic (pH 0) conditions and displayed significant stability with up to 16 hours of H2 generation with no degradation. 755 However, none of these catalysts have been able to perform at the level of a platinum electrode in a DSPEC and bias voltages are required to drive H2 evolution even with platinum, with just a few exceptions. Nevertheless, the applied bias is typically due to improper alignment between the conduction band of the photoanode material and the redox potential of the H<sup>+</sup>/H<sub>2</sub> couple rather than overpotential issues related to the proton reduction catalyst. DSPEC studies where water oxidation at the photoanode is accompanied by CO2 reduction at the photocathode are scarce. Ishitani and co-workers have reported CO<sub>2</sub> reduction to CO at a CuGaO<sub>2</sub> photocathode using a chromophore-catalyst assembly consisting of a [Ru(bpy)<sub>3</sub>]<sup>2+</sup>- type chromophore and a [Re(bpy)(CO)<sub>3</sub>(Br)] catalyst. <sup>761</sup> Nevertheless this was not a true DSPEC, because water oxidation was carried out by direct bandgap excitation of the photoanode rather than by sensitization. Meyer and co-workers reported an integrated photocathode based on the [Re(bpy)(CO)<sub>3</sub>(Cl)] catalyst for CO<sub>2</sub> reduction to CO in a CO<sub>2</sub>-saturated bicarbonate aqueous solution. The integrated photocathode was stable toward CO<sub>2</sub> reduction for over 10 h with a faradaic efficiency of  $\sim$ 65%. <sup>766</sup> Meyer and co-workers also reported a series of photocathodes using [Ru(bpy)(CO)<sub>2</sub>Cl<sub>2</sub>] as the catalyst for CO<sub>2</sub> reduction. The photocathodes reduced CO<sub>2</sub> to formate at stable photocurrent densities of around -1.1 mA cm<sup>-2</sup> during 20 h of irradiation with faradaic efficiencies of up to 64% in CO<sub>2</sub>-saturated bicarbonate aqueous solution. <sup>762</sup>

#### 6.4 Electrode materials

Electrode materials play several key roles in DSPECs. They serve as the solid support for chromophores and catalysts, and in many cases they play a role in chromophore-catalyst integration strategies. In addition, electrode materials are also key in charge separation, and electron collection and delivery.

### 6.4.1 Electrode materials for photoanodes.

As in the case of DSCs, mesoporous thin films of TiO<sub>2</sub> have been the workhorse electrode material for photoanodes in DSPECs since the initial reports of Meyer et al. 700 and Mallouk et al. 701 In the last decade, however, the use of core-shell electrode materials has proven to be more advantageous. Core-shell structures with a conductive core (tin-doped indium oxide, ITO, and tindoped antimony oxide, ATO) for fast and efficient electron collection and transport, and a TiO2 shell for electron injection introduced by ALD were used in 2013 in a DSPEC for water splitting where the photoanode was the disc in a rotating ring-disc electrode system. 706 A chromophore-catalyst assembly containing the catalyst [Ru(tpy)(Mebim-py)(OH<sub>2</sub>)]<sup>2+</sup> (Fig. 51) was anchored to the TiO<sub>2</sub> layer via phosphonic acid groups on the chromophore. Light was introduced from the bottom of the cell and the oxygen generated at the photoanode disc was detected and quantified at the ring (Pt). In 2015, the same chromophore-catalyst assembly was used in a more conventional DSPEC setup but with a SnO<sub>2</sub>-TiO<sub>2</sub> core-shell as photoanode material. <sup>713</sup> The replacement of ITO with SnO2 as the core led to a 5-fold enhancement in photocurrent, reaching up to 1.97 mA cm<sup>-2</sup> in a pH 7 phosphate buffer. The stability of the cell was improved by introducing Al<sub>2</sub>O<sub>3</sub> or TiO<sub>2</sub> overlayers via ALD to protect the anchoring groups, a clear example of the many roles played by electrode materials in DSPECs.

The use of  $SnO_2$ -TiO<sub>2</sub> core-shell electrode materials combined with the use of  $[Ru(bda)(pic)_2]$ -type water oxidation catalysts (Fig. 51) has led to significant developments in DSPECs.  $^{718,723,728-731,738,788,789}$  In the case of  $SnO_2$ -TiO<sub>2</sub> coreshell electrodes the initial rationale for their better performance compared to just  $TiO_2$  electrodes was based on the difference in the conduction band positions of  $SnO_2$  and  $TiO_2$ . The more positive conduction band of  $SnO_2$  should act as a sink from which recombination of injected electrons should be significantly slower.

Initial studies by Meyer and co-workers supported this with oxidized chromophores persisting into the millisecond timescale when anchored onto SnO<sub>2</sub>-TiO<sub>2</sub> core-shell surfaces. <sup>790</sup> However, follow up studies by the same group discovered that there is actually a new electronic state at the SnO<sub>2</sub>-TiO<sub>2</sub> interface located more positive than both SnO<sub>2</sub> and TiO<sub>2</sub>. <sup>764</sup> The success of coreshell electrode materials in DSPECs and other applications is a clear example that finding new materials is not always the only solution. Oftentimes creative solutions with known materials might provide similar or even better outcomes.

# 6.4.2 Electrode materials for photocathodes.

NiO has been the dominant wide bandgap p-type semiconductor material for sensitized photocathodes since its first report as a photocathode in a DSC. <sup>522</sup> As previously mentioned, problems associated with the high density of traps and low hole mobility have been identified as the main limitations of this material. <sup>537</sup> The use of aqueous solutions in DSPECs brings additional complications due to the appearance of localized electronic states centered on surface -OH groups associated with Ni vacancies. As a result, proton-coupled charge transfer processes affect the performance of aqueous NiO photocathodes. <sup>753</sup> Other photocathode materials such as CuCrO<sub>2</sub> <sup>758,759</sup> and CuGaO<sub>2</sub> <sup>761</sup> have shown more promise than NiO but their performance is still lacking compared to the photoanode side.

Meyer and co-workers used boron-doped Si as the p-type material, protected by a 10 nm Ti layer with an additional 3.0 nm layer of TiO<sub>2</sub> for anchoring of chromophores. The integrated photocathode was capable of delivering a photocurrent density of  $\sim -1.0$  mA cm $^{-2}$  for hydrogen generation under zero applied bias (vs. NHE) using a NiL<sub>2</sub> catalyst for proton reduction to H<sub>2</sub>.

Strategies that creatively combine known materials could prove to be a viable alternative to finding new materials with ideal properties. For example, Meyer and co-workers reported a binary p–n junction strategy to prepare photocathodes that integrate a semiconductor p–n junction (Si/n-GaN) and surface-bound molecular assemblies for light absorption and catalysis. The photocathodes reduce  ${\rm CO}_2$  to formate at stable photocurrent densities of  $-1.1~{\rm mA~cm^{-2}}$  during 20 h of irradiation with faradaic efficiencies of up to 64%.  $^{762}$ 

# 6.5 Tandem devices

In natural photosynthesis, the net conversion of water and carbon dioxide to oxygen and reduced carbon products is driven by the absorbed energy of two photons per each electron involved in the process (two photosystems in tandem). In natural photosynthesis, however, the two photosystems absorb essentially the same spectral range and this is one of the reasons that makes this process relatively inefficient.  $^{791,792}$  A detailed thermodynamic analysis shows that for both natural and artificial photosynthesis a tandem junction approach in which the two photosystems use complementary spectral regions is essential to maximize the efficiency of solar energy to fuel conversion.  $^{791,793,794}$  Fig. 52 shows a schematic diagram of a tandem DSPEC for solar-driven CO<sub>2</sub> splitting into CO and O<sub>2</sub> by the net reaction  $2\,\mathrm{CO}_2 + 4\,\mathrm{hv} \rightarrow 2\,\mathrm{CO} + \mathrm{O}_2$ .  $^{699}$  Replacement of the CO<sub>2</sub> reduction

catalyst in the photocathode with a proton/water reduction catalyst results in a DSPEC for water splitting into  $O_2$  and  $H_2$ . Ideally, the chromophores in the photoanode and photocathode should have complementary spectral absorption profiles.

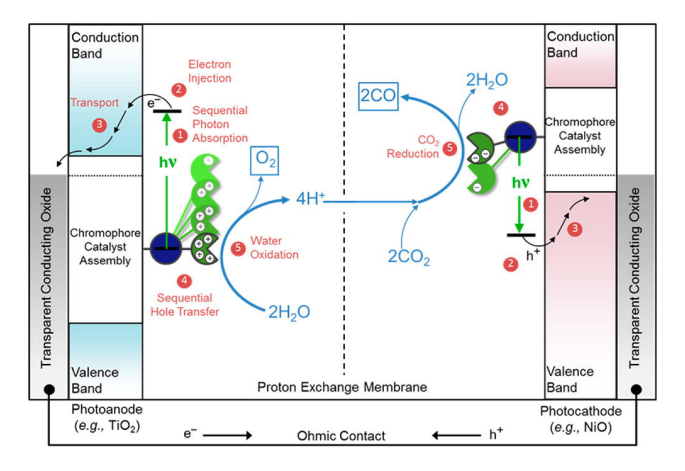


Fig. 52 Schematic diagram for a DSPEC for light-driven  $CO_2$  splitting into CO and  $O_2$  with an assembly-derivatized  $TiO_2$  photoanode for water oxidation to  $O_2$  and an assembly-derivatized photocathode for  $CO_2$  reduction to CO. Reprinted with permission from ref. 699. Copyright 2015 American Chemical Society.

Sun and co-workers reported an organic dye-sensitized tandem DSPEC for light-driven water splitting. The photoanode consisted of a thin film (8 µm) of TiO2 as electrode material, a triphenylamine-based organic dye and a molecular Ru-based catalyst for water oxidation. The photocathode consisted of a thin film (1 µm) of NiO, a triphenylamine-based organic dye and a molecular Co-based catalyst for water reduction. 717 In a 50 mM phosphate buffer at pH 7, the cell reached photocurrent densities of 70  $\mu A~cm^{-2}$  for water splitting under 100 mW  $cm^{-2}$  irradiation with no applied bias. Meyer and co-workers reported a tandem DSPEC with sustained photocurrents of 250  $\mu A \text{ cm}^{-2}$ over a 2.5 h irradiation time with faradaic efficiencies of 73% and 54% for O<sub>2</sub> and H<sub>2</sub>, respectively. <sup>748</sup> The photoanode consisted of a SnO<sub>2</sub>-TiO<sub>2</sub> core-shell electrode with a RuP<sub>2</sub><sup>2+</sup> chromophore and a Ru(bda) water oxidation catalyst assembled using the layerby-layer approach. The photocathode, described in the previous section, consisted of a boron-doped p-type Si protected with a 10 nm Ti layer with an additional 3.0 nm layer of TiO2 for PDI' chromophore anchoring. A NiL2 proton reduction catalyst was assembled with the PDI' chromophore via a zirconyl bridge using the layer-by-layer assembly strategy. High energy photons were used at the photoanode for water oxidation and low energy photons were used at the photocathode for proton reduction. The performance of the tandem device was limited by the photoanode. Sherman and co-workers reported an alternative approach to tandem DSPEC devices for water splitting. It combines a typical water splitting DSPEC with a DSC to use more efficiently the solar spectrum and eliminate the need for an applied bias, Fig. 53.724,725

The fully assembled tandem cell system consisted of a DSPEC incorporating a  $SnO_2$ - $TiO_2$  core-shell electrode, a  $RuP_2^{2+}$  chromophore and a Ru(bda) water oxidation catalyst. The chro-

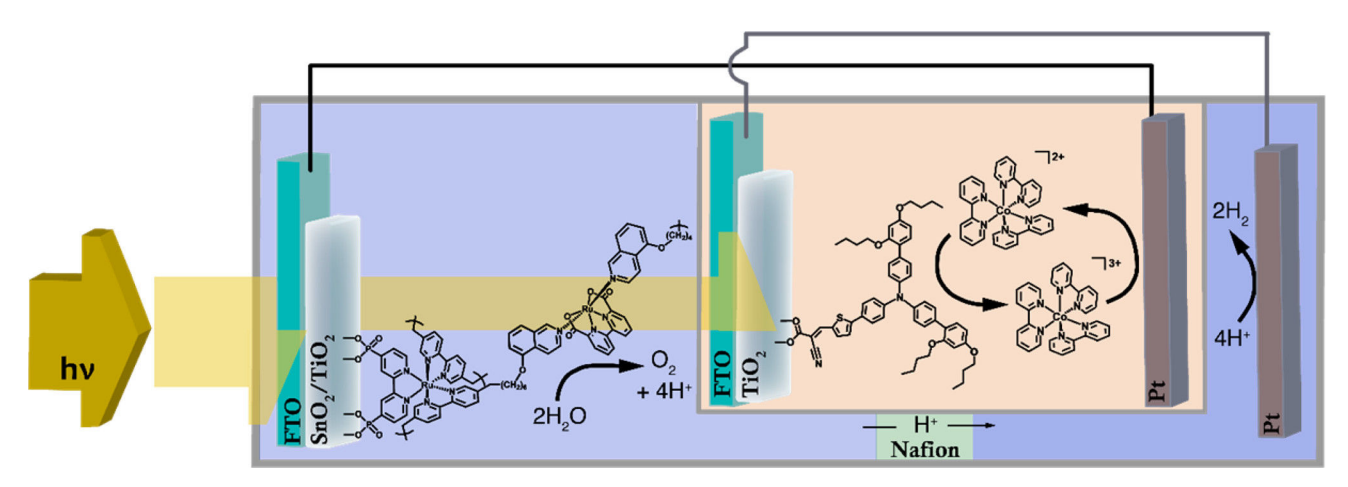


Fig. 53 Schematic diagram of a DSPEC wired in series with a DSC. Reprinted with permission from ref. 725. Copyright 2016 American Chemical Society.

mophore and catalyst were assembled on the surface of the coreshell electrode via electropolymerization. The photoanode and a dark Pt cathode were wired in series with a DSC employing either the N719 dye and  $I^-/I_3^-$  mediator or a D35 dye and the Co(bpy<sub>3</sub> mediator. The tandem cell achieved unbiased photocurrents of 40 µA cm<sup>-2</sup> under simulated solar illumination with a solar to hydrogen efficiency of 0.06%.

# Industrialization and commercialization

The Nature paper by Grätzel and O'Regan<sup>6</sup> triggered expectations for a novel low-cost photovoltaic technology with potential to challenge silicon solar cells, which at the time were still forecast to be expensive to manufacture on a large scale. Shortly thereafter, a few pioneering device manufacturing companies initiated DSC development with commercial ambitions, such as Glas Trösch, Leclanché, and Asulab from Switzerland, ABB and INAP in Germany, Ekologisk Energi in Sweden, Solterra in Italy, and Dyesol in Australia. Since then, a range of industrialisation initiatives in different parts of the world have been created. The most intense period was during 2000-2010, when Asian activities were keen, dominated by Japan. An example of the vast Japanese development activities is the fact that >50% of the >2000 novel DSC patent families submitted in the years 2000-2010 had Japanese origin. 795 Examples of Japanese companies with strong DSC development during this period are Sharp, Sony, Toyota, Hitachi Maxell, Sanyo, Nippon Oil, Fuji Film, Aisin-Seiki, Fujikura, J-Power Co., Gunze Ltd., Mitsubishi Paper Mills., Sekisui Jushi Corporation, Dai Nippon Printing Company, Nissha Printing, Taiyo Yuden Co., Panasonic Denko, TDK, Spark Plug Co. and Eneos Co Ltd. Equivalent examples from other Asian countries are Dongjin Semichem and Samsung SDI from South Korea and J touch from Taiwan. Further examples of companies with DSC activities during this period are BASF, Bosch, Merck and Tata Steel. Most of these industrial DSC initiatives have been abandoned, whereas some have changed direction during their development, typically from outdoor panels to low-power devices targeting IoT (Internet of Things) applications. In the past 10 years period, commercial-oriented DSC device activities have been more or less exclusively directed towards see-through aesthetic devices for BIPV applications and small-area devices for low-power applications. Looking at commercialization efforts of the DSC technology throughout the past 30 years, three categories appear: (i) panels to challenge Si, (ii) BIPV via aesthetic devices, (iii) niche products for electronic applications. These are discussed in Section 7.2. Throughout the DSC commercialization efforts, a set of module concepts have been used and thoroughly investigated, each one with their respective strengths and challenges (Section 7.1). In parallel to the device-oriented commercialization activities, there has been supplementary industrialization of required material components, manufacturing equipment and services. However, as the major DSC commercial breakthrough has not taken place yet, these industries still operate at a small scale, with various peaks during the most intense DSC commercialization periods.

As pointed out by Hagfeldt et al., 9 a complexity involved in reviewing the performance of DSC modules is that different definitions of device efficiency are used. In some cases the efficiency of the active area is used, whereas in other cases the efficiency of the module's total area is used. Moreover, various module sizes are used, and measurements are taken at different light intensities. Lower efficiency values are in general obtained in publications dealing with module stability. Caution should thus be taken when comparing DSC module results from different publications. In the present table of record solar cell efficiencies, 359 a DSC mini-module efficiency of 10.7% by Sharp from the year 2013 is listed.

#### 7.1 DSC module design

The thorough overview of the five basic DSC module designs presented by Hagfeldt et al. is still relevant. 9 Likewise, their definition of a DSC module is still valid, i.e. a device that - in relation to a test cell - is significantly increased in size in both the x and y directions, and carries specific solutions to decrease the energy (resistive) losses caused by electron transport in the device. The terms sandwich and monolithic are still used to define a device structure carrying the working and counter electrodes either on two different substrates or on the same one, respectively.

As discussed by Hagfeldt et al., 9 the manufacturing, reliability, performance, and stability of a DSC module are more complex compared to a test cell, due to the larger size. Moreover, the interconnection of cells in a DSC module may lead to new efficiency loss pathways, such as mismatched performance of the connected cells or unwanted mass transport of electrolyte between adjacent cells. The five sandwich and monolithic module concepts, i.e. (i) sandwich Z-interconnection, (ii) sandwich W-interconnection, (iii) sandwich current collection, (iv) monolithic serial connection, and (v) monolithic current collection have constituted the basis throughout 30 years of DSC device development and commercialization. Their respective advantages and challenges are discussed by Hagfeldt et al. 9 Even though there has been an evolution in DSC chemistry, represented by e.g. organic dyes, Cubased redox mediators and the so-called "zombie cell", 467 the five module designs remain.

One complementary module design deserving attention is the work by Takashima et al. from NGK Spark Club. 796 Their socalled ball-grid DSC solution is based on a hybrid copper polyimide flexible substrate covered with a dense carbon counter electrode. The working electrode is contacted to the copper via polymer-cored solder balls. The design efficiently enlarges a DSC cell by combining an efficient current collection grid with a high ratio of active area (95%). In addition, a few interesting novel DSC module design options - driven by simplified production processes - have been presented in the past few years at conferences by representatives of the present DSC industry, such as Exeger in Sweden and Song Textile in South Korea. However, as these designs - to the best of our knowledge - have not been presented in the literature, they are not part of this review. Moreover, Ricoh in Japan have recently launched commercial solid-state DSC products where the device concept has not been found in the literature.

### 7.2 Application categories and commercialization efforts

Despite the different nature of commercialization initiatives performed over the past 30 years, there are few main product categories that can be identified. As a consequence of this, we have divided the targeted applications for DSC into three categories: (i) panels to challenge Si, (ii) BIPV via Aesthetic devices, and (iii) niche products for electronic applications. The evolution of each category and their status are discussed below.

# 7.2.1 Challenge Si.

In the nineties, solar cells were still treated as a highly interesting energy source for the future. Even though there was a rapidly increasing amount on photovoltaic installations, they were from a low level. In addition, most installations were the results of various national programs. The German so-called 1000-roof program (1990-1994) was followed by e.g. the Japanese Residential Roofs Program (1994-1995). However, it was the German 100 000 Roof Program in 1999 that dramatically changed the market for photovoltaics. All of this was realized under the opinion that silicon solar cells would face difficulties in reaching manufacturing costs that would make it competitive with conventional energy sources; i.e. there was a need for novel photovoltaic technologies with lower production costs. The leading technologies from this aspect were thin-film PV such as CIS, CIGS and CdTe. Whereas these technologies were targeting high efficiencies and advanced manufacturing processes, characterized by massive investment costs, DSC entered the field from a totally different and unexpected angle, characterized by lower efficiency but basic manufacturing processes and low-cost, scalable raw materials. The investment costs for initiating a DSC production line were foreseen to be a fraction compared to silicon or thin-film technologies. As a result of all of this, DSC attracted many companies that wanted to take on the challenge to commercialize the technology. Moreover, it was a possibility for companies that were not active in the photovoltaic industry to enter the field. As a result of all of this, almost all industrial DSC efforts during 1990-2005 targeted the future global massive PV market. In their 2010 review, Hagfeldt et al. presented a number of DSC device examples from this period that were driven by the target of challenging silicon. 9 In the 10-year period 2005-2015, the manufacturing costs of silicon solar cells decreased as a result of the massive Chinese commercialization activities. The previous dream target of manufacturing costs of 1 USD per W<sub>peak</sub> were suddenly dramatically surpassed. As a result of this, more emphasis was given to the increase of device efficiency. Consequently, the arguments for DSC as a candidate for future large-scale photovoltaic establishments disappeared, as dramatic efficiency improvements were now required. Even though this coincided with the DSC efficiency breakthrough from Feldt et al. <sup>271</sup> and Yella et al., <sup>289</sup> the entrance of the perovskite technology in 2012 changed overnight the prerequisites for DSC. 797,798 The perovskite technology shared the basic features of DSC, namely cost-efficient scalable manufacturing methods and material components. Even the recent DSC record efficiency of 13.0% in year 2021 13 is still low compared to those obtained by perovskite solar cells, with a present efficiency record of 25.2%. <sup>799</sup> As a result of all this, there are today very few industrial DSC initiatives targeted at challenging silicon PV. In order to change this situation, a significant fundamental scientific breakthrough is required, opening for massive efficiency improvements. Nevertheless, the collective industrial and academic efforts devoted to developing competitive DSC devices for outdoor applications have left important technology testimonies such as module and production technology, proven durability at outdoor conditions, life cycle 800 and cost analyses. 801 In fact, this collective output has dramatically influenced the development of DSC for BIPV (Section 7.2.2) and low-power applications (Section 7.2.3), as well as the entire perovskite technology.

### 7.2.2 BIPV via aesthetic devices.

The aesthetic properties of the DSC technology have been known since the beginning. The fact that dye molecules have a central part immediately opened for discussions regarding colourful devices in one or several colors, in both opaque and see-through variations. However, the activities for these applications were minor in relation to the hunt for a low-cost DSC solar cell technology to challenge silicon photovoltaics. During the past ten years, however, see-through DSC panels in various colors for BIPV applications have been increasingly investigated by various companies.

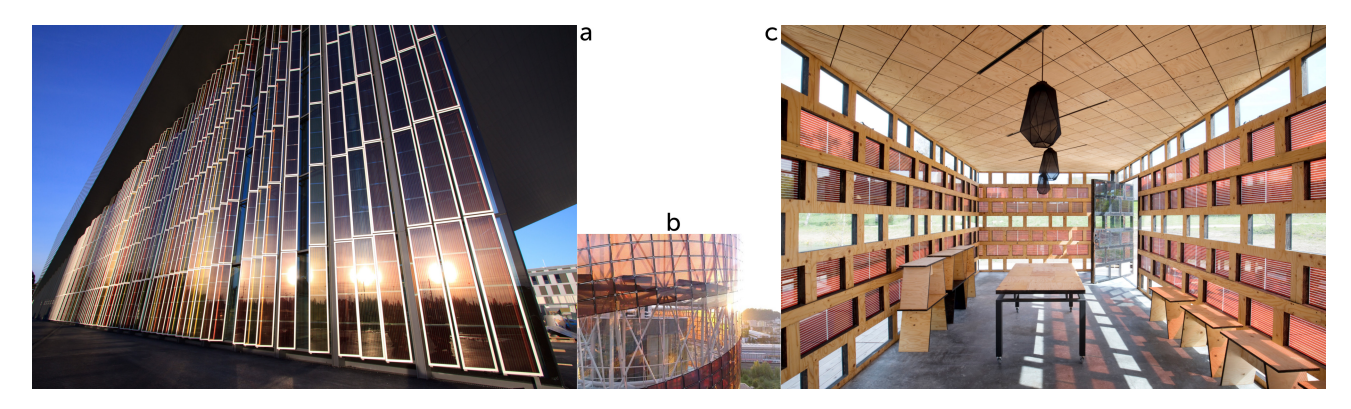
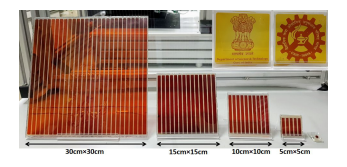


Fig. 54 (a) The DSC installation at the Conference Centre in Lausanne, Switerland, consisting of 1400 W-connected modules of the size  $35 \times 50$  cm<sup>2</sup> (in total approx. 150 m<sup>2</sup>), manufactured by Solaronix in Switzerland. Reproduced with permission from Solaronix S.A. (b) The DSC installation at the Science Tower in Graz, Austria, consisting of 896 W-connected red DSC devices of  $0.6 \text{ m}^2$  area each (in total approx.  $500 \text{ m}^2$ ), manufactured by H.Glass in Switzerland. Reproduced with permission from H.Glass S.A. (c) The DSC installation at the Solar Pavillon at Roskilde University in Denmark, consisting of 196 W-connected red DSC panels of area  $900 \text{ cm}^2$  each (in total approx.  $180 \text{ m}^2$ ) made by Dongjin Semichem in South Korea. Architect Jane Ostermann-Petersen. Reproduced with permission from Karina Tengberg.

One of the early publications in the field was from Sastrawan et al., who in the year 2006 displayed red semi-transparent DSC modules. 802 Examples of early industrial initiatives to develop aesthetic see-through DSC for BIPV applications came from TDK, Samsung, Dongjin Semichem, Dyesol, Peccell, Aisin Seiki and Toyota. Despite many impressive prototypes, the milestone for aesthetic DSC panels occurred in 2014 when the novel Conference centre at EPFL in Lausanne was inaugurated, containing a see-through wall of DSC modules in five different colors: light red, dark red, light green, dark green and orange. In total, 1400 modules of the size  $35 \times 50$  cm<sup>2</sup> have been produced and installed at the Conference centre by Solaronix in Switzerland, Fig. 54a. The installation is impressive and displays the attractive architectural features of DSC. However, from visual inspections at the site, it stands clear that many modules have experienced various degradation modes, such as leakage, electrophoresis, chemical reactions between current collectors and electrolyte, and vertical electrolyte concentration gradients, likely caused by the formation of polyiodide chains. The EPFL installation was followed by a range of aesthetic installations from H.Glass in Switzerland (originally glass2energy). Their most impressive installation is the Science Tower in Graz, Austria, where 896 red DSC devices (each 0.6 m<sup>2</sup>) are placed on top of the 60 m tall building, Fig. 54b. Another DSC see-through installation deserving attention is the Solar Pavillon at Roskilde University in Denmark (Fig. 54c). The 196 DSC panels (each 900 cm<sup>2</sup>), made by Dongjin Semichem, are integrated directly into the pavilion's glass facade constituting the basic element of its architectural motive, and providing charge stations for mobile phones and tablets to visitors. Further examples of intense industrial development of similar see-through DSC devices came from the Dyepower consortium in Italy. In 2015, they reported an active area conversion efficiency of 5.6% on a Z-connected 600 cm<sup>2</sup> device realized in their pilot line facility. 803 In addition, these devices successfully passed the UV preconditioning test, the humidity freeze test and the damp heat test of the IEC 61646 Standard. The Dyepower consortium also performed a thorough evaluation of the environmental profile of semi-transparent DSC. 804

All of the aforementioned initiatives were foreseen to represent the commercial breakthrough of aesthetic DSCs for BIPV applications. However, this has not been realized. On the contrary, the industrial activities on see-through aesthetic DSCs seem to have decreased in the past 2-3 years. A tentative explanation for this is that the energy production, i.e. the device efficiencies, were too low to balance the additional cost compared to coloured glass or alternative architectural features, potentially in combination with question marks regarding the product life. However, other similar initiatives are still ongoing, such as the Indian collaboration between Elixir Technologies and CSIR-National Institute for Interdisciplinary Science & Technology (NIIST) (Fig. 55).



**Fig. 55** Indian semi-transparent DSC prototypes from Elixir Technologies and CSIR-National Institute for Interdisciplinary Science & Technology (NIIST). Reproduced with permission from the Indian Ministry of Science and Technology.

All devices in the installations in Fig. 54a and 54b use a module concept based on W-interconnects, i.e. the double-substrate module design carries cells with alternating working and counter electrodes on each substrate. Consequently, every second cell is illuminated through the counter electrode side, which conventionally means lower current values compared to the illumination through the working electrode side. A challenge involved is thus to match the current output from adjacent inverted cells. This has commonly been overcome by making the cells illuminated through the counter electrode slightly broader, i.e. a larger active area to compensate for the lower current output. One drawback of this solution is that the ratio of current output from front- and back-side illumination varies with light intensity and illumination angle. Moreover, as semi-transparent devices are illuminated

from both sides, the illumination conditions are complicated and unpredictable. Consequently, it is practically impossible to avoid an imbalance in current output between cells. Such imbalance will decrease the overall device performance but it may also result in performance degradation over time. Interestingly enough, we have not found any literature on e.g. the device chemistry and/or the delivered energy values from these installations. This is surprising and unfortunate as these installations would provide highly interesting results and information regarding DSC, ranging from device performance to potential degradation modes over time.

### 7.2.3 Niche products for electronic applications.

As for aesthetic devices, the low-light properties of the DSC technology have been known since the beginning. The nanostructured working electrode efficiently absorbs diffused light, making it an ideal candidate for low-power devices. Two industrial pioneers in the fields were the Swiss companies Asulab and Leclanché, which already in the mid-nineties were active in prototyping DSC devices for watch-making applications and various electronic gadgets, respectively. Papageorgiou et al., 805 Pettersson et al. 806 and S. Burnside et al. 807 are all examples of early papers regarding material components, cell and modules performance, long-term stability and manufacturing methods for low-power DSCs.

Around the beginning of the millennium, activities on flexible DSC were taking off. Companies such as Konarka Technologies, USA, and Sekisui Chemical, Taiyo Yuden Co. and Peccell Technologies, Japan, developed such technologies. The DSC technology of Konarka was a few years later taken over by G24 Innovations (later G24 Power), who initiated a massive effort to commercialize the technology for low-power applications. Their factory in Wales is generally considered as the first large-scale mass production facility for DSC. Various products, such as Logitech keyboards, solar backpacks, solar chargers and solar iBeacons were launched. Whereas G24 targeted large-volume production for broad applications, there were several parallel Japanese initiatives where DSCs were used in solar art demonstrators, e.g. aesthetic devices powering lamps and fans. The lamp charger Hana-Akiri from Sony received a lot of attention, Fig. 56. Similar artistic DSC devices from the same period came from e.g. J Touch Co., Aisin Seiki and Nissha Printing. Retrospectively, it can be concluded that all of these, and many other low-power DSC commercial initiatives in the period 2000-2010, did not trigger a sustainable market demand.



56 An example of artistic DSC devices from Sony displayed at the 10th Eco-Products Conference in Tokyo in 2008. Reproduced with permission from Satoshi Uchida.

The arguments for indoor low-power DSC received novel fuel

from the work of Feldt et al., 271 where it stood clear that the combination of organic dyes and 1-electron Co-based redox mediators resulted in major performance improvements, with high voltage levels also at low light conditions. In addition, low-power PV became of interest as a result of the increased global activities on IoT applications with forecast billions of small systems requiring low-power supply. As a result, there has been a revival for and a rapid increase in industrial initiatives targeting low-power DSC. The interest for low-power DSC was taken to the next level by the work of Freitag et al. 341 By using Cu-based 1-electron redox mediators in combination with organic dyes, low-power efficiencies of 28.9% were obtained at 1000 lux. This was followed up by a 32% cell efficiency at 1000 lux by Cao et al, 277 a 34% cell efficiency at 1000 lux by Michaels et al., 33 and a 34.5% cell efficiency at 1000 lux by Zhang et al. 13 Interestingly enough, all these pieces of work used the same illumination source (Osram 930 Warm White fluorescent light). However, we highlight that characterization of low-power devices is a somewhat confusing part of the PV world since there is no established standard for the illumination and caution should be taken when comparing values. 808 An interesting comparison to low-power perovskite solar cells, however, can be made by the values reported by Meng Li et al. 809 They achieved conversion efficiencies up to 35.2% at a device size of 9 mm<sup>2</sup> (23.2% at 4 cm<sup>2</sup>) and 1000 lux using a fluorescent light source (Osram L18W/82). In contrast to the DSC values from Michaels et al., 33 the efficiencies for the perovskite devices were dramatically reduced with a lower light intensity: 25.7% and 19.5% efficiencies were obtained at 500 and 100 lux, respectively. These perovskite devices include lead, which may be a limitation for commercial exploitation in electronic applications. In addition to DSC and perovskite solar cells, organic solar cells (OPV) represent an additional technology candidate for lowpower applications, with confirmed efficiency values up to 28.1% at 1000 lux. 810 It is thus a product segment that is becoming crowded by various upcoming technologies. From a strict efficiency point of view, it appears as DSC devices deliver the highest efficiency values at indoor illumination, at least at 500 lux and 100 lux, and at 1000 lux for device sizes >1 cm<sup>2</sup>. This gives companies commercializing low-power DSC the prerequisites to realize the best-performing low-power products. In the commercial race, however, other additional selling points other than indoor efficiency will likely be important, such as price, colour, weight, thickness and flexibility in size and voltage.

The new era of DSC industrialization for niche applications in general, and low-power devices in particular, is confirmed by recent product launches. The DSCs of Fujikura in Japan are already used in wireless multi-sensor device systems such as heatstroke prevention systems and management of large warehouses in Japan, Fig. 57a. 811 3GSolar in Israel offers DSC devices in various transparency (0, 30 and 50%) and in three different colours (red, black and green) for various niche applications, such as wireless sensor networks (Fig. 57b), medical and sports devices, security sensors and cameras, agriculture monitors, beacons and electronic signs, computer peripherals, and wearable electronics. Exeger in Sweden has announced that their DSC devices will be used in headphones from JBL and in various other devices, such as tablets, e-readers, and safe helmets. In 2020, Ricoh in Japan launched their RICOH EH DSC series. This is a solid-state DSC version, i.e. the liquid electrolyte has been replaced by a hole conductor. These devices are used in applications such as remote controls for projectors and to power IoT sensor systems, Fig. 57c.

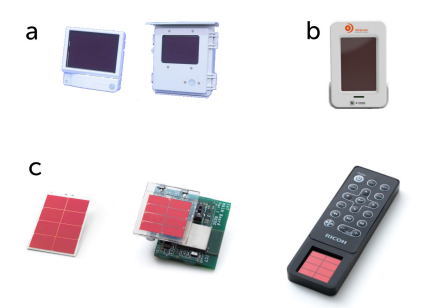


Fig. 57 a) DSC-containing sensor systems from Fujikura in Japan for indoor (left) and outdoor (right) applications, respectively. Reproduced with permission from Fujikura Ltd. b) DSC-containing sensor system from 3GSolar in Israel in collaboration with the company e-peas for measuring of temperature, humidity and luminosity in smart buildings. The size of the single solar cell is 7.4  $\times$  5.0  $\text{cm}^2.$  Reproduced with permission from 3GSolar Ltd. c) Examples of products from Ricoh containing their solid-state DSC devices: environmental sensors for measuring temperature, humidity, illumination, atmospheric pressure, etc. and remote controls for projectors. Reproduced with permission from Ricoh Company

Out of these DSC products, it is noticeable that Fujikura has different devices for outdoor and indoor use (Fig. 57a). This is likely attributed to the fact that Fujikura worked on outdoor DSC module development before focusing on low-power devices, i.e. they had access to the required chemistry and manufacturing methods for outdoor applications. 812 Ricoh appears to be the only producer using solid-state DSC. Moreover, it is worth noticing that devices from Exeger are marketed as solar cells that are integrated without being seen, Fig. 58, opening for their vision to use their devices on all imaginary surfaces ranging from electronic gadgets to buildings via e.g. blinds, walls, vehicles, bags and furniture.



Fig. 58 Various prototypes including non-visible DSC devices from Exeger in Sweden. Reproduced with permission from Exeger A.B.

An unexpected side effect of low-power DSC development is the technology Focus-Induced Photoresponse (FIP technique). This technology is based on the discovery that the power output from a DSC is not only dependent on the total flux of incident photons, but also on the size of the area in which they fall. Consequently, when probe light from an object is cast on a detector through a lens, the sensor response depends on how far in or out of focus the object is, i.e. a novel way to measure distances with photodetectors. 813 The technology was invented and commercialized by the company Trinamix in Germany, a wholly owned subsidiary of BASF.

# Outlook: colourful

Every significant advance over the previous decade in the development of DSCs has been made by the introduction of new principles, techniques, and materials. DSCs are becoming part of the future of electric power generation due to the following characteristics: (i) they are easy to fabricate, (ii) they are manufactured from low-cost materials, (iii) they are environmentally friendly, (iv) they have high conversion efficiencies, and (v) they perform well in diffused light and at high temperatures, conditions in which other technologies cannot compete. Based on creative research work, power conversion efficiencies of up to 20% for DSCs and 45% for ambient light DSCs can be anticipated.

Detailed understanding of many aspects of the dye-sensitized solar cell is still lacking. Charge recombination is currently the major cause of efficiency loss in DSCs and other solar cells. When one of the components (dye, redox shuttle, or semiconductor) is modified, many processes are impacted, which may boost or degrade overall performance. This needs to always be considered when new materials are introduced, and the overall system has to be adapted. DSCs are complex devices and the improvement of only one of their components will not lead to the desired targets in efficiency and stability.

Theory and computation. From the computational perspective, new theoretical tools are needed to push forward our understanding of DSCs beyond the established, successful applications outlined above. Fortunately, thanks to continuously increasing computer power and new computational paradigms, this is the right time for such developments. In silico design and optimization of materials will need to shift from single components to coupled dye/electrode or, ideally, dye/electrode/electrolyte ensembles. New algorithms based on artificial intelligence and machine learning fit to this purpose, with training databases obtained from high-throughput computations. Still, the results of such automated discoveries will need to be validated with the magnifying glass of atomistic first-principles calculations, able to dissect electronic and dynamic properties beyond the ideal picture of interfaces considered so far. In particular, we foresee a crucial role of studies addressing defects and additives that can be game changers for reaching desired efficiencies and, regarding processes, charge transfer and recombination events under operating conditions. These advancements in models and methods will bridge the gap between theory and experiments, so that computer and bench can jointly tackle the design and optimization of new DSCs.

Materials. High efficiency and panchromatic organic dye systems have been developed. These are a non toxic, low cost, sustainable, and conveniently accessible option. The next step will be to achieve a fundamental understanding of electron injection from the dye in its excited state into the conduction band of the semiconductor, in order to minimize potential and overall conversion efficiency losses at this interface. The semiconductor requires a modification of the position and of the nature of its conduction band, which can be reached through doping, morphology variation or the use of alternatives to TiO<sub>2</sub>. The dye's LUMO level should be tuned to match the potential of the conduction band edge of the semiconductor closely, to provide efficient electron injection and minimize energy losses.

In a more idealistic direction, DSCs could benefit significantly from the design of a photoinduced molecular rectification strategy built into the chromophore design. The idea of a facile electron transfer to the semiconductor with the cation trapped for extended time from the surface could ease demands on the rate of dye regeneration by slowing down the competitive back reaction, which could lead to high fill factors thanks to an increase in regeneration efficiency at the maximum power point. The D- $\pi$ -A dye design is a simple example of this approach that revolutionized the DSC field. If new designs with dramatically higher rectification effects retaining near unity quantum yields for electron injection could be put forward, another revolution within DSCs could be induced, leading to another massive gain in power conversion efficiencies.

Another consideration is the position and packing of molecules on the semiconductor surface, as well as how these factors influence electron transfer kinetics in DSCs. With examples of dyes having exceptionally low recombination losses and exceptionally high conversion efficiencies in devices operating with absorption onsets up to 700 nm in mind, several key directions remain important with regard to DSC dye design. The utilization of photons with >800 nm wavelength with the same efficiency as is observed at 700 nm is another target of the DSC field, with maximal single photoelectrode devices expected to peak at absorption onsets of 950 nm. Additionally, tandem type systems require new chromophores at both high and low energy absorption onsets (high voltage dyes and NIR dyes) with paired appropriate redox shuttles for devices where dye energy levels are well positioned to minimize energy losses. The development of these systems is key for DSCs to exceed the single photoelectrode Shockley-Queisser limit. DSCs have shown exceptional photovoltage outputs from higher energy visible light photons, and the design of dyes maximizing performance in the blue spectral region and of more positive potential redox shuttle systems could be transformative by giving tandem systems to be paired with any solar cell technology. The development of 1-electron redox shuttles that have high performances with transition metal-based sensitizers could provide a needed answer to the lower energy absorption onset challenge, since good sensitizer options already exist but are incompatible with most redox shuttle systems. Furthermore, electron transport in mesoporous semiconductor electrodes is normally described in terms of multiple trapping/detrapping, but the nature of the traps involved is unclear. It has been suggested that the electrostatic interaction between electrons in the semiconductor and ions in the electrolyte could in fact be the origin of such traps.

Future research should also concentrate on electrolyte interactions with electrodes and sensitized dyes, as well as on the impact of these interactions on photoelectrical conversion processes, and on the creation of alternative charge carrier materials to increase charge carrier's transport performance, minimize recombination losses, and improve long-term stability. Another factor to consider in these systems is the replacement of the liquid electrolyte with a solid-state electrolyte or charge transport material to avoid leakage, solvent volatilization, dye photodegradation and desorption, and counter electrode corrosion. This goal has been partially reached thanks to the introduction of metal coordination complexes, but their development is still far behind the efforts made in dye development.

Solar fuels. Most DSPEC studies to date have been carried out at pH values between 4.5 and 8.0, where the injection efficiency of the most commonly used chromophores into the conduction band of wide bandgap semiconductors such as TiO<sub>2</sub> is below 50%. In addition, stability of catalysts, chromophores and anchors also decrease as the pH is increased. There are opportunities for significant improvements in DSPEC performance and stability at low pH (e.g. pH 1) where injection efficiencies are close to 100%. Most DSPEC require an applied bias for efficient H<sub>2</sub> generation and release. Combining DSPECs and DSCs will eliminate the need for an applied bias and open the door for CO<sub>2</sub> reduction photocathodes which typically operate at larger overpotentials than proton reduction photocathodes.

Applications. The high sensitivity and efficiency of DSCs in low and ambient light conditions is one of their major benefits. They can be used where diffused solar light prevails over direct solar illumination. For this reason, the essential use of DSCs in building windows is that they operate well not just on the roof, as is the case with direct solar light irradiation in silicon cells. In the light of the global energy report, this advantage of the DSC's would also reduce the energy usage represented by buildings. This industry is a major contributor to green house emissions, consuming between 34% and 39% of electricity worldwide. The colors that DSCs can implement are another appealing feature for businesses. DSCs can be used as thin colored and transparent panels, transforming typical walls, skylights, and glass facades into electricity generators.

With continued research, it is certain that more interesting features will be revealed that could lead to improved performance of DSCs or lead to spin-off applications. The aforementioned directions are currently being pursued by researchers and exciting results are expected.

### Author contributions

ABMG and MP wrote Section 3. IB wrote Section 2.2, edited the manuscript, compiled tables and drew molecular structures. GB wrote Sections 2.1, 2.3, 2.4, 2.5 and 4.1. JJC wrote Section 6. JHD wrote Section 4.2. EAG wrote Section 5. GJM wrote Section 2.6. HP wrote Section 7. AH wrote Section 1. MF wrote Sections 4.3 and 4.4., conceptualized and oversaw the completion of the article. All authors contributed to the writing of the outlook, substantially contributed to the conception and design of the article by interpreting the relevant literature, and contributed to the critical revision and review of the manuscript.

# Conflicts of interest

GB, HP and AH are co-founders and co-owners of Dyenamo AB.

# Acknowledgements

The authors would like to thank Dr. Leif Häggman for taking the SEM image for Fig. 16. ABMG and MP acknowledge funding from the Italian Ministry of Economic Development in the framework of the Operating Agreement with ENEA for Research on the Electric System. IB acknowledges financial support from the Cloud City government. GB thanks for the support through the STandUP for Energy program. JJC's contribution has been supported by the U.S. Department of Energy, Office of Science, Division of Chemical Sciences, Geosciences, & Biosciences, Office of Basic Energy Sciences under contract DESC0012704 at Brookhaven National Laboratory. JHD acknowledges financial support from the National Science Foundation (NSF-1954922). EAG thanks The North East Centre for Energy Materials EP/R021503/1 and the ERC, starting grant, p-TYPE 715354. GJM gratefully acknowledges support from the Division of Chemical Sciences, Office of Basic Energy Sciences, Office of Energy Research, US Department of Energy (Grant DE-SC0013461). MF acknowledges the support by the Royal Society through the University Research Fellowship (URF\R1\191286) and Research Grant 2021 (RGS\R1\211321).

# Notes and references

- 1 H. Ritchie, *Energy Mix*, https://ourworldindata.org/energymix.
- 2 H. Ritchie, *Electricity Mix*, https://ourworldindata.org/electricity-mix.
- 3 D. Archer, *Global Warming: Understanding the Forecast*, John Wiley & Sons, 2nd edn, 2012.
- 4 H. Ritchie and M. Roser, *Renewable Energy*, https://ourworldindata.org/renewable-energy.
- 5 IEA, *Renewables 2020*, International Energy Agency doi:10.1787/c74616c1-en, 2020.
- 6 B. O'Regan and M. Grätzel, Nature, 1991, 353, 737-740.
- 7 H. Gerischer, J. Electrochem. Soc., 1966, 113, 1174.
- 8 H. Gerischer, Electrochimica Acta, 1990, 35, 1677–1699.
- 9 A. Hagfeldt, G. Boschloo, L. Sun, L. Kloo and H. Pettersson, *Chem. Rev.*, 2010, **110**, 6595–6663.
- 10 M. Stojanović, N. Flores-Diaz, Y. Ren, N. Vlachopoulos, L. Pfeifer, Z. Shen, Y. Liu, S. M. Zakeeruddin, J. V. Milić and A. Hagfeldt, *Helv. Chim. Acta*, 2021, n/a, year.
- 11 I. Benesperi, H. Michaels and M. Freitag, *J. Mater. Chem. C*, 2018, **6**, 11903–11942.
- 12 M. Freitag and G. Boschloo, *Current Opinion in Electrochemistry*, 2017, **2**, 111–119.
- 13 D. Zhang, M. Stojanovic, Y. Ren, Y. Cao, F. T. Eickemeyer, E. Socie, N. Vlachopoulos, J.-E. Moser, S. M. Zakeeruddin, A. Hagfeldt and M. Grätzel, *Nat. Commun.*, 2021, 12, 1777.
- 14 M. Grätzel, Journal of Photochemistry and Photobiology C: Photochemistry Reviews, 2003, 4, 145–153.
- 15 Y. Saygili, M. Söderberg, N. Pellet, F. Giordano, Y. Cao, A. B. Muñoz-García, S. M. Zakeeruddin, N. Vlachopoulos, M. Pavone, G. Boschloo, L. Kavan, J.-E. Moser, M. Grätzel, A. Hagfeldt and M. Freitag, J. Am. Chem. Soc., 2016, 138, 15087–15096.

- 16 R. Harikisun and H. Desilvestro, *Solar Energy*, 2011, **85**, 1179–1188.
- 17 A. Hinsch, J. M. Kroon, R. Kern, I. Uhlendorf, J. Holzbock, A. Meyer and J. Ferber, *Prog. Photovolt. Res. Appl.*, 2001, 9, 425–438.
- 18 J. Gao, M. B. Achari and L. Kloo, Chem. Commun., 2014, 50, 6249–6251.
- 19 W. Yang, Y. Hao, P. Ghamgosar and G. Boschloo, *Electrochimica Acta*, 2016, **213**, 879–886.
- 20 B. Li, L. Wang, B. Kang, P. Wang and Y. Qiu, *Solar Energy Materials and Solar Cells*, 2006, **90**, 549–573.
- 21 J.-H. Yum, P. Chen, M. Grätzel and M. K. Nazeeruddin, *ChemSusChem*, 2008, 1, 699–707.
- 22 I. Chung, B. Lee, J. He, R. P. H. Chang and M. G. Kanatzidis, *Nature*, 2012, **485**, 486–489.
- 23 P. Docampo, A. Hey, S. Guldin, R. Gunning, U. Steiner and H. J. Snaith, *Adv. Funct. Mater.*, 2012, **22**, 5010–5019.
- 24 J. Zhang, N. Vlachopoulos, M. Jouini, M. B. Johansson, X. Zhang, M. K. Nazeeruddin, G. Boschloo, E. M. J. Johansson and A. Hagfeldt, *Nano Energy*, 2016, **19**, 455–470.
- 25 K. Kakiage, Y. Aoyama, T. Yano, K. Oya, J.-i. Fujisawa and M. Hanaya, *Chem. Commun.*, 2015, **51**, 15894–15897.
- 26 E. Becquerel, C. R. Acad. Sci., 1839, 9, 561–567.
- 27 A. Einstein, Ann. Phys., 1905, 322, 891-921.
- 28 G. Nofuentes, B. García-Domingo, J. V. Muñoz and F. Chenlo, *Applied Energy*, 2014, **113**, 302–309.
- 29 C. A. Gueymard, D. Myers and K. Emery, *Solar Energy*, 2002, 73, 443–467.
- 30 C. A. Gueymard, Solar Energy, 2004, 76, 423-453.
- 31 Nick84, Spectrum of Solar Radiation (Earth), 14 February 2013, 15:38:46.
- 32 J. F. Randall and J. Jacot, *Renewable Energy*, 2003, **28**, 1851–1864.
- 33 H. Michaels, M. Rinderle, R. Freitag, I. Benesperi, T. Edvinsson, R. Socher, A. Gagliardi and M. Freitag, *Chem. Sci.*, 2020, 11, 2895–2906.
- 34 N. Tanabe, Fujikura Technical Review, 2013, **42**, 109–113.
- 35 F. De Rossi, T. Pontecorvo and T. M. Brown, *Applied Energy*, 2015, **156**, 413–422.
- 36 I. Mathews, P. J. King, F. Stafford and R. Frizzell, *IEEE J. Photovolt.*, 2016, **6**, 230–235.
- 37 I. Mathews, S. N. Kantareddy, T. Buonassisi and I. M. Peters, *Joule*, 2019, **3**, 1415–1426.
- 38 H. Michaels, I. Benesperi and M. Freitag, Chem. Sci., 2021.
- 39 ASTM Standard E948 16, Test Method for Electrical Performance of Photovoltaic Cells Using Reference Cells Under Simulated Sunlight, ASTM International technical report, 2020.
- 40 A. J. Frank, N. Kopidakis and J. van de Lagemaat, *Coordination Chemistry Reviews*, 2004, **248**, 1165–1179.
- 41 W. Yang, M. Pazoki, A. I. K. Eriksson, Y. Hao and G. Boschloo, *Phys. Chem. Chem. Phys.*, 2015, **17**, 16744–16751.
- 42 L. Han, N. Koide, Y. Chiba, A. Islam, R. Komiya, N. Fuke, A. Fukui and R. Yamanaka, *Appl. Phys. Lett.*, 2005, **86**, 213501.

- 43 G. Liu, H. Wang, X. Li, Y. Rong, Z. Ku, M. Xu, L. Liu, M. Hu, Y. Yang, P. Xiang, T. Shu and H. Han, *Electrochimica Acta*, 2012, 69, 334–339.
- 44 J. Kwon, N.-G. Park, J. Y. Lee, M. J. Ko and J. H. Park, *ACS Appl. Mater. Interfaces*, 2013, **5**, 2070–2074.
- 45 F. Behrouznejad, N. Taghavinia and N. Ghazyani, *Organic Electronics*, 2018, **57**, 194–200.
- 46 U. Bach, D. Lupo, P. Comte, J. E. Moser, F. Weissörtel, J. Salbeck, H. Spreitzer and M. Grätzel, *Nature*, 1998, 395, 583–585.
- 47 Y. Kashiwa, Y. Yoshida and S. Hayase, *Appl. Phys. Lett.*, 2008, **92**, 033308.
- 48 Y. Yoshida, S. S. Pandey, K. Uzaki, S. Hayase, M. Kono and Y. Yamaguchi, *Appl. Phys. Lett.*, 2009, **94**, 093301.
- 49 K. Takagi, S. Magaino, H. Saito, T. Aoki and D. Aoki, *Journal of Photochemistry and Photobiology C: Photochemistry Reviews*, 2013, **14**, 1–12.
- 50 N. Koide and L. Han, *Review of Scientific Instruments*, 2004, **75**, 2828–2831.
- 51 R. Jiang and G. Boschloo, *J. Mater. Chem. A*, 2018, **6**, 10264–10276.
- 52 H. J. Snaith, Nat. Photonics, 2012, 6, 337-340.
- 53 Y. Hao, W. Yang, L. Zhang, R. Jiang, E. Mijangos, Y. Saygili, L. Hammarström, A. Hagfeldt and G. Boschloo, *Nat. Commun.*, 2016, 7, 13934.
- 54 F. Fabregat-Santiago, G. Garcia-Belmonte, I. Mora-Seró and J. Bisquert, *Phys. Chem. Chem. Phys.*, 2011, **13**, 9083–9118.
- 55 F. Fabregat-Santiago, J. Bisquert, E. Palomares, L. Otero, D. Kuang, S. M. Zakeeruddin and M. Grätzel, *J. Phys. Chem. C*, 2007, **111**, 6550–6560.
- 56 Q. Wang, J.-E. Moser and M. Grätzel, *J. Phys. Chem. B*, 2005, **109**, 14945–14953.
- 57 P. R. F. Barnes, K. Miettunen, X. Li, A. Y. Anderson, T. Bessho, M. Gratzel and B. C. O'Regan, *Adv. Mater.*, 2013, **25**, 1881– 1922.
- 58 M. Pazoki, U. B. Cappel, E. M. J. Johansson, A. Hagfeldt and G. Boschloo, *Energy Environ. Sci.*, 2017, **10**, 672–709.
- 59 R. García-Rodríguez, R. Jiang, E. J. Canto-Aguilar, G. Oskam and G. Boschloo, *Phys. Chem. Chem. Phys.*, 2017, **19**, 32132–32142.
- 60 Y. Hao, Y. Saygili, J. Cong, A. Eriksson, W. Yang, J. Zhang, E. Polanski, K. Nonomura, S. M. Zakeeruddin, M. Grätzel, A. Hagfeldt and G. Boschloo, ACS Appl. Mater. Interfaces, 2016, 8, 32797–32804.
- 61 H. Tributsch and H. Gerischer, *Berichte Bunsenges. Für Phys. Chem.*, 1969, **73**, 850–854.
- 62 A. Zaban, S. Ferrere, J. Sprague and B. A. Gregg, *J. Phys. Chem. B*, 1997, **101**, 55–57.
- 63 S. Ardo, D. Achey, A. J. Morris, M. Abrahamsson and G. J. Meyer, *J. Am. Chem. Soc.*, 2011, **133**, 16572–16580.
- 64 K. Hu, K. C. D. Robson, E. E. Beauvilliers, E. Schott, X. Zarate, R. Arratia-Perez, C. P. Berlinguette and G. J. Meyer, *J. Am. Chem. Soc.*, 2014, **136**, 1034–1046.
- 65 L. Gundlach and F. Willig, ChemPhysChem, 2012, 13, 2877-

- 2881.
- 66 J. E. Halls and J. D. Wadhawan, *Encyclopedia of Applied Electrochemistry*, Springer, New York, NY, 2014, pp. 1556–1578.
- 67 F. Liu, M. Yang and G. J. Meyer, Handbook of Sol-Gel Science and Technology: Processing Characterization and Application; Volume II: Characterization of Sol-Gel Materials and Products, Kluwer Academic Publishers, 2005, pp. 400–428.
- 68 D. F. Zigler, Z. A. Morseth, L. Wang, D. L. Ashford, M. K. Brennaman, E. M. Grumstrup, E. C. Brigham, M. K. Gish, R. J. Dillon, L. Alibabaei, G. J. Meyer, T. J. Meyer and J. M. Papanikolas, J. Am. Chem. Soc., 2016, 138, 4426–4438.
- 69 M. C. Carey, S. L. Adelman and J. K. McCusker, *Chem. Sci.*, 2018, **10**, 134–144.
- 70 C. R. Tichnell, J. N. Miller, C. Liu, S. Mukherjee, E. Jakubikova and J. K. McCusker, *J. Phys. Chem. C*, 2020, **124**, 1794–1811.
- 71 E. Jakubikova and D. N. Bowman, *Acc. Chem. Res.*, 2015, **48**, 1441–1449.
- 72 D. N. Bowman, A. Bondarev, S. Mukherjee and E. Jakubikova, *Inorg. Chem.*, 2015, **54**, 8786–8793.
- 73 L. A. Fredin, M. Pápai, E. Rozsályi, G. Vankó, K. Wärnmark, V. Sundström and P. Persson, J. Phys. Chem. Lett., 2014, 5, 2066–2071.
- 74 T. C. B. Harlang, Y. Liu, O. Gordivska, L. A. Fredin, C. S. Ponseca, P. Huang, P. Chábera, K. S. Kjaer, H. Mateos, J. Uhlig, R. Lomoth, R. Wallenberg, S. Styring, P. Persson, V. Sundström and K. Wärnmark, *Nat. Chem.*, 2015, 7, 883–889.
- 75 Y. Liu, P. Persson, V. Sundström and K. Wärnmark, *Acc. Chem. Res.*, 2016, **49**, 1477–1485.
- 76 P. Chábera, K. S. Kjaer, O. Prakash, A. Honarfar, Y. Liu, L. A. Fredin, T. C. B. Harlang, S. Lidin, J. Uhlig, V. Sundström, R. Lomoth, P. Persson and K. Wärnmark, J. Phys. Chem. Lett., 2018, 9, 459–463.
- 77 P. Zimmer, L. Burkhardt, A. Friedrich, J. Steube, A. Neuba, R. Schepper, P. Müller, U. Flörke, M. Huber, S. Lochbrunner and M. Bauer, *Inorg. Chem.*, 2018, 57, 360–373.
- 78 J. Huang, O. Buyukcakir, M. W. Mara, A. Coskun, N. M. Dimitrijevic, G. Barin, O. Kokhan, A. B. Stickrath, R. Ruppert, D. M. Tiede, J. F. Stoddart, J.-P. Sauvage and L. X. Chen, *Angew. Chem. Int. Ed.*, 2012, 51, 12711–12715.
- 79 E. C. Brigham, D. Achey and G. J. Meyer, *Polyhedron*, 2014, 82, 181–190.
- 80 R. L. Milot and C. A. Schmuttenmaer, *Acc. Chem. Res.*, 2015, **48**, 1423–1431.
- 81 S. H. Lee, K. P. Regan, S. Hedström, A. J. Matula, S. Chaudhuri, R. H. Crabtree, V. S. Batista, C. A. Schmuttenmaer and G. W. Brudvig, *J. Phys. Chem. C*, 2017, **121**, 22690–22699.
- 82 J. Jiang, J. R. Swierk, K. L. Materna, S. Hedström, S. H. Lee, R. H. Crabtree, C. A. Schmuttenmaer, V. S. Batista and G. W. Brudvig, *J. Phys. Chem. C*, 2016, **120**, 28971–28982.
- 83 B. Abraham, H. Fan, E. Galoppini and L. Gundlach, *J. Phys. Chem. A*, 2018, **122**, 2039–2045.
- 84 R. S. Oliboni, H. Yan, H. Fan, B. Abraham, J. P. Avenoso, E. Galoppini, V. S. Batista, L. Gundlach and L. G. C. Rego, *J.*

- Phys. Chem. C, 2019, 123, 12599-12607.
- 85 L. Troian-Gautier, M. D. Turlington, S. A. M. Wehlin, A. B. Maurer, M. D. Brady, W. B. Swords and G. J. Meyer, *Chem. Rev.*, 2019, 119, 4628–4683.
- 86 J. G. Rowley, B. H. Farnum, S. Ardo and G. J. Meyer, *J. Phys. Chem. Lett.*, 2010, 1, 3132–3140.
- 87 G. Boschloo and A. Hagfeldt, Acc. Chem. Res., 2009, 42, 1819–1826.
- 88 K. C. D. Robson, K. Hu, G. J. Meyer and C. P. Berlinguette, *J. Am. Chem. Soc.*, 2013, **135**, 1961–1971.
- 89 F. Li, J. R. Jennings and Q. Wang, ACS Nano, 2013, 7, 8233–8242.
- 90 B. N. DiMarco, R. N. Sampaio, E. M. James, T. J. Barr, M. T. Bennett and G. J. Meyer, *ACS Appl. Mater. Interfaces*, 2020, 12, 23923–23930.
- 91 W. B. Swords, S. J. C. Simon, F. G. L. Parlane, R. K. Dean, C. W. Kellett, K. Hu, G. J. Meyer and C. P. Berlinguette, *Angew. Chem. Int. Ed.*, 2016, **55**, 5956–5960.
- 92 S. J. C. Simon, F. G. L. Parlane, W. B. Swords, C. W. Kellett, C. Du, B. Lam, R. K. Dean, K. Hu, G. J. Meyer and C. P. Berlinguette, *J. Am. Chem. Soc.*, 2016, **138**, 10406–10409.
- 93 F. G. L. Parlane, C. Mustoe, C. W. Kellett, S. J. Simon, W. B. Swords, G. J. Meyer, P. Kennepohl and C. P. Berlinguette, *Nat. Commun.*, 2017, **8**, 1761.
- 94 L. Casarin, W. B. Swords, S. Caramori, C. A. Bignozzi and G. J. Meyer, *Inorg. Chem.*, 2017, **56**, 7324–7327.
- 95 Y. Saygili, M. Stojanovic, H. Michaels, J. Tiepelt, J. Teuscher, A. Massaro, M. Pavone, F. Giordano, S. M. Zakeeruddin, G. Boschloo, J.-E. Moser, M. Grätzel, A. B. Muñoz-García, A. Hagfeldt and M. Freitag, ACS Appl. Energy Mater., 2018, 1, 4950–4962.
- 96 M. Freitag, F. Giordano, W. Yang, M. Pazoki, Y. Hao, B. Zietz, M. Grätzel, A. Hagfeldt and G. Boschloo, J. Phys. Chem. C, 2016, 120, 9595–9603.
- 97 B. Selvaraj, G. Shanmugam, S. Kamaraj, A. Gunasekeran and A. Sambandam, *Inorg. Chem.*, 2021, **60**, 1937–1947.
- 98 Y. Saygili, M. Stojanovic, H.-S. Kim, J. Teuscher, R. Scopelliti, M. Freitag, S. M. Zakeeruddin, J.-E. Moser, M. Grätzel and A. Hagfeldt, *J. Phys. Chem. C*, 2020, **124**, 7071–7081.
- 99 A. Glinka, M. Gierszewski, B. Gierczyk, G. Burdziński, H. Michaels, M. Freitag and M. Ziółek, J. Phys. Chem. C, 2020, 124, 2895–2906.
- 100 K. Kannankutty, C.-C. Chen, V. S. Nguyen, Y.-C. Lin, H.-H. Chou, C.-Y. Yeh and T.-C. Wei, ACS Appl. Mater. Interfaces, 2020, 12, 5812–5819.
- 101 T. Higashino, H. Iiyama, S. Nimura, Y. Kurumisawa and H. Imahori, *Inorg. Chem.*, 2020, **59**, 452–459.
- 102 S. O. Fürer, R. A. Milhuisen, M. K. Kashif, S. R. Raga, S. S. Acharya, C. Forsyth, M. Liu, L. Frazer, N. W. Duffy, C. A. Ohlin, A. M. Funston, Y. Tachibana and U. Bach, *Adv. Energy Mater.*, 2020, 10, 2002067.
- 103 I. R. Perera, T. Daeneke, S. Makuta, Z. Yu, Y. Tachibana, A. Mishra, P. Bäuerle, C. A. Ohlin, U. Bach and L. Spiccia, *Angew. Chem. Int. Ed.*, 2015, **54**, 3758–3762.

- 104 J. Nelson, S. A. Haque, D. R. Klug and J. R. Durrant, *Phys. Rev. B*, 2001, **63**, 205321.
- 105 J. Nelson and R. E. Chandler, *Coordination Chemistry Reviews*, 2004, **248**, 1181–1194.
- 106 J. Nelson, Phys. Rev. B, 1999, 59, 15374-15380.
- 107 S. Ardo and G. J. Meyer, J. Am. Chem. Soc., 2010, 132, 9283–9285.
- 108 S. Ardo and G. J. Meyer, *J. Am. Chem. Soc.*, 2011, **133**, 15384–15396.
- 109 M. D. Brady, L. Troian-Gautier, T. C. Motley, M. D. Turlington and G. J. Meyer, *ACS Appl. Mater. Interfaces*, 2019, **11**, 27453–27463.
- D. Moia, A. Szumska, V. Vaissier, M. Planells, N. Robertson,
   B. C. O'Regan, J. Nelson and P. R. F. Barnes, *J. Am. Chem. Soc.*, 2016, 138, 13197–13206.
- 111 A. V. Müller, K. T. de Oliveira, G. J. Meyer and A. S. Polo, *ACS Appl. Mater. Interfaces*, 2019, **11**, 43223–43234.
- 112 R. N. Sampaio, A. V. Müller, A. S. Polo and G. J. Meyer, *ACS Appl. Mater. Interfaces*, 2017, **9**, 33446–33454.
- 113 R. N. Sampaio, B. N. DiMarco and G. J. Meyer, *ACS Energy Lett.*, 2017, **2**, 2402–2407.
- 114 D. Moia, M. Abe, P. Wagner, H. Saguchi, N. Koumura, J. Nelson, P. R. F. Barnes and S. Mori, *J. Phys. Chem. C*, 2020, **124**, 6979–6992.
- 115 E. C. Brigham and G. J. Meyer, *J. Phys. Chem. C*, 2014, **118**, 7886–7893.
- 116 P. Xu, C. L. Gray, L. Xiao and T. E. Mallouk, *J. Am. Chem. Soc.*, 2018, **140**, 11647–11654.
- 117 R. N. Sampaio, L. Troian-Gautier and G. J. Meyer, *Angew. Chem. Int. Ed.*, 2018, **57**, 15390–15394.
- 118 R. E. Bangle and G. J. Meyer, *J. Phys. Chem. C*, 2019, **123**, 25967–25976.
- 119 R. E. Bangle, J. Schneider, E. J. Piechota, L. Troian-Gautier and G. J. Meyer, J. Am. Chem. Soc., 2020, 142, 674–679.
- 120 B. N. DiMarco, L. Troian-Gautier, R. N. Sampaio and G. J. Meyer, *Chem. Sci.*, 2018, **9**, 940–949.
- 121 L. Troian-Gautier, B. N. DiMarco, R. N. Sampaio, S. L. Marquard and G. J. Meyer, *J. Am. Chem. Soc.*, 2018, **140**, 3019–3029.
- 122 R. N. Sampaio, R. M. O'Donnell, T. J. Barr and G. J. Meyer, *J. Phys. Chem. Lett.*, 2014, **5**, 3265–3268.
- 123 R. M. O'Donnell, R. N. Sampaio, T. J. Barr and G. J. Meyer, *J. Phys. Chem. C*, 2014, **118**, 16976–16986.
- 124 B. N. DiMarco, R. M. O'Donnell and G. J. Meyer, *J. Phys. Chem. C*, 2015, **119**, 21599–21604.
- 125 K. Hu, A. D. Blair, E. J. Piechota, P. A. Schauer, R. N. Sampaio, F. G. L. Parlane, G. J. Meyer and C. P. Berlinguette, *Nat. Chem.*, 2016, **8**, 853–859.
- 126 R. N. Sampaio, E. J. Piechota, L. Troian-Gautier, A. B. Maurer, K. Hu, P. A. Schauer, A. D. Blair, C. P. Berlinguette and G. J. Meyer, *PNAS*, 2018, **115**, 7248–7253.
- 127 E. J. Piechota, L. Troian-Gautier, R. N. Sampaio, M. K. Brennaman, K. Hu, C. P. Berlinguette and G. J. Meyer, *J. Am. Chem. Soc.*, 2018, **140**, 7176–7186.

- 128 E. J. Piechota, R. N. Sampaio, L. Troian-Gautier, A. B. Maurer, C. P. Berlinguette and G. J. Meyer, *J. Phys. Chem. C*, 2019, **123**, 3416–3425.
- 129 F. Labat, T. Le Bahers, I. Ciofini and C. Adamo, *Acc. Chem. Res.*, 2012, **45**, 1268–1277.
- 130 M. Pastore, Computation, 2017, 5, 5.
- 131 F. De Angelis, Acc. Chem. Res., 2014, 47, 3349-3360.
- 132 N. Martsinovich and A. Troisi, Energy Environ. Sci., 2011, 4, 4473–4495.
- 133 J. P. Menzel, A. Papadopoulos, J. Belić, H. J. M. de Groot, L. Visscher and F. Buda, *J. Phys. Chem. C*, 2020, **124**, 27965– 27976.
- 134 J. Massin, M. Bräutigam, S. Bold, M. Wächtler, M. Pavone, A. B. Muñoz-García, B. Dietzek, V. Artero and M. Chavarot-Kerlidou, J. Phys. Chem. C, 2019, 123, 17176–17184.
- 135 S. Piccinin, D. Rocca and M. Pastore, *J. Phys. Chem. C*, 2017, **121**, 22286–22294.
- 136 H. S. Yu, S. L. Li and D. G. Truhlar, *J. Chem. Phys.*, 2016, **145**, 130901.
- 137 C. Adamo and D. Jacquemin, *Chem. Soc. Rev.*, 2013, **42**, 845–856.
- 138 K. Burke, J. Chem. Phys., 2012, 136, 150901.
- 139 P. Huang and E. A. Carter, *Annu. Rev. Phys. Chem.*, 2008, **59**, 261–290.
- 140 M. S. Hybertsen and S. G. Louie, *Phys. Rev. B*, 1986, **34**, 5390–5413.
- 141 F. Bruneval and X. Gonze, Phys. Rev. B, 2008, 78, 085125.
- 142 J. Harl, L. Schimka and G. Kresse, Phys. Rev. B, 2010, 81, 115126.
- 143 M. K. Nazeeruddin, F. De Angelis, S. Fantacci, A. Selloni, G. Viscardi, P. Liska, S. Ito, B. Takeru and M. Grätzel, *J. Am. Chem. Soc.*, 2005, **127**, 16835–16847.
- 144 F. De Angelis, S. Fantacci, A. Selloni and M. K. Nazeeruddin, *Chemical Physics Letters*, 2005, **415**, 115–120.
- 145 S. Kim, J. K. Lee, S. O. Kang, J. Ko, J.-H. Yum, S. Fantacci, F. De Angelis, D. Di Censo, M. K. Nazeeruddin and M. Grätzel, *J. Am. Chem. Soc.*, 2006, **128**, 16701–16707.
- 146 S. A. Mewes, F. Plasser, A. Krylov and A. Dreuw, *J. Chem. Theory Comput.*, 2018, **14**, 710–725.
- 147 D. Jacquemin, E. A. Perpète, G. E. Scuseria, I. Ciofini and C. Adamo, *J. Chem. Theory Comput.*, 2008, 4, 123–135.
- 148 A. Ottochian, C. Morgillo, I. Ciofini, M. J. Frisch, G. Scalmani and C. Adamo, *J. Comput. Chem.*, 2020, **41**, 1242–1251.
- 149 N. Santhanamoorthi, C.-M. Lo and J.-C. Jiang, *J. Phys. Chem. Lett.*, 2013, 4, 524–530.
- 150 A. Amat, C. Miliani, A. Romani and S. Fantacci, *Phys. Chem. Chem. Phys.*, 2015, **17**, 6374–6382.
- 151 J. Massin, S. Lyu, M. Pavone, A. B. Muñoz-García, B. Kauffmann, T. Toupance, M. Chavarot-Kerlidou, V. Artero and C. Olivier, *Dalton Trans.*, 2016, 45, 12539–12547.
- 152 D. Jacquemin, A. Planchat, C. Adamo and B. Mennucci, *J. Chem. Theory Comput.*, 2012, **8**, 2359–2372.
- 153 J. Wen, B. Han, Z. Havlas and J. Michl, *J. Chem. Theory Comput.*, 2018, **14**, 4291–4297.

- 154 M. Pastore, F. De Angelis and C. Angeli, *Theor Chem Acc*, 2016, **135**, 108.
- 155 C. Suellen, R. G. Freitas, P.-F. Loos and D. Jacquemin, *J. Chem. Theory Comput.*, 2019, **15**, 4581–4590.
- 156 F. Rizzo, M. Cavazzini, S. Righetto, F. D. Angelis, S. Fantacci and S. Quici, *Eur. J. Org. Chem.*, 2010, **2010**, 4004–4016.
- 157 S. Lyu, J. Massin, M. Pavone, A. B. Muñoz-García, C. Labrugère, T. Toupance, M. Chavarot-Kerlidou, V. Artero and C. Olivier, ACS Appl. Energy Mater., 2019, 2, 4971–4980.
- 158 T. Le Bahers, C. Adamo and I. Ciofini, *J. Chem. Theory Comput.*, 2011, 7, 2498–2506.
- 159 G. García, C. Adamo and I. Ciofini, *Phys. Chem. Chem. Phys.*, 2013, **15**, 20210–20219.
- 160 S. D. Sousa, S. Lyu, L. Ducasse, T. Toupance and C. Olivier, *J. Mater. Chem. A*, 2015, **3**, 18256–18264.
- 161 M. Olaru, E. Rychagova, S. Ketkov, Y. Shynkarenko, S. Yakunin, M. V. Kovalenko, A. Yablonskiy, B. Andreev, F. Kleemiss, J. Beckmann and M. Vogt, *J. Am. Chem. Soc.*, 2020, 142, 373–381.
- 162 L. Huet, A. Perfetto, F. Muniz-Miranda, M. Campetella, C. Adamo and I. Ciofini, J. Chem. Theory Comput., 2020, 16, 4543–4553.
- 163 E. Mosconi, J.-H. Yum, F. Kessler, C. J. Gómez García, C. Zuccaccia, A. Cinti, M. K. Nazeeruddin, M. Grätzel and F. De Angelis, *J. Am. Chem. Soc.*, 2012, **134**, 19438–19453.
- 164 S. M. Feldt, P. W. Lohse, F. Kessler, M. K. Nazeeruddin, M. Grätzel, G. Boschloo and A. Hagfeldt, *Phys. Chem. Chem. Phys.*, 2013, **15**, 7087–7097.
- 165 K. B. Ørnsø, E. Ö. Jónsson, K. W. Jacobsen and K. S. Thygesen, J. Phys. Chem. C, 2015, 119, 12792–12800.
- 166 G. Scalmani, M. J. Frisch, B. Mennucci, J. Tomasi, R. Cammi and V. Barone, *J. Chem. Phys.*, 2006, **124**, 094107.
- 167 J. A. Lemkul, J. Huang, B. Roux and A. D. MacKerell, *Chem. Rev.*, 2016, **116**, 4983–5013.
- 168 M. J. Field, P. A. Bash and M. Karplus, *J. Comput. Chem.*, 1990, **11**, 700–733.
- 169 L. W. Chung, W. M. C. Sameera, R. Ramozzi, A. J. Page, M. Hatanaka, G. P. Petrova, T. V. Harris, X. Li, Z. Ke, F. Liu, H.-B. Li, L. Ding and K. Morokuma, *Chem. Rev.*, 2015, 115, 5678–5796.
- 170 J. Preat, A. Hagfeldt and E. A. Perpète, *Energy Environ. Sci.*, 2011, **4**, 4537–4549.
- 171 S. Yun, A. Hagfeldt and T. Ma, Adv. Mater., 2014, 26, 6210–6237.
- 172 C.-T. Li, H.-Y. Chang, Y.-Y. Li, Y.-J. Huang, Y.-L. Tsai, R. Vittal, Y.-J. Sheng and K.-C. Ho, ACS Appl. Mater. Interfaces, 2015, 7, 28254–28263.
- 173 S. Tontapha, W. Sang-aroon, T. Promgool, S. Kanokmedhakul, W. Maiaugree, E. Swatsitang, V. Homrahad and V. Amornkitbumrung, *Materials Today Communications*, 2020, **22**, 100742.
- 174 X. Cui, J. Xiao, Y. Wu, P. Du, R. Si, H. Yang, H. Tian, J. Li, W.-H. Zhang, D. Deng and X. Bao, *Angew. Chem. Int. Ed.*, 2016, 55, 6708–6712.

- 175 E. German, R. Faccio and A. W. Mombrú, Applied Surface Science, 2018, 428, 118-123.
- 176 I. de P. R. Moreira, F. Illas and R. L. Martin, Phys. Rev. B, 2002, **65**, 155102.
- 177 Z. M. Gibbs, F. Ricci, G. Li, H. Zhu, K. Persson, G. Ceder, G. Hautier, A. Jain and G. J. Snyder, Npj Comput. Mater., 2017, 3, 1–7.
- 178 E. Schiavo, C. Latouche, V. Barone, O. Crescenzi, A. B. Muñoz-García and M. Pavone, Phys. Chem. Chem. Phys., 2018, **20**, 14082–14089.
- 179 B. A. Odeke, G. D. Chung, J. A. Fajemisin, K. S. Suraj, D. K. Tonui, A. R. Tobi, T. C. Bewaale, J. A. Ajibola and N. Y. Dzade, Materials, 2020, 13, 5765.
- 180 T. Olsen, C. E. Patrick, J. E. Bates, A. Ruzsinszky and K. S. Thygesen, *Npj Comput. Mater.*, 2019, **5**, 1–23.
- 181 M. C. Toroker, D. K. Kanan, N. Alidoust, L. Y. Isseroff, P. Liao and E. A. Carter, Phys. Chem. Chem. Phys., 2011, 13, 16644-16654.
- 182 H. Chen, Y. Gong, Á. Vázquez-Mayagoitia, J. Zhang and J. M. Cole, ACS Appl. Energy Mater., 2020, 3, 423-430.
- 183 P. Umari, L. Giacomazzi, F. De Angelis, M. Pastore and S. Baroni, J. Chem. Phys., 2013, 139, 014709.
- 184 O. V. Kontkanen, M. Niskanen, T. I. Hukka and T. T. Rantala, Phys. Chem. Chem. Phys., 2016, 18, 14382-14389.
- 185 M. Planells, L. Pellejà, J. N. Clifford, M. Pastore, F. D. Angelis, N. López, S. R. Marder and E. Palomares, Energy Environ. Sci., 2011, 4, 1820-1829.
- 186 M. Wykes, F. Odobel, C. Adamo, I. Ciofini and F. Labat, J Mol Model, 2016, 22, 289.
- 187 A. B. Muñoz-García, L. Caputo, E. Schiavo, C. Baiano, P. Maddalena and M. Pavone, Front. Chem., 2019, 7, 158.
- 188 K. J. Chen, A. D. Laurent, F. Boucher, F. Odobel and D. Jacquemin, J. Mater. Chem. A, 2016, 4, 2217-2227.
- 189 A. B. Muñoz-García and M. Pavone, Phys. Chem. Chem. Phys., 2015, 17, 12238-12246.
- 190 A. Carella, R. Centore, F. Borbone, M. Toscanesi, M. Trifuoggi, F. Bella, C. Gerbaldi, S. Galliano, E. Schiavo, A. Massaro, A. B. Muñoz-García and M. Pavone, Electrochimica Acta, 2018, 292, 805-816.
- 191 C. Dong, X. Li, W. Zhao, P. Jin and J. Qi, J. Phys. Chem. C, 2013, 117, 9092–9103.
- 192 W. Ma, Y. Jiao, H. Li, H. Guo, E. Kaxiras and S. Meng, ACS Appl. Mater. Interfaces, 2020, 12, 49174-49181.
- 193 M. Pastore and F. De Angelis, J. Phys. Chem. Lett., 2013, 4, 956-974.
- 194 S. I. Allec, A. Kumar and B. M. Wong, Dye-Sensitized Solar Cells, Academic Press, 2019, pp. 171–201.
- 195 R. Sánchez-de-Armas, J. Oviedo López, M. A. San-Miguel, J. F. Sanz, P. Ordejón and M. Pruneda, J. Chem. Theory Comput., 2010, 6, 2856-2865.
- 196 A. V. Akimov, A. J. Neukirch and O. V. Prezhdo, Chem. Rev., 2013, 113, 4496-4565.
- 197 Q. Huaulmé, V. M. Mwalukuku, D. Joly, J. Liotier, Y. Kervella, P. Maldivi, S. Narbey, F. Oswald, A. J. Riquelme, J. A. Anta

- and R. Demadrille, Nat. Energy, 2020, 5, 468-477.
- 198 Z. Yang, K. Li, C. Lin, L. R. Devereux, W. Zhang, C. Shao, J. M. Cole and D. Cao, ACS Appl. Energy Mater., 2020, 3, 4367-4376.
- 199 F. Li, X. Peng, Z. Wang, Y. Zhou, Y. Wu, M. Jiang and M. Xu, ENERGY Environ. Mater., 2019, 2, 280-291.
- 200 J. Westermayr and P. Marquetand, Chem. Rev., 2020.
- 201 L. Ju, M. Li, L. Tian, P. Xu and W. Lu, Materials Today Communications, 2020, 25, 101604.
- 202 Q. Arooj and F. Wang, Solar Energy, 2019, 188, 1189–1200.
- 203 V. Venkatraman, R. Raju, S. P. Oikonomopoulos and B. K. Alsberg, Journal of Cheminformatics, 2018, 10, 18.
- 204 H. N. Tsao and M. Grätzel, ACS Appl. Mater. Interfaces, 2018, 10, 36602-36607.
- 205 Y. Wen, L. Fu, G. Li, J. Ma and H. Ma, Sol. RRL, 2020, 4, 2000110.
- 206 C. B. Cooper, E. J. Beard, Á. Vázquez-Mayagoitia, L. Stan, G. B. G. Stenning, D. W. Nye, J. A. Vigil, T. Tomar, J. Jia, G. B. Bodedla, S. Chen, L. Gallego, S. Franco, A. Carella, K. R. J. Thomas, S. Xue, X. Zhu and J. M. Cole, Adv. Energy Mater., 2019, 9, 1802820.
- 207 R. Pollice, G. dos Passos Gomes, M. Aldeghi, R. J. Hickman, M. Krenn, C. Lavigne, M. Lindner-D'Addario, A. Nigam, C. T. Ser, Z. Yao and A. Aspuru-Guzik, Acc. Chem. Res., 2021, 54, 849-860.
- 208 P. M. Sommeling, B. C. O'Regan, R. R. Haswell, H. J. P. Smit, N. J. Bakker, J. J. T. Smits, J. M. Kroon and J. A. M. van Roosmalen, J. Phys. Chem. B, 2006, 110, 19191–19197.
- 209 S. Ito, T. N. Murakami, P. Comte, P. Liska, C. Grätzel, M. K. Nazeeruddin and M. Grätzel, Thin Solid Films, 2008, 516, 4613-4619.
- 210 H.-S. Kim, S.-B. Ko, I.-H. Jang and N.-G. Park, Chem. Commun., 2011, 47, 12637-12639.
- 211 A. Yella, S. Mathew, S. Aghazada, P. Comte, M. Grätzel and M. K. Nazeeruddin, J. Mater. Chem. C, 2017, 5, 2833-2843.
- 212 B. Roose, S. Pathak and U. Steiner, Chem. Soc. Rev., 2015, 44, 8326-8349.
- 213 K. Kakiage, H. Osada, Y. Aoyama, T. Yano, K. Oya, S. Iwamoto, J.-i. Fujisawa and M. Hanaya, Sci. Rep., 2016, **6**, 35888.
- 214 J. Tian, Z. Zhao, A. Kumar, R. I. Boughton and H. Liu, Chem. Soc. Rev., 2014, 43, 6920-6937.
- 215 F. Sauvage, D. Chen, P. Comte, F. Huang, L.-P. Heiniger, Y.-B. Cheng, R. A. Caruso and M. Graetzel, ACS Nano, 2010, 4, 4420-4425.
- 216 E. J. W. Crossland, N. Noel, V. Sivaram, T. Leijtens, J. A. Alexander-Webber and H. J. Snaith, Nature, 2013, 495, 215-
- 217 W. Li, Z. Wu, J. Wang, A. A. Elzatahry and D. Zhao, Chem. Mater., 2014, 26, 287-298.
- 218 M. Pazoki, N. Taghavinia, A. Hagfeldt and G. Boschloo, J. Phys. Chem. C, 2014, 118, 16472-16478.
- 219 M. Pazoki, J. Oscarsson, L. Yang, B. W. Park, E. M. J. Johansson, H. Rensmo, A. Hagfeldt and G. Boschloo, RSC Adv.,

- 2014, 4, 50295-50300.
- 220 D. Chen, L. Cao, F. Huang, P. Imperia, Y.-B. Cheng and R. A. Caruso, *J. Am. Chem. Soc.*, 2010, **132**, 4438–4444.
- 221 A. Fujishima, X. Zhang and D. A. Tryk, *Surface Science Reports*, 2008, **63**, 515–582.
- 222 Q. Zhang, C. S. Dandeneau, X. Zhou and G. Cao, *Adv. Mater.*, 2009, **21**, 4087–4108.
- 223 R. Vittal and K.-C. Ho, Renewable and Sustainable Energy Reviews, 2017, **70**, 920–935.
- 224 Q. Wali, A. Fakharuddin and R. Jose, *Journal of Power Sources*, 2015, **293**, 1039–1052.
- 225 J. Wan, L. Tao, B. Wang, J. Zhang, H. Wang and P. D. Lund, *Journal of Power Sources*, 2019, **438**, 227012.
- 226 T. Peng, J. Xu and R. Chen, *Chemical Physics Letters*, 2020, **738**, 136902.
- 227 N. Memarian, I. Concina, A. Braga, S. M. Rozati, A. Vomiero and G. Sberveglieri, *Angew. Chem. Int. Ed.*, 2011, **50**, 12321–12325.
- 228 Y.-F. Wang, K.-N. Li, W.-Q. Wu, Y.-F. Xu, H.-Y. Chen, C.-Y. Su and D.-B. Kuang, *RSC Adv.*, 2013, **3**, 13804–13810.
- 229 L. Tao, Z. Sun, L. Chen, M. Liang and S. Xue, *Chem. Commun.*, 2020, **56**, 5042–5045.
- 230 S. S. Shin, J. H. Suk, B. J. Kang, W. Yin, S. J. Lee, J. H. Noh, T. K. Ahn, F. Rotermund, I. S. Cho and S. I. Seok, *Energy Environ. Sci.*, 2019, **12**, 958–964.
- 231 V. Ganapathy, B. Karunagaran and S.-W. Rhee, *Journal of Power Sources*, 2010, **195**, 5138–5143.
- 232 C.-Y. Cho, S. Baek, K. Kim and J. H. Moon, *RSC Adv.*, 2016, **6**, 74003–74008.
- 233 B. E. Hardin, H. J. Snaith and M. D. McGehee, *Nat. Photonics*, 2012, **6**, 162–169.
- 234 C.-Y. Chen, M. Wang, J.-Y. Li, N. Pootrakulchote, L. Alibabaei, C.-h. Ngoc-le, J.-D. Decoppet, J.-H. Tsai, C. Grätzel, C.-G. Wu, S. M. Zakeeruddin and M. Grätzel, ACS Nano, 2009, 3, 3103–3109.
- 235 H. Ozawa, Y. Okuyama and H. Arakawa, *Dalton Trans.*, 2012, **41**, 5137–5139.
- 236 H. Ozawa, T. Sugiura, T. Kuroda, K. Nozawa and H. Arakawa, *J. Mater. Chem. A*, 2016, **4**, 1762–1770.
- 237 T. Kono, N. Masaki, M. Nishikawa, R. Tamura, H. Matsuzaki, M. Kimura and S. Mori, ACS Appl. Mater. Interfaces, 2016, 8, 16677–16683.
- 238 L. E. Polander, A. Yella, B. F. E. Curchod, N. Ashari Astani, J. Teuscher, R. Scopelliti, P. Gao, S. Mathew, J.-E. Moser, I. Tavernelli, U. Rothlisberger, M. Grätzel, M. K. Nazeeruddin and J. Frey, *Angew. Chem. Int. Ed.*, 2013, **52**, 8731–8735.
- 239 S. Aghazada, P. Gao, A. Yella, G. Marotta, T. Moehl, J. Teuscher, J.-E. Moser, F. De Angelis, M. Grätzel and M. K. Nazeeruddin, *Inorg. Chem.*, 2016, **55**, 6653–6659.
- 240 S. Aghazada, Y. Ren, P. Wang and M. K. Nazeeruddin, *Inorg. Chem.*, 2017, **56**, 13437–13445.
- 241 K.-L. Wu, A. J. Huckaba, J. N. Clifford, Y.-W. Yang, A. Yella, E. Palomares, M. Grätzel, Y. Chi and M. K. Nazeeruddin, *In-org. Chem.*, 2016, 55, 7388–7395.

- 242 K.-L. Wu, Y. Hu, C.-T. Chao, Y.-W. Yang, T.-Y. Hsiao, N. Robertson and Y. Chi, *J. Mater. Chem. A*, 2014, 2, 19556– 19565.
- 243 M. V. Bobo, A. Paul, A. J. Robb, A. M. Arcidiacono, M. D. Smith, K. Hanson and A. K. Vannucci, *Inorg. Chem.*, 2020, 59, 6351–6358.
- 244 T. Yamaguchi, T. Miyabe, T. Ono and H. Arakawa, *Chem. Commun.*, 2010, **46**, 5802–5804.
- 245 K.-L. Wu, S.-T. Ho, C.-C. Chou, Y.-C. Chang, H.-A. Pan, Y. Chi and P.-T. Chou, *Angew. Chem. Int. Ed.*, 2012, **51**, 5642–5646.
- 246 T. Kinoshita, K. Nonomura, N. Joong Jeon, F. Giordano, A. Abate, S. Uchida, T. Kubo, S. I. Seok, M. K. Nazeeruddin, A. Hagfeldt, M. Grätzel and H. Segawa, *Nat. Commun.*, 2015, 6, 8834.
- 247 S. Fuse, S. Sugiyama, M. M. Maitani, Y. Wada, Y. Ogomi, S. Hayase, R. Katoh, T. Kaiho and T. Takahashi, *Chem. Eur. J.*, 2014, **20**, 10685–10694.
- 248 K. Matsumura, S. Yoshizaki, M. M. Maitani, Y. Wada, Y. Ogomi, S. Hayase, T. Kaiho, S. Fuse, H. Tanaka and T. Takahashi, *Chem. Eur. J.*, 2015, **21**, 9742–9747.
- 249 D. J. Schipper and K. Fagnou, Chem. Mater., 2011, 23, 1594– 1600.
- 250 S. Tamba, R. Fujii, A. Mori, K. Hara and N. Koumura, *Chem. Lett.*, 2011, **40**, 922–924.
- 251 W. Wang, X. Li, J. Lan, D. Wu, R. Wang and J. You, *J. Org. Chem.*, 2018, **83**, 8114–8126.
- 252 J. Zhang, W. Chen, A. J. Rojas, E. V. Jucov, T. V. Timofeeva, T. C. Parker, S. Barlow and S. R. Marder, *J. Am. Chem. Soc.*, 2013, **135**, 16376–16379.
- 253 X. Kang, J. Zhang, D. O'Neil, A. J. Rojas, W. Chen, P. Szymanski, S. R. Marder and M. A. El-Sayed, *Chem. Mater.*, 2014, 26, 4486–4493.
- 254 K. Okamoto, J. Zhang, J. B. Housekeeper, S. R. Marder and C. K. Luscombe, *Macromolecules*, 2013, **46**, 8059–8078.
- 255 P.-H. Lin, T.-J. Lu, D.-J. Cai, K.-M. Lee and C.-Y. Liu, *Chem-SusChem*, 2015, **8**, 3222–3227.
- 256 N. P. Liyanage, A. Yella, M. Nazeeruddin, M. Grätzel and J. H. Delcamp, *ACS Appl. Mater. Interfaces*, 2016, **8**, 5376–5384.
- 257 A. Baumann, J. Watson and J. H. Delcamp, *ChemSusChem*, 2020, **13**, 283–286.
- 258 Y.-S. Ciou, P.-H. Lin, W.-M. Li, K.-M. Lee and C.-Y. Liu, *J. Org. Chem.*, 2017, **82**, 3538–3551.
- 259 S. Ito, H. Miura, S. Uchida, M. Takata, K. Sumioka, P. Liska, P. Comte, P. Péchy and M. Grätzel, *Chem. Commun.*, 2008, 5194–5196.
- 260 W. Zhang, Y. Wu, X. Li, E. Li, X. Song, H. Jiang, C. Shen, H. Zhang, H. Tian and W.-H. Zhu, *Chem. Sci.*, 2017, 8, 2115– 2124.
- 261 J. Yang, P. Ganesan, J. Teuscher, T. Moehl, Y. J. Kim, C. Yi, P. Comte, K. Pei, T. W. Holcombe, M. K. Nazeeruddin, J. Hua, S. M. Zakeeruddin, H. Tian and M. Grätzel, *J. Am. Chem. Soc.*, 2014, 136, 5722–5730.
- 262 J.-H. Yum, T. W. Holcombe, Y. Kim, K. Rakstys, T. Moehl,

- J. Teuscher, J. H. Delcamp, M. K. Nazeeruddin and M. Grätzel, *Sci. Rep.*, 2013, **3**, 2446.
- 263 R. Li, J. Liu, N. Cai, M. Zhang and P. Wang, *J. Phys. Chem. B*, 2010, **114**, 4461–4464.
- 264 H. Cheema, J. Watson, A. Peddapuram and J. H. Delcamp, *Chem. Commun.*, 2020, **56**, 1741–1744.
- 265 P. Brogdon, F. Giordano, G. A. Puneky, A. Dass, S. M. Za-keeruddin, M. K. Nazeeruddin, M. Grätzel, G. S. Tschumper and J. H. Delcamp, *Chem. Eur. J.*, 2016, **22**, 694–703.
- 266 H. Cheema, J. Watson and J. H. Delcamp, *Solar Energy*, 2020, **208**, 747–752.
- 267 H. Cheema, J. Watson, P. S. Shinde, R. R. Rodrigues, S. Pan and J. H. Delcamp, *Chem. Commun.*, 2020, **56**, 1569–1572.
- 268 H. Cheema and J. H. Delcamp, Adv. Energy Mater., 2019, 9, 1900162.
- 269 P. Wang, L. Yang, H. Wu, Y. Cao, J. Zhang, N. Xu, S. Chen, J.-D. Decoppet, S. M. Zakeeruddin and M. Grätzel, *Joule*, 2018, 2, 2145–2153.
- 270 A. Baumann, C. Curiac and J. H. Delcamp, *ChemSusChem*, 2020, **13**, 2503–2512.
- 271 S. M. Feldt, E. A. Gibson, E. Gabrielsson, L. Sun, G. Boschloo and A. Hagfeldt, *J. Am. Chem. Soc.*, 2010, **132**, 16714– 16724.
- 272 H. N. Tsao, C. Yi, T. Moehl, J.-H. Yum, S. M. Zakeeruddin, M. K. Nazeeruddin and M. Grätzel, *ChemSusChem*, 2011, 4, 591–594.
- 273 J.-H. Yum, E. Baranoff, F. Kessler, T. Moehl, S. Ahmad, T. Bessho, A. Marchioro, E. Ghadiri, J.-E. Moser, C. Yi, M. K. Nazeeruddin and M. Grätzel, *Nat. Commun.*, 2012, **3**, 631.
- 274 W. Zhang, Y. Wu, H. W. Bahng, Y. Cao, C. Yi, Y. Saygili, J. Luo, Y. Liu, L. Kavan, J.-E. Moser, A. Hagfeldt, H. Tian, S. M. Zakeeruddin, W.-H. Zhu and M. Grätzel, *Energy Envi*ron. Sci., 2018, 11, 1779–1787.
- 275 Y. Wu, W.-H. Zhu, S. M. Zakeeruddin and M. Grätzel, *ACS Appl. Mater. Interfaces*, 2015, 7, 9307–9318.
- 276 Y. Liu, Y. Cao, W. Zhang, M. Stojanovic, M. I. Dar, P. Péchy, Y. Saygili, A. Hagfeldt, S. M. Zakeeruddin and M. Grätzel, *Angew. Chem. Int. Ed.*, 2018, **57**, 14125–14128.
- 277 Y. Cao, Y. Liu, S. M. Zakeeruddin, A. Hagfeldt and M. Grätzel, *Joule*, 2018, **2**, 1108–1117.
- 278 L. Yang, S. Chen, J. Zhang, J. Wang, M. Zhang, X. Dong and P. Wang, *J. Mater. Chem. A*, 2017, **5**, 3514–3522.
- 279 Z. Yao, M. Zhang, H. Wu, L. Yang, R. Li and P. Wang, *J. Am. Chem. Soc.*, 2015, **137**, 3799–3802.
- 280 Y. Ren, D. Sun, Y. Cao, H. N. Tsao, Y. Yuan, S. M. Zakeeruddin, P. Wang and M. Grätzel, *J. Am. Chem. Soc.*, 2018, **140**, 2405–2408.
- 281 H. Wu, X. Xie, Y. Mei, Y. Ren, Z. Shen, S. Li and P. Wang, *ACS Photonics*, 2019, **6**, 1216–1225.
- 282 L. Zhang, X. Yang, W. Wang, G. G. Gurzadyan, J. Li, X. Li, J. An, Z. Yu, H. Wang, B. Cai, A. Hagfeldt and L. Sun, *ACS Energy Lett.*, 2019, 4, 943–951.
- 283 K. Kakiage, Y. Aoyama, T. Yano, K. Oya, T. Kyomen and M. Hanaya, *Chem. Commun.*, 2015, **51**, 6315–6317.

- 284 K. Kakiage, Y. Aoyama, T. Yano, T. Otsuka, T. Kyomen, M. Unno and M. Hanaya, *Chem. Commun.*, 2014, **50**, 6379–6381.
- 285 J. Sobuś, B. Gierczyk, G. Burdziński, M. Jancelewicz, E. Polanski, A. Hagfeldt and M. Ziółek, *Chem. Eur. J.*, 2016, **22**, 15807–15818.
- 286 R. R. Rodrigues, A. Peddapuram, A. L. Dorris, N. I. Hammer and J. H. Delcamp, *ACS Appl. Energy Mater.*, 2019, **2**, 5547–5556.
- 287 R. R. Rodrigues, H. Cheema and J. H. Delcamp, *Angew. Chem. Int. Ed.*, 2018, **57**, 5472–5476.
- 288 T. Bessho, S. M. Zakeeruddin, C.-Y. Yeh, E. W.-G. Diau and M. Grätzel, *Angew. Chem. Int. Ed.*, 2010, **49**, 6646–6649.
- 289 A. Yella, H.-W. Lee, H. N. Tsao, C. Yi, A. K. Chandiran, M. K. Nazeeruddin, E. W.-G. Diau, C.-Y. Yeh, S. M. Zakeeruddin and M. Grätzel, *Science*, 2011, **334**, 629–634.
- 290 A. Yella, C.-L. Mai, S. M. Zakeeruddin, S.-N. Chang, C.-H. Hsieh, C.-Y. Yeh and M. Grätzel, *Angew. Chem. Int. Ed.*, 2014, 53, 2973–2977.
- 291 S. Mathew, A. Yella, P. Gao, R. Humphry-Baker, B. F. E. Curchod, N. Ashari-Astani, I. Tavernelli, U. Rothlisberger, M. K. Nazeeruddin and M. Grätzel, *Nat. Chem.*, 2014, 6, 242–247.
- 292 S. H. Kang, M. J. Jeong, Y. K. Eom, I. T. Choi, S. M. Kwon, Y. Yoo, J. Kim, J. Kwon, J. H. Park and H. K. Kim, *Adv. Energy Mater.*, 2017, 7, 1602117.
- 293 Y. K. Eom, S. H. Kang, I. T. Choi, Y. Yoo, J. Kim and H. K. Kim, *J. Mater. Chem. A*, 2017, **5**, 2297–2308.
- 294 S. Mathew, N. A. Astani, B. F. E. Curchod, J. H. Delcamp, M. Marszalek, J. Frey, U. Rothlisberger, M. K. Nazeeruddin and M. Grätzel, *J. Mater. Chem. A*, 2016, 4, 2332–2339.
- 295 J. Luo, M. Xu, R. Li, K.-W. Huang, C. Jiang, Q. Qi, W. Zeng, J. Zhang, C. Chi, P. Wang and J. Wu, J. Am. Chem. Soc., 2014, 136, 265–272.
- 296 J. Luo, J. Zhang, K.-W. Huang, Q. Qi, S. Dong, J. Zhang, P. Wang and J. Wu, J. Mater. Chem. A, 2016, 4, 8428–8434.
- 297 H.-H. Chou, K. S. K. Reddy, H.-P. Wu, B.-C. Guo, H.-W. Lee, E. W.-G. Diau, C.-P. Hsu and C.-Y. Yeh, ACS Appl. Mater. Interfaces, 2016, 8, 3418–3427.
- 298 Y. Wang, B. Chen, W. Wu, X. Li, W. Zhu, H. Tian and Y. Xie, *Angew. Chem. Int. Ed.*, 2014, **53**, 10779–10783.
- 299 Y. Xie, Y. Tang, W. Wu, Y. Wang, J. Liu, X. Li, H. Tian and W.-H. Zhu, *J. Am. Chem. Soc.*, 2015, **137**, 14055–14058.
- 300 Y. Tang, Y. Wang, X. Li, H. Ågren, W.-H. Zhu and Y. Xie, *ACS Appl. Mater. Interfaces*, 2015, 7, 27976–27985.
- 301 H. Zhou, J.-M. Ji, S. H. Kang, M. S. Kim, H. S. Lee, C. H. Kim and H. K. Kim, *J. Mater. Chem. C*, 2019, 7, 2843–2852.
- 302 G. Yang, Y. Tang, X. Li, H. Ågren and Y. Xie, *ACS Appl. Mater. Interfaces*, 2017, **9**, 36875–36885.
- 303 N. V. Krishna, J. V. S. Krishna, S. P. Singh, L. Giribabu, L. Han, I. Bedja, R. K. Gupta and A. Islam, *J. Phys. Chem.* C, 2017, 121, 6464–6477.
- 304 W. Li, Z. Liu, H. Wu, Y.-B. Cheng, Z. Zhao and H. He, *J. Phys. Chem. C*, 2015, **119**, 5265–5273.
- 305 T. Higashino, Y. Fujimori, K. Sugiura, Y. Tsuji, S. Ito and

- H. Imahori, Angew. Chem. Int. Ed., 2015, 54, 9052-9056.
- 306 L. Si, H. He and K. Zhu, New J. Chem., 2014, 38, 1565-1572.
- 307 C.-C. Chen, J.-S. Chen, V. S. Nguyen, T.-C. Wei and C.-Y. Yeh, *Angew. Chem. Int. Ed.*, 2021, **60**, 4886–4893.
- 308 C.-L. Wang, M. Zhang, Y.-H. Hsiao, C.-K. Tseng, C.-L. Liu, M. Xu, P. Wang and C.-Y. Lin, *Energy Environ. Sci.*, 2016, 9, 200–206.
- 309 H. Cheema, A. Baumann, E. K. Loya, P. Brogdon, L. E. Mc-Namara, C. A. Carpenter, N. I. Hammer, S. Mathew, C. Risko and J. H. Delcamp, *ACS Appl. Mater. Interfaces*, 2019, **11**, 16474–16489.
- 310 S. Chakraborty, H.-C. You, C.-K. Huang, B.-Z. Lin, C.-L. Wang, M.-C. Tsai, C.-L. Liu and C.-Y. Lin, *J. Phys. Chem. C*, 2017, **121**, 7081–7087.
- 311 K. Zeng, W. Tang, C. Li, Y. Chen, S. Zhao, Q. Liu and Y. Xie, *J. Mater. Chem. A*, 2019, **7**, 20854–20860.
- 312 K. Zeng, Y. Lu, W. Tang, S. Zhao, Q. Liu, W. Zhu, H. Tian and Y. Xie, *Chem. Sci.*, 2019, **10**, 2186–2192.
- 313 K. Zeng, Y. Chen, W.-H. Zhu, H. Tian and Y. Xie, *J. Am. Chem. Soc.*, 2020, **142**, 5154–5161.
- 314 R. Bisht, M. F. Mele Kavungathodi and J. Nithyanandhan, *Chem. Eur. J.*, 2018, **24**, 16368–16378.
- 315 A. Alagumalai, M. F. M. K., P. Vellimalai, M. C. Sil and J. Nithyanandhan, *ACS Appl. Mater. Interfaces*, 2016, **8**, 35353–35367.
- 316 J. H. Delcamp, Y. Shi, J.-H. Yum, T. Sajoto, E. Dell'Orto, S. Barlow, M. K. Nazeeruddin, S. R. Marder and M. Grätzel, *Chem. Eur. J.*, 2013, **19**, 1819–1827.
- 317 F. M. Jradi, X. Kang, D. O'Neil, G. Pajares, Y. A. Getmanenko, P. Szymanski, T. C. Parker, M. A. El-Sayed and S. R. Marder, Chem. Mater., 2015, 27, 2480–2487.
- 318 F. M. Jradi, D. O'Neil, X. Kang, J. Wong, P. Szymanski, T. C. Parker, H. L. Anderson, M. A. El-Sayed and S. R. Marder, Chem. Mater., 2015, 27, 6305–6313.
- 319 T. Maeda, S. Arikawa, H. Nakao, S. Yagi and H. Nakazumi, *New J. Chem.*, 2013, **37**, 701–708.
- 320 S. Paek, H. Choi, C. Kim, N. Cho, S. So, K. Song, M. K. Nazeeruddin and J. Ko, *Chem. Commun.*, 2011, **47**, 2874–2876.
- 321 J.-Y. Li, C.-Y. Chen, W.-C. Ho, S.-H. Chen and C.-G. Wu, *Org. Lett.*, 2012, **14**, 5420–5423.
- 322 V. Punitharasu, M. F. Mele Kavungathodi, A. K. Singh and J. Nithyanandhan, *ACS Appl. Energy Mater.*, 2019, **2**, 8464–8472.
- 323 C. Qin, Y. Numata, S. Zhang, X. Yang, A. Islam, K. Zhang, H. Chen and L. Han, *Adv. Funct. Mater.*, 2014, **24**, 3059–3066.
- 324 G. H. Rao, A. Venkateswararao, L. Giribabu, L. Han, I. Bedja, R. K. Gupta, A. Islam and S. P. Singh, *Phys. Chem. Chem. Phys.*, 2016, **18**, 14279–14285.
- 325 N. Asim, K. Sopian, S. Ahmadi, K. Saeedfar, M. A. Alghoul, O. Saadatian and S. H. Zaidi, *Renewable and Sustainable Energy Reviews*, 2012, **16**, 5834–5847.
- 326 M. S. Su'ait, M. Y. A. Rahman and A. Ahmad, Solar Energy,

- 2015, **115**, 452–470.
- 327 S. Ahmad, E. Guillén, L. Kavan, M. Grätzel and M. K. Nazeeruddin, *Energy Environ. Sci.*, 2013, **6**, 3439–3466.
- 328 S. Mastroianni, I. Asghar, K. Miettunen, J. Halme, A. Lanuti, T. M. Brown and P. Lund, *Phys. Chem. Chem. Phys.*, 2014, **16**, 6092–6100.
- 329 M. I. Asghar, K. Miettunen, J. Halme, P. Vahermaa, M. Toivola, K. Aitola and P. Lund, *Energy Environ. Sci.*, 2010, **3**, 418–426.
- 330 M. K. Kashif, J. C. Axelson, N. W. Duffy, C. M. Forsyth, C. J. Chang, J. R. Long, L. Spiccia and U. Bach, *J. Am. Chem. Soc.*, 2012, **134**, 16646–16653.
- 331 J. Wu, Z. Lan, J. Lin, M. Huang, Y. Huang, L. Fan and G. Luo, Chem. Rev., 2015, 115, 2136–2173.
- 332 S. Mozaffari, M. R. Nateghi and M. B. Zarandi, *Renewable and Sustainable Energy Reviews*, 2017, **71**, 675–686.
- 333 G. P. Salvador, D. Pugliese, F. Bella, A. Chiappone, A. Sacco, S. Bianco and M. Quaglio, *Electrochimica Acta*, 2014, 146, 44–51.
- 334 C.-Y. Hsu, Y.-C. Chen, R. Y.-Y. Lin, K.-C. Ho and J. T. Lin, *Phys. Chem. Chem. Phys.*, 2012, **14**, 14099–14109.
- 335 S. M. Feldt, G. Wang, G. Boschloo and A. Hagfeldt, *J. Phys. Chem. C*, 2011, **115**, 21500–21507.
- 336 U. B. Cappel, S. M. Feldt, J. Schöneboom, A. Hagfeldt and G. Boschloo, *J. Am. Chem. Soc.*, 2010, **132**, 9096–9101.
- 337 L. Kavan, Current Opinion in Electrochemistry, 2017, **2**, 88–96.
- 338 J.-W. Shiu, Y.-C. Chang, C.-Y. Chan, H.-P. Wu, H.-Y. Hsu, C.-L. Wang, C.-Y. Lin and E. W.-G. Diau, *J. Mater. Chem. A*, 2014, 3, 1417–1420.
- 339 Y. Bai, Q. Yu, N. Cai, Y. Wang, M. Zhang and P. Wang, *Chem. Commun.*, 2011, **47**, 4376–4378.
- 340 S. Tatay, S. A. Haque, B. O'Regan, J. R. Durrant, W. J. H. Verhees, J. M. Kroon, A. Vidal-Ferran, P. Gaviña and E. Palomares, *J. Mater. Chem.*, 2007, 17, 3037–3044.
- 341 M. Freitag, J. Teuscher, Y. Saygili, X. Zhang, F. Giordano, P. Liska, J. Hua, S. M. Zakeeruddin, J.-E. Moser, M. Grätzel and A. Hagfeldt, *Nat. Photonics*, 2017, **11**, 372–378.
- 342 T. J. Zerk, C. T. Saouma, J. M. Mayer and W. B. Tolman, *Inorg. Chem.*, 2019, **58**, 14151–14158.
- 343 S. C. Pradhan, A. Hagfeldt and S. Soman, *J. Mater. Chem. A*, 2018, **6**, 22204–22214.
- 344 M. Magni, R. Giannuzzi, A. Colombo, M. P. Cipolla, C. Dragonetti, S. Caramori, S. Carli, R. Grisorio, G. P. Suranna, C. A. Bignozzi, D. Roberto and M. Manca, *Inorg. Chem.*, 2016, **55**, 5245–5253.
- 345 R. R. Rodrigues, J. M. Lee, N. S. Taylor, H. Cheema, L. Chen, R. C. Fortenberry, J. H. Delcamp and J. W. Jurss, *Dalton Trans.*, 2020, **49**, 343–355.
- 346 H. Michaels, I. Benesperi, T. Edvinsson, A. B. Muñoz-Garcia, M. Pavone, G. Boschloo and M. Freitag, *Inorganics*, 2018, 6, 53.
- 347 T. Higashino and H. Imahori, *Dalton Trans.*, 2015, **44**, 448–463.

- 348 M. Freitag, W. Yang, L. A. Fredin, L. D'Amario, K. M. Karlsson, A. Hagfeldt and G. Boschloo, ChemPhysChem, 2016, 17, 3845-3852.
- 349 W. Yang, N. Vlachopoulos, Y. Hao, A. Hagfeldt and G. Boschloo, Phys. Chem. Chem. Phys., 2015, 17, 15868-
- 350 J. Burschka, V. Brault, S. Ahmad, L. Breau, M. K. Nazeeruddin, B. Marsan, S. M. Zakeeruddin and M. Grätzel, Energy Environ. Sci., 2012, 5, 6089-6097.
- 351 C.-H. Tsai, C.-Y. Lu, M.-C. Chen, T.-W. Huang, C.-C. Wu and Y.-W. Chung, Organic Electronics, 2013, 14, 3131-3137.
- 352 F. Bella and R. Bongiovanni, Journal of Photochemistry and Photobiology C: Photochemistry Reviews, 2013, 16, 1-21.
- 353 A. Gagliardi, D. Gentilini and A. D. Carlo, J. Phys. Chem. C, 2012, 116, 23882–23889.
- 354 S. Ardo and G. J. Meyer, Chem. Soc. Rev., 2008, 38, 115-164.
- 355 Z. Yu, N. Vlachopoulos, M. Gorlov and L. Kloo, Dalton Trans., 2011, 40, 10289-10303.
- 356 Z. Yu, M. Gorlov, J. Nissfolk, G. Boschloo and L. Kloo, J. Phys. Chem. C, 2010, 114, 10612-10620.
- 357 H. Iftikhar, G. G. Sonai, S. G. Hashmi, A. F. Nogueira and P. D. Lund, Materials, 2019, 12, 1998.
- 358 Q. Yu, D. Zhou, Y. Shi, X. Si, Y. Wang and P. Wang, Energy Environ. Sci., 2010, 3, 1722-1725.
- 359 M. A. Green, E. D. Dunlop, J. Hohl-Ebinger, M. Yoshita, N. Kopidakis and X. Hao, Prog. Photovolt. Res. Appl., 2020, **28**, 629-638.
- 360 M. Gorlov, H. Pettersson, A. Hagfeldt and L. Kloo, Inorg. Chem., 2007, 46, 3566-3575.
- 361 G. Oskam, B. V. Bergeron, G. J. Meyer and P. C. Searson, J. Phys. Chem. B, 2001, 105, 6867-6873.
- 362 Y. Saygili, M. Stojanovic, N. Flores-Díaz, S. M. Zakeeruddin, N. Vlachopoulos, M. Grätzel and A. Hagfeldt, Inorganics, 2019, 7, 30.
- 363 Y. Liu, J. R. Jennings, Y. Huang, Q. Wang, S. M. Zakeeruddin and M. Grätzel, J. Phys. Chem. C, 2011, 115, 18847-18855.
- 364 H. Ellis, S. K. Eriksson, S. M. Feldt, E. Gabrielsson, P. W. Lohse, R. Lindblad, L. Sun, H. Rensmo, G. Boschloo and A. Hagfeldt, J. Phys. Chem. C, 2013, 117, 21029-21036.
- 365 H. Ellis, I. Schmidt, A. Hagfeldt, G. Wittstock and G. Boschloo, J. Phys. Chem. C, 2015, 119, 21775-21783.
- 366 M. Nasr-Esfahani, M. Zendehdel, N. Y. Nia, B. Jafari and M. K. Babadi, RSC Adv., 2014, 4, 15961-15967.
- 367 S. Koussi-Daoud, D. Schaming, L. Fillaud, G. Trippé-Allard, F. Lafolet, E. Polanski, K. Nonomura, N. Vlachopoulos, A. Hagfeldt and J.-C. Lacroix, Electrochimica Acta, 2015, **179**, 237-240.
- 368 M. K. Kashif, M. Nippe, N. W. Duffy, C. M. Forsyth, C. J. Chang, J. R. Long, L. Spiccia and U. Bach, Angew. Chem. Int. Ed., 2013, **52**, 5527–5531.
- 369 M. K. Kashif, R. A. Milhuisen, M. Nippe, J. Hellerstedt, D. Z. Zee, N. W. Duffy, B. Halstead, F. D. Angelis, S. Fantacci, M. S. Fuhrer, C. J. Chang, Y.-B. Cheng, J. R. Long, L. Spiccia and U. Bach, Adv. Energy Mater., 2016, 6, 1600874.

- 370 W. Xiang, W. Huang, U. Bach and L. Spiccia, Chem. Commun., 2013, 49, 8997-8999.
- 371 C. Dong, W. Xiang, F. Huang, D. Fu, W. Huang, U. Bach, Y.-B. Cheng, X. Li and L. Spiccia, Angew. Chem. Int. Ed., 2014, **53**, 6933–6937.
- 372 H. Ellis, R. Jiang, S. Ye, A. Hagfeldt and G. Boschloo, Phys. Chem. Chem. Phys., 2016, 18, 8419-8427.
- 373 S. Hattori, Y. Wada, S. Yanagida and S. Fukuzumi, J. Am. Chem. Soc., 2005, 127, 9648-9654.
- 374 K. D. Karlin and J. K. Yandell, Inorg. Chem., 1984, 23, 1184-
- 375 J. Cong, D. Kinschel, Q. Daniel, M. Safdari, E. Gabrielsson, H. Chen, P. H. Svensson, L. Sun and L. Kloo, J. Mater. Chem. A, 2016, 4, 14550–14554.
- 376 M. Magni, A. Colombo, C. Dragonetti and P. Mussini, Electrochimica Acta, 2014, 141, 324-330.
- 377 A. Colombo, C. Dragonetti, M. Magni, D. Roberto, F. Demartin, S. Caramori and C. A. Bignozzi, ACS Appl. Mater. Interfaces, 2014, 6, 13945-13955.
- 378 C. Dragonetti, M. Magni, A. Colombo, F. Melchiorre, P. Biagini and D. Roberto, ACS Appl. Energy Mater., 2018, 1, 751-756.
- 379 A. Colombo, G. Di Carlo, C. Dragonetti, M. Magni, A. Orbelli Biroli, M. Pizzotti, D. Roberto, F. Tessore, E. Benazzi, C. A. Bignozzi, L. Casarin and S. Caramori, Inorg. Chem., 2017, **56**, 14189–14197.
- 380 E. Benazzi, M. Magni, A. Colombo, C. Dragonetti, S. Caramori, C. A. Bignozzi, R. Grisorio, G. P. Suranna, M. P. Cipolla, M. Manca and D. Roberto, Electrochimica Acta, 2018, 271, 180-189.
- 381 W. L. Hoffeditz, M. J. Katz, P. Deria, G. E. Cutsail III, M. J. Pellin, O. K. Farha and J. T. Hupp, J. Phys. Chem. C, 2016, **120**, 3731–3740.
- 382 Y. Wang and T. W. Hamann, Chem. Commun., 2018, 54, 12361-12364.
- 383 M. Karpacheva, F. J. Malzner, C. Wobill, A. Büttner, E. C. Constable and C. E. Housecroft, Dyes and Pigments, 2018, **156**, 410–416.
- 384 T. Daeneke, T.-H. Kwon, A. B. Holmes, N. W. Duffy, U. Bach and L. Spiccia, Nat Chem, 2011, 3, 211-215.
- 385 I. A. Rutkowska, A. Andrearczyk, S. Zoladek, M. Goral, K. Darowicki and P. J. Kulesza, J Solid State Electrochem, 2011, 15, 2545–2552.
- 386 T. Daeneke, A. J. Mozer, T.-H. Kwon, N. W. Duffy, A. B. Holmes, U. Bach and L. Spiccia, Energy Environ. Sci., 2012, **5**, 7090–7099.
- 387 A. M. Spokoyny, T. C. Li, O. K. Farha, C. W. Machan, C. She, C. L. Stern, T. J. Marks, J. T. Hupp and C. A. Mirkin, Angew. Chem., 2010, 122, 5467-5471.
- 388 M. F. Hawthorne, J. I. Zink, J. M. Skelton, M. J. Bayer, C. Liu, E. Livshits, R. Baer and D. Neuhauser, Science, 2004, 303, 1849-1851.
- 389 T. C. Li, A. M. Spokoyny, C. She, O. K. Farha, C. A. Mirkin, T. J. Marks and J. T. Hupp, J. Am. Chem. Soc., 2010, 132,

- 4580-4582.
- 390 I. R. Perera, A. Gupta, W. Xiang, T. Daeneke, U. Bach, R. A. Evans, C. A. Ohlin and L. Spiccia, *Phys. Chem. Chem. Phys.*, 2014, 16, 12021–12028.
- 391 S. Carli, E. Benazzi, L. Casarin, T. Bernardi, V. Bertolasi, R. Argazzi, S. Caramori and C. A. Bignozzi, *Phys. Chem. Chem. Phys.*, 2016, **18**, 5949–5956.
- 392 K. Oyaizu, N. Hayo, Y. Sasada, F. Kato and H. Nishide, *Dalton Trans.*, 2013, **42**, 16090–16095.
- 393 A. Apostolopoulou, M. Vlasiou, P. A. Tziouris, C. Tsiafoulis, A. C. Tsipis, D. Rehder, T. A. Kabanos, A. D. Keramidas and E. Stathatos, *Inorg. Chem.*, 2015, 54, 3979–3988.
- 394 X. Li, Z. Ku, Y. Rong, G. Liu, L. Liu, T. Liu, M. Hu, Y. Yang, H. Wang, M. Xu, P. Xiang and H. Han, *Phys. Chem. Chem. Phys.*, 2012, **14**, 14383–14390.
- 395 L. Liu, X. Li, J. Chen, Y. Rong, Z. Ku and H. Han, *Sci. Rep.*, 2013, **3**, 2413.
- 396 Z. Zhang, P. Chen, T. N. Murakami, S. M. Zakeeruddin and M. Grätzel, *Adv. Funct. Mater.*, 2008, **18**, 341–346.
- 397 J. Cong, Y. Hao, G. Boschloo and L. Kloo, *ChemSusChem*, 2015, **8**, 264–268.
- 398 F. Kato, A. Kikuchi, T. Okuyama, K. Oyaizu and H. Nishide, *Angew. Chem. Int. Ed.*, 2012, **51**, 10177–10180.
- 399 Y. Liu, J. R. Jennings and Q. Wang, *ChemSusChem*, 2013, **6**, 2124–2131.
- 400 N. Flores-Díaz, A. Soto-Navarro, M. Freitag, G. Lamoureux and L. W. Pineda, *Solar Energy*, 2018, **167**, 76–83.
- 401 M. Cheng, X. Yang, C. Chen, J. Zhao, F. Zhang and L. Sun, *Phys. Chem. Chem. Phys.*, 2013, **15**, 15146–15152.
- 402 J. N. de Freitas, A. F. Nogueira and M.-A. D. Paoli, *J. Mater. Chem.*, 2009, **19**, 5279–5294.
- 403 Z. Chen, F. Li, H. Yang, T. Yi and C. Huang, *ChemPhysChem*, 2007, **8**, 1293–1297.
- 404 Y. Rong, Z. Ku, M. Xu, L. Liu, M. Hu, Y. Yang, J. Chen, A. Mei, T. Liu and H. Han, *RSC Adv.*, 2014, **4**, 9271–9274.
- 405 C.-P. Lee and K.-C. Ho, European Polymer Journal, 2018, 108, 420–428.
- 406 P. Wang, S. M. Zakeeruddin, P. Comte, I. Exnar and M. Grätzel, *J. Am. Chem. Soc.*, 2003, **125**, 1166–1167.
- 407 L. Fan, S. Kang, J. Wu, S. Hao, Z. Lan and J. Lin, Energy Sources Part Recovery Util. Environ. Eff., 2010, 32, 1559–1568.
- 408 P. Wang, S. M. Zakeeruddin, J. E. Moser, M. K. Nazeeruddin, T. Sekiguchi and M. Grätzel, *Nat. Mater.*, 2003, 2, 402–407.
- 409 F. Bella, N. Vlachopoulos, K. Nonomura, S. M. Zakeeruddin, M. Grätzel, C. Gerbaldi and A. Hagfeldt, *Chem. Commun.*, 2015, 51, 16308–16311.
- 410 J. N. de Freitas, A. d. S. Gonçalves, M.-A. De Paoli, J. R. Durrant and A. F. Nogueira, *Electrochimica Acta*, 2008, **53**, 7166–7172.
- 411 W. Kubo, K. Murakoshi, T. Kitamura, S. Yoshida, M. Haruki, K. Hanabusa, H. Shirai, Y. Wada and S. Yanagida, *J. Phys. Chem. B*, 2001, **105**, 12809–12815.
- 412 F. Bella, J. R. Nair and C. Gerbaldi, RSC Adv., 2013, 3,

- 15993-16001.
- 413 F. Bella, D. Pugliese, J. R. Nair, A. Sacco, S. Bianco, C. Gerbaldi, C. Barolo and R. Bongiovanni, *Phys. Chem. Chem. Phys.*, 2013, **15**, 3706–3711.
- 414 F. Bella, A. Lamberti, A. Sacco, S. Bianco, A. Chiodoni and R. Bongiovanni, *Journal of Membrane Science*, 2014, **470**, 125–131.
- 415 F. Bella, E. D. Ozzello, A. Sacco, S. Bianco and R. Bongiovanni, *International Journal of Hydrogen Energy*, 2014, **39**, 3036–3045.
- 416 F. Bella, R. Bongiovanni, R. S. Kumar, M. A. Kulandainathan and A. M. Stephan, *J. Mater. Chem. A*, 2013, **1**, 9033–9036.
- 417 A. Chiappone, F. Bella, J. R. Nair, G. Meligrana, R. Bongiovanni and C. Gerbaldi, *ChemElectroChem*, 2014, 1, 1350–1358.
- 418 K. S. Lee, Y. Jun and J. H. Park, *Nano Lett.*, 2012, **12**, 2233–2237.
- 419 H.-S. Lee, C.-H. Han, Y.-M. Sung, S. S. Sekhon and K.-J. Kim, *Current Applied Physics*, 2011, **11**, S158–S162.
- 420 A. Hagfeldt and N. Vlachopoulos, The Future of Semiconductor Oxides in Next-Generation Solar Cells, Elsevier, 2018, pp. 183–239.
- 421 S. Kitagawa, R. Kitaura and S.-i. Noro, *Angew. Chem. Int. Ed.*, 2004, **43**, 2334–2375.
- 422 T. Stergiopoulos, I. M. Arabatzis, G. Katsaros and P. Falaras, *Nano Lett.*, 2002, **2**, 1259–1261.
- 423 M. S. Michael, M. M. E. Jacob, S. R. S. Prabaharan and S. Radhakrishna, *Solid State Ionics*, 1997, **98**, 167–174.
- 424 K. M. Abraham, Z. Jiang and B. Carroll, *Chem. Mater.*, 1997, **9**, 1978–1988.
- 425 J. Li, H. Wang, G. Zhou and Z.-S. Wang, *Chem. Commun.*, 2013, **49**, 9446–9448.
- 426 F. Bella, N. N. Mobarak, F. N. Jumaah and A. Ahmad, *Electrochimica Acta*, 2015, **151**, 306–311.
- 427 Y. Li, H. Li, C. Zhong, G. Sini and J.-L. Brédas, *Npj Flex. Electron.*, 2017, 1, 1–8.
- 428 I. Yavuz and K. N. Houk, J. Phys. Chem. C, 2017, 121, 993–999.
- 429 J. Melas-Kyriazi, I.-K. Ding, A. Marchioro, A. Punzi, B. E. Hardin, G. F. Burkhard, N. Tétreault, M. Grätzel, J.-E. Moser and M. D. McGehee, *Adv. Energy Mater.*, 2011, **1**, 407–414.
- 430 Y. Zhang, K. Cao, X. Zhu, X. Li, X. Qiao, G. Tu, B. Zhang, D. Huang, Y. Shen and M. Wang, *RSC Adv.*, 2013, **3**, 14037–14043
- 431 M. Rawolle, K. Sarkar, M. A. Niedermeier, M. Schindler, P. Lellig, J. S. Gutmann, J.-F. Moulin, M. Haese-Seiller, A. S. Wochnik, C. Scheu and P. Müller-Buschbaum, ACS Appl. Mater. Interfaces, 2013, 5, 719–729.
- 432 M. Juozapavicius, B. C. O'Regan, A. Y. Anderson, J. V. Grazulevicius and V. Mimaite, *Organic Electronics*, 2012, **13**, 23–30.
- 433 J. Burschka, A. Dualeh, F. Kessler, E. Baranoff, N.-L. Cevey-Ha, C. Yi, M. K. Nazeeruddin and M. Grätzel, *J. Am. Chem. Soc.*, 2011, **133**, 18042–18045.

- 434 S. Benhattab, R. Nakar, J. W. Rodriguez Acosta, N. Berton, J. Faure-Vincent, J. Bouclé, F. Tran Van and B. Schmaltz, Dyes and Pigments, 2018, 151, 238-244.
- 435 P. Liu, B. Xu, K. M. Karlsson, J. Zhang, N. Vlachopoulos, G. Boschloo, L. Sun and L. Kloo, J. Mater. Chem. A, 2015, 3,
- 436 B. Xu, H. Tian, D. Bi, E. Gabrielsson, E. M. J. Johansson, G. Boschloo, A. Hagfeldt and L. Sun, J. Mater. Chem. A, 2013, **1**, 14467–14470.
- 437 T. Malinauskas, D. Tomkute-Luksiene, R. Sens, M. Daskeviciene, R. Send, H. Wonneberger, V. Jankauskas, I. Bruder and V. Getautis, ACS Appl. Mater. Interfaces, 2015, 7, 11107-11116.
- 438 Y. Hua, J. Zhang, B. Xu, P. Liu, M. Cheng, L. Kloo, E. M. J. Johansson, K. Sveinbjörnsson, K. Aitola, G. Boschloo and L. Sun, Nano Energy, 2016, 26, 108-113.
- 439 W. H. Nguyen, C. D. Bailie, E. L. Unger and M. D. McGehee, J. Am. Chem. Soc., 2014, 136, 10996-11001.
- 440 A. Abate, T. Leijtens, S. Pathak, J. Teuscher, R. Avolio, M. E. Errico, J. Kirkpatrik, J. M. Ball, P. Docampo, I. McPherson and H. J. Snaith, Phys. Chem. Chem. Phys., 2013, 15, 2572-2579.
- 441 D.-G. Ha, J.-J. Kim and M. A. Baldo, AIP Advances, 2016, 6,
- 442 H. Uratani, S. Kubo, K. Shizu, F. Suzuki, T. Fukushima and H. Kaji, Sci. Rep., 2016, 6, 39128.
- 443 P. Agarwala and D. Kabra, J. Mater. Chem. A, 2017, 5, 1348-1373.
- 444 M. Degbia, B. Schmaltz, J. Bouclé, J. V. Grazulevicius and F. Tran-Van, Polym. Int., 2014, 63, 1387-1393.
- 445 B. Xu, E. Sheibani, P. Liu, J. Zhang, H. Tian, N. Vlachopoulos, G. Boschloo, L. Kloo, A. Hagfeldt and L. Sun, Adv. Mater., 2014, **26**, 6629–6634.
- 446 M. Planells, A. Abate, D. J. Hollman, S. D. Stranks, V. Bharti, J. Gaur, D. Mohanty, S. Chand, H. J. Snaith and N. Robertson, J. Mater. Chem. A, 2013, 1, 6949-6960.
- 447 L. Yang, B. Xu, D. Bi, H. Tian, G. Boschloo, L. Sun, A. Hagfeldt and E. M. J. Johansson, J. Am. Chem. Soc., 2013, **135**, 7378–7385.
- 448 W. Yuan, H. Zhao and G. L. Baker, Organic Electronics, 2014, **15**, 3362–3369.
- 449 B. Xu, H. Tian, L. Lin, D. Qian, H. Chen, J. Zhang, N. Vlachopoulos, G. Boschloo, Y. Luo, F. Zhang, A. Hagfeldt and L. Sun, Adv. Energy Mater., 2015, 5, 1401185.
- 450 P. Liu, B. Xu, Y. Hua, M. Cheng, K. Aitola, K. Sveinbjörnsson, J. Zhang, G. Boschloo, L. Sun and L. Kloo, Journal of Power Sources, 2017, 344, 11-14.
- 451 B. Xu, D. Bi, Y. Hua, P. Liu, M. Cheng, M. Grätzel, L. Kloo, A. Hagfeldt and L. Sun, Energy Environ. Sci., 2016, 9, 873-877.
- 452 B. Kim, J. K. Koh, J. Kim, W. S. Chi, J. H. Kim and E. Kim, ChemSusChem, 2012, 5, 2173-2180.
- 453 J. Zhang, L. Häggman, M. Jouini, A. Jarboui, G. Boschloo, N. Vlachopoulos and A. Hagfeldt, ChemPhysChem, 2014, 15,

- 1043-1047.
- 454 J. Zhang, N. Vlachopoulos, Y. Hao, T. W. Holcombe, G. Boschloo, E. M. J. Johansson, M. Grätzel and A. Hagfeldt, ChemPhysChem, 2016, 17, 1441–1445.
- 455 W.-C. Chen, Y.-H. Lee, C.-Y. Chen, K.-C. Kau, L.-Y. Lin, C.-A. Dai, C.-G. Wu, K.-C. Ho, J.-K. Wang and L. Wang, ACS Nano, 2014, 8, 1254-1262.
- 456 Q. Liu, C. Li, K. Jiang, Y. Song and J. Pei, Particuology, 2014, **15**, 71–76.
- 457 M. Chevrier, H. Hawashin, S. Richeter, A. Mehdi, M. Surin, R. Lazzaroni, P. Dubois, B. Ratier, J. Bouclé and S. Clément, Synthetic Metals, 2017, 226, 157–163.
- 458 N. Alonso-Vante, J.-F. Nierengarten and J.-P. Sauvage, J. Chem. Soc., Dalton Trans., 1994, 1649-1654.
- 459 H. Yan, X. Wang, M. Yao and X. Yao, Progress in Natural Science: Materials International, 2013, 23, 402-407.
- 460 K. Rajeshwar, Encyclopedia of Electrochemistry, American Cancer Society, 2007.
- 461 B. Lee, C. C. Stoumpos, N. Zhou, F. Hao, C. Malliakas, C.-Y. Yeh, T. J. Marks, M. G. Kanatzidis and R. P. H. Chang, J. Am. Chem. Soc., 2014, 136, 15379-15385.
- 462 H. Sakamoto, S. Igarashi, M. Uchida, K. Niume and M. Nagai, Organic Electronics, 2012, 13, 514-518.
- 463 E. V. A. Premalal, N. Dematage, G. R. R. A. Kumara, R. M. G. Rajapakse, M. Shimomura, K. Murakami and A. Konno, Journal of Power Sources, 2012, 203, 288-296.
- 464 K. Hasan, A. K. Bansal, I. D. W. Samuel, C. Roldán-Carmona, H. J. Bolink and E. Zysman-Colman, Sci. Rep., 2015, 5, 12325.
- 465 M. Wałęsa-Chorab, R. Banasz, D. Marcinkowski, M. Kubicki and V. Patroniak, RSC Adv., 2017, 7, 50858-50867.
- 466 Z. Wei, J. Fan, C. Dai, Z. Pang and S. Han, ACS Omega, 2018, **3**, 6874–6879.
- 467 M. Freitag, Q. Daniel, M. Pazoki, K. Sveinbjörnsson, J. Zhang, L. Sun, A. Hagfeldt and G. Boschloo, Energy Environ. Sci., 2015, 8, 2634-2637.
- 468 Y. Cao, Y. Saygili, A. Ummadisingu, J. Teuscher, J. Luo, N. Pellet, F. Giordano, S. M. Zakeeruddin, J.-E. Moser, M. Freitag, A. Hagfeldt and M. Grätzel, Nat. Commun., 2017, **8**, 15390.
- 469 T. M. Koh, K. Nonomura, N. Mathews, A. Hagfeldt, M. Grätzel, S. G. Mhaisalkar and A. C. Grimsdale, J. Phys. Chem. C, 2013, 117, 15515-15522.
- 470 T. Stergiopoulos, E. Rozi, C.-S. Karagianni and P. Falaras, Nanoscale Res Lett, 2011, 6, 307.
- 471 P. Ferdowsi, Y. Saygili, S. M. Zakeeruddin, J. Mokhtari, M. Grätzel, A. Hagfeldt and L. Kavan, Electrochimica Acta, 2018, **265**, 194–201.
- 472 J.-Y. Kim, J. Y. Kim, D.-K. Lee, B. Kim, H. Kim and M. J. Ko, J. Phys. Chem. C, 2012, 116, 22759-22766.
- 473 L. Yang, R. Lindblad, E. Gabrielsson, G. Boschloo, H. Rensmo, L. Sun, A. Hagfeldt, T. Edvinsson and E. M. J. Johansson, ACS Appl. Mater. Interfaces, 2018, 10, 11572-11579.

- 474 M. K. Nazeeruddin, A. Kay, I. Rodicio, R. Humphry-Baker, E. Mueller, P. Liska, N. Vlachopoulos and M. Graetzel, *J. Am. Chem. Soc.*, 1993, **115**, 6382–6390.
- 475 S. A. Haque, Y. Tachibana, R. L. Willis, J. E. Moser, M. Grätzel, D. R. Klug and J. R. Durrant, *J. Phys. Chem. B*, 2000, **104**, 538–547.
- 476 J. Krüger, R. Plass, M. Grätzel, P. J. Cameron and L. M. Peter, *J. Phys. Chem. B*, 2003, **107**, 7536–7539.
- 477 J. Krüger, R. Plass, L. Cevey, M. Piccirelli, M. Grätzel and U. Bach, *Appl. Phys. Lett.*, 2001, **79**, 2085–2087.
- 478 Q. Yu, Y. Wang, Z. Yi, N. Zu, J. Zhang, M. Zhang and P. Wang, *ACS Nano*, 2010, **4**, 6032–6038.
- 479 J. Luo, J. Xia, H. Yang, L. Chen, Z. Wan, F. Han, H. A. Malik, X. Zhu and C. Jia, *Energy Environ. Sci.*, 2018, 11, 2035– 2045.
- 480 Y. Hou, X. Du, S. Scheiner, D. P. McMeekin, Z. Wang, N. Li, M. S. Killian, H. Chen, M. Richter, I. Levchuk, N. Schrenker, E. Spiecker, T. Stubhan, N. A. Luechinger, A. Hirsch, P. Schmuki, H.-P. Steinrück, R. H. Fink, M. Halik, H. J. Snaith and C. J. Brabec, *Science*, 2017, 358, 1192– 1197.
- 481 U. B. Cappel, T. Daeneke and U. Bach, *Nano Lett.*, 2012, **12**, 4925–4931.
- 482 J. Burschka, F. Kessler, M. K. Nazeeruddin and M. Grätzel, *Chem. Mater.*, 2013, **25**, 2986–2990.
- 483 D.-Y. Chen, W.-H. Tseng, S.-P. Liang, C.-I. Wu, C.-W. Hsu, Y. Chi, W.-Y. Hung and P.-T. Chou, *Phys. Chem. Chem. Phys.*, 2012, **14**, 11689–11694.
- 484 M. Xu, Y. Rong, Z. Ku, A. Mei, X. Li and H. Han, *J. Phys. Chem. C*, 2013, **117**, 22492–22496.
- 485 B. Xu, E. Gabrielsson, M. Safdari, M. Cheng, Y. Hua, H. Tian, J. M. Gardner, L. Kloo and L. Sun, *Adv. Energy Mater.*, 2015, **5**, 1402340.
- 486 X. Yang, W. Wang, Y. Zhang and L. Sun, *Solar Energy*, 2018, **170**, 1001–1008.
- 487 W. Wang, X. Yang, J. Li, H. Wang, J. An, L. Zhang, X. Jiang, Z. Yu and L. Sun, *Energy Technol.*, 2018, **6**, 752–758.
- 488 J. Wu, Z. Lan, J. Lin, M. Huang, Y. Huang, L. Fan, G. Luo, Y. Lin, Y. Xie and Y. Wei, *Chem. Soc. Rev.*, 2017, **46**, 5975–6023.
- 489 L. Wang, M. Al-Mamun, P. Liu, Y. Wang, H. G. Yang, H. F. Wang and H. Zhao, *NPG Asia Mater.*, 2015, 7, e226–e226.
- 490 Z. Tang, J. Wu, M. Zheng, J. Huo and Z. Lan, *Nano Energy*, 2013, **2**, 622–627.
- 491 G. Calogero, P. Calandra, A. Irrera, A. Sinopoli, I. Citro and G. D. Marco, *Energy Environ. Sci.*, 2011, 4, 1838–1844.
- 492 L. Kavan, H. Krysova, P. Janda, H. Tarabkova, Y. Saygili, M. Freitag, S. M. Zakeeruddin, A. Hagfeldt and M. Grätzel, *Electrochimica Acta*, 2017, **251**, 167–175.
- 493 I. K. Popoola, M. A. Gondal, J. M. AlGhamdi and T. F. Qahtan, Sci. Rep., 2018, 8, 12864.
- 494 H. Ellis, N. Vlachopoulos, L. Häggman, C. Perruchot, M. Jouini, G. Boschloo and A. Hagfeldt, *Electrochimica Acta*, 2013, 107, 45–51.

- 495 C. H. Yoon, R. Vittal, J. Lee, W.-S. Chae and K.-J. Kim, *Electrochimica Acta*, 2008, **53**, 2890–2896.
- 496 G. Yue, J. Wu, Y. Xiao, M. Huang, J. Lin, L. Fan and Z. Lan, *Electrochimica Acta*, 2013, **92**, 64–70.
- 497 J. G. Nam, Y. J. Park, B. S. Kim and J. S. Lee, *Scripta Materialia*, 2010, **62**, 148–150.
- 498 S. Suresh, G. E. Unni, M. Satyanarayana, A. Sreekumaran Nair and V. P. Mahadevan Pillai, *Journal of Colloid and Interface Science*, 2018, **524**, 236–244.
- 499 R. S. Moraes, E. Saito, D. M. G. Leite, M. Massi and A. S. da Silva Sobrinho, *Applied Surface Science*, 2016, **364**, 229–234.
- 500 X. Li, D. Zhang, S. Chen, H. Zhang, Z. Sun, S. Huang and X. Yin, *Nano-Micro Lett.*, 2011, **3**, 195–199.
- 501 J. Briscoe and S. Dunn, Adv. Mater., 2016, 28, 3802-3813.
- 502 W. Wei, H. Wang and Y. H. Hu, *Int. J. Energy Res.*, 2014, **38**, 1099–1111.
- 503 M. Wu and T. Ma, ChemSusChem, 2012, 5, 1343–1357.
- 504 A. Hauch and A. Georg, *Electrochimica Acta*, 2001, **46**, 3457–3466.
- 505 G. Wang, Y. Lin, X. Xiao, X. Li and W. Wang, Surf. Interface Anal., 2004, 36, 1437–1440.
- 506 E. Olsen, G. Hagen and S. Eric Lindquist, *Solar Energy Materials and Solar Cells*, 2000, **63**, 267–273.
- 507 A. R. Oganov, R. J. Hemley, R. M. Hazen and A. P. Jones, *Reviews in Mineralogy and Geochemistry*, 2013, **75**, 47–77.
- 508 L. Kavan, J.-H. Yum and M. Grätzel, *Nano Lett.*, 2011, **11**, 5501–5506.
- 509 Y. Gao, L. Chu, M. Wu, L. Wang, W. Guo and T. Ma, *Journal of Photochemistry and Photobiology A: Chemistry*, 2012, **245**, 66–71.
- 510 K. Saranya, M. Rameez and A. Subramania, European Polymer Journal, 2015, 66, 207–227.
- 511 J. Xia, L. Chen and S. Yanagida, *J. Mater. Chem.*, 2011, **21**, 4644–4649.
- 512 X. Fang, T. Ma, M. Akiyama, G. Guan, S. Tsunematsu and E. Abe, *Thin Solid Films*, 2005, **472**, 242–245.
- 513 Y. Saito, T. Kitamura, Y. Wada and S. Yanagida, *Chem. Lett.*, 2002, **31**, 1060–1061.
- 514 H. N. Tsao, J. Burschka, C. Yi, F. Kessler, M. K. Nazeeruddin and M. Grätzel, *Energy Environ. Sci.*, 2011, 4, 4921–4924.
- 515 M. Dinari, M. M. Momeni and M. Goudarzirad, *J Mater Sci*, 2016, **51**, 2964–2971.
- 516 T. Xu, W. Cao, D. Kong, X. Qin, J. Song, K. Kou, L. Chen, Q. Qiao and W. Huang, *Materials Today Communications*, 2020, **25**, 101313.
- 517 E. Benazzi, J. Mallows, G. H. Summers, F. A. Black and E. A. Gibson, *J. Mater. Chem. C*, 2019, 7, 10409–10445.
- 518 A. Nattestad, I. Perera and L. Spiccia, *Journal of Photochemistry and Photobiology C: Photochemistry Reviews*, 2016, **28**, 44–71.
- 519 M. Green, *Third Generation Photovoltaics: Advanced Solar Energy Conversion*, Springer-Verlag, Berlin Heidelberg, 2003.
- 520 J. He, H. Lindström, A. Hagfeldt and S.-E. Lindquist, *Solar Energy Materials and Solar Cells*, 2000, **62**, 265–273.

- 521 Y. Farré, M. Raissi, A. Fihey, Y. Pellegrin, E. Blart, D. Jacquemin and F. Odobel, *ChemSusChem*, 2017, **10**, 2618–2625.
- 522 J. He, H. Lindström, A. Hagfeldt and S.-E. Lindquist, *J. Phys. Chem. B*, 1999, **103**, 8940–8943.
- 523 A. Nattestad, A. J. Mozer, M. K. R. Fischer, Y.-B. Cheng, A. Mishra, P. Bäuerle and U. Bach, *Nat. Mater.*, 2010, **9**, 31–35.
- 524 E. L. Miller and R. E. Rocheleau, *J. Electrochem. Soc.*, 1997, **144**, 1995.
- 525 A. Nattestad, M. Ferguson, R. Kerr, Y.-B. Cheng and U. Bach, *Nanotechnology*, 2008, **19**, 295304.
- 526 Q. Wu, Y. Shen, L. Li, M. Cao, F. Gu and L. Wang, *Applied Surface Science*, 2013, **276**, 411–416.
- 527 M. Awais, E. Gibson, J. G. Vos, D. P. Dowling, A. Hagfeldt and D. Dini, *ChemElectroChem*, 2014, 1, 384–391.
- 528 S. Uehara, S. Sumikura, E. Suzuki and S. Mori, *Energy Environ. Sci.*, 2010, **3**, 641–644.
- 529 M. Bonomo, G. Naponiello, I. Venditti, V. Zardetto, A. D. Carlo and D. Dini, *J. Electrochem. Soc.*, 2017, **164**, H137.
- 530 C. J. Flynn, E. E. Oh, S. M. McCullough, R. W. Call, C. L. Donley, R. Lopez and J. F. Cahoon, *J. Phys. Chem. C*, 2014, 118, 14177–14184.
- 531 C. J. Wood, G. H. Summers, C. A. Clark, N. Kaeffer, M. Braeutigam, L. R. Carbone, L. D'Amario, K. Fan, Y. Farré, S. Narbey, F. Oswald, L. A. Stevens, C. D. J. Parmenter, M. W. Fay, A. L. Torre, C. E. Snape, B. Dietzek, D. Dini, L. Hammarström, Y. Pellegrin, F. Odobel, L. Sun, V. Artero and E. A. Gibson, *Phys. Chem. Chem. Phys.*, 2016, 18, 10727–10738.
- 532 S. Sumikura, S. Mori, S. Shimizu, H. Usami and E. Suzuki, *Journal of Photochemistry and Photobiology A: Chemistry*, 2008, **199**, 1–7.
- 533 R. Brisse, R. Faddoul, T. Bourgeteau, D. Tondelier, J. Leroy, S. Campidelli, T. Berthelot, B. Geffroy and B. Jousselme, *ACS Appl. Mater. Interfaces*, 2017, **9**, 2369–2377.
- 534 P. Qin, H. Zhu, T. Edvinsson, G. Boschloo, A. Hagfeldt and L. Sun, *J. Am. Chem. Soc.*, 2008, **130**, 8570–8571.
- 535 L. Li, E. A. Gibson, P. Qin, G. Boschloo, M. Gorlov, A. Hagfeldt and L. Sun, *Adv. Mater.*, 2010, **22**, 1759–1762.
- 536 S. Mori, S. Fukuda, S. Sumikura, Y. Takeda, Y. Tamaki, E. Suzuki and T. Abe, *J. Phys. Chem. C*, 2008, **112**, 16134– 16139.
- 537 L. D'Amario, J. Föhlinger, G. Boschloo and L. Hammarström, *Chem. Sci.*, 2017, **9**, 223–230.
- 538 P. Ho, L. Q. Bao, K.-S. Ahn, R. Cheruku and J. H. Kim, *Synthetic Metals*, 2016, **217**, 314–321.
- 539 L. D'Amario, R. Jiang, U. B. Cappel, E. A. Gibson, G. Boschloo, H. Rensmo, L. Sun, L. Hammarström and H. Tian, *ACS Appl. Mater. Interfaces*, 2017, **9**, 33470–33477.
- 540 C. Xin, Y. Wang, S. Zhang, L. Xu, Y. Yu, H. Xiang, W. Wu and J. Hua, *Phys. Status Solidi RRL Rapid Res. Lett.*, 2017, **11**, 1700258.
- 541 G. Natu, Z. Huang, Z. Ji and Y. Wu, *Langmuir*, 2012, **28**, 950–956.

- 542 Y. Yu, X. Li, Z. Shen, X. Zhang, P. Liu, Y. Gao, T. Jiang and J. Hua, *Journal of Colloid and Interface Science*, 2017, **490**, 380–390.
- 543 C. J. Flynn, S. M. McCullough, L. Li, C. L. Donley, Y. Kanai and J. F. Cahoon, *J. Phys. Chem. C*, 2016, **120**, 16568– 16576.
- 544 L. Favereau, Y. Pellegrin, L. Hirsch, A. Renaud, A. Planchat, E. Blart, G. Louarn, L. Cario, S. Jobic, M. Boujtita and F. Odobel, *Adv. Energy Mater.*, 2017, 7, 1601776.
- 545 Z. Huang, X. Zeng, H. Wang, W. Zhang, Y. Li, M. Wang, Y.-B. Cheng and W. Chen, *RSC Adv.*, 2014, **4**, 60670–60674.
- 546 M. Zannotti, C. J. Wood, G. H. Summers, L. A. Stevens, M. R. Hall, C. E. Snape, R. Giovanetti and E. A. Gibson, *ACS Appl. Mater. Interfaces*, 2015, 7, 24556–24565.
- 547 G. Natu, P. Hasin, Z. Huang, Z. Ji, M. He and Y. Wu, *ACS Appl. Mater. Interfaces*, 2012, **4**, 5922–5929.
- 548 L. D'Amario, G. Boschloo, A. Hagfeldt and L. Hammarström, *J. Phys. Chem. C*, 2014, **118**, 19556–19564.
- 549 H. Yang, G. H. Guai, C. Guo, Q. Song, S. P. Jiang, Y. Wang, W. Zhang and C. M. Li, J. Phys. Chem. C, 2011, 115, 12209– 12215.
- 550 M. Zannotti, E. Benazzi, L. A. Stevens, M. Minicucci, L. Bruce, C. E. Snape, E. A. Gibson and R. Giovannetti, ACS Appl. Energy Mater., 2019, 2, 7345–7353.
- 551 J. Bai, X. Xu, L. Xu, J. Cui, D. Huang, W. Chen, Y. Cheng, Y. Shen and M. Wang, *ChemSusChem*, 2013, **6**, 622–629.
- 552 Z. Huang, M. He, M. Yu, K. Click, D. Beauchamp and Y. Wu, *Angew. Chem. Int. Ed.*, 2015, **54**, 6857–6861.
- 553 Z. Yu, I. R. Perera, T. Daeneke, S. Makuta, Y. Tachibana, J. J. Jasieniak, A. Mishra, P. Bäuerle, L. Spiccia and U. Bach, *NPG Asia Mater.*, 2016, **8**, e305–e305.
- 554 O. Langmar, C. R. Ganivet, P. Schol, T. Scharl, G. de la Torre,
   T. Torres, R. D. Costa and D. M. Guldi, *J. Mater. Chem. C*,
   2018, 6, 5176–5180.
- T. Jiang, M. Bujoli-Doeuff, Y. Farré, Y. Pellegrin, E. Gautron,
  M. Boujtita, L. Cario, S. Jobic and F. Odobel, RSC Adv., 2016,
  6, 112765–112770.
- 556 O. Langmar, C. R. Ganivet, G. de la Torre, T. Torres, R. D. Costa and D. M. Guldi, *Nanoscale*, 2016, **8**, 17963–17975.
- O. Langmar, C. R. Ganivet, T. Scharl, G. de la Torre, T. Torres,R. D. Costa and D. M. Guldi, ACS Appl. Energy Mater., 2018,1, 6388–6400.
- 558 S. Du, P. Cheng, P. Sun, B. Wang, Y. Cai, F. Liu, J. Zheng and G. Lu, *Chem. Res. Chin. Univ.*, 2014, **30**, 661–665.
- 559 T. Jiang, M. Bujoli-Doeuff, E. Gautron, Y. Farré, L. Cario, Y. Pellegrin, M. Boujtita, F. Odobel and S. Jobic, *Journal of Alloys and Compounds*, 2018, 769, 605–610.
- 560 H. Kawazoe, M. Yasukawa, H. Hyodo, M. Kurita, H. Yanagi and H. Hosono, *Nature*, 1997, **389**, 939–942.
- 561 J. Bandara and J. P. Yasomanee, *Semicond. Sci. Technol.*, 2006, **22**, 20–24.
- 562 J. Ahmed, C. K. Blakely, J. Prakash, S. R. Bruno, M. Yu, Y. Wu and V. V. Poltavets, *Journal of Alloys and Compounds*, 2014, **591**, 275–279.

- 563 D. Ursu, M. Miclau, R. Banica and N. Vaszilcsin, *Materials Letters*, 2015, **143**, 91–93.
- 564 D. Xiong, Z. Xu, X. Zeng, W. Zhang, W. Chen, X. Xu, M. Wang and Y.-B. Cheng, *J. Mater. Chem.*, 2012, **22**, 24760–24768.
- 565 D. Xiong, H. Wang, W. Zhang, X. Zeng, H. Chang, X. Zhao, W. Chen and Y.-B. Cheng, *Journal of Alloys and Compounds*, 2015, 642, 104–110.
- 566 M. Yu, T. I. Draskovic and Y. Wu, *Phys. Chem. Chem. Phys.*, 2014, **16**, 5026–5033.
- 567 T. Zhu, Z. Deng, X. Fang, Z. Huo, S. Wang, W. Dong, J. Shao, R. Tao, C. Song and L. Wang, *Journal of Alloys and Com*pounds, 2016, 685, 836–840.
- 568 M. Yu, G. Natu, Z. Ji and Y. Wu, J. Phys. Chem. Lett., 2012, 3, 1074–1078.
- 569 Z. Xu, D. Xiong, H. Wang, W. Zhang, X. Zeng, L. Ming, W. Chen, X. Xu, J. Cui, M. Wang, S. Powar, U. Bach and Y.-B. Cheng, J. Mater. Chem. A, 2014, 2, 2968–2976.
- 570 A. Renaud, L. Cario, P. Deniard, E. Gautron, X. Rocquefelte, Y. Pellegrin, E. Blart, F. Odobel and S. Jobic, *J. Phys. Chem. C*, 2014, **118**, 54–59.
- 571 D. Ursu, N. Vaszilcsin, R. Bănica and M. Miclau, *J. of Materi Eng and Perform*, 2016, **25**, 59–63.
- 572 X. Xu, J. Cui, J. Han, J. Zhang, Y. Zhang, L. Luan, G. Alemu, Z. Wang, Y. Shen, D. Xiong, W. Chen, Z. Wei, S. Yang, B. Hu, Y. Cheng and M. Wang, *Sci. Rep.*, 2014, **4**, 3961.
- 573 D. Xiong, W. Zhang, X. Zeng, Z. Xu, W. Chen, J. Cui, M. Wang, L. Sun and Y.-B. Cheng, *ChemSusChem*, 2013, 6, 1432–1437.
- 574 U. Daniel, D. Anamaria, I. Sebarchievicia and M. Miclau, *Energy Procedia*, 2017, **112**, 497–503.
- 575 D. Xiong, Q. Zhang, S. K. Verma, H. Li, W. Chen and X. Zhao, *Journal of Alloys and Compounds*, 2016, **662**, 374–380.
- 576 A. Renaud, L. Cario, Y. Pellegrin, E. Blart, M. Boujtita, F. Odobel and S. Jobic, *RSC Adv.*, 2015, **5**, 60148–60151.
- 577 Z. Shi, H. Lu, Q. Liu, K. Deng, L. Xu, R. Zou, J. Hu, Y. Bando, D. Golberg and L. Li, *Energy Technol.*, 2014, **2**, 517–521.
- 578 Z. Shi, H. Lu, Q. Liu, F. Cao, J. Guo, K. Deng and L. Li, *Nanoscale Research Letters*, 2014, **9**, 608.
- 579 F. Odobel and Y. Pellegrin, *J. Phys. Chem. Lett.*, 2013, 4, 2551–2564.
- 580 K. Aiempanakit, P. Rakkwamsuk and S. Dumrongrattana, *Agric. Nat. Resour.*, 2008, **42**, 351–356.
- 581 S. Das, S. Saha, D. Sen, U. K. Ghorai, D. Banerjee and K. K. Chattopadhyay, *J. Mater. Chem. C*, 2014, **2**, 1321–1330.
- 582 J. Ghijsen, L. H. Tjeng, J. van Elp, H. Eskes, J. Westerink, G. A. Sawatzky and M. T. Czyzyk, *Phys. Rev. B*, 1988, **38**, 11322–11330.
- 583 M. E. Aguirre, R. Zhou, A. J. Eugene, M. I. Guzman and M. A. Grela, *Applied Catalysis B: Environmental*, 2017, **217**, 485–493.
- 584 J. Piippo, T. Saario, T. Laitinen, M. Bojinov and J. Hinttala, *Mater. Sci. Forum*, 1998, **289-292**, 429–438.
- 585 B. J. Ingram, T. O. Mason, R. Asahi, K. T. Park and A. J. Freeman, *Phys. Rev. B*, 2001, **64**, 155114.

- 586 M. Lee, D. Kim, Y. T. Yoon and Y. I. Kim, *Bull. Korean Chem. Soc.*, 2014, **35**, 3261–3266.
- 587 F. A. Benko and F. P. Koffyberg, *Journal of Physics and Chemistry of Solids*, 1987, **48**, 431–434.
- 588 K. Ueda and H. Hosono, *Journal of Applied Physics*, 2002, **91**, 4768–4770.
- 589 K. Ueda, S. Inoue, H. Hosono, N. Sarukura and M. Hirano, *Appl. Phys. Lett.*, 2001, **78**, 2333–2335.
- 590 B. Cui, H. Lin, Y.-z. Liu, J.-b. Li, P. Sun, X.-c. Zhao and C.-j. Liu, *J. Phys. Chem. C*, 2009, **113**, 14083–14087.
- 591 Y. Pellegrin, L. Le Pleux, E. Blart, A. Renaud, B. Chavillon, N. Szuwarski, M. Boujtita, L. Cario, S. Jobic, D. Jacquemin and F. Odobel, *Journal of Photochemistry and Photobiology* A: Chemistry, 2011, 219, 235–242.
- 592 F. Brunner, N. Marinakis, C. Wobill, M. Willgert, C. D. Ertl, T. Kosmalski, M. Neuburger, B. Bozic-Weber, T. Glatzel, E. C. Constable and C. E. Housecroft, *J. Mater. Chem. C*, 2016, 4, 9823–9833.
- 593 Y. Dong, L. Wei, R. Fan, Y. Yang and P. Wang, RSC Adv., 2016, 6, 39972–39981.
- 594 G. Alemu, J. Cui, K. Cao, J. Li, Y. Shen and M. Wang, *RSC Adv.*, 2014, **4**, 51374–51380.
- 595 J. Cui, J. Lu, X. Xu, K. Cao, Z. Wang, G. Alemu, H. Yuang, Y. Shen, J. Xu, Y. Cheng and M. Wang, J. Phys. Chem. C, 2014, 118, 16433–16440.
- 596 E. A. Gibson, A. L. Smeigh, L. Le Pleux, J. Fortage, G. Boschloo, E. Blart, Y. Pellegrin, F. Odobel, A. Hagfeldt and L. Hammarström, *Angew. Chem. Int. Ed.*, 2009, 48, 4402–4405.
- 597 F. Odobel, Y. Pellegrin, E. A. Gibson, A. Hagfeldt, A. L. Smeigh and L. Hammarström, Coordination Chemistry Reviews, 2012, 256, 2414–2423.
- 598 S. Wrede and H. Tian, *Phys. Chem. Chem. Phys.*, 2020, **22**, 13850–13861.
- 599 M. Buchalska, J. Kuncewicz, E. Świętek, P. Łabuz, T. Baran, G. Stochel and W. Macyk, *Coordination Chemistry Reviews*, 2013, **257**, 767–775.
- 600 C. J. Wood, K. C. D. Robson, P. I. P. Elliott, C. P. Berlinguette and E. A. Gibson, *RSC Adv.*, 2014, **4**, 5782–5791.
- 601 Z. Ji, G. Natu and Y. Wu, *ACS Appl. Mater. Interfaces*, 2013, 5, 8641–8648.
- 602 Z. Ji, G. Natu, Z. Huang, O. Kokhan, X. Zhang and Y. Wu, *J. Phys. Chem. C*, 2012, **116**, 16854–16863.
- 603 S. Lyu, Y. Farré, L. Ducasse, Y. Pellegrin, T. Toupance, C. Olivier and F. Odobel, RSC Adv., 2016, 6, 19928–19936.
- 604 N. Marinakis, M. Willgert, E. C. Constable and C. E. House-croft, *Sustainable Energy Fuels*, 2017, **1**, 626–635.
- 605 M. He, Z. Ji, Z. Huang and Y. Wu, J. Phys. Chem. C, 2014, 118, 16518–16525.
- 606 M. Gennari, F. Légalité, L. Zhang, Y. Pellegrin, E. Blart, J. Fortage, A. M. Brown, A. Deronzier, M.-N. Collomb, M. Boujtita, D. Jacquemin, L. Hammarström and F. Odobel, J. Phys. Chem. Lett., 2014, 5, 2254–2258.
- 607 A. Sinopoli, F. A. Black, C. J. Wood, E. A. Gibson and P. I. P.

- Elliott, Dalton Trans., 2017, 46, 1520-1530.
- 608 A. Sinopoli, C. J. Wood, E. A. Gibson and P. I. P. Elliott, *Eur. J. Inorg. Chem.*, 2016, **2016**, 2887–2890.
- 609 A. Sinopoli, C. J. Wood, E. A. Gibson and P. I. P. Elliott, *Dyes and Pigments*, 2017, **140**, 269–277.
- 610 P. Qin, M. Linder, T. Brinck, G. Boschloo, A. Hagfeldt and L. Sun, Adv. Mater., 2009, 21, 2993–2996.
- 611 P. Qin, J. Wiberg, E. A. Gibson, M. Linder, L. Li, T. Brinck, A. Hagfeldt, B. Albinsson and L. Sun, *J. Phys. Chem. C*, 2010, 114, 4738–4748.
- 612 C. J. Wood, G. H. Summers and E. A. Gibson, *Chem. Commun.*, 2015, **51**, 3915–3918.
- 613 Q.-Q. Zhang, K.-J. Jiang, J.-H. Huang, C.-W. Zhao, L.-P. Zhang, X.-P. Cui, M.-J. Su, L.-M. Yang, Y.-L. Song and X.-Q. Zhou, *J. Mater. Chem. A*, 2015, 3, 7695–7698.
- 614 Z. Liu, W. Li, S. Topa, X. Xu, X. Zeng, Z. Zhao, M. Wang, W. Chen, F. Wang, Y.-B. Cheng and H. He, *ACS Appl. Mater. Interfaces*, 2014, 6, 10614–10622.
- 615 Z. Liu, D. Xiong, X. Xu, Q. Arooj, H. Wang, L. Yin, W. Li, H. Wu, Z. Zhao, W. Chen, M. Wang, F. Wang, Y.-B. Cheng and H. He, ACS Appl. Mater. Interfaces, 2014, 6, 3448–3454.
- 616 P. Naik, A. Planchat, Y. Pellegrin, F. Odobel and A. Vasudeva Adhikari, *Solar Energy*, 2017, **157**, 1064–1073.
- 617 S. Karamshuk, S. Caramori, N. Manfredi, M. Salamone, R. Ruffo, S. Carli, C. A. Bignozzi and A. Abbotto, *Energies*, 2016, **9**, 33.
- 618 R. Brisse, C. Praveen, V. Maffeis, T. Bourgeteau, D. Tondelier, T. Berthelot, B. Geffroy, T. Gustavsson, J. M. Raimundo and B. Jousselme, *Sustainable Energy Fuels*, 2018, 2, 648–654.
- 619 A. R. Marri, F. A. Black, J. Mallows, E. A. Gibson and J. Fielden, *Dyes and Pigments*, 2019, **165**, 508–517.
- 620 C. J. Wood, M. Cheng, C. A. Clark, R. Horvath, I. P. Clark, M. L. Hamilton, M. Towrie, M. W. George, L. Sun, X. Yang and E. A. Gibson, J. Phys. Chem. C, 2014, 118, 16536– 16546.
- 621 F. Wu, S. Zhao, C. Zhong, Q. Song and L. Zhu, *RSC Adv.*, 2015, **5**, 93652–93658.
- 622 F. Wu, L. Zhu, S. Zhao, Q. Song and C. Yang, *Dyes and Pigments*, 2016, **124**, 93–100.
- 623 L. Zhu, H. B. Yang, C. Zhong and C. M. Li, *Dyes and Pigments*, 2014, **105**, 97–104.
- 624 K. A. Click, D. R. Beauchamp, B. R. Garrett, Z. Huang, C. M. Hadad and Y. Wu, *Phys. Chem. Chem. Phys.*, 2014, 16, 26103–26111.
- 625 E. Sheibani, L. Zhang, P. Liu, B. Xu, E. Mijangos, G. Boschloo, A. Hagfeldt, L. Hammarström, L. Kloo and H. Tian, RSC Adv., 2016, 6, 18165–18177.
- 626 Z. Ji, G. Natu, Z. Huang and Y. Wu, *Energy Environ. Sci.*, 2011, **4**, 2818–2821.
- 627 H. D. Weldekirstos, M.-C. Kuo, S.-R. Li, W.-L. Su, M. A. Desta, W.-T. Wu, C.-H. Kuo and S.-S. Sun, *Dyes and Pigments*, 2019, 163, 761–774.
- 628 N. T. Z. Potts, T. Sloboda, M. Wächtler, R. A. Wahyuono, V. D'Annibale, B. Dietzek, U. B. Cappel and E. A. Gibson, *J.*

- Chem. Phys., 2020, 153, 184704.
- 629 J.-F. Lefebvre, X.-Z. Sun, J. A. Calladine, M. W. George and E. A. Gibson, *Chem. Commun.*, 2014, **50**, 5258–5260.
- 630 G. H. Summers, J.-F. Lefebvre, F. A. Black, E. S. Davies, E. A. Gibson, T. Pullerits, C. J. Wood and K. Zidek, *Phys. Chem. Chem. Phys.*, 2015, 18, 1059–1070.
- 631 Y. Higashino, S. Erten-Ela and Y. Kubo, *Dyes and Pigments*, 2019, **170**, 107613.
- 632 F. Wu, J. Liu, X. Li, Q. Song, M. Wang, C. Zhong and L. Zhu, *Eur. J. Org. Chem.*, 2015, **2015**, 6850–6857.
- 633 Y.-S. Yen, W.-T. Chen, C.-Y. Hsu, H.-H. Chou, J. T. Lin and M.-C. P. Yeh, *Org. Lett.*, 2011, **13**, 4930–4933.
- 634 C.-H. Chang, Y.-C. Chen, C.-Y. Hsu, H.-H. Chou and J. T. Lin, *Org. Lett.*, 2012, **14**, 4726–4729.
- 635 L. Zhang and J. M. Cole, *ACS Appl. Mater. Interfaces*, 2015, 7, 3427–3455.
- 636 B. Jin, W. Wu, X. Zhang, F. Guo, Q. Zhang and J. Hua, *Chem. Lett.*, 2013, **42**, 1271–1272.
- 637 Y. Farré, F. Maschietto, J. Föhlinger, M. Wykes, A. Planchat, Y. Pellegrin, E. Blart, I. Ciofini, L. Hammarström and F. Odobel, *ChemSusChem*, 2020, **13**, 1844–1855.
- 638 F. A. Black, C. J. Wood, S. Ngwerume, G. H. Summers, I. P. Clark, M. Towrie, J. E. Camp and E. A. Gibson, *Faraday Discuss.*, 2017, **198**, 449–461.
- 639 G. H. Summers, G. Lowe, J.-F. Lefebvre, S. Ngwerume, M. Bräutigam, B. Dietzek, J. E. Camp and E. A. Gibson, *ChemPhysChem*, 2017, 18, 406–414.
- 640 K. Yun, S. Zhang, F. Yu, H. Ye and J. Hua, *Journal of Energy Chemistry*, 2018, **27**, 728–735.
- 641 J. Warnan, Y. Pellegrin, E. Blart, L. Zhang, A. Brown, L. Hammarström, D. Jacquemin and F. Odobel, *Dyes and Pigments*, 2014, **105**, 174–179.
- 642 E. Benazzi, G. H. Summers, F. A. Black, I. V. Sazanovich, I. P. Clark and E. A. Gibson, *Philosophical Transactions of the Royal Society A: Mathematical, Physical and Engineering Sciences*, 2019, 377, 20180338.
- 643 Y. M. Klein, N. Marinakis, E. C. Constable and C. E. House-croft, *Crystals*, 2018, **8**, 389.
- 644 A. Morandeira, G. Boschloo, A. Hagfeldt and L. Hammarström, *J. Phys. Chem. B*, 2005, **109**, 19403–19410.
- 645 A. Morandeira, J. Fortage, T. Edvinsson, L. Le Pleux, E. Blart, G. Boschloo, A. Hagfeldt, L. Hammarström and F. Odobel, *J. Phys. Chem. C*, 2008, 112, 1721–1728.
- 646 N. Grzegorzek, A. Zieleniewska, A. Schür, C. Maichle-Mössmer, M. S. Killian, D. M. Guldi and E. T. Chernick, *ChemPlusChem*, 2019, **84**, 766–771.
- 647 J. Warnan, J. Gardner, L. Le Pleux, J. Petersson, Y. Pellegrin, E. Blart, L. Hammarström and F. Odobel, *J. Phys. Chem. C*, 2014, **118**, 103–113.
- 648 Y. Farré, L. Zhang, Y. Pellegrin, A. Planchat, E. Blart, M. Boujtita, L. Hammarström, D. Jacquemin and F. Odobel, *J. Phys. Chem. C*, 2016, **120**, 7923–7940.
- 649 D. Ameline, S. Diring, Y. Farre, Y. Pellegrin, G. Naponiello, E. Blart, B. Charrier, D. Dini, D. Jacquemin and F. Odobel,

- RSC Adv., 2015, 5, 85530-85539.
- 650 L. Zhang, L. Favereau, Y. Farre, A. Maufroy, Y. Pellegrin, E. Blart, M. Hissler, D. Jacquemin, F. Odobel and L. Hammarström, RSC Adv., 2016, 6, 77184–77194.
- 651 H. Tian, J. Oscarsson, E. Gabrielsson, S. K. Eriksson, R. Lindblad, B. Xu, Y. Hao, G. Boschloo, E. M. J. Johansson, J. M. Gardner, A. Hagfeldt, H. Rensmo and L. Sun, *Sci. Rep.*, 2014, 4, 4282.
- 652 A. Maufroy, L. Favereau, F. B. Anne, Y. Pellegrin, E. Blart, M. Hissler, D. Jacquemin and F. Odobel, *J. Mater. Chem. A*, 2015, 3, 3908–3917.
- 653 V. Nikolaou, F. Plass, A. Planchat, A. Charisiadis, G. Charalambidis, P. A. Angaridis, A. Kahnt, F. Odobel and A. G. Coutsolelos, *Phys. Chem. Chem. Phys.*, 2018, **20**, 24477–24489.
- 654 J. Lu, Z. Liu, N. Pai, L. Jiang, U. Bach, A. N. Simonov, Y.-B. Cheng and L. Spiccia, *ChemPlusChem*, 2018, **83**, 711–720.
- 655 M. Bonomo, N. Barbero, F. Matteocci, A. D. Carlo, C. Barolo and D. Dini, *J. Phys. Chem. C*, 2016, **120**, 16340–16353.
- 656 G. H. Summers and E. A. Gibson, *ChemPhotoChem*, 2018, **2**, 498–506.
- 657 M. Bonomo, A. Di Carlo, R. Centore, D. Dini and A. Carella, *Solar Energy*, 2018, **169**, 237–241.
- 658 M. Borgström, E. Blart, G. Boschloo, E. Mukhtar, A. Hagfeldt, L. Hammarström and F. Odobel, *J. Phys. Chem. B*, 2005, **109**, 22928–22934.
- 659 C. J. Wood, C. A. McGregor and E. A. Gibson, *ChemElectroChem*, 2016, **3**, 1827–1836.
- 660 H. Liu, W. Xiang and H. Tao, *Journal of Photochemistry and Photobiology A: Chemistry*, 2017, **344**, 199–205.
- 661 E. A. Gibson, L. Le Pleux, J. Fortage, Y. Pellegrin, E. Blart, F. Odobel, A. Hagfeldt and G. Boschloo, *Langmuir*, 2012, 28, 6485–6493.
- 662 X. Xu, B. Zhang, J. Cui, D. Xiong, Y. Shen, W. Chen, L. Sun, Y. Cheng and M. Wang, *Nanoscale*, 2013, **5**, 7963–7969.
- 663 S. Powar, R. Bhargava, T. Daeneke, G. Götz, P. Bäuerle, T. Geiger, S. Kuster, F. A. Nüesch, L. Spiccia and U. Bach, *Electrochimica Acta*, 2015, **182**, 458–463.
- 664 Y. Farré, M. Raissi, A. Fihey, Y. Pellegrin, E. Blart, D. Jacquemin and F. Odobel, *Dyes and Pigments*, 2018, **148**, 154–166.
- 665 E. A. Gibson, A. L. Smeigh, L. Le Pleux, L. Hammarström, F. Odobel, G. Boschloo and A. Hagfeldt, J. Phys. Chem. C, 2011, 115, 9772–9779.
- 666 S. Powar, T. Daeneke, M. T. Ma, D. Fu, N. W. Duffy, G. Götz, M. Weidelener, A. Mishra, P. Bäuerle, L. Spiccia and U. Bach, Angew. Chem. Int. Ed., 2013, 52, 602–605.
- 667 L. L. Pleux, A. L. Smeigh, E. Gibson, Y. Pellegrin, E. Blart, G. Boschloo, A. Hagfeldt, L. Hammarström and F. Odobel, *Energy Environ. Sci.*, 1390, 4, 2075–2084.
- 668 W. Xiang, J. Marlow, P. Bäuerle, U. Bach and L. Spiccia, *Green Chem.*, 2016, **18**, 6659–6665.
- 669 T. Ueda, ChemElectroChem, 2018, 5, 823-838.
- 670 H. E. Moll, F. A. Black, C. J. Wood, A. Al-Yasari, A. R. Marri,

- I. V. Sazanovich, E. A. Gibson and J. Fielden, *Phys. Chem. Chem. Phys.*, 2017, **19**, 18831–18835.
- 671 T. M. A. Bakker, S. Mathew and J. N. H. Reek, *Sustainable Energy Fuels*, 2018, **3**, 96–100.
- 672 L. Zhang, G. Boschloo, L. Hammarström and H. Tian, *Phys. Chem. Chem. Phys.*, 2016, **18**, 5080–5085.
- 673 T. T. T. Pham, S. K. Saha, D. Provost, Y. Farré, M. Raissi, Y. Pellegrin, E. Blart, S. Vedraine, B. Ratier, D. Aldakov, F. Odobel and J. Bouclé, *J. Phys. Chem. C*, 2017, **121**, 129–139.
- 674 B. Xu, S. Wrede, A. Curtze, L. Tian, P. B. Pati, L. Kloo, Y. Wu and H. Tian, *ChemSusChem*, 2019, **12**, 3243–3248.
- 675 L. Tian, J. Föhlinger, P. B. Pati, Z. Zhang, J. Lin, W. Yang, M. Johansson, T. Kubart, J. Sun, G. Boschloo, L. Hammarström and H. Tian, *Phys. Chem. Chem. Phys.*, 2017, 20, 36–40.
- 676 L. Tian, J. Föhlinger, Z. Zhang, P. B. Pati, J. Lin, T. Kubart, Y. Hua, J. Sun, L. Kloo, G. Boschloo, L. Hammarström and H. Tian, *Chem. Commun.*, 2018, **54**, 3739–3742.
- 677 B. Xu, L. Tian, A. S. Etman, J. Sun and H. Tian, *Nano Energy*, 2019, **55**, 59–64.
- 678 J. Bandara and H. Weerasinghe, *Solar Energy Materials and Solar Cells*, 2005, **85**, 385–390.
- 679 A. L. Smeigh, L. L. Pleux, J. Fortage, Y. Pellegrin, E. Blart, F. Odobel and L. Hammarström, *Chem. Commun.*, 2011, 48, 678–680.
- 680 F. A. Black, C. A. Clark, G. H. Summers, I. P. Clark, M. Towrie, T. Penfold, M. W. George and E. A. Gibson, *Phys. Chem. Chem. Phys.*, 2017, **19**, 7877–7885.
- 681 Z. Huang, G. Natu, Z. Ji, M. He, M. Yu and Y. Wu, *J. Phys. Chem. C*, 2012, **116**, 26239–26246.
- 682 T. Daeneke, Z. Yu, G. P. Lee, D. Fu, N. W. Duffy, S. Makuta, Y. Tachibana, L. Spiccia, A. Mishra, P. Bäuerle and U. Bach, Adv. Energy Mater., 2015, 5, 1401387.
- 683 R. J. Dillon, L. Alibabaei, T. J. Meyer and J. M. Papanikolas, *ACS Appl. Mater. Interfaces*, 2017, **9**, 26786–26796.
- 684 M. Bonomo, D. Gatti, C. Barolo and D. Dini, *Coatings*, 2018,8, 232.
- 685 X. L. Zhang, Z. Zhang, F. Huang, P. Bäuerle, U. Bach and Y.-B. Cheng, *J. Mater. Chem.*, 2012, **22**, 7005–7009.
- 686 H. Zhu, A. Hagfeldt and G. Boschloo, *J. Phys. Chem. C*, 2007, **111**, 17455–17458.
- 687 Z. Huang, G. Natu, Z. Ji, P. Hasin and Y. Wu, *J. Phys. Chem. C*, 2011, **115**, 25109–25114.
- 688 Z. Bian, T. Tachikawa, S.-C. Cui, M. Fujitsuka and T. Majima, *Chem. Sci.*, 2012, **3**, 370–379.
- 689 O. Langmar, D. Saccone, A. Amat, S. Fantacci, G. Viscardi, C. Barolo, R. D. Costa and D. M. Guldi, *ChemSusChem*, 2017, 10, 2385–2393.
- 690 Q. Liu, L. Wei, S. Yuan, X. Ren, Y. Zhao, Z. Wang, M. Zhang, L. Shi and D. Li, *J Mater Sci*, 2015, **50**, 6668–6676.
- 691 M. Bonomo, N. Barbero, G. Naponiello, M. Giordano, D. Dini and C. Barolo, *Front. Chem.*, 2019, 7, 99.
- 692 M. Bonomo, C. Magistris, R. Buscaino, A. Fin, C. Barolo and

- D. Dini, ChemistrySelect, 2018, 3, 1066-1075.
- 693 L. Zhang, L. Favereau, Y. Farré, E. Mijangos, Y. Pellegrin, E. Blart, F. Odobel and L. Hammarström, *Phys. Chem. Chem. Phys.*, 2016, 18, 18515–18527.
- 694 L. D'Amario, L. J. Antila, B. Pettersson Rimgard, G. Boschloo and L. Hammarström, *J. Phys. Chem. Lett.*, 2015, **6**, 779–783.
- 695 J. C. Freys, J. M. Gardner, L. D'Amario, A. M. Brown and L. Hammarström, *Dalton Trans.*, 2012, **41**, 13105–13111.
- 696 O. Langmar, E. Fazio, P. Schol, G. de la Torre, R. D. Costa, T. Torres and D. M. Guldi, *Angew. Chem. Int. Ed.*, 2019, 58, 4056–4060.
- 697 A. Kolay, P. Ghosal and M. Deepa, *ACS Sustainable Chem. Eng.*, 2020, **8**, 8593–8603.
- 698 I. C. Kaya, S. Akin, H. Akyildiz and S. Sonmezoglu, *Solar Energy*, 2018, **169**, 196–205.
- 699 D. L. Ashford, M. K. Gish, A. K. Vannucci, M. K. Brennaman, J. L. Templeton, J. M. Papanikolas and T. J. Meyer, *Chem. Rev.*, 2015, **115**, 13006–13049.
- 700 J. A. Treadway, J. A. Moss and T. J. Meyer, *Inorg. Chem.*, 1999, **38**, 4386–4387.
- 701 W. J. Youngblood, S.-H. A. Lee, Y. Kobayashi, E. A. Hernandez-Pagan, P. G. Hoertz, T. A. Moore, A. L. Moore, D. Gust and T. E. Mallouk, J. Am. Chem. Soc., 2009, 131, 926–927.
- 702 L. Li, L. Duan, Y. Xu, M. Gorlov, A. Hagfeldt and L. Sun, *Chem. Commun.*, 2010, **46**, 7307–7309.
- 703 E. S. Andreiadis, M. Chavarot-Kerlidou, M. Fontecave and V. Artero, *Photochem. Photobiol.*, 2011, **87**, 946–964.
- 704 L. Duan, L. Tong, Y. Xu and L. Sun, *Energy Environ. Sci.*, 2011, **4**, 3296–3313.
- 705 Y. Zhao, J. R. Swierk, J. D. Megiatto, B. Sherman, W. J. Youngblood, D. Qin, D. M. Lentz, A. L. Moore, T. A. Moore, D. Gust and T. E. Mallouk, *PNAS*, 2012, **109**, 15612–15616.
- 706 L. Alibabaei, M. K. Brennaman, M. R. Norris, B. Kalanyan, W. Song, M. D. Losego, J. J. Concepcion, R. A. Binstead, G. N. Parsons and T. J. Meyer, *PNAS*, 2013, 110, 20008– 20013.
- 707 Y. Gao, X. Ding, J. Liu, L. Wang, Z. Lu, L. Li and L. Sun, *J. Am. Chem. Soc.*, 2013, **135**, 4219–4222.
- 708 H. Luo, W. Song, P. G. Hoertz, K. Hanson, R. Ghosh, S. Rangan, M. K. Brennaman, J. J. Concepcion, R. A. Binstead, R. A. Bartynski, R. Lopez and T. J. Meyer, *Chem. Mater.*, 2013, 25, 122–131.
- 709 X. Ding, Y. Gao, L. Zhang, Z. Yu, J. Liu and L. Sun, *ACS Catal.*, 2014, 4, 2347–2350.
- 710 W. Song, A. K. Vannucci, B. H. Farnum, A. M. Lapides, M. K. Brennaman, B. Kalanyan, L. Alibabaei, J. J. Concepcion, M. D. Losego, G. N. Parsons and T. J. Meyer, *J. Am. Chem. Soc.*, 2014, 136, 9773–9779.
- 711 J. R. Swierk, N. S. McCool, T. P. Saunders, G. D. Barber and T. E. Mallouk, *J. Am. Chem. Soc.*, 2014, **136**, 10974–10982.
- 712 L. Zhang, Y. Gao, X. Ding, Z. Yu and L. Sun, *ChemSusChem*, 2014, 7, 2801–2804.

- 713 L. Alibabaei, B. D. Sherman, M. R. Norris, M. K. Brennaman and T. J. Meyer, *PNAS*, 2015, **112**, 5899–5902.
- 714 D. L. Ashford, B. D. Sherman, R. A. Binstead, J. L. Templeton and T. J. Meyer, *Angew. Chem. Int. Ed.*, 2015, **54**, 4778– 4781.
- 715 R. L. House, N. Y. M. Iha, R. L. Coppo, L. Alibabaei, B. D. Sherman, P. Kang, M. K. Brennaman, P. G. Hoertz and T. J. Meyer, *Journal of Photochemistry and Photobiology C: Photochemistry Reviews*, 2015, **25**, 32–45.
- 716 F. Li, K. Fan, L. Wang, Q. Daniel, L. Duan and L. Sun, *ACS Catal.*, 2015, **5**, 3786–3790.
- 717 F. Li, K. Fan, B. Xu, E. Gabrielsson, Q. Daniel, L. Li and L. Sun, *J. Am. Chem. Soc.*, 2015, **137**, 9153–9159.
- 718 B. D. Sherman, D. L. Ashford, A. M. Lapides, M. V. Sheridan, K.-R. Wee and T. J. Meyer, *J. Phys. Chem. Lett.*, 2015, 6, 3213–3217.
- 719 J. R. Swierk, N. S. McCool and T. E. Mallouk, *J. Phys. Chem. C*, 2015, **119**, 13858–13867.
- 720 Z. Yu, F. Li and L. Sun, Energy Environ. Sci., 2015, 8, 760–775.
- 721 N. Armaroli and V. Balzani, Chem. Eur. J., 2016, 22, 32-57.
- 722 R. W. Call, L. Alibabaei, R. J. Dillon, R. R. Knauf, A. Nayak, J. L. Dempsey, J. M. Papanikolas and R. Lopez, ACS Appl. Mater. Interfaces, 2016, 8, 12282–12290.
- 723 M. V. Sheridan, B. D. Sherman, R. L. Coppo, D. Wang, S. L. Marquard, K.-R. Wee, N. Y. Murakami Iha and T. J. Meyer, *ACS Energy Lett.*, 2016, 1, 231–236.
- 724 B. D. Sherman, J. J. Bergkamp, C. L. Brown, A. L. Moore, D. Gust and T. A. Moore, *Energy Environ. Sci.*, 2016, 9, 1812–1817.
- 725 B. D. Sherman, M. V. Sheridan, K.-R. Wee, S. L. Marquard, D. Wang, L. Alibabaei, D. L. Ashford and T. J. Meyer, *J. Am. Chem. Soc.*, 2016, **138**, 16745–16753.
- 726 K.-R. Wee, B. D. Sherman, M. K. Brennaman, M. V. Sheridan, A. Nayak, L. Alibabaei and T. J. Meyer, J. Mater. Chem. A, 2016, 4, 2969–2975.
- 727 M. Yamamoto, L. Wang, F. Li, T. Fukushima, K. Tanaka, L. Sun and H. Imahori, *Chem. Sci.*, 2016, 7, 1430–1439.
- 728 L. Alibabaei, R. J. Dillon, C. E. Reilly, M. K. Brennaman, K.-R. Wee, S. L. Marquard, J. M. Papanikolas and T. J. Meyer, *ACS Appl. Mater. Interfaces*, 2017, **9**, 39018–39026.
- 729 M. V. Sheridan, D. J. Hill, B. D. Sherman, D. Wang, S. L. Marquard, K.-R. Wee, J. F. Cahoon and T. J. Meyer, *Nano Lett.*, 2017, 17, 2440–2446.
- 730 B. D. Sherman, Y. Xie, M. V. Sheridan, D. Wang, D. W. Shaffer, T. J. Meyer and J. J. Concepcion, ACS Energy Lett., 2017, 2, 124–128.
- 731 D. Wang, M. V. Sheridan, B. Shan, B. H. Farnum, S. L. Marquard, B. D. Sherman, M. S. Eberhart, A. Nayak, C. J. Dares, A. K. Das, R. M. Bullock and T. J. Meyer, *J. Am. Chem. Soc.*, 2017, 139, 14518–14525.
- 732 O. Suryani, Y. Higashino, J. Y. Mulyana, M. Kaneko, T. Hoshi, K. Shigaki and Y. Kubo, *Chem. Commun.*, 2017, 53, 6784–6787.

- 733 D. Wang, B. H. Farnum, M. V. Sheridan, S. L. Marquard, B. D. Sherman and T. J. Meyer, *ACS Appl. Mater. Interfaces*, 2017, 9, 33533–33538.
- 734 K. P. Sokol, W. E. Robinson, J. Warnan, N. Kornienko, M. M. Nowaczyk, A. Ruff, J. Z. Zhang and E. Reisner, *Nat. Energy*, 2018, 3, 944–951.
- 735 D. Wang, S. L. Marquard, L. Troian-Gautier, M. V. Sheridan, B. D. Sherman, Y. Wang, M. S. Eberhart, B. H. Farnum, C. J. Dares and T. J. Meyer, *J. Am. Chem. Soc.*, 2018, 140, 719–726.
- 736 P. Xu, T. Huang, J. Huang, Y. Yan and T. E. Mallouk, *PNAS*, 2018, **115**, 6946–6951.
- 737 S. Yun, N. Vlachopoulos, A. Qurashi, S. Ahmad and A. Hagfeldt, *Chem. Soc. Rev.*, 2019, **48**, 3705–3722.
- 738 D. Wang, L. Wang, M. D. Brady, C. J. Dares, G. J. Meyer, T. J. Meyer and J. J. Concepcion, J. Phys. Chem. C, 2019, 123, 30039–30045.
- 739 D. Wang, J. Hu, B. D. Sherman, M. V. Sheridan, L. Yan, C. J. Dares, Y. Zhu, F. Li, Q. Huang, W. You and T. J. Meyer, *PNAS*, 2020, 117, 13256–13260.
- 740 J. J. Concepcion, J. W. Jurss, P. G. Hoertz and T. J. Meyer, *Angew. Chem. Int. Ed.*, 2009, **48**, 9473–9476.
- 741 D. L. Ashford, W. Song, J. J. Concepcion, C. R. K. Glasson, M. K. Brennaman, M. R. Norris, Z. Fang, J. L. Templeton and T. J. Meyer, J. Am. Chem. Soc., 2012, 134, 19189–19198.
- 742 D. M. Ryan, M. K. Coggins, J. J. Concepcion, D. L. Ashford, Z. Fang, L. Alibabaei, D. Ma, T. J. Meyer and M. L. Waters, *Inorg. Chem.*, 2014, 53, 8120–8128.
- 743 L. Duan, A. Fischer, Y. Xu and L. Sun, *J. Am. Chem. Soc.*, 2009, **131**, 10397–10399.
- 744 L. Duan, F. Bozoglian, S. Mandal, B. Stewart, T. Privalov, A. Llobet and L. Sun, *Nat. Chem.*, 2012, 4, 418–423.
- 745 K. Hanson, D. A. Torelli, A. K. Vannucci, M. K. Brennaman, H. Luo, L. Alibabaei, W. Song, D. L. Ashford, M. R. Norris, C. R. K. Glasson, J. J. Concepcion and T. J. Meyer, *Angew. Chem. Int. Ed.*, 2012, 51, 12782–12785.
- 746 H. Lee, L. J. Kepley, H. G. Hong and T. E. Mallouk, *J. Am. Chem. Soc.*, 1988, **110**, 618–620.
- 747 H. Lee, L. J. Kepley, H. G. Hong, S. Akhter and T. E. Mallouk, *J. Phys. Chem.*, 1988, **92**, 2597–2601.
- 748 B. Shan, M. K. Brennaman, L. Troian-Gautier, Y. Liu, A. Nayak, C. M. Klug, T.-T. Li, R. M. Bullock and T. J. Meyer, J. Am. Chem. Soc., 2019, 141, 10390–10398.
- 749 R. J. Kamire, K. L. Materna, W. L. Hoffeditz, B. T. Phelan, J. M. Thomsen, O. K. Farha, J. T. Hupp, G. W. Brudvig and M. R. Wasielewski, J. Phys. Chem. C, 2017, 121, 3752–3764.
- 750 L. Wang, D. E. Polyansky and J. J. Concepcion, *J. Am. Chem. Soc.*, 2019, **141**, 8020–8024.
- 751 C. J. Flynn, S. M. McCullough, E. Oh, L. Li, C. C. Mercado, B. H. Farnum, W. Li, C. L. Donley, W. You, A. J. Nozik, J. R. McBride, T. J. Meyer, Y. Kanai and J. F. Cahoon, ACS Appl. Mater. Interfaces, 2016, 8, 4754–4761.
- 752 S. M. McCullough, J. M. Evans, T. Moot, A. D. Taggart, L. Troian-Gautier and J. F. Cahoon, *ACS Appl. Energy Mater.*,

- 2020, 3, 1496–1505.
- 753 A. D. Taggart, J. M. Evans, L. Li, K. J. Lee, J. L. Dempsey, Y. Kanai and J. F. Cahoon, *ACS Appl. Energy Mater.*, 2020, **3**, 10702–10713.
- 754 L. Li, L. Duan, F. Wen, C. Li, M. Wang, A. Hagfeldt and L. Sun, *Chem. Commun.*, 2012, **48**, 988–990.
- 755 K. A. Click, D. R. Beauchamp, Z. Huang, W. Chen and Y. Wu, *J. Am. Chem. Soc.*, 2016, **138**, 1174–1179.
- 756 N. Kaeffer, J. Massin, C. Lebrun, O. Renault, M. Chavarot-Kerlidou and V. Artero, *J. Am. Chem. Soc.*, 2016, **138**, 12308–12311.
- 757 R. J. Kamire, M. B. Majewski, W. L. Hoffeditz, B. T. Phelan, O. K. Farha, J. T. Hupp and M. R. Wasielewski, *Chem. Sci.*, 2016, **8**, 541–549.
- 758 C. E. Creissen, J. Warnan and E. Reisner, *Chem. Sci.*, 2018, **9**, 1439–1447.
- 759 C. E. Creissen, J. Warnan, D. Antón-García, Y. Farré, F. Odobel and E. Reisner, *ACS Catal.*, 2019, **9**, 9530–9538.
- 760 G. Sahara, R. Abe, M. Higashi, T. Morikawa, K. Maeda, Y. Ueda and O. Ishitani, *Chem. Commun.*, 2015, **51**, 10722– 10725.
- 761 H. Kumagai, G. Sahara, K. Maeda, M. Higashi, R. Abe and O. Ishitani, *Chem. Sci.*, 2017, **8**, 4242–4249.
- 762 B. Shan, S. Vanka, T.-T. Li, L. Troian-Gautier, M. K. Brennaman, Z. Mi and T. J. Meyer, *Nat. Energy*, 2019, **4**, 290–299.
- 763 D. F. Watson, A. Marton, A. M. Stux and G. J. Meyer, *J. Phys. Chem. B*, 2003, **107**, 10971–10973.
- 764 E. M. James, T. J. Barr and G. J. Meyer, *ACS Appl. Energy Mater.*, 2018, **1**, 859–867.
- 765 K. L. Materna, R. H. Crabtree and G. W. Brudvig, *Chem. Soc. Rev.*, 2017, **46**, 6099–6110.
- 766 T.-T. Li, B. Shan and T. J. Meyer, *ACS Energy Lett.*, 2019, **4**, 629–636.
- 767 L. Wu, M. K. Brennaman, A. Nayak, M. Eberhart, A. J. M. Miller and T. J. Meyer, *ACS Cent. Sci.*, 2019, **5**, 506–514.
- 768 L. Wu, M. Eberhart, B. Shan, A. Nayak, M. K. Brennaman, A. J. M. Miller, J. Shao and T. J. Meyer, *ACS Appl. Mater. Interfaces*, 2019, **11**, 4560–4567.
- 769 D. L. Ashford, C. R. K. Glasson, M. R. Norris, J. J. Concepcion, S. Keinan, M. K. Brennaman, J. L. Templeton and T. J. Meyer, *Inorg. Chem.*, 2014, 53, 5637–5646.
- 770 D. L. Ashford, M. K. Brennaman, R. J. Brown, S. Keinan, J. J. Concepcion, J. M. Papanikolas, J. L. Templeton and T. J. Meyer, *Inorg. Chem.*, 2015, 54, 460–469.
- 771 L. Wang, D. W. Shaffer, G. F. Manbeck, D. E. Polyansky and J. J. Concepcion, *ACS Catal.*, 2020, **10**, 580–585.
- 772 C. Decavoli, C. L. Boldrini, N. Manfredi and A. Abbotto, *Eur. J. Inorg. Chem.*, 2020, **2020**, 978–999.
- 773 V. Nikolaou, A. Charisiadis, G. Charalambidis, A. G. Coutsolelos and F. Odobel, *J. Mater. Chem. A*, 2017, **5**, 21077–21113.
- 774 J. J. Concepcion, J. W. Jurss, M. R. Norris, Z. Chen, J. L. Templeton and T. J. Meyer, *Inorg. Chem.*, 2010, 49, 1277–1279.

- 775 Z. Chen, J. J. Concepcion and T. J. Meyer, *Dalton Trans.*, 2011, **40**, 3789–3792.
- 776 M. R. Norris, J. J. Concepcion, D. P. Harrison, R. A. Binstead, D. L. Ashford, Z. Fang, J. L. Templeton and T. J. Meyer, J. Am. Chem. Soc., 2013, 135, 2080–2083.
- 777 M. R. Norris, J. J. Concepcion, Z. Fang, J. L. Templeton and T. J. Meyer, *Angew. Chem. Int. Ed.*, 2013, **52**, 13580–13583.
- 778 J. J. Concepcion, D. K. Zhong, D. J. Szalda, J. T. Muckerman and E. Fujita, *Chem. Commun.*, 2015, **51**, 4105–4108.
- 779 D. W. Shaffer, Y. Xie and J. J. Concepcion, *Chem. Soc. Rev.*, 2017, **46**, 6170–6193.
- 780 R. Matheu, M. Z. Ertem, J. Benet-Buchholz, E. Coronado, V. S. Batista, X. Sala and A. Llobet, *J. Am. Chem. Soc.*, 2015, 137, 10786–10795.
- 781 N. Vereshchuk, R. Matheu, J. Benet-Buchholz, M. Pipelier, J. Lebreton, D. Dubreuil, A. Tessier, C. Gimbert-Suriñach, M. Z. Ertem and A. Llobet, J. Am. Chem. Soc., 2020, 142, 5068–5077.
- 782 Y. Xie, D. W. Shaffer, A. Lewandowska-Andralojc, D. J. Szalda and J. J. Concepcion, *Angew. Chem. Int. Ed.*, 2016, **55**, 8067–8071.
- 783 D. W. Shaffer, Y. Xie, D. J. Szalda and J. J. Concepcion, *J. Am. Chem. Soc.*, 2017, **139**, 15347–15355.
- 784 M. L. Helm, M. P. Stewart, R. M. Bullock, M. R. DuBois and D. L. DuBois, *Science*, 2011, **333**, 863–866.
- 785 A. D. Wilson, R. H. Newell, M. J. McNevin, J. T. Muckerman, M. Rakowski DuBois and D. L. DuBois, *J. Am. Chem. Soc.*, 2006, **128**, 358–366.
- 786 T. E. Rosser, M. A. Gross, Y.-H. Lai and E. Reisner, *Chem. Sci.*, 2016, 7, 4024–4035.
- 787 B. Shan, B. D. Sherman, C. M. Klug, A. Nayak, S. L. Marquard, Q. Liu, R. M. Bullock and T. J. Meyer, *J. Phys. Chem. Lett.*, 2017, **8**, 4374–4379.
- 788 M. S. Eberhart, D. Wang, R. N. Sampaio, S. L. Marquard, B. Shan, M. K. Brennaman, G. J. Meyer, C. Dares and T. J. Meyer, J. Am. Chem. Soc., 2017, 139, 16248–16255.
- 789 M. D. Brady, R. N. Sampaio, D. Wang, T. J. Meyer and G. J. Meyer, *J. Am. Chem. Soc.*, 2017, **139**, 15612–15615.
- 790 M. K. Gish, A. M. Lapides, M. K. Brennaman, J. L. Templeton, T. J. Meyer and J. M. Papanikolas, J. Phys. Chem. Lett., 2016, 7, 5297–5301.
- 791 R. E. Blankenship, D. M. Tiede, J. Barber, G. W. Brudvig, G. Fleming, M. Ghirardi, M. R. Gunner, W. Junge, D. M. Kramer, A. Melis, T. A. Moore, C. C. Moser, D. G. Nocera, A. J. Nozik, D. R. Ort, W. W. Parson, R. C. Prince and R. T. Sayre, *Science*, 2011, 332, 805–809.
- 792 D. R. Ort, S. S. Merchant, J. Alric, A. Barkan, R. E. Blankenship, R. Bock, R. Croce, M. R. Hanson, J. M. Hibberd, S. P. Long, T. A. Moore, J. Moroney, K. K. Niyogi, M. A. J. Parry, P. P. Peralta-Yahya, R. C. Prince, K. E. Redding, M. H. Spalding, K. J. van Wijk, W. F. J. Vermaas, S. von Caemmerer, A. P. M. Weber, T. O. Yeates, J. S. Yuan and X. G. Zhu, *PNAS*, 2015, 112, 8529–8536.
- 793 J. R. Bolton, S. J. Strickler and J. S. Connolly, *Nature*, 1985, 316, 495–500.

- 794 M. C. Hanna and A. J. Nozik, *Journal of Applied Physics*, 2006, **100**, 074510.
- 795 H. Pettersson, K. Nonomura, L. Kloo and A. Hagfeldt, *Energy Environ. Sci.*, 2012, **5**, 7376–7380.
- 796 J. Takashima, T. Fujii and K. Furusaki, *Meet. Abstr.*, 2008, MA2008-02, 478.
- 797 M. M. Lee, J. Teuscher, T. Miyasaka, T. N. Murakami and H. J. Snaith, *Science*, 2012, **338**, 643–647.
- 798 H.-S. Kim, C.-R. Lee, J.-H. Im, K.-B. Lee, T. Moehl, A. Marchioro, S.-J. Moon, R. Humphry-Baker, J.-H. Yum, J. E. Moser, M. Grätzel and N.-G. Park, Sci. Rep., 2012, 2, 591.
- 799 J. Jeong, M. Kim, J. Seo, H. Lu, P. Ahlawat, A. Mishra, Y. Yang, M. A. Hope, F. T. Eickemeyer, M. Kim, Y. J. Yoon, I. W. Choi, B. P. Darwich, S. J. Choi, Y. Jo, J. H. Lee, B. Walker, S. M. Zakeeruddin, L. Emsley, U. Rothlisberger, A. Hagfeldt, D. S. Kim, M. Grätzel and J. Y. Kim, *Nature*, 2021.
- 800 N. Mariotti, M. Bonomo, L. Fagiolari, N. Barbero, C. Gerbaldi, F. Bella and C. Barolo, *Green Chem.*, 2020, **22**, 7168–7218.
- 801 J. M. Kroon, N. J. Bakker, H. J. P. Smit, P. Liska, K. R. Thampi, P. Wang, S. M. Zakeeruddin, M. Grätzel, A. Hinsch, S. Hore, U. Würfel, R. Sastrawan, J. R. Durrant, E. Palomares, H. Pettersson, T. Gruszecki, J. Walter, K. Skupien and G. E. Tulloch, *Prog. Photovolt. Res. Appl.*, 2007, **15**, 1–18.
- 802 R. Sastrawan, J. Beier, U. Belledin, S. Hemming, A. Hinsch, R. Kern, C. Vetter, F. M. Petrat, A. Prodi-Schwab, P. Lechner and W. Hoffmann, *Prog. Photovolt. Res. Appl.*, 2006, 14, 697–709.
- BO3 D. Magistri, A. Lembo, V. Mirruzzo, G. Viscardi, P. Mariani,
  R. Manfredi, V. Liparoti, A. Lanuti, C. Bignozzi, T. M. Brown,
  L. Bonandini, E. Busatto, D. Colonna, A. Di Carlo, A. Giglielmotti, A. Guidobaldi, R. Boaretto, D. Prencipe, C. Barolo,
  R. Tagliaferro, S. Caramori, L. Vesce, G. Soscia, A. Smarra,
  R. Riccitelli and A. Reale, HOPV15, 2015.
- 804 M. L. Parisi, S. Maranghi, L. Vesce, A. Sinicropi, A. Di Carlo and R. Basosi, *Renewable and Sustainable Energy Reviews*, 2020, **121**, 109703.
- 805 N. Papageorgiou, Y. Athanassov, M. Armand, P. Bonhôte, H. Pettersson, A. Azam and M. Grätzel, *J. Electrochem. Soc.*, 1996, **143**, 3099.
- 806 H. Pettersson, T. Gruszecki, L.-H. Johansson and P. Johander, *Solar Energy Materials and Solar Cells*, 2003, 77, 405–413.
- 807 S. Burnside, S. Winkel, K. Brooks, V. Shklover, M. Gra"tzel, A. Hinsch, R. Kinderman, C. Bradbury, A. Hagfeldt and H. Pettersson, *Journal of Materials Science: Materials in Electronics*, 2000, 11, 355–362.
- 808 N. Yan, C. Zhao, S. You, Y. Zhang and W. Li, *Chinese Chemical Letters*, 2020, **31**, 643–653.
- 809 M. Li, C. Zhao, Z.-K. Wang, C.-C. Zhang, H. K. H. Lee, A. Pockett, J. Barbé, W. C. Tsoi, Y.-G. Yang, M. J. Carnie, X.-Y. Gao, W.-X. Yang, J. R. Durrant, L.-S. Liao and S. M. Jain, Adv. Energy Mater., 2018, 8, 1801509.
- 810 H. K. H. Lee, J. Wu, J. Barbé, S. M. Jain, S. Wood, E. M.

- Speller, Z. Li, F. A. Castro, J. R. Durrant and W. C. Tsoi, J. Mater. Chem. A, 2018, 6, 5618-5626.
- 811 H. Matsui, K. Yamamoto and K. Okada, OPTICS & PHOTON-ICS International Congress 2019, 2019.
- 812 H. Matsui, K. Okada, T. Kitamura and N. Tanabe, Solar En-
- ergy Materials and Solar Cells, 2009, **93**, 1110–1115.
- 813 O. Pekkola, C. Lungenschmied, P. Fejes, A. Handreck, W. Hermes, S. Irle, C. Lennartz, C. Schildknecht, P. Schillen, P. Schindler, R. Send, S. Valouch, E. Thiel and I. Bruder, Sci. Rep., 2018, 8, 9208.



Ana Belen Muñoz García is Associate Professor of Physical Chemistry at the Department of Physics "Ettore Pancini" of the University of Naples Federico II since March 2021. She obtained her PhD in Theoretical Chemistry in 2011 under the supervision of prof. L. Seijo at the Universidad Autónoma de Madrid, with research stages with Prof. E. Artacho (University of Cambridge, 2008) and Prof. Emily A. Carter (Princeton University, 2010). After one year as Postdoctoral Research Associate in the Carter group at Princeton University, she joined the University of Naples Federico II as Assistant Professor at the Department of Chemical Sciences (2012-2017, untenured) and then at the Department of Physics (2018-2021, tenured). Her scientific activity addresses the simulations of complex physico-chemical processes in functional materials with ab initio methods, from DFT-based approaches to post-HF methods. Her current research focuses on heterogeneous functional materials for energy conversion and storage, and she is PI of a three-year project on solar cells funded by the Italian Agency on Energy and Environment. Among other awards, she has been selected by Physical Chemistry Chemical Physics among the Emerging Investigators 2020 in the field of Physical Chemistry and Atomic and Molecular Physics.



Dr Iacopo Benesperi received his MSc in Materials Science from the Department of Chemistry, Turin University, Italy, under the supervision of Prof Barolo. During his PhD in Chemistry at Monash University, Melbourne, Australia, he worked on hole conducting materials for perovskite solar cells under the supervision of the late Prof. Spiccia, Dr Simonov, Prof. Bach and Prof. Cheng. After two years as a research fellow at Uppsala University in Dr

Freitag's group, researching on copper complex charge transport materials for thin-film solar cells, he is now working with Dr Freitag at Newcastle University.



Gerrit Boschloo is associate professor in physical chemistry at Uppsala University (Sweden), where he leads a research group focusing on perovskite solar cells, dye-sensitized solar cells and fundamental studies of the semiconductor / electrolyte interface. He received his PhD in 1996 at Delft University of Technology (the Netherlands). He is author of more than 250 peer-reviewed papers (h-index 75), and is co-founder of Dyenamo AB.



Dr Javier J. Concepcion received his B.S. in Chemistry from Universidad Central de Las Villas in Cuba and his Ph.D. from Pontificia Universidad Catolica de Chile. Following postdoctoral work at Georgia Tech with William S. Rees, Jr. and UNC-Chapel Hill with Thomas J. Meyer, he worked as Senior Scientist in the Energy Frontier Research Center (EFRC) at UNC-Chapel Hill from 2009 to 2013. He is currently the group leader of the Artificial Photosynthesis group at Brookhaven National Laboratory (BNL) and he serves as BNL's Institutional Coordinator in the solar energy hub Center for Hybrid Approaches in Solar Energy to Liquid Fuels (CHASE). His research interests include chemical, electrochemical and photochemical catalytic processes related to artificial photosynthesis. Ground and excited state proton-coupled electron transfer (PCET), kinetic and mechanistic studies related to homogeneous and heterogeneous small molecule activation with a combination of experimental techniques and high-level theoretical calculations.



Professor Jared Delcamp received his PhD degree from the University of Illinois Urbana-Champaign (United States, advisor M. Christina White) in 2010. After postdoctoral stays at the Swiss Federal Institute of Technology Lausanne (EPFL, Switzerland, advisor Michael Grätzel) and Georgia Institute of Technology (United States, advisor Seth Marder), he began his independent career at the University of Mississippi in 2013. Jared is currently an associate professor at the University of Mississippi in the Department of Chemistry and Biochemistry studying the photophysical properties of photocatalysts for CO2 reduction as well as organic materials for dye-sensitized solar cells, fundamental electron transfer reactions, and NIR/SWIR emissive material applications.



Dr Libby Gibson joined Newcastle University as a Lecturer in Physical Chemistry in 2014 and was promoted to Reader in Energy Materials in 2018. Prior to her current role, she held a University of Nottingham Anne McLaren Research Fellowship and a Royal Society Dorothy Hodgkin Research Fellowship. She obtained her PhD in 2007 from the University of York, supervised by Robin Perutz FRS and Anne-Kathrin Duhme-Klair. Research in her group focuses on solar cell and solar fuel devices that function at a molecular level and challenge the conventional solid-state photovoltaic technologies. Her current ERC-funded project focuses on developing transparent p-type semiconductors for tandem solar cells and artificial photosynthesis.



Professor Gerald (Jerry) J. Meyer attended the State University of New York at Albany (B.S. Chemistry and Mathematics, 1985) and the University of Wisconsin at Madison (Ph.D., 1989), working with Arthur B. Ellis. Following a post-doctoral appointment with Thomas J. Meyer at the University of North Carolina at Chapel Hill, he joined the faculty at Johns Hopkins University in 1991 where he served as Chair and was the Bernard N. Baker Chair of Chemistry. In 2014, he moved to the Chemistry Department at UNC-Chapel Hill where he is now a Professor of Chemistry, Vice-Chair for Diversity, and Director of the Solar Hub entitled CHASE: the Center for Hybrid Approaches in Solar Energy to Liquid Fuels. Professor Meyer has published over 250 peerreviewed papers, 5 book chapters, and 3 patents. Jerry takes particular pride in the success of the outstanding undergraduate students (35), graduate students (53) and post-doctoral associates (13) he has had the pleasure to work with over the last thirty years. Outside of chemistry Jerry enjoys trail running, camping, fishing, kayaking, tennis, and hiking with his friends and family.



Michele Pavone is Associate Professor of Physical Chemistry at the Department of Chemical Sciences of the University of Naples Federico II. After the PhD in theoretical spectroscopy (2007) with prof. Vincenzo Barone in Naples and a two-year post-doctoral fellowship with prof. Emily Carter at Princeton University (2010-2012), he started his independent research group that is active in the field of quantum chemistry applied to molecular and materials sciences. During the last decade he has been PI of several national grants on the design of new hybrid materials for energy conversion and storage. His achievements in the field of physical chemistry and theoretical chemistry have been recognized by the Italian Chemical Society with the Semerano Prize 2008 and Roetti Prize 2016, and he has been featured by the Journal of Materials Chemistry A among the Emerging Investigators 2017.



Henrik Pettersson, CEO of Dyenamo AB, has more than 20 years of experience in the field of dye-sensitized solar cells and modules. He is specialized in applied aspects of the DSC, such as module technology, reliability testing and production technology.



Professor Anders Hagfeldt is Vice-Chancellor of Uppsala University since 2021 and Professor of Physical Chemistry. He obtained his PhD at Uppsala University in 1993. His research has

focused on the fields of dye-sensitized solar cells, perovskite solar cells and solar fuels. He has published more than 560 scientific papers that have received over 94,000 citations. 2014-2020 he was Professor at The Swiss Federal Institute of Technology in Lausanne (EPFL).



Dr Marina Freitag is presently a Royal Society University Research Fellow and Newcastle Academic Track Fellow at School of Natural and Environmental Sciences, Newcastle University, UK. She is continuing her work in coordination chemistry, energy relevant materials and solar cells. Previously, she held as an Assistant Professor at the Department of Chemistry, Uppsala University and a post-doc position at EPFL (Prof. Anders Hagfeldt's). She received her PhD degree with Prof. Galoppini from Rutgers University, USA, and her BSc, in Chemistry from Freie Universität Berlin, Germany. She is the inventor of the so-called Zombie-cell and she contributed to recent breakthroughs in dye-sensitized solar cells for low-power applications.